



ANALYTICAL STUDY OF STRESS FIELDS IN WIND TURBINE BLADES

Dissertation

submitted to and approved by the

Department of Architecture, Civil Engineering and Environmental Sciences
University of Braunschweig – Institute of Technology

and the

Department of Civil and Environmental Engineering
University of Florence

in candidacy for the degree of a

Doktor-Ingenieur (Dr.-Ing.) /

Dottore di Ricerca in Civil and Environmental Engineering^{*)}

by

Luca Taglialegne

born September 7th, 1979

from Pisa, Italy

Submitted on	23 August, 2018
Oral examination on	08 November, 2018
Professorial advisors	Prof. Laura De Lorenzis Prof. Stefano Bennati

2019

^{*)} Either the German or the Italian form of the title may be used.



UNIVERSITÀ
DEGLI STUDI
FIRENZE



UNIVERSITÀ
DEGLI STUDI
DI PERUGIA



UNIVERSITÀ
DI PISA



Technische
Universität
Braunschweig

International Doctorate “Civil and Environmental Engineering” – XXX cycle
Universities of Florence, Perugia and Pisa – TU Braunschweig

ANALYTICAL STUDY OF
STRESS FIELDS IN WIND TURBINE BLADES

Candidate: Luca Taglialegne

Supervisors: Stefano Bennati (University of Pisa)
Paolo S. Valvo (University of Pisa)
Laura De Lorenzis (TU Braunschweig)

Curriculum: Solid, Fluid and Materials Mechanics

Contents

Index	i
Preface	v
Summary	vii
Acknowledgments	ix
I Introduction and state of the art	3
1 Wind energy and wind turbines	5
1.1 Background	5
1.2 Wind as a resource	6
1.2.1 Wind in Europe	6
1.3 Wind turbines	6
1.3.1 Classification	6
1.3.2 Horizontal Axis Wind Turbines (HAWT)	9
1.3.3 Betz's elementary theory	9
1.4 Wind turbine blades	12
1.4.1 Aerodynamics of wind turbine blades	13
1.4.2 Structural design of wind turbine blades	16
1.4.3 Blade materials	16
1.4.4 Loads	17
1.4.5 Design Standards	19
1.5 Structural analysis of wind turbine blades	21
1.5.1 Full 3D models	21
1.5.2 1D FE models	22
1.5.3 Cross-sectional analysis models	24
1.6 Final remarks	25
2 Analysis of variable cross sections beams	27
2.1 Beams of variable cross section	27
2.2 Definition of beam	27
2.3 Geometric classification of beams	28
2.4 Variable cross section beams: state of the art	29
2.4.1 Stress analysis	30
2.4.2 Beam models	32
2.5 Remarks on the application to wind turbine blades	32

3	Objectives and methods	33
3.1	Objectives of the thesis	33
3.2	Methods	34
3.2.1	Simplification of a complex problem	34
3.2.2	Application to real blades	36
3.3	Outline of the thesis	36
II	Theory	39
4	Wedge and truncated wedge	41
4.1	Wedge	41
4.1.1	Problem of Michell	41
4.1.2	Problem of Carothers	42
4.1.3	Finite wedge clamped at one end	43
4.1.4	Non-dimensionalisation of the solution	49
4.1.5	Dimensionless functions	51
4.1.6	Discussion of results	55
4.1.7	Final remarks	58
4.2	Truncated wedge	65
4.2.1	Definition of the problem	65
4.2.2	Non-dimensionalisation of the solution	66
4.2.3	Solution for stresses	68
4.2.4	Discussion of results	71
4.2.5	Final remarks	83
5	Extended shear stress formula	89
5.1	The need for a different approach	89
5.2	Extended shear stress formula for tapered beams	90
5.2.1	Derivation of the extended shear stress formula	90
5.2.2	Linearly tapered rectangular cross section beam	92
5.2.3	Negligible distributed loads	93
5.3	Final remarks	93
III	Results	95
6	Linearly tapered beams	97
6.1	Thin rectangular cross section beam	97
6.1.1	Numerical example: geometry and loads	98
6.1.2	Discussion of the results	99
6.2	Box girder	105
6.2.1	Vertically tapered box girder	107
6.2.2	Horizontally tapered box girder	118
6.2.3	Doubly tapered box girder	121
6.3	Conical beam	123
6.3.1	Numerical results	125
7	10MW DTU wind turbine blade	131
7.1	DTU 10MW Reference Wind Turbine	131
7.2	Simplification of the geometry	136
7.3	Numerical results	140

7.3.1	Definition of the load cases	140
7.3.2	Finite element analysis	141
7.3.3	Comments on the results	146
IV	Conclusions	157
8	Conclusions and future developments	159
8.1	Conclusions	159
8.2	Future developments	160
	Bibliography	163

Preface

Nowadays, energy production based on the burning of fossil fuels or the splitting of the uranium atom have been increasingly questioned due to the associated environmental hazards. Air, water, and soil pollution have reached such high levels that a decisive change not only in the habits of industrialised populations, but in energy policy as well can no longer be avoided or postponed. One possible solution has been envisaged in the development of a network of power generators driven by different renewable energy sources: wind energy is one of those promising “green” sources. Supporting such change toward environmentally less affecting technologies is not only an economic matter, but also a moral commitment.

As a child, I’ve always been a lover of nature. Environmental disasters have always been a great concern to me. Then, I grew up as an engineer. Huge complex structures – which are made of innovative materials, which are subjected to long and demanding life cycles, which are difficult to design, to manufacture and to keep in service – fascinate and lure me. Modern wind turbines are a challenge. I like challenges.

This thesis is the final report of the research activities conducted as a Ph.D. student of the “International Doctorate in Civil and Environmental Engineering”, a joint programme between the Universities of Florence, Perugia, and Pisa, Italy, and the TU Braunschweig, Germany. The programme lasted for three years, starting from November 2014.

The majority of my research activity was conducted at the Department of Civil and Industrial Engineering of the University of Pisa under the supervision of Prof. Stefano Bennati and Prof. Paolo S. Valvo. In my first year, I spent three months and a half at the Institute of Scientific Computing, TU Braunschweig, hosted by Prof. Hermann G. Matthies. In my second year, I carried out a three-month visit at the Department of Wind Energy at the Technical University of Denmark (DTU Wind Energy), collaborating with Dr. Martin A. Eder. There, I had the opportunity to meet numerous experts in the field of wind energy, and in particular to learn many aspects of the structural design of wind turbine blades. In my last year of the Ph.D. programme, I spent five months at the Institute of Applied Mechanics, TU Braunschweig, working under the guidance of my German supervisor, Prof. Laura De Lorenzis.

Summary

The thesis investigates the stress distributions in wind turbine blades with thin-walled variable cross sections, considering the effects of variable geometry – in particular taper – along the length.

The structural design of wind turbine blades is a challenging task due to many specific aspects: complex geometry, material anisotropy and inhomogeneity, stochastic loading conditions, fluid-structure interaction, etc. [DNV-GL-0376; GDWT-2002]. From a mechanical perspective, a rotor blade can be schematised as a long rotating cantilever beam with hollow cross section. The outer contour is shaped as an aerodynamic airfoil formed by two shell structures glued together. In the inner part of the cross section, a box-like structure (the so-called *box-girder*) bears the intense loads and furnishes strength and stiffness to the structure [GDWT-2002]. Due to taper and twisting, the geometrical characteristics of the cross sections differ from one another. It is known from the literature that a variable cross section affects the stress distribution within a beam [Timoshenko and Gere, 1972]. Nevertheless, there are only a few specific studies aiming at quantifying such effects [Balduzzi, Aminbaghai, Sacco, Füssl, Eberhardsteiner, and Auricchio, 2016; Hodges, Rajagopal, Ho, and Yu, 2010].

The thesis aims at shedding light on the differences in the stress distributions acting in prismatic and non-prismatic beams. The approach strategy has been to drastically simplify the initial problem with the aim of identifying the relevant governing parameters. The geometry of a real wind turbine blade has been first simplified: from the multi-cellular airfoil to a box girder and to a single web panel. Once solved the simplest problems, various sources of complexity have been gradually reintegrated into the problem in the attempt of applying the obtained results to a real wind turbine blade. For the sake of simplicity, the effects of curved centrelines and twisting cross sections have not been taken into account. Thus, focus is on the effects of taper. Furthermore, when material properties have been considered, the hypotheses of homogeneity and isotropic linear elasticity have been assumed. Attention has been focused on the box-girder, under the commonly accepted assumption that this structural component bears the most relevant and intense loadings [GDWT-2002]. As a further step in simplification, the analysis has been restricted to the web panel of the box girder, which can be schematised as a tapered cantilever beam with a thin rectangular cross section.

First, the web panel has been modelled in the context of elasticity theory. The web can be regarded as a truncated wedge, clamped at one end (the *root*) and loaded at the other one (the *tip*). This probably represents the simplest example of tapered beam. The solution to this problem has been obtained through the proper superposition [Knops and Villaggio, 1999] of the solutions to the classical problems of Mitchell [Mitchell, 1900] and of Carothers [Carothers, 1914], related to an infinite elastic wedge loaded by a tip load and a couple, respectively. As the classical solutions are given in polar coordinates, a relevant task was to express them in Cartesian coordinates. Next, by properly rotating the reference system, the expressions for the stresses on the sections of the wedge were obtained. Also, strains and displacements (under the hypothesis of homogeneous and isotropic material) were derived, imposing the boundary conditions equivalent to a clamped mid-line at the root section.

Even though the analytical expressions of such a solution are not user-friendly, many interesting pieces of information could be retrieved from this analysis. In particular, neglecting boundary effects at the root, such a solution can be considered an exact solution. It was possible to point out that not only shear force, but also axial force and bending moment introduce shear stresses in the sections. Those stresses related to the taper are of the same order of magnitude of those introduced by the shear force, and

therefore have a relevant effect on the overall stress distribution. Also, the analysis of the exact solution confirmed that the normal stresses due to bending show a substantially linear distribution equivalent to that of the well-known Navier equation [Timoshenko and Goodier, 1951]. Lastly, finite element (FE) analyses conducted with Abaqus software [Dassault Systèmes, 2013] showed an excellent agreement between the analytical and numerical solutions.

Under the assumption that Navier's equation still holds for tapered beams – hypothesis confirmed by the results obtained on the truncated wedge and here extrapolated to more complex cross-section geometries – a more user-friendly, yet analytical, solution was then derived. Following Jourawski's classical approach, from the equilibrium of a portion of a tapered beam, an extended shear stress formula is derived. The extended shear stress formula extends some previous results by Bleich [Bleich, 1932]. The obtained formula takes into account the variation along the length of the beam of the section area, first and second moments of area, as well as the possible presence of distributed loads (not accounted for in Bleich's approach).

Based on Navier's equation and the extended shear stress formula, a complete solution for the stress field in a thin rectangular cross-section beam was deduced through equilibrium considerations. This solution was then compared with the exact solution stemming from the classical theory of elasticity, and with FE results. No substantial differences were detected in the three different approaches. This results encourages the attempt of extending the extended shear stress formula to more general cases. Hence, the applicability of the extended shear stress formula also to spatial problems was verified: in particular, for a linearly tapered beam of rectangular cross section (the so-called box girder), and a truncated conical beam of hollow section. For both problems, analytical expressions for the full stress tensor were determined. Comparison with FE analyses resulted in practically identical results.

Finally, the box-girder solution was applied for the stress analysis of the 10MW Reference Wind Turbine blade developed at the Danish Technical University (DTU) [Bak, Zahle, Bitsche, Yde, Henriksen, and Hansen, 2013b]. Good agreement with the results of FE analyses was obtained. Moreover, the comparison between the stresses computed according to the prismatic and tapered beam solutions shows relevant differences between the two approaches and highlights importance of choosing the more accurate model proposed in the thesis.

In conclusion, it can be stated confidently that taper significantly affects the stress distribution in beams. This difference is particularly evident concerning the shear stresses, whose behaviour may change both qualitatively and quantitatively with respect to what is predicted by the classical prismatic beam theory. Although the differences in the shear stress components may have a relatively small impact on the overall stress in terms of von Mises stresses (in particular for cases in which the normal stresses are prevalent), however the shear stresses introduced by taper could impact on specific aspects of the design of wind turbine blades, for example the many adhesively joined elements of the cross-section. Thus, it is hoped that the obtained results can be translated into rules and tools for the practical design of wind turbine blades, with advantage of the wind energy industry in terms of cost and material savings.

The thesis consists of three parts. In the first part, some pieces of information on the technology of wind energy and wind turbines are given. Also, the state of the art of the modeling of non-prismatic beams is discussed, with focus on tapered beams. After some first remarkable results obtained at the beginning of the 20th century, the literature survey shows that only in recent years there has been an increase of interest on the subject. In the second part, all the theoretical details that lead to the approach which is subject of the present thesis are deepened. In the third part, the results of the application of the proposed strategy to both elementary and more complex geometries are shown. Lastly, application to the 10MW Reference Wind Turbine blade [GDWT-2002] is illustrated and discussed.

Acknowledgments

If you are reading this dissertation, this means that I was able to conclude part of a long journey. And if so, I need to confess that I was never alone on my way, and that many people gave their contribution, directly or indirectly.

First of all, and for sure, I have to thank all of my supervisors. I would like to thank Professor Stefano Bennati because it is only his merit if I was able to begin such journey. Professor Paolo S. Valvo was precious for his wise suggestions, his warming humour, and his true friendship. Professor Laura De Lorenzis had a fundamental role with her pragmatism and constructive criticism, that very often helps more than compliments.

I would also like to cite Professor Hermann G. Matthies, along with his many collaborators (Cosima, Thilo, Noemi, and many others), that in my first year abroad welcomed me at TU Braunschweig and made me feel like at home.

A really special thank and a warm salute goes to Martin A. Eder, who invited me at Risø, offering me more than a mere supervision. He warmly welcomed me in the new – for me – land of wind energy.

Thanks to Paolo, so similar to me, so different from me: he was a good friend and a good adviser. It was always nice to share with him the office in Pisa.

And speaking of friends, when you depart for a new journey you can never imagine who you will meet far from home: I found ten Ph.D. students, which were both colleagues, and fellows. And which now, I call them all friends.

There are people that are not physically with you, but never leave you alone. Emily was not there, but was always there. And I know, she will always be there, in my heart. Thanks!

Finally, I would like to thank my parents: in their way, they were always on my side. I feel it even if I usually don't show.

Thanks to all those that I have just cited!

Thanks to all those which I could not cite here. Don't hate me! I know you! I will remember you!

STRESS FIELDS IN WIND TURBINE BLADES WITH THIN-WALLED VARIABLE CROSS SECTIONS

How many roads must a man walk down
Before you can call him a man?
How many seas must a white dove sail
Before she sleeps in the sand?
Yes, how many times must the cannon balls fly
Before they're forever banned?
The answer my friend is blowin' in the wind
The answer is blowin' in the wind.

Bob Dylan, "*Blowin' in the wind*" (1962)

Part I

Introduction and state of the art

Chapter 1

Wind energy and wind turbines

Summary. In this first chapter, a brief introduction to the basic concepts of wind energy are given. In particular, the basics of Betz's elementary theory are discussed, giving the explanation to the steady increase of rotor swept area size in the past decades.

Also, some preliminary considerations on different wind turbine designs are given: attention is focused on those aspects of aerodynamics and structural design which justify the shape of wind turbine blades (tapered, twisted and curved).

Some notes are given on the structural analysis tools used for the design of wind turbine blades. In particular, there are discussed the main differences between full 3D finite elements analyses and equivalent 1D beam models. Unfortunately, those tools have been designed on the assumption that the beam is a prismatic beam, and no reassurance are given that the same approach is still valid for non-prismatic beams.

1.1 Background

Nowadays, energy production based on the burning of fossil fuels or the splitting of the uranium atom have been increasingly questioned not only due to the continual increases in oil prices and concerns over limited fossil fuel resources, but also to the associated environmental hazards. Air, water and soil pollution have reached such high levels that a decisive change not only in the habits of industrialised populations, but in energy policy as well can no longer be avoided or postponed.

One possible solution has been found in the development of a network of power generators driven by different renewable energy sources, characterised by low CO₂ associated emissions and a great potential in mitigating climate change [Burton, Jenkins, Sharpe, and Bossanyi, 2011; Hau, 2013]. In 2007 the European Union adopted policies by which 20% of all energy production should be from renewable sources by 2020 [Commission Européenne, 2008]. Such changes in energy policy continue to be enacted rapidly, with many countries adopting ambitious programs to reduce greenhouse gas emissions by up to 80% by 2050.

Wind energy has the potentials of effectively contribute in reaching those challenging objectives.

The idea of harvesting power from the wind is by no means a modern one: ancient windmills are integral parts of the landscape in many parts of the European countryside. The primary purposes of those machines were to pump water or grind grain. The use of turbines with the objective to generate electric energy from wind was first attempted in the early 20th century, thanks to the Danish scientist and inventor Poul La-Cour (Figure 1.1). Since his first pioneering attempts, many advancements have been made to optimise the design and increase the energy output of wind turbines. During the 1970s the so-called Danish wind turbine concept emerged as the most successful: it consists of a three-bladed, upwind, variable speed, horizontal rotor with full-span control of the blade pitch and an induction generator drive train. This apparently simple architecture proved to be remarkably efficient and has nowadays become the standard adopted by the major large-scale wind turbine producers [Hau, 2013].



Figure 1.1: Poul La-Cour, 1846–1908 [Hau, 2013].

1.2 Wind as a resource

Wind energy utilisation is an indirect form of solar energy utilisation. The radiation from the Sun is absorbed by the Earth surface and then returned to the atmosphere above. Such absorption of solar energy depends on both the nature of Earth's surface (clear land, forest, water, etc.) and time (in particular, the time of the day and the seasonal change in climate induced by the axial tilt of the Earth). The non-uniform heat absorption produces gradients of temperature, density and pressure, resulting in air masses moving from one place to another. It has been calculated that the overall power of those moving masses of air is $4 \cdot 10^{12}$ kW·h [Hau, 2013].

Moreover, wind flow speed and direction are influenced by topography, such as mountain ranges or valleys.

1.2.1 Wind in Europe

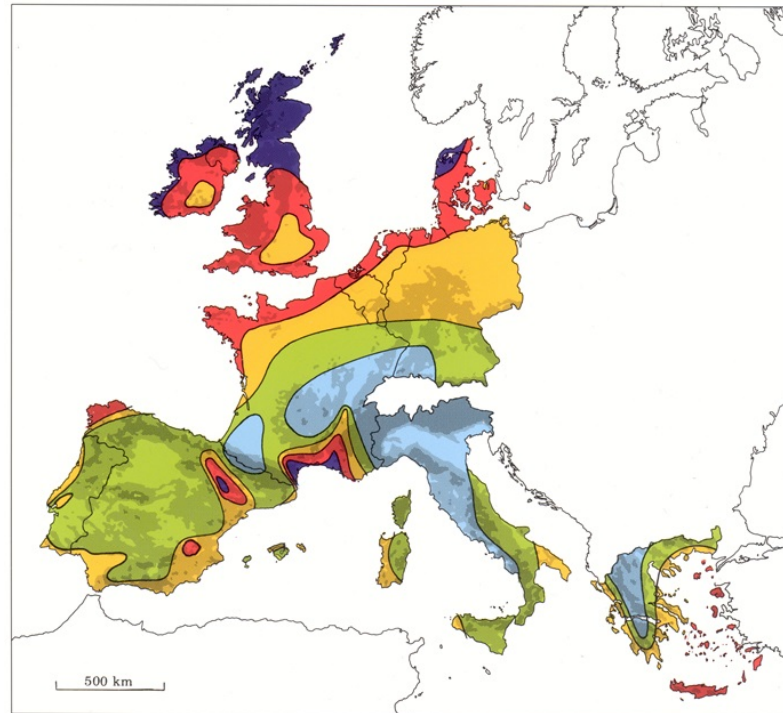
Due to the great geographical diversity of Europe, two areas with completely different meteorological conditions can be identified: the Northern area and the Mediterranean area [Hau, 2013].

The map from the European Wind Atlas (Figure 1.2) shows the mean annual wind speed at 50 m height, divided into five zones. In addition, the data for five roughness classes from *open sea* to *protected terrain* are specified. Moreover, the wind atlas specifies the mean specific annual energy content in watts per square meter of rotor-swept area. High wind velocities occur primarily from the North-Western coastal region of France up to Denmark, along the British and Irish coasts, and in the Southern France. In the Mediterranean zone, relatively high wind speeds are found on the islands, for example on Sardinia and the islands of the Eastern Mediterranean Sea. Also, relatively large areas in the European interior exhibit reasonable wind speeds [Troen and Petersen, 1989].

1.3 Wind turbines

1.3.1 Classification

Wind energy converters, or turbines, can be classified in accordance with their aerodynamic function and according to their constructional design (Table 1.1).



Wind resources ¹ at 50 metres above ground level for five different topographic conditions									
Sheltered terrain ²		Open plain ³		At a sea coast ⁴		Open sea ⁵		Hills and ridges ⁶	
$m s^{-1}$	Wm^{-2}	$m s^{-1}$	Wm^{-2}	$m s^{-1}$	Wm^{-2}	$m s^{-1}$	Wm^{-2}	$m s^{-1}$	Wm^{-2}
> 6.0	> 250	> 7.5	> 500	> 8.5	> 700	> 9.0	> 800	> 11.5	> 1800
5.0-6.0	150-250	6.5-7.5	300-500	7.0-8.5	400-700	8.0-9.0	600-800	10.0-11.5	1200-1800
4.5-5.0	100-150	5.5-6.5	200-300	6.0-7.0	250-400	7.0-8.0	400-600	8.5-10.0	700-1200
3.5-4.5	50-100	4.5-5.5	100-200	5.0-6.0	150-250	5.5-7.0	200-400	7.0- 8.5	400- 700
< 3.5	< 50	< 4.5	< 100	< 5.0	< 150	< 5.5	< 200	< 7.0	< 400

1. The resources refer to the power present in the wind. A wind turbine can utilize between 20 and 30% of the available resource. The resources are calculated for an air density of $1.23 kg m^{-3}$, corresponding to standard sea level pressure and a temperature of $15^{\circ}C$. Air density decreases with height but up to 1000 m a.s.l. the resulting reduction of the power densities is less than 10%.
2. Urban districts, forest and farm land with many windbreaks (roughness class 3).
3. Open landscapes with few windbreaks (roughness class 1). In general, the most favourable inland sites on level land are found here.
4. The classes pertain to a straight coastline, a uniform wind rose and a land surface with few windbreaks (roughness class 1). Resources will be higher, and closer to open sea values, if winds from the sea occur more frequently, i.e. the wind rose is not uniform and/or the land protrudes into the sea. Conversely, resources will generally be smaller, and closer to land values, if winds from land occur more frequently.
5. More than 10 km offshore (roughness class 0).
6. The classes correspond to 50% overspeeding and were calculated for a site on the summit of a single axisymmetric hill with a height of 400 metres and a base diameter of 4 km. The overspeeding depends on the height, length and specific setting of the hill.

Figure 1.2: European Wind Atlas [Troen and Petersen, 1989].

From the aerodynamic point of view, the converter may capture the wind power thanks to the aerodynamic *drag* of the air stream impacting on the surfaces of the rotor; otherwise, it may take advantage of the aerodynamic *lift*, i.e. the force generated by the motion of the air around suitably shaped surfaces called *airfoils*.

The orientation of the axis of rotation of the rotor determines another classification criterion of wind turbines. In particular, a turbine with a shaft mounted horizontally is known as a Horizontal Axis Wind Turbine (HAWT). A Vertical Axis Wind Turbine (VAWT) has its shaft normal to the ground [Schubel and Crossley, 2012].

One of the most elementary VAWT concepts is the Savonius rotor, in which the rotor is put in rotation by the drag force acting on simply shaped curved sheets. On the other hand, in the Darrieus rotor the blades (shaped as a *troposkein*¹) produce lift while rotating. The shape of the Darrieus rotor is useful for decrease the stress experienced by the blades, but increases the difficulty of the manufacture. The concept of VAWT has the advantage of a simple design – including the possibility of housing mechanical (i.e. the *gearbox*) and electrical (i.e. the *generator*) components at ground level – and avoids the need of yaw

¹The troposkein is a curve which has the shape of a rope anchored at its ends and spun around its long axis at a constant angular velocity [Ashwill and Leonard, 1986].

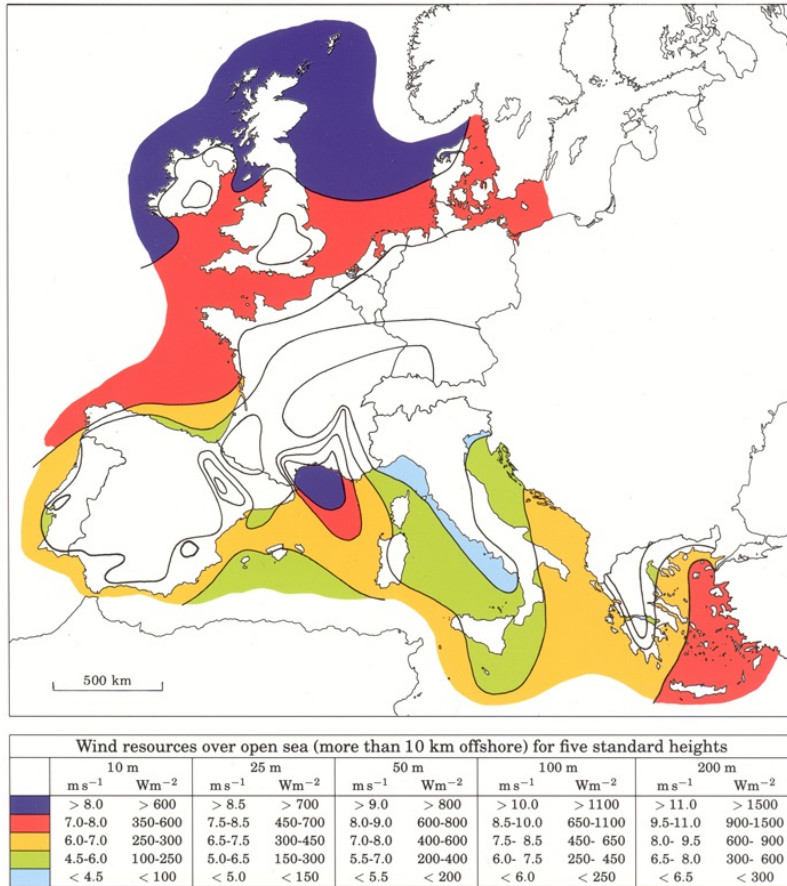


Figure 1.3: European offshore resources [Troen and Petersen, 1989].

Design	Orientation	Aerodynamic force	Diagram
Savonius rotor	VAWT	Drag	
Darrieus rotor	VAWT	Lift	
Modern Wind Turbine	HAWT	Lift	

Table 1.1: some of the modern rotor designs [Hau, 2013].

systems. This is countered by disadvantages such as its inability to self-start (in case of Darrieus rotors) and not being able to control power output, or speed, by pitching the rotor blades [Hau, 2013].

On the other hand, the superiority shown by HAWTs is largely based on the fact that rotor speed and

power output can be controlled by pitching the rotor blades about their longitudinal axis. At the same time, the ability to control the pitch is an effective protection against overspeed in extreme wind conditions. Moreover, the blades can be more easily optimised to the aim of achieving highest aerodynamic efficiency. As a matter of fact, the HAWT has emerged as the dominant design configuration [Burton et al., 2011]. In the following of this thesis, the attention will be focused on HAWTs and their blades.

1.3.2 Horizontal Axis Wind Turbines (HAWT)

In Figure 1.4 a schematic view of a generic HAWT is depicted. The wind energy is caught by the *rotor*. The rotor may have different numbers of *rotor blades*, ranging from one to three depending on the specific design. The rotor blades are connected to the *rotor shaft* by means of a *hub*, which contains the blade *bearings* and the blade *pitch mechanism*. The *drive train* of the wind turbine consists of the mechanical components which convert the energy harvested by the rotor rotation into electrical energy. In particular, the rotor hub, the rotor shaft, the *gearbox*, and the *generator* are all parts of the drive train. The gearbox converts the low-speed motion of the rotor shaft to the high-speed motion of the generator shaft. In particular, the rotational speed of a wind turbine rotor is approximately 20 to 50 rpm and the rotational speed of the generator shafts ranges approximately from 1000 to 3000 rpm [Hansen, 2008]. All the drive train components are housed in the *nacelle*, which is mounted on top of a *tower*. The nacelle and rotor are turned into the wind direction by the *yaw system*. The tower also contains the access stairs to the nacelle, and houses the *power cables* that descend to the ground level. At the ground, the *transformer* and the connection to the electrical grid are located.

1.3.3 Betz's elementary theory

The purpose of a wind turbine is the conversion of the kinetic energy contained in the wind into mechanical energy, and then into electrical energy. By applying simple physical laws, Betz [1928] (English translation from the original article in German [Betz, 1927]) was able to show that the power extractable from an air stream passing through a given cross-sectional area, A , is proportional to the power contained in the air stream itself.

We define the power of the wind, P , as the kinetic energy of the air mass flowing at velocity v across a given cross section per unit time:

$$P = \frac{1}{2} \rho A v^3, \quad (1.1)$$

where ρ is the density of the air.

Following the motion of the mass flow across the rotor, the extraction of energy from the wind implies a reduction of the kinetic energy in the stream. Under the hypothesis of incompressible fluid, this means that the flow velocity behind the wind turbine must decrease. Betz's theory relies on the equilibrium between the conditions in front of and behind the wind turbine. As depicted in Figure 1.6, let us refer to the cross sections of the stream as: cross section 1 (sufficiently far in front of the rotor, so that the motion of the fluid is undisturbed by the rotor), and cross section 2 (behind the rotor).

Thus, the mechanical output of the wind turbine is:

$$P_{\text{mech}} = \frac{1}{2} c_P \rho A v_1^3, \quad (1.2)$$

where c_P is called *ideal power coefficient*. It can be proved that, being

$$c_P = \frac{1}{2} \left[1 - \left(\frac{v_2}{v_1} \right)^2 \right] \left(1 + \frac{v_2}{v_1} \right), \quad (1.3)$$

c_P cannot theoretically exceed the value 0.593, which is widely known as *Betz's factor*. In Figure 1.7 the variation of the ideal power coefficient depending on the flow velocity ratio $\frac{v_2}{v_1}$ is shown. In such a plot the theoretical limit of c_P is clearly evident.

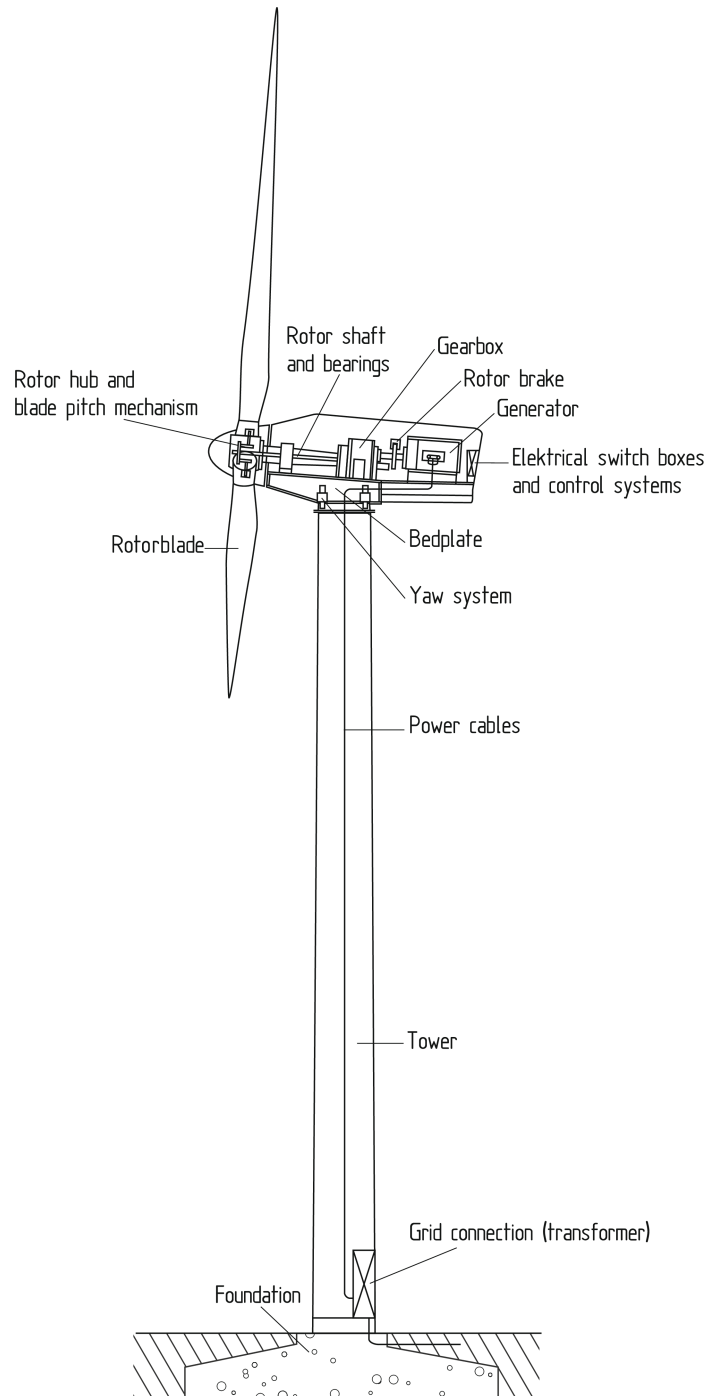


Figure 1.4: components of a HAWT [Hau, 2013].



Figure 1.5: Albert Betz, 1885–1968 [Hau, 2013].

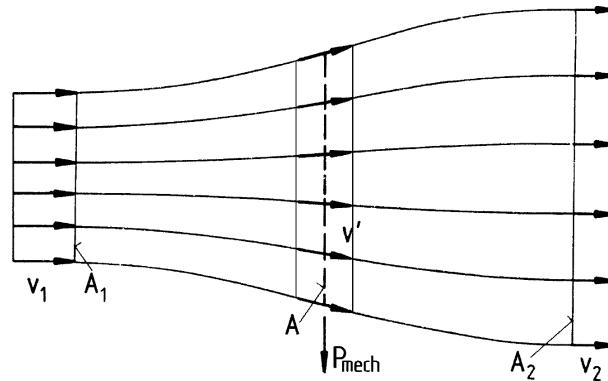


Figure 1.6: flow of a stream of air crossing a wind turbine rotor [Hau, 2013].

For the derivation and a more detailed presentation of the elementary theory of Betz we suggest to refer to Betz [1928] and Hau [2013].

The ideal power coefficient c_P is a theoretical parameter which has been derived upon some rough simplifications and cannot describe the real behaviour of a wind turbine rotor. Nevertheless, it gives important information on the upper limit of the efficiency that can be reachable by a real wind turbine. More detailed aerodynamic analyses enable the definition of a “corrected” parameter, called *rotor power coefficient*, or c_{PR} , that more realistically takes into account the efficiency of the rotor. Each rotor design shows a specific power coefficient [Hau, 2013]. This result also justifies the prevailing adoption of HAWTs (see Figure 1.8, where the *tip speed ratio*, λ , is the ratio between the tangential velocity of the rotor blade tip and the undisturbed wind velocity). HAWTs, relying mainly on the generation of lift to put the rotor in rotation, outclass the performances of other designs. Moreover, HAWTs with at least three blades show an excellent behaviour, being their associated rotor power coefficient very close to the theoretical Betz limit factor [Hansen, 2008].

A detailed analysis on the efficiency of the different rotor designs is far behind the present thesis, but the brief description presented here helps us to justify the need that wind turbine producers has to increase the size of the rotors. In fact, Equation 1.2 shows that the only choice to enhance the production of electric energy is to increase the cross section of the rotor (and consequently the blade length), once the location of a wind plant (and so the average wind speed typical of such location) and the specific design of rotor are selected.

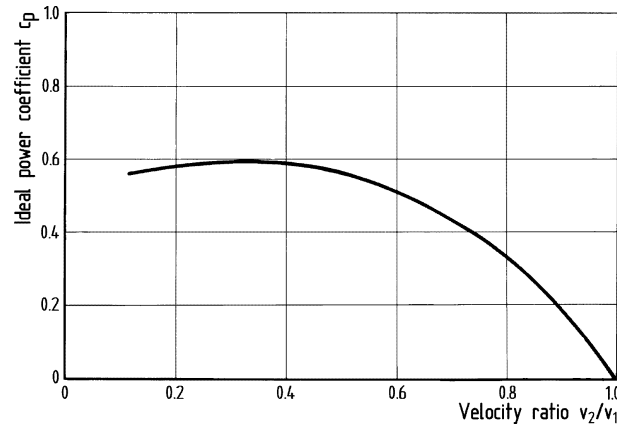


Figure 1.7: ideal power coefficient versus the flow velocity ratio [Hau, 2013].

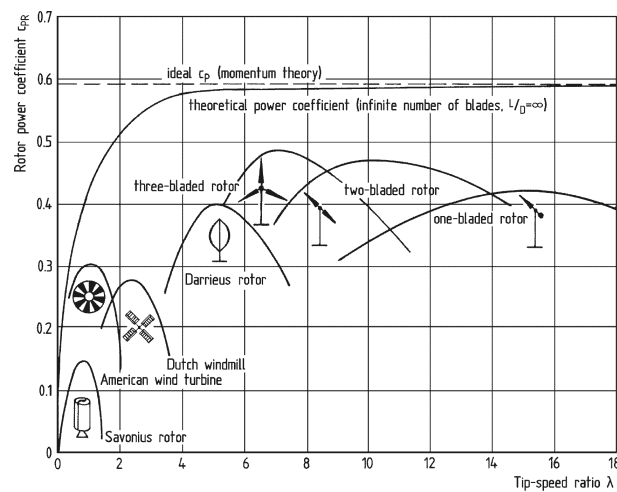


Figure 1.8: rotor power coefficients of different designs versus the tip-speed ratio [Hau, 2013].

1.4 Wind turbine blades

Blade designs must satisfy a wide range of objectives, many in conflict with each other [Burton et al., 2011; Hau, 2013]:

- maximise the average energy captured for specific wind speeds;
- allow control on the output power;
- resist extreme and fatigue loads (the design lifetime of modern wind turbines is of 20 years);
- restrict tip deflections to avoid collisions between blade and tower;
- avoid resonances which could result in catastrophic failures;
- minimise weight and cost.

The design process can be split into two stages: the aerodynamic design and the structural design. The aerodynamic design consists of the selection of the best geometry of the blade external surface which is defined by the airfoil family and the chord, twist, and thickness distributions [Abbott and von Doenhoff, 1959]. Being the aerodynamic lift the prime driving force which puts the rotor in rotation, much higher power coefficients can be achieved with a careful aerodynamic design. The structural design consists of blade material selection and definition of a structural cross section housed within the external envelope,

or skin. It is then evident why there has to be an interaction between those two stages: i.e. the blade thickness needs to be sufficiently small to enhance the aerodynamic performances, but also should be large enough to accommodate a structurally efficient box-girder [Hau, 2013]. The real rotor therefore is always a compromise of the ideal aerodynamic shape and the requirements coming from strength and stiffness, and last but not least, by considering the manufacturing costs.

1.4.1 Aerodynamics of wind turbine blades

Even though not being the subject of the present thesis, the above-mentioned interactions between structural and aerodynamic design require us to give some brief informations also on the aerodynamics of wind turbine blades.

Aerodynamics studies the motion of air and of bodies moving through air. Such moving objects experience aerodynamic forces (expressed by distributions of pressure on the solid surface) due to the interaction between the shape of the body itself and the moving fluid surrounding it. The *lift*, L , is the component of the aerodynamic force which is perpendicular to the direction of motion of the fluid. Meanwhile, the *drag*, D , is the component of aerodynamic force opposite to the direction of motion. The ratio between the lift and drag is called the *aerodynamic efficiency*,

$$E = \frac{L}{D}. \quad (1.4)$$

The shape of an airfoil (Figure 1.9) is specifically designed so that the intensity of lift is much greater

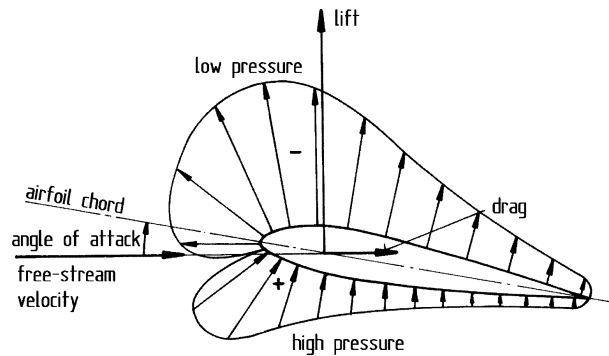


Figure 1.9: distribution of pressures on an airfoil [Hau, 2013].

than that of drag.

The *airfoil chord*, c , is the reference line which connects the *leading edge* and the *trailing edge* of the airfoil (Figures 1.9 and 1.10). The angle formed between the chord and the direction of motion is called *angle of attack*, or *incidence*, α . Lift and drag are functions of the angle of attack: in a plot lift versus incidence (also known as *polar* of the airfoil), lift is linear for small angles of attack. In aerodynamics it is common practice to refer to non-dimensional quantities. Thus the *lift coefficient* is defined as

$$c_l = \frac{L}{\frac{1}{2}\rho v^2 c^2} \quad (1.5)$$

Analogous coefficients are defined also for the drag and the pitching moment. In Figure 1.11 from Hansen [2008], this trend is clearly visible. Exceeding a particular value of the angle of attack, the aerodynamic profile stalls, leading to a loss of lift and to a drastic drop in efficiency.

Once the two-dimensional problem has been investigated, moving to the three-dimensional flow around the blade is not an immediate task, but requires specific dissertation that will be omitted here. For a detailed study of wings and propellers (not conceptually different from wind turbine blades), we suggest to refer to Abbott and von Doenhoff [1959] and Milne-Thomson [1973]. References on wind turbine aerodynamics can be found in Burton et al. [2011], Hansen [2008] and Hau [2013].

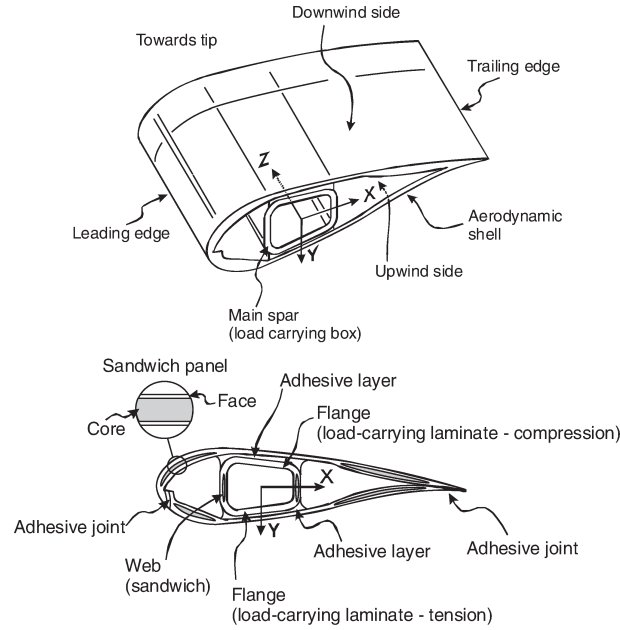


Figure 1.10: main structural parts of a typical wind turbine blade [Sørensen et al., 2010].

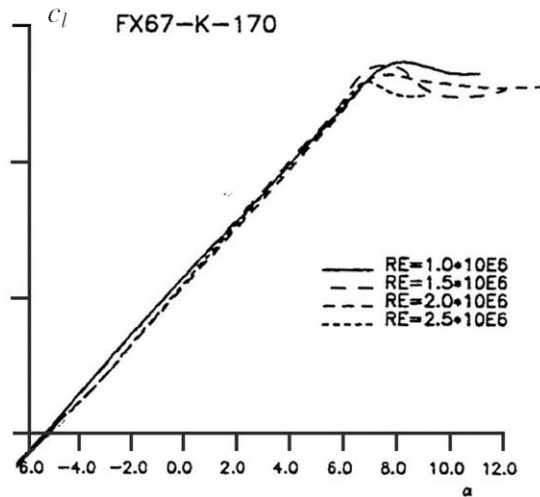


Figure 1.11: experimental c_l curve of the FX67-K-170 airfoil [Hansen, 2008].

The mechanical power captured by the rotor is influenced by the geometrical shape of the rotor blades. It can be proven that at each blade radius r (the distance from the axis of rotation), the speed of the wind which is crossing the rotor, v_W , should be reduced to two thirds of its undisturbed value, v_{WD} . This requirement can be met if the product between the local lift coefficient and the local chord length follows a hyperbolic curve over the blade length [Hau, 2013].

The local lift coefficient must be derived from the polar curves of the selected airfoil and by considering the local angle of attack. In fact, referring to a fixed reference system integrated with the blade, each airfoil experiences a different local angle of attack due to the composition of the velocity of the upcoming wind, v_r , and the velocity of rotation of the rotor, $r\omega$, where ω is the rotation speed of the rotor (Figure 1.12). To allow that all the airfoils along the blade are keep working at the best efficiency possible, the blade have then to be properly twisted. The aerodynamically optimum chord distribution over the blade length, c_{opt} , can then be calculated using the following Equation:

$$c_{opt} = \frac{2\pi r}{N} \frac{8}{9c_L} \frac{v_{WD}^2}{\lambda v_r}, \quad (1.6)$$

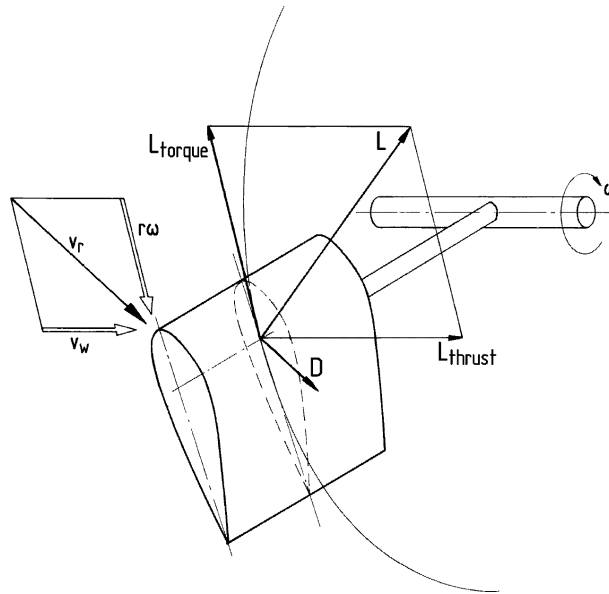


Figure 1.12: composition of velocities for the determining of the local angle of attack [Hansen, 2008].

where N is the number of blades. The optimum chord length distribution and the local twist angle are inversely proportional to rotor radius [Hansen, 2008]. Figure 1.13 shows the theoretical shape of the rotor blades at different tip-speed ratios for rotor designs with one, two, three, and four blades [Hau, 2013]. Chord length distribution should remain as close as possible to the theoretical optimums shape.

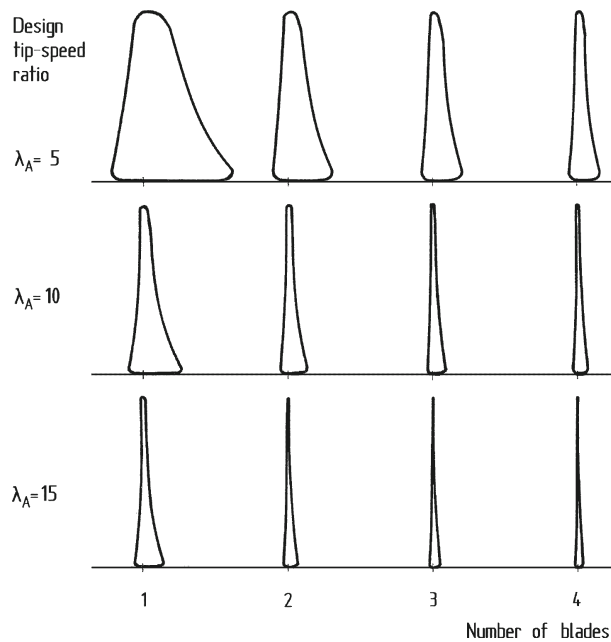


Figure 1.13: optimum blade chord distributions for different designs [Hansen, 2008].

However, the inboard section of the blade makes only a small contribution to the total power output. Then in practice, the aerofoil section is generally not continued inboard of about 15% of the rotor radius, and the chord at sections closer to the root is substantially reduced. A common expedient is then to taper the chord uniformly over the active length of the blade, with the tip chord and chord taper set so that the chord distribution approximates closely to the optimum over the outboard half of the blade, while the shape of sections closer to the root gradually changes from airfoil to circular.

Rotor blade thickness is an example of the conflict between aerodynamic efficiency and rotor blade

stiffness and strength requirements. The aerodynamic design strikes for the thinnest possible rotor blades, to allow the use of high-performance airfoils [Abbott and von Doenhoff, 1959]. In contrast, structural requirements demand a sufficiently thick cross section for the load-bearing elements. The maximum thickness is the crucial parameter for meeting the stiffness requirements when designing a low weight structure. These two requirements of good aerodynamics and sufficient stiffness run counter to each other. The only possible solution is finding the best compromise which allows the fulfillment of all the requirements (aerodynamic, structural, of low weight, of low costs, ect...) [Hau, 2013].

1.4.2 Structural design of wind turbine blades

If the aerodynamic design defines the outer shape of the cross sections of the blade, the structural design deals with the fulfilment of stiffness and strength requirements.

A hollow shell corresponding to the defined airfoil section could provide a simple and efficient structure to resist flexural and torsional loads. However, such a shell structure is not very efficient at resisting shear loads out of the plane of the blade, so one or more shear webs oriented perpendicular to the blade are included in the design [Burton et al., 2011]. The spar webs or spar boxes are manufactured separately and, after the lower shell has been moulded, are inserted into it and bonded. The webs and spar boxes absorb the largest share of the load, particularly the bending moment which is why special care must be exercised during the process of manufacture and bonding with the rotor blade shells.

In Figure 1.14 some examples are shown. While the solution with one shear web may be appropriate when high performances are not required, multiple webs and box-girder configurations are preferred by the large majority of blade manufacturers [GDWT-2002; Hau, 2013].

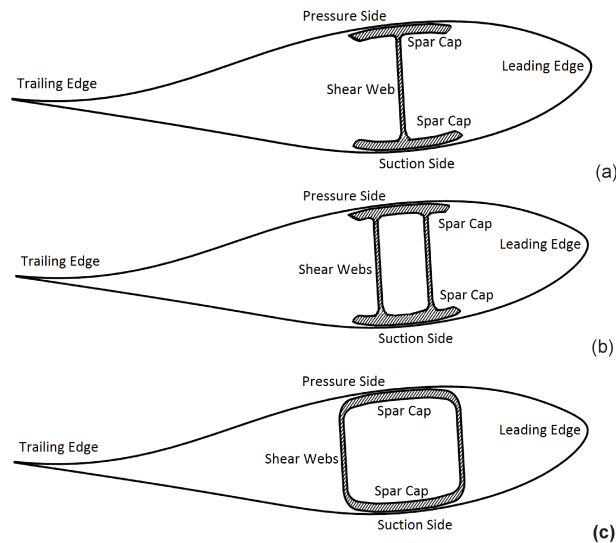


Figure 1.14: different cross section design solutions: (a) with one shear web, (b) with two shear web and (c) with a box-girder [Quispitupa et al., 2013].

1.4.3 Blade materials

The ideal material for blade construction should combine excellent structural properties (such a slow density, high strength to weight ratio, fatigue life, stiffness) with low manufacturing and service costs. Also the ease of manufacturing is a crucial element which has to be taken into account, being necessary a strong accordance to the design geometry of the blade and strict the tolerances on the final shape. Large parts of the blades are made of composite materials. The outer shells are typically constructed using laminated composites and sandwich laminates (consisting of laminated composite sheets and lightweight closed-cell polymer foam or balsa wood cores). The box girder is constructed using glass fibre compos-

Material	Ultimate tensile strength [MPa]	Specific gravity [-]	Fatigue strength at 10^7 cycles (amplitude) [MPa]	Young's Modulus [GPa]	Stiffness to weight ratio [GPa]
Steel alloy	680	7.85	70	210	27
Aluminium alloy	480	2.71	40	70	26
Titanium alloy	900	4.5	–	110	24
Glass/epoxy	420	1.7	35	15	9
Carbon/epoxy	550	1.4	100	44	31
Aramide/epoxy	450	1.25	–	24	19
Balsa	<25	0.16	–	<3	≈ 25
Sitka Spruce	<65	0.38	<20	<8	≈ 21

Table 1.2: structural properties of materials for wind turbine blades [Burton et al., 2011; Hau, 2013].

ites (or, more recently, carbon fibre composites) [Sørensen et al., 2010]. In the outer thinner blade sections foam material or balsa wood is also used instead of webs.

In table 1.2, the structural properties of composite materials in use for blade manufacture are shown and compared with most common engineering materials (i.e. steel and aluminium). Also in the Table some kind of wood (Sitka Spruce) is enlisted, even though nowadays wind turbine manufacturers are abandoning such traditional materials, and more often polymer foam is used for sandwich cores due to more homogeneous and predictable mechanical characteristics and less susceptibility to extreme environmental conditions. Moreover, it should be noted that the low strength of wood laminate compared with other materials renders wood unsuitable for blades with slender chords operating at high tip speed, where the flapwise bending moments during operation are inevitably high in relation to blade thickness. Thus, it is evident that glass and carbon-fibre composites show a higher strength-to-weight ratio compared with the other materials. However, this apparent advantage is not as decisive as it appears: the relatively low Young modulus of these composites means that resistance to buckling of the thin skins may govern the design rather than simple compression yielding [Burton et al., 2011].

Fatigue performance is conveniently measured by mean fatigue strength at 10^7 cycles, as a percentage of ultimate compressive strength: carbon fibres show the best performance.

The low value for classical construction materials, such as steel, aluminium and titanium, combined with their low strength-to-weight ratio, renders them uncompetitive for large diameter machines where fatigue loading – induced also by inertia and self-weight – becomes important.

From the above brief survey, it is apparent that the material with the best structural properties is carbon-fibre composite. However, it has not yet found common use because it is an order of magnitude more costly than other materials. Carbon fibre-reinforced composite material can, therefore, be regarded as a material with a promising future, and it is progressively being introduced in blades as reinforcement [Hau, 2013]. The most popular material are still glass fibre composites.

In Figure 1.15 (extracted from Hau [2013]) a collection of wind turbine blades are listed, showing the gradual evolution of designs. In the plot is shown the clear trend of progressive decrease in specific mass of the blade and the increase in swept area of the rotor.

1.4.4 Loads

Wind turbines are subjected to loads and stresses of different nature. Even though the main problem may appear to be the stability in heavy storms and hurricanes, even under normal wind conditions the continuous alternating loads reveal to be problematic. The sizes of the blades present a further problem. Large structures are inevitably deformable and the changing loads thus create a complex aeroelastic interplay which induces vibrations and resonances and can produce dangerous dynamic loads [GDWT-

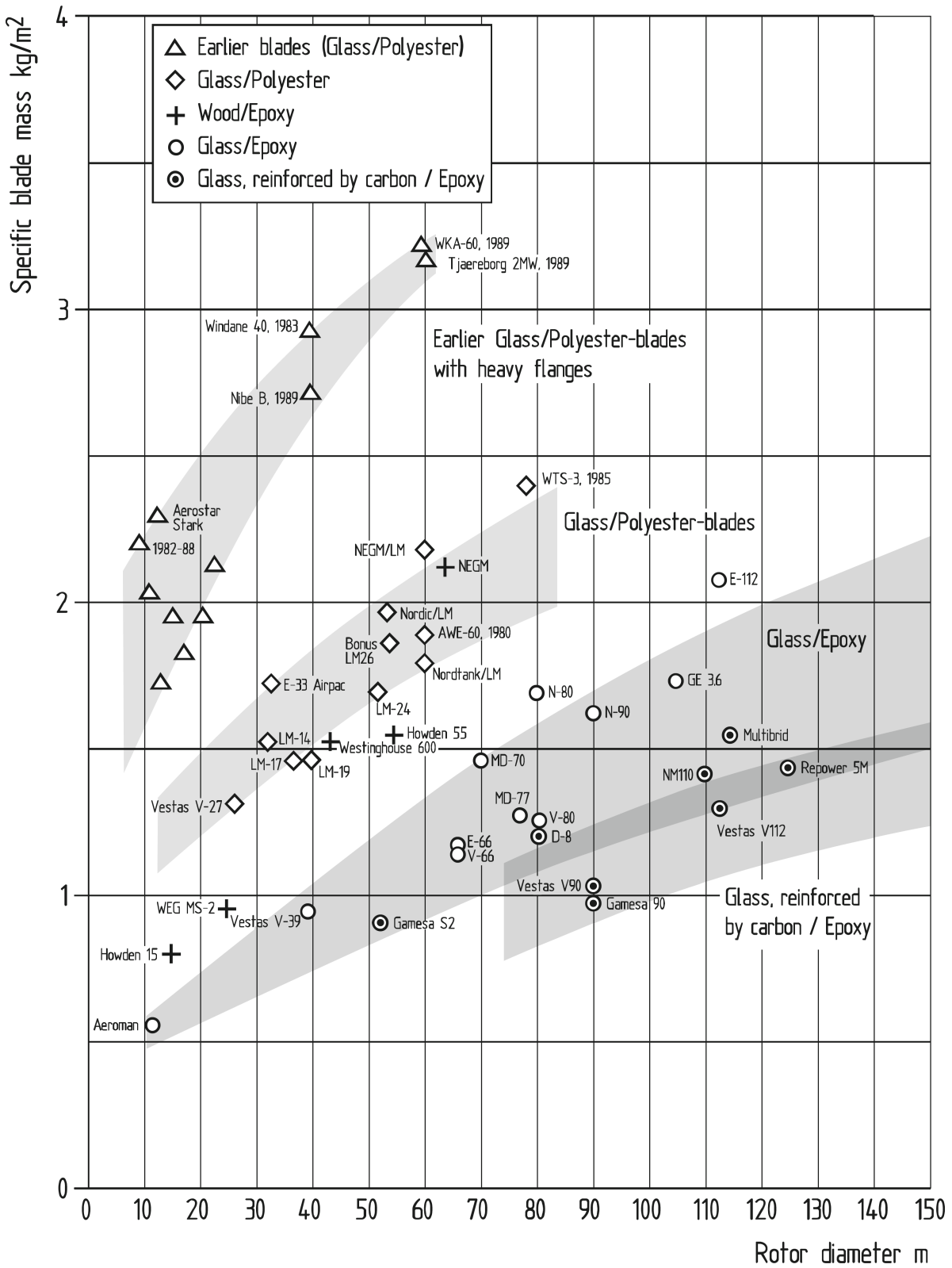


Figure 1.15: specific mass of rotor blades of different design concepts with respect to the rotor area [Hau, 2013].

2002].

The structural design of a wind turbine blades mainly concerns about three different aspects. First of all, attention must be paid to ensure that the components are designed for the extreme loads encountered. The second requirement is that the fatigue life of the components must be guaranteed for their service life (ranging around 20 or 30 years). The third aspect concerns the correct assessment of the stiffness of components: highly deformable structures usually show a longer fatigue life, but on the other hand, are also more prone to dangerous vibrations, hazardous resonances, and additional dynamic loads [Voutsinas, 2010].

Even before the structural design loads are calculated, the situations in which those loads occur have to be defined. This requires a complete overview of all external operating conditions and of possible malfunctions of the turbine: on such bases, the *load cases* can be defined [Bak et al., 2013b; GDWT-2002].

Summarizing, the main causes of loads on the rotor are related to the effects of aerodynamic, gravitational and inertial forces. The different loads and stresses can be classified according to their effect upon time on the rotating rotor (Figure 1.16):

- aerodynamic loads with uniform steady wind speed, and centrifugal forces, generate steady-state loads as long as the rotor is running at a constant speed;
- an air flow which is steady, but non-uniform over the rotor swept area induces cyclic loads. This includes also the interference due to flow around the tower;
- inertia forces due to the dead weight of the rotor blades also cause loads which are periodic and thus unsteady. Moreover, the gyroscopic forces produced when the rotor is yawed must also be considered among those which increase or alternate at each revolution of the rotor;
- in addition to the steady-state and cyclically changing loads, the rotor is subjected to non-periodic stochastic loads caused by wind turbulence.

It is not possible to recognise *a priori* which of the loads within the entire range of loads will be dominant. As is the case in all structures, the larger the turbine and the greater will be importance of gravitational loads [Hau, 2013].

1.4.5 Design Standards

Design standards were initially developed on a national basis, until the International Electrotechnical Commission (IEC) took over this task on an international basis in 1988. Today the national rules and regulations have largely been replaced by such IEC standards, although the national standards are still in existence since the European standards still do not have unrestricted legal force [Hau, 2013].

Up to now the following regulations have been published by the IEC [IEC Online Collections, 2017]:

- IEC 61400-1:2005+AMD1:2010 – Part 1: Design requirements
- IEC 61400-2:2013 – Part 2: Small wind turbines
- IEC 61400-3:2009 – Part 3: Design requirements for offshore wind turbines
- IEC 61400-11:2012 – Part 11: Acoustic noise measurement techniques
- IEC 61400-12-1:2017 – Part 12-1: Power performance measurements of electricity producing wind turbines
- IEC 61400-13:2015 – Part 13: Measurement of mechanical loads
- IEC 61400-21:2008 – Part 21: Measurement and assessment of power quality characteristics of grid connected wind turbines

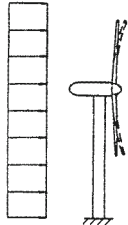

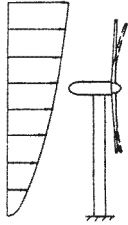
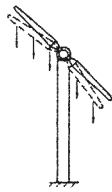
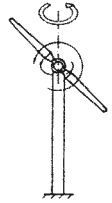
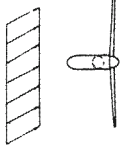
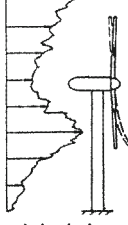
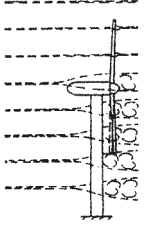
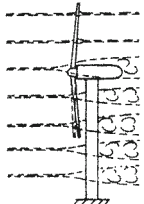
		Aerodynamic forces	Inertial and gravity forces
steady loads		 <p>steady mean wind speed</p>	 <p>centrifugal forces</p>
	cyclic loads	 <p>vertical wind shear</p>	 <p>gravity forces</p>  <p>gyroscopic forces</p>
		 <p>cross winds yaw angle</p>	
non-cyclic loads	 <p>wind turbulence</p>	 <p>tower shadow downwind rotors</p>  <p>tower dam upwind rotors</p>	

Figure 1.16: effect of aerodynamic, gravitational and inertial loads of the rotor [Hau, 2013].

- IEC 61400-23:2014 – Part 23: Full-scale structural testing of rotor blades
- IEC 61400-24:2010 – Part 24: Lightning protection
- IEC 61400-25:2017 – Part 25: Communications for monitoring and control of wind power plants

The main document with regard to the load assumptions is the IEC 61400-1 (Design requirements). On the basis of the IEC standards numerous certification organisations offer an independent certification service for wind turbines. They also consider to a certain extent inhouse or national standards for some aspects of the design or for the load calculations. One of the most important classification organizations which grant certifications for wind turbines is the *Det Norske Veritas* (DNV) [DNV-GL-0376]. The DNV, in cooperation with the Danish Risø National Laboratory, issue also the “Guidelines for the Design of Wind Turbines” [GDWT-2002].

1.5 Structural analysis of wind turbine blades

A wind turbine blade is usually globally modelled as a cantilever beam, albeit different complexity sources attend in large numbers. In the attempt to reach the best possible design, various combinations of both isotropic and anisotropic materials may be used (i.e. carbon- and glass-fibre reinforced composites, polyethylene terephthalate (PET) foam cores, etc.). Also, the nature, conditions, and combinations of the external loads and actions are extremely variable. Not only static, but also dynamic, and aeroelastic responses should be carefully investigated. A wide range of effects produce relevant design loading conditions: i.e. aerodynamic forces, self-weight and inertial forces, bird and hail impacts, etc. Blades are also prone to multiple failure modes, ranging from local and global buckling to fracture at different scales and delamination, as well as fatigue of structural components, joints, etc. (see Figure 1.17, taken from Sørensen et al. [2010]).

In order to perform a structural analysis of wind turbine blades, a structural model is needed. When building such a model, all the complexities enumerated in the above should be taken somehow into account. Nowadays, the study of wind turbine blades is mainly performed by means of computational mechanics, and in particular Finite Element (FE) methods are widely used [Hau, 2013].

Structural FE models of wind turbine blades can be roughly categorised into two groups: full 3D models and 1D equivalent beam models. In a 3D model, blades are generally discretised using composite shell elements – which are capable of describing composite layer characteristics throughout the shell thickness – or solid elements. In a 1D equivalent beam model, the blade is discretised into a series of beam elements (Figure 1.18).

1.5.1 Full 3D models

An example of a 3D model of a wind turbine blade is illustrated in Figure 1.19.

A 3D model is a powerful tool for assessing a detailed depiction of the blade behaviour, ranging from stress distributions, displacements, analysis of the fracture toughness of the structure, and quantifying its buckling resistance also. As can be easily imagined, generating a 3D model of a blade using general-purpose commercial finite-element software (such as Abaqus [Dassault Systèmes, 2013]) can be time-consuming due to the complicated aerodynamic shapes and structural layout of the composite materials. Also, the computational demand is extremely high due to the number of degrees of freedom necessary to gain reasonably accurate results. Attempts have been made to couple the 3D FE models with efficient aerodynamic models, in order to save the overall computational costs. However, this coupled approach still is not efficient enough and has not been used in industrial applications in the modelling of blades [Wang et al., 2016].

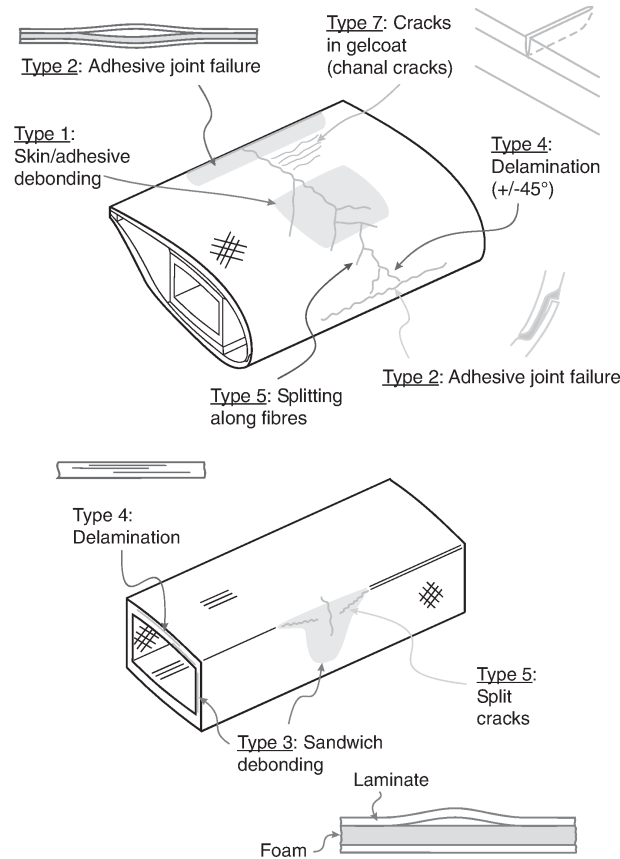


Figure 1.17: some sketches of possible failure modes in a wind turbine blade [Sørensen et al., 2010].

1.5.2 1D FE models

Having one of their dimensions significantly larger than the other two, wind turbine blades can be modelled as slender beams. The beam axis is defined along the largest dimension, and a cross section perpendicular to such axis is considered to be varying along the span of the beam (Figure 1.20).

A number of beam models exist, mainly differing in the kinematic assumptions about the deformation of the beam axis and cross sections. Models of the literature can be roughly categorised into two groups:

- linear;
- non-linear.

Widely used linear beam models are based on the Euler-Bernoulli beam model [Bauchau and Craig, 2009] and the Timoshenko beam model [Timoshenko and Goodier, 1951]. The Euler-Bernoulli beam model, also known as the classical beam model, deals with slender beams subjected to extensional, torsional, and bending loads. Although shear forces may be present, their effects in terms of deformation are ignored in such a model. Conversely, the Timoshenko beam model takes into account shear deformation at first order, which makes it more suitable for describing the behaviour of stocky beams with respect to the Euler-Bernoulli beam model [Ghorashi, 2016]. Regarding the thin and slender wind turbine blades, the Timoshenko beam model shows little difference from the Euler-Bernoulli beam model – due to its easier implementation, Euler-Bernoulli beam model has been used as base for the majority of blade structural numerical models [Wang et al., 2016]. Both the Euler-Bernoulli and Timoshenko beam models are based on the assumption of small displacements, which is clearly invalid for very flexible blades that experience large deflections. Handling large displacements requires non-linear beam models which account for the geometric non-linearities caused by such large deflections. Compared to full 3D models, 1D beam models are much faster and save a lot of computational time. They are also capable of providing accurate results in terms of displacements and natural frequencies [Ghorashi, 2016].

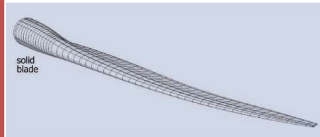
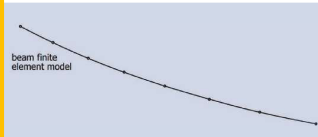
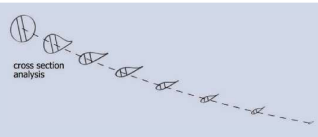
	Full 3D model	1D beam model	Cross section analysis
			
Elements:	Solid or shell elements	Beam elements	Shell elements
Output:	Displacements, strains, stresses, and buckling, fracture and fatigue behaviour	Displacements, stresses, natural frequencies	Stiffness and mass matrix, stresses, fracture and fatigue
Advantage:	Extremely refined solution, local and global behaviour	Fast computation, interfacing with aero-elastic codes	Fast computation
Disadvantage:	Computationally very demanding	No local stresses, geometric variations not into account	Only local behaviour, geometric variations not taken into account

Figure 1.18: different approaches to the structural analysis of wind turbine blades [Blasques et al., 2014; Wang et al., 2016].

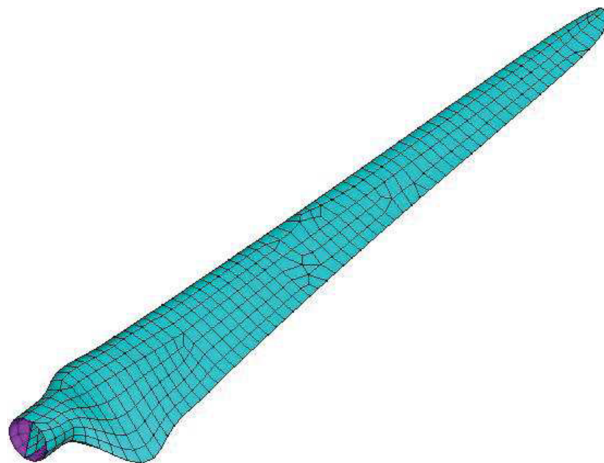


Figure 1.19: an example of 3D FE model [Song et al., 2011].

In order to discretise the blade into a series of 1D beam elements, three types of discretisation methods are often used: 1D FE analysis, modal approach, and multi-body dynamics [Oñate, 2013].

The 1D FE method consists of the analysis of an assemblage of finite elements, which are interconnected by nodes (Figure 1.20). Such approach enables a more comprehensive and accurate deformation description, and only requires slightly more computational resources than the other two approaches. The method is suitable to describe a wide range of conditions, ranging from static to aeroelastic assessment. Therefore, the 1D FE analysis is even more frequently adopted [Wang et al., 2016].

In the modal approach, the deflection shape of the flexible bodies is described as a linear combination of a set of mode shapes – which are usually obtained from a finite element pre-processor. Using mode shapes is an effective way to reduce the number of degrees of freedom. Therefore, the modal approach is more computationally efficient, resulting in a rapid simulation (see Wang et al. [2016] for further details). For this reason, the majority of the present commercial codes for the aeroelastic simulation of

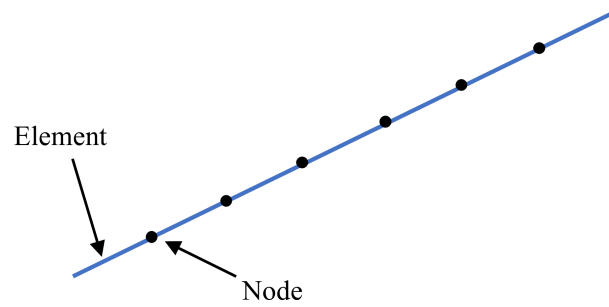


Figure 1.20: an example of 1D equivalent beam model [Wang et al., 2016].

wind turbine blades use the modal approach to calculate the structural dynamic response of the blades.

Lastly, in the multi-body dynamics method, the structure is discretised into a number of bodies, which can be either flexible or rigid. These bodies are interconnected by force elements (such as springs) or kinematic constraints (such as joints). The behaviour of the structure can then be evaluated using equations of motion, which are usually derived from Lagrange's equations or Newton-Euler equations. Compared to the modal approach, the multi-body dynamics method requires more computational resources, but it enables an increased number of degrees of freedom to be modelled [Downer, Park, and Chiou, 1992].

1.5.3 Cross-sectional analysis models

In order to effectively describe the effective three-dimensional system by means of a mono-dimensional model, the above-mentioned 1D FE beam models requires as an input the cross-sectional properties of the beam, such as the mass properties per unit length and elastic stiffnesses. Various cross-sectional analysis methods have been developed in order to obtain the cross-sectional properties of thin walled composite beams. Those methods can be categorised into three groups: 3D FE-based method, 2D FE-based method, and classical lamination theory-based method [Wang et al., 2016].

3D FE based method

Despite its capability for accurate displacement and stress analysis, 3D FE cannot directly yield the cross-sectional properties of the beam. Instead, it relies upon computationally complex post-processing of force-displacement data. Thus, it is the most complex method to calculate the cross-sectional properties. An example of such post-processing tool is the Blade Properties Extractor (BPE), which applies unit loads at the blade tip and then transfers the displacement results to routines, which calculate the stiffness matrices for the equivalent beam elements. In principle, BPE should be capable of providing the most accurate cross-sectional properties because all 3D information can be captured by the 3D FE model. Decreasing the length of the beam segment may result in a singular stiffness matrix under some extreme situations, such as a blade having highly twisted or considerably distorted cross sections [Malcolm and Laird, 2007].

2D FE based model

Several cross-sectional analysis tools based on 2D FE have also been developed.

Cesnik and Hodges [1997] developed the Variational Asymptotic Beam Sectional (VABS) analysis based on a variational asymptotic method, in which the 3D structural model is replaced with a 2D model in terms of an asymptotic series of several small parameters of the structure. VABS needs a 2D finite-element discretisation of the cross section to yield its input files, which are the 2D mesh of the cross section and the corresponding materials.

Blasques et al. [2014] developed the BEam Cross section Analysis Software (BECAS), a cross-sectional analysis tool based on the theory published by Giavotto, Borri, Mantegazza, Ghiringhelli, Car-

maschi, Maffioli, and Mussi [1983] for calculating the stiffness and stresses of a beam section made of anisotropic and non-homogeneous materials. Somehow similar to VABS, BECAS also needs a 2D finite-element discretisation of the cross section. Once the internal forces acting on the cross-section are known,

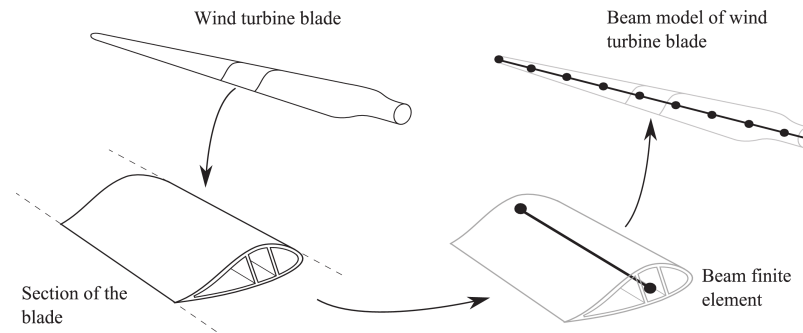


Figure 1.21: the generation of the beam finite element model [Blasques, 2011].

BECAS is also able to determine the stress distribution in the cross-section of the beam.

Compared to 3D FE-based cross-sectional analysis, 2D FE-based cross-sectional analysis requires fewer computational resources [Blasques et al., 2014; Cesnik and Hodges, 1997; Ghorashi, 2016].

Classical lamination theory based method

Classical lamination theory based method is an extension of the classical plate theory to laminated plates [Reddy, 2003]. It combines the properties of each ply in a given stacking sequence, to determine the overall effective performance of a laminated structure [Jones, 1999]. This technique has been extensively and effectively utilised for analysing the structural performance of composite material structures in many fields of application [Wang et al., 2016].

1.6 Final remarks

Concluding, the rotor blades of current wind turbines reflect the different compromises between the optimum aerodynamic shape, the requirements of strength and stiffness, and concessions to economic manufacturing. Nearly all rotor blades have a tapered shape which more or less approximates the optimum aerodynamic contour, and the aspect ratio is remarkably high. Moreover, the high slenderness results in an aerodynamically optimum blade thickness which does not enable the requirements for the necessary strength and stiffness to be fulfilled. Thus, the thickness-to-chord ratios of the airfoils used must be carefully chosen with consideration of stiffness and strength aspects. As a consequence, the best compromise between aerodynamics and structural requirements can be more easily fulfilled by design concepts involving glass fibre composite.

From a structural point of view, wind turbine blades can be globally modelled as cantilever beams. The majority of the design approaches relies on computational tools which have been developed on the assumption that the beam is a prismatic beam, and no reassurance are given that the same approach is still valid for non-prismatic beams.

Chapter 2

Analysis of variable cross sections beams

Summary. In this Chapter a simple classification of non-prismatic beams is given, along with a brief literature review focused on the study of tapered beams.

2.1 Beams of variable cross section

Beams with variable cross section are traditionally used in both civil and industrial engineering, as they allow for a more efficient use of material in comparison to beams of constant cross section. In fact, the use of a variable cross section in general leads to a more uniform distribution of stresses and a consequent reduction in the weight of the overall structure [Peery, 2011; Rivello, 1969].

This optimisation process relies on the effective assessment of the stress distributions in the structure. It is evident that, if the predicted stresses anyhow deviate from the effective ones, then the uncertainty on the actual state of stress in the structure will grow. This will inevitably force the designers to increase the safety factors taken into account. This increase in the safety factors is in clear contrast with the initial purpose of designing an optimised low-weight structure. Besides, if the inaccuracy in stress prediction is ignored or neglected, then the design will result in structures with reduced strength or service lifetime.

A reliable assessment of the stresses in beams with variable cross section is then a crucial objective of modern designers.

2.2 Definition of beam

Broadly speaking, a beam can be defined as a three-dimensional, slender body having one dimension much larger than the other two. Rivello [1969] states also that a *beam* is a member designed to resist to bending moments. The latter definition is too much restrictive, and in what follows we will assume being *beams* also those elements which in literature are often referred to as *rods* or *columns*.

A mathematically rigorous definition had been proposed by Antman [2005], while a more application-oriented approach is followed by Bauchau and Craig [2009]. Also, a comprehensive review of beam theories has been given by Eugster [2015].

Here, we consider the following geometric definition of a beam (Figure 2.1). In a Euclidean space \mathcal{E} , let \mathcal{L} be an open, simple, smooth curve, which is defined with respect to a fixed origin O by a vector function $\mathbf{r}(s)$, where s is the arc-length parameter and L is the length of the curve. To each value of the parameter s , a bounded, connected, flat surface $\mathbf{S}(s)$ is associated. At each point P of \mathcal{L} , identified by a value of s , a local Frenet-Serret frame [Kreyszig, 1991] – consisting of a unit tangent vector, $\mathbf{t}(s)$, a unit principal normal vector, $\mathbf{p}(s)$, and a unit binormal vector, $\mathbf{b}(s)$ – is defined.

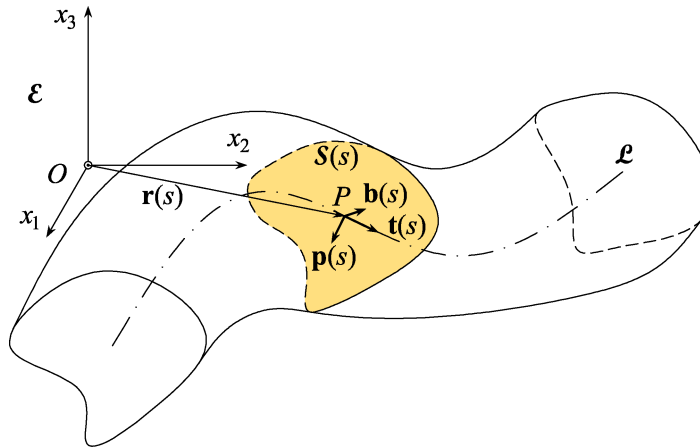


Figure 2.1: geometric definition of a beam.

If \mathcal{L} is straight, the unit vectors $\mathbf{p}(s)$ and $\mathbf{b}(s)$ are not unequivocally defined; in that case, we assume that such vectors are suitably fixed and kept constant with s . Hence, the surface $\mathbf{S}(s)$ is placed with its geometric centre at P and its normal unit vector coincident with $\mathbf{t}(s)$.

The principal axes of the second moment of area of $\mathbf{S}(s)$ may in general be rotated with respect to the Frenet-Serret frame.

Assuming that $\mathbf{S}(s)$ varies smoothly with s and no overlaps occur, the solid spanned by the surface $\mathbf{S}(s)$ when s varies from 0 to L is the region occupied by the beam in its reference configuration. With the above definitions, \mathcal{L} is the centreline and $\mathbf{S}(s)$ is the (variable) cross section of the beam. Slender beams are characterised by a generalised diameter of the cross section, $D(s) = \text{diam} \mathbf{S}(s)$, much smaller than L .

2.3 Geometric classification of beams

Based on the previous definition, beams can be classified as follows (Figure 2.2):

1. *prismatic beams*, having straight centreline, constant cross section, and fixed cross-section principal axes (with respect to the Frenet-Serret frame);
2. *non-prismatic beams*, having either curved centreline, or variable cross section, or rotating cross-section principal axes; non-prismatic beams include:
 - 2.1 *curved beams*, with constant cross section and non-straight centreline;
 - 2.2 *twisted beams*, with constant cross section and rotating principal axes;
 - 2.3 *variable cross-section beams*, whose cross section does vary with s ;
 - 2.3.1 *tapered beams*, here defined as a particular type of variable cross-section beams, whose cross section have fixed principal axes;
 - 2.3.1.1 *linearly tapered beams*, are a particular type of tapered beams in which the cross section dimensions changes linearly along the length of the beam.

It is worth noting that a similar, yet different, classification is given by Balduzzi et al. [2016]. The present thesis focusses on the influences of taper on the distribution of stresses in tapered beams defined as above. In particular, we will deal with tapered beams with straight centreline.

In the above mentioned geometrical classification, no evident distinction between the mechanical behaviour of beams with thin-walled cross sections and solid cross sections has been made. It is well known that an accurate study of thin-walled beams would require careful handling and devoted models (i.e. the Vlasov [1961] theory for thin-walled beams), being the classical De Saint-Venant approach not always reliable for such beams [Rivello, 1969; Timoshenko and Goodier, 1951]. In the present thesis

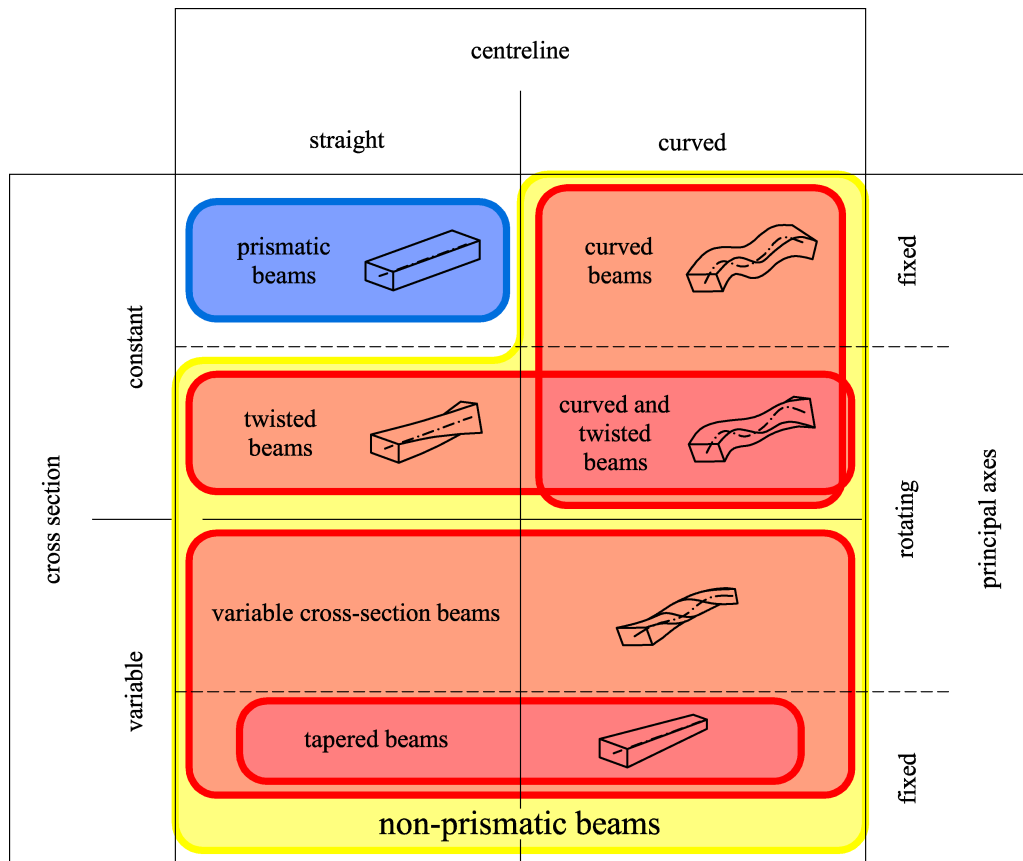


Figure 2.2: geometric classification of a beam.

however, this fundamental distinction will be neglected, and the rigorous extension to general thin-walled beams will be postponed to subsequent research activities.

Moreover, we will focus on beams whose cross sections have at least two symmetry axes – or one coincident with the direction of application of the shear force – so that the centre of shear is unequivocally located and torsion associated to shear do not occurs.

2.4 Variable cross section beams: state of the art

When dealing with non prismatic beams, a wide range of aspects should be investigated. Nevertheless, as stated also by Balduzzi, Sacco, Auricchio, and Füssl [2017b], regulation codes emphasise the assessment of the beam fatigue and buckling resistance, giving no advices on the procedures suggested for the estimate of the cross section resistance. This leads somehow to the tacit assumption that the well-known formulae appropriate for prismatic beams also extend their validity to non-prismatic beams. Even if not directly stated, such an assumption may also be tacked down in highly valued structural mechanics textbooks, and as a consequence it may be wrongly assumed acceptable in practice. As an example (see Figure 2.3), in Zienkiewicz, Taylor, and Zhu [2013] is suggested to determine the displacements of the tip of a tapered beam by discretizing the system into equal length segments of constant area. Assuming that such modelling strategy could give reasonable approximation of the longitudinal displacements, no sure information are given on stresses, and generalizing the approach may lead to an inaccurate stress assessment.

It is long known in the scientific literature that variable cross section beams, and in particular tapered beams, may show a significantly different behaviour with respect to prismatic beams [Bruhns, 2003]. However, till now the majority of the literature production on the subject has not received a significant attention both in academia and industry. The displacement analysis of variable cross section beams is

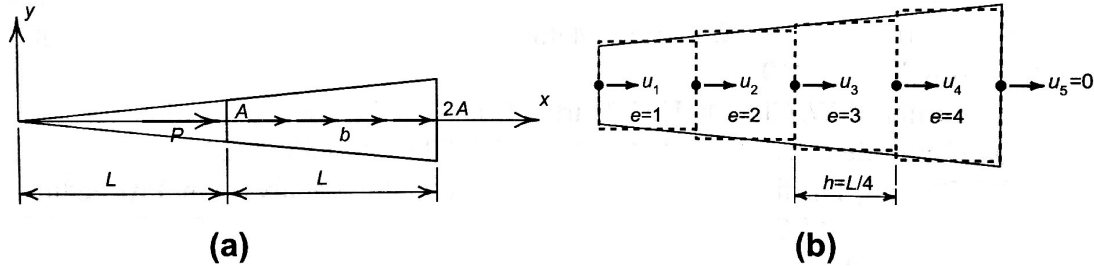


Figure 2.3: (a) geometry of a tapered beam and (b) its approximation by 4 segments [Zienkiewicz et al., 2013].

often based on Euler-Bernoulli or Timoshenko beam theories [Timoshenko and Young, 1965], in which cross section area and inertia are simply handled as functions varying along the beam axis [Shooshtari and Khajavi, 2010]. Unfortunately, these modelling approaches may fail in describing the real behaviour of the beams and the stress distributions on the section, and may lead to fallacious results, as highlighted in Boley [1963].

Focusing on the fundamental static behaviour of tapered beams, in the literature it is possible to identify different approaches. In particular:

- the evaluation of the distributions of the cross-sectional stresses;
- the derivation of a beam model which could properly predict the global structural characteristics (displacements, internal forces in statically undetermined structures, etc.), and eventually the proposal of an appropriate beam element for FE analysis.

Also, models have been proposed in attempt the unravel both the above-mentioned aspects.

2.4.1 Stress analysis

The first rigorous attempt to recover the stress distribution in tapered beams can be attributed to Bleich [1932] and consists of a generalisation of the Jourawski theory on the approximate shear stress [Timoshenko, 1953; Timoshenko and Gere, 1972]. Dealing with steel thin-walled beams, Bleich shows that in beams of variable cross section the shear stresses arise not only in the presence of shear force Q , but also as a result of bending moment M and axial force N . In his derivation, distributed loads are not present. Furthermore, he arbitrarily – and apparently not justifiably – neglects some contributions in the attempt to determine the maximum shear stresses in the beam. Nevertheless, he delivers a fundamental result, and in the following we will refer to his contribution as the *Bleich formula* or *theory* – as a generalisation of Jourawski’s ones. In Bleich’s formula, the mean of the shear stress, τ_m , along a chord b of the section is

$$\tau_m = \frac{S^* Q}{Ib} - \frac{M}{Ib} \left(\frac{S dI}{I dz} - \frac{A}{2} \tan \alpha \right) - \frac{N}{Ab} \left(b \tan \alpha - \frac{A^* dA}{A dz} \right), \quad (2.1)$$

where α denotes the angle of taper in the respective cross section, and A and I are the area and the second moment of area of the section. A^* and S^* are the geometric properties of the hatched portion of section delimited by the chord b (see Figure 2.4). Equation 2.1 and its derivation strategy will be the basis for the extended shear stress formula deduced in Chapter 5.

Few years later, Atkin proposes a different approach based on classical elasticity, defining proper stress functions for specific aeronautical problems [Atkin, 1938a,b].

Subsequently, Krahula [1975] compares the predictions of Bleich’s formula – even though not citing directly Bleich [1932] but referring to Timoshenko and Gere [1972] – and the solution of a two-dimensional elasticity problem for a tapered cantilever beam loaded by a concentrated shear force at its

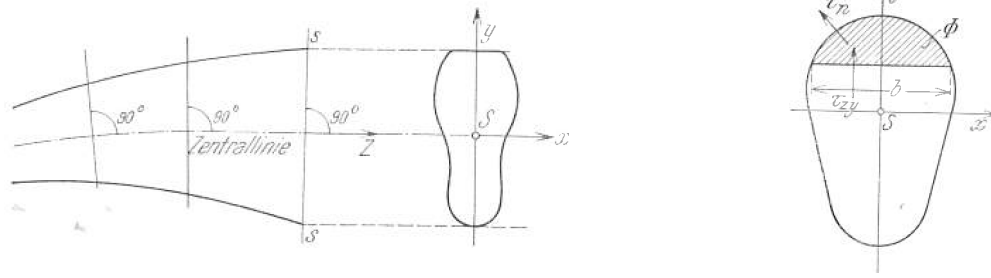


Figure 2.4: two figures showing the definition of tapered beam and general cross section, extracted from the original book from Bleich [1932].

free end. The shear stress formula adopted by Krahula is

$$\tau_m = \frac{1}{b} \frac{d}{dz} \left(\frac{S^* M}{I} \right). \quad (2.2)$$

Medwadowski [1984] derives the differential equations which governs the elastic problem of a tapered beam under the assumption that the shear stresses on the cross sections are the superposition of the classical Jourawski parabolic stresses and a linear distribution due to the bending moment. Depending only on the value of two constants, such arbitrary distribution is determined by imposing two boundary conditions on the inner and outer surfaces of the beam.

Elasticity theory has been used to model tapered beams also by Timoshenko and Gere [1972], by Knops and Villaggio [1999], and more recently by Trahair and Ansourian [2016]. Such approach lies on the assumption that a tapered beam could be modelled as a slender truncated wedge. In such a case it is possible to determine the state of stress in the beam by properly superposing two elementary solutions well known in literature. The first one is known as the *Michell problem* [Michell, 1900], and gives the stress fields induced by a concentrated force applied at the vertex of a infinite wedge. The second one is known as *Carothers' problem* [Carothers, 1914], and defines the stresses induced in the same infinite wedge by a couple applied at the vertex. Both those solutions are given in polar coordinates. A detailed review on two-dimensional elasticity problems and their history can be found in Meleshko [2003]. Despite the rigorous approach adopted, and being misled by the Jourawski solution, Knops and Villaggio [1999] state that the maximum of the shear stress distribution on a cross section – induced by a shear force – is located on the centreline of the tapered beam. Also, Hwu and Ting [1990] approach the problem from the point of view of classical continuum mechanics to extend the derivation to anisotropic elastic wedges, but focusing their attention on the *Carothers' paradox* (see Section 4.1.2 for further details).

The same approach followed by Bleich has been also pursued by multiple authors for different specific applications. For example, Russo and Garic [1992] analyse the specific geometry of a symmetrically tapered cantilever beam with thin rectangular cross section, observing that the shear stresses arise also when the beam is loaded by an axial force, but ignoring the fundamental contribution of the bending moment. On the contrary, Vu-Quoc and Léger [1992], Romano [1996], and Dumitrache [2012] completely neglect the axial force contribution.

It is noteworthy that the original contribution of Bleich seems to have been forgotten in the majority of the subsequent literature – with only the few above-mentioned exceptions. Only more recently a critical and extended review on the original Bleich textbook [Paglietti and Carta, 2009] finally attributes back the originality of the formula to Bleich, and denounces the general underestimation of the distribution of shear stresses in tapered beams which is shown in practical design.

Hodges et al. [2010] propose numerical models for tapered beams based on the variational approach, comparing the results with the classical elasticity solutions.

More recently, Jadan [2012] specialise Bleich's approach to symmetrically tapered beams realised in bi-linear elastic materials, which shows different elastic moduli for compression and for extension.

A similar approach to that of Medwadowski [1984] is also proposed by Balduzzi et al. [2016], which suggest that the shear stresses due to the bending moment could be assessed assuming a parabolic distribution of stresses, which depends on three unknown parameters. The first two parameters can be calculated imposing that the normal stresses on the surfaces of the beam are null. The last parameter is calculated observing that the resultant of the shear stresses – due to the bending moment – in the direction of the shear force has also to be null. Balduzzi, Amindaghai, Auricchio, and Füssl [2018] extend the previews work of Balduzzi et al. [2016] to the case of layered tapered beams.

Considering two-dimensional cross sections made of different materials and re-deriving Bleich's formula, Zhou, Zhang, Zhong, and Zhao [2016] study the shear stresses in the corrugated steel web of a box girder. Assuming also non-symmetric tapered beams, the authors assume cross sections which are not perpendicular to the centreline of the beam, leaving some doubts on the general effectiveness of the suggested approach.

2.4.2 Beam models

Apart from the assessment of the distribution of stresses (discussed in Section 2.4.1), tapered beams have been widely investigated, and many mechanical models have been proposed for specific purposes. A huge amount of literature deepens in specific aspects – i.e. dynamics [Mabie and Roger, 1964], buckling [Karabalis and Beskos, 1983], etc. But even if it is undoubtedly necessary to investigate also those aspects, it has to be said that a clear understanding of the mechanics of tapered beams is still far from been achieved – i.e. the behaviour of statically indeterminate structures under static loading conditions [Balduzzi, Hochreiner, Füssl, and Auricchio, 2017a].

Particular efforts have been devoted to the derivation of the transversal displacements of tapered beams. Banerjee and Williams [1985], Tena-Culinga [1996], and Ronagh, Bradford, and Attard [2000] independently attempt a closed-form analytical solution to the problem. On the other hand, many different approaches in the field of computational mechanics are proposed by many authors – i.e. Eisenberger and Reich [1989], Hinnant [1989], and Cleghorn and Tabarrok [1992].

The huge amount of literature concerning more specific aspects – dynamic response, buckling, second order effects, ect. – are far behind the scopes of this thesis, and will be omitted. A short review of all such studies can be found in Ho [2009].

2.5 Remarks on the application to wind turbine blades

When studying the behaviour of wind turbine blades, such structures can be schematised as statically determined simple cantilever beams, so that the stress resultants on the cross sections can be easily determined. Despite that, the turbine blades are still complex three-dimensional structures and the assessment of the real distribution of stresses in the structure may not be so trivial.

The scientific above-mentioned works are all devoted to the more simple study of two-dimensional problems and thin rectangular cross section tapered beams. To the knowledge of the author, a theory which could take into account also the spatiality of the problem has not been yet proposed.

For the moment, the attention of our research activity has been focused on investigating the effects of taper on the distribution of stresses – and in particular shear stresses – on the variable cross section of thin-walled wind turbine blades. The study of the displacements is still an open question, and will have to be part of the future developments of the current research activity.

Chapter 3

Objectives and methods

Summary. The Chapter introduces the main objectives of the thesis and outlines the adopted methodology.

3.1 Objectives of the thesis

As mentioned in Section 1.4.2, wind turbine blades are built by adhesively bonding different parts – i.e. the outer shells and the elements of the box girder (Figure 1.14 at Page 16). Under loading, the different

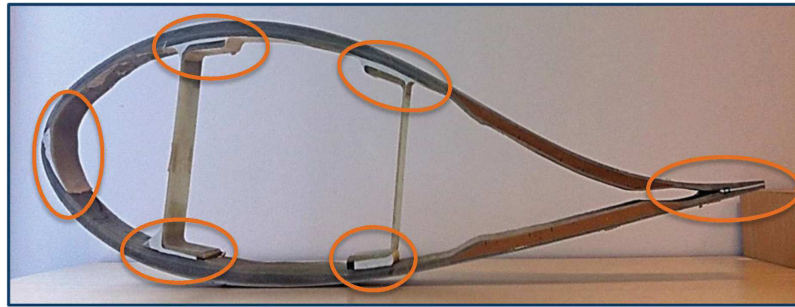


Figure 3.1: a typical blade cross section; the adhesively bonded joints are highlighted.

parts behave as a single cross section only if the load transfer between the connected structural elements is effective, so that the cross section is kept flat and its integrity is assured.

The integrity and performance of adhesively bonded joints are significantly influenced by the efficiency of load transfer of the adhesive. In particular, the joint has to show adequate stiffness – to ensure the sound deformation of the section – and toughness – to reduce the probability of failure Gleich [2002]. The shear stress plays a primary role in governing the failure modes and the overall strength of the joint [Wang and Rose, 1997]. In particular, adhesively bonded joints are particularly prone to shear failure due to the low shear resistance of the adhesive if compared to that of the monolithic material [Adams and Wake, 1984; Chaves, da Silva, de Moura, Dillard, and Esteves, 2014]. In da Silva, das Neves, Adams, and Spelt [2009], an exhaustive literature review on the mechanics of adhesively bonded joints can be found. In Figure 3.1, the section of a typical wind turbine blade is shown. The highlighted zones locate the adhesively bonded joints, which are characterized by high adhesive thicknesses.

In correspondence of the joints, uncertain intensities of the shear stress induce the designers to increase the surface and the thickness of the adhesive layers to keep satisfactory safety levels, but this may lead to an excessive use of adhesive (on the single cross section and consequently on the entire blade). With the steady increase of the length of the blades, this excessive use may lead to a consistent economical loss for the blade designer, and to an unnecessary and undesired increase in the weight of the structure. A more careful and effective design of the adhesively bonded joints could bring to a more

aware design, with the direct consequence of a remarkable reduction in both the waste of unnecessary adhesive and manufacture costs. This cannot be achieved without an effective stress recovery technique.

Only a full 3D FE analysis grants a reliable stress assessment, but in the design process also fast computations are often required. On the other hand, the 1D FE analysis tools mentioned in Section 1.5 – as well as the cross section analysis tools – are derived under the assumption that the beam is a prismatic beam (Section 2.3). To this day, no specific and conclusive investigations have been conducted to assess the applicability of those techniques to non-prismatic beams. Nonetheless, it is common practice to use such instruments in the design of wind turbine blades, in association with high safety factors, which are the sole strength that the designers can use to minimise the failure probability.

Then, the main objective of the present thesis is to verify how the taper affects the distribution of stresses in wind turbine blades, and to evaluate the suitability of the classical prismatic beam theory to assess the stress distribution in tapered beams. Great attention is given to the shear stresses in the cross sections, due to the role that those particular stresses play in the resistance of the adhesively bonded joints.

Moreover, only the effects of the global geometric taper of the beam will be investigated, and the effects of specific design details – such as the local changes in the thickness of the elements of the structure – have not been yet considered and could be the subject of subsequent investigations. Thus, the main aim of the research activities leading to the redaction of the present thesis was to quantify the amount of error committed when studying wind turbine blades, modelled as non-prismatic beams by means of the classical beam theory.

3.2 Methods

3.2.1 Simplification of a complex problem

To approach the complexity behind the study of real wind turbine blades, it was decided to drastically simplify the initial problem. Our study started from a very simplified version of the wind turbine blade. Then, the strategy has been to gradually reintroduce step-by-step single factors of complexity. The aim

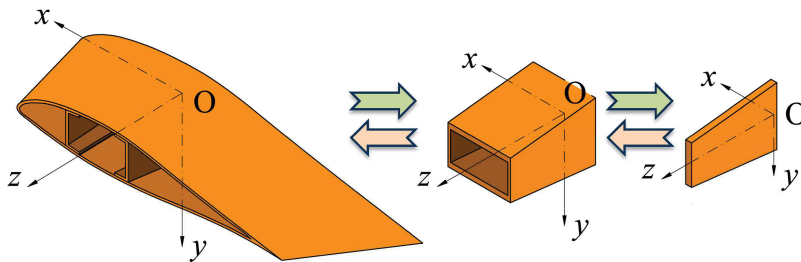


Figure 3.2: the approach strategy to the complexity of studying wind turbine blades .

of this strategy is to identify the most relevant factors which influence the problem – in particular the distribution of stresses in non-prismatic beams.

Due to the fact that the primary objective of the research is the effect of the geometry of the beam, it was chosen to consider the beam as made of isotropic elastic and homogeneous material.

Box girder analysis

Focus was given to the box girder as the major load-carrying element of the cross section of a wind turbine blade in most of the loading conditions – in particular in the flap-wise direction. In fact, the lift generating shell collects the aerodynamic forces and transfers these to the load-carrying girder. Even though the trailing edge panels are reinforced by sandwich core structures, the stiffness of such parts is not comparable to that of the box girder, and their contribution to the resistance under flap-wise loading

is small [GDWT-2002]. For that reason, also the geometry of the beam has been simplified ignoring the airfoil-shaped cross section in the following analyses (Figure 3.2).

The outlined approach is used in design for the flap-wise loading, but is less applicable under edge-wise loading, where of course the aerodynamic shell significantly contributes to the load-carrying mechanism, due to the greater cross-sectional second moment of area.

Rather than the box girder alone, the entire airfoil section contributes to the torsional stiffness, consisting of a multicellular hollow section. Thus, the torsion loading condition will be for the moment discarded and we will focus on shear and axial forces and bending moments.

The box girder is in most cases a untwisted tapered beam with rectangular cross sections [Bak et al., 2013b].

Here and in what follows, we will refer to a *doubly-tapered* box girder if both the width and the height of the rectangular cross sections are variable functions of the axial coordinate (see Figure 3.3 for a schematic example). Furthermore, if the width is constant along the length of the beam, it will be referred

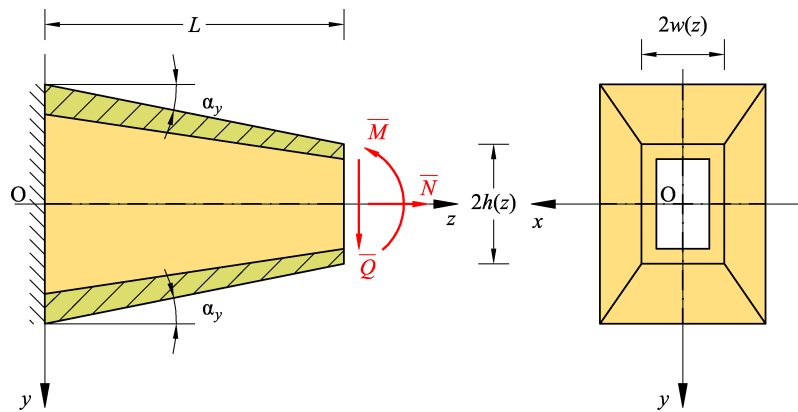


Figure 3.3: doubly-tapered box girder.

to as a *vertically-tapered* box girder. Otherwise if the height is constant, the box girder will be termed *horizontally-tapered*.

Web panel analysis

As a second step of this *geometrical simplification*, we focused on the study of the sole web panel of a vertically-tapered box girder. In fact, such web panel can be easily modelled as a tapered cantilever beam of thin rectangular cross section (Figure 3.4). Moreover, this plane stress problem has been widely

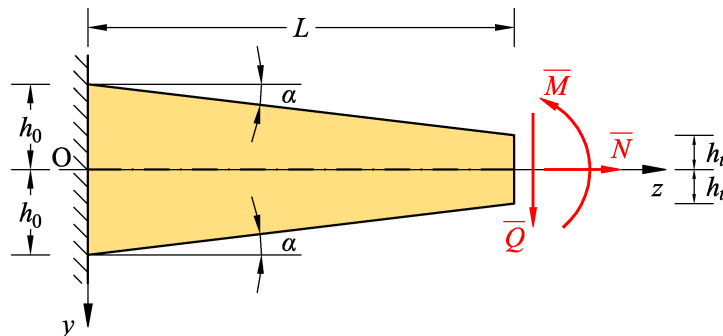


Figure 3.4: the web panel, schematised as a truncated wedge.

investigated in the literature (see Chapter 2 for more details).

Different approaches to the truncated wedge problem have been proposed in the past.

Among the others, Knops and Villaggio [1999] proposed to determine the stress distributions in a truncated wedge from those of a corresponding wedge. In the literature, the solution of simple problems

for an infinite wedge loaded at its vertex can be found [Carothers, 1914; Michell, 1900]. The same strategy has been followed, determining a reasonable approximation of the stress distributions on the cross sections of the beam, and the displacements too.

Under the hypothesis of an elastic homogeneous material, and apart from the boundary sections of the beam, such elastic solution appears to be a good approximation of an effective beam in terms of stresses, strains and displacements (see Chapter 4). Nevertheless, the mathematical expressions which describe that solution are also extremely long and complex. The mathematical expressions were handled using the Mathematica [Wolfram Research, Inc., 2008], and Matlab [The MathWorks, Inc., 2016] software.

Extended shear stress formula

To the aim of simplification, also a completely different approach has been attempted (see Chapter 5).

Following the derivation from Bleich [1932], an extended shear stress formula has been derived as an extension of the well known Jourawski formula. Basing on the shear stresses predicted by such equation, the complete stress field has been determined for the linearly tapered beam with thin rectangular cross section.

The same approach has been also extended to the more complex box girder. Again, the complete stress field have been deduced for the single- and double-tapered box girders, and for the truncated hollow cone.

Numerical analyses

Finite Element (FE) analyses were conducted with the aim of validating both the classical elasticity solution and the extended shear stress formula. All the above-mentioned cases – the linearly tapered beam with thin rectangular cross section, the box girder, and the cone – have been investigated.

The software used for the FE analyses was Abaqus [Dassault Systèmes, 2013].

3.2.2 Application to real blades

As a final step, the extended shear stress formula has been applied to the geometry of the box girder of the blade of the DTU 10MW Reference Turbine [Bak et al., 2013b] (see Chapter 7).

In particular, the extended shear stress formula has been compared with FE analyses in three simple elementary cases. In doing so, a strategy has been proposed for the application of the derived extended solution also to non-linearly tapered beams.

3.3 Outline of the thesis

The thesis consists of four parts.

The Part I consists in three chapters.

In Chapter 1, some brief information on the wind energy production, and some details on the design of the wind turbines and of the blades are given. Also, the most common analysis tools for the mechanical analysis in the blades are summarized in the last part of the chapter.

In Chapter 2, the state of the art of the modeling of non-prismatic beams is discussed, with a particular focus on tapered beams. After some first remarkable results obtained at the beginning of the 20th century, the literature survey shows that only in recent years there has been an increase of interest on the subject.

In Chapter 3, the objectives and the methods of the present thesis are discussed. The main objective of the research activities is to quantify the error committed when studying wind turbine blades modelled as non-prismatic beams, by means of the classical beam theory.

The Part II consists in two chapters.

In Chapter 4, the solution within the Theory of elasticity is presented for a plane truncated wedge clamped on a base, and loaded at its free end, under the assumptions of linearly elastic behaviour,

isotropy, and homogeneity of the material. The solution is obtained by superposition of the classical solutions for an infinite wedge loaded at its vertex.

In Chapter 5, the main result of the thesis is presented, and the derivation of the *extended shear stress formula* is shown. Based on equilibrium considerations on a portion of an element of the beam, a general extension of the Jourawski shear stress formula can be obtained for tapered beams. It is evident that shear stresses arise in the cross section not only as a consequence of the application of a shear force, but also when an axial force and a bending moment are applied.

The Part III consists in two chapters.

In Chapter 6, the results of the application of the extended shear stress formula to both elementary and more complex geometries are shown. In particular, a tapered beam with rectangular thin cross section, vertically and horizontally tapered box girders, and a thin walled hollow conical beam are analysed. Comparison between the analytical results of the extended shear stress formula and FE analysis are shown.

In Chapter 7, a brief introduction to the 10MW DTU wind turbine blade is given, with a focus on the box girder of the blade. Such box girder is a non-linearly double tapered beam with curved centreline. A strategy to apply the extended shear stress formula to such a complex structural element is proposed here, and a comparison between the classical and extended shear stress formula, and the FE analysis results is shown.

In Part IV – which consists in Chapter 8 – the conclusions and the future development are presented.

Part II
Theory

Chapter 4

Wedge and truncated wedge

Summary. In this Chapter the solution is presented for a plane truncated wedge clamped on a base, and loaded at its free end. Within the Theory of elasticity, the solution can be obtained by a proper superposition of the elementary solutions for a wedge loaded at its vertex by a force – Problem of Michell [1900] – and a couple – Problem of Carothers [1914]. To this end, the solutions for the stress fields in polar coordinates as given in the literature are first expressed in Cartesian coordinates. Then, under the assumptions of linearly elastic behaviour, isotropy, and homogeneity of the material, the strain components are obtained. Lastly, through integration and imposition of the boundary conditions, a solution is deduced also for the displacement field.

4.1 Wedge

Infinite wedges with various load conditions have tickled the imagination of many researchers. The related problems are a well known subject in the classical Theory of elasticity [Meleshko, 2003; Timoshenko, 1953].

Here, we focus our attention to wedges whose faces are free and unloaded. Concentrated forces and couples are applied only at the vertex.

The Superposition Principle allows us to decompose the loading system into three elementary cases: extension, pure bending, and shear (Figure 4.19). In the literature, the stresses in polar coordinates for each of those simple cases are well known [Timoshenko and Goodier, 1951]. In the following we recall those stress fields, which constitute the exact solutions for an infinite wedge [Carothers, 1914; Michell, 1900; Timoshenko and Goodier, 1951].

Subsequently, we derive the stress tensor in a proper Cartesian coordinate system, and we determine the strains under the assumptions of linearly elastic behaviour, isotropy, and homogeneity of the material. Finally, we integrate the strains to obtain the displacements and apply the boundary conditions for a clamped centreline in the case of a finite wedge.

4.1.1 Problem of Michell

Let us consider an infinite wedge. The angle between the faces of the wedge is here defined 2α . A polar coordinate system $\{O: r, \theta\}$ is applied at the vertex O , as shown in Figure 4.1a. Also a Cartesian reference system $\{O: X, Y\}$ is defined. A concentrated force F is applied to the vertex, inclined at an angle β with the axis X .

The stress field in polar coordinate system is given by Timoshenko and Goodier [1951] and its derivation is due to Michell [1900].

For the system shown in Figure 4.1a, Michell [1900] hypothesises that only radial stresses are present. The force F can be decomposed into its normal, N_0 , and shearing, Q_0 , components along the X - and

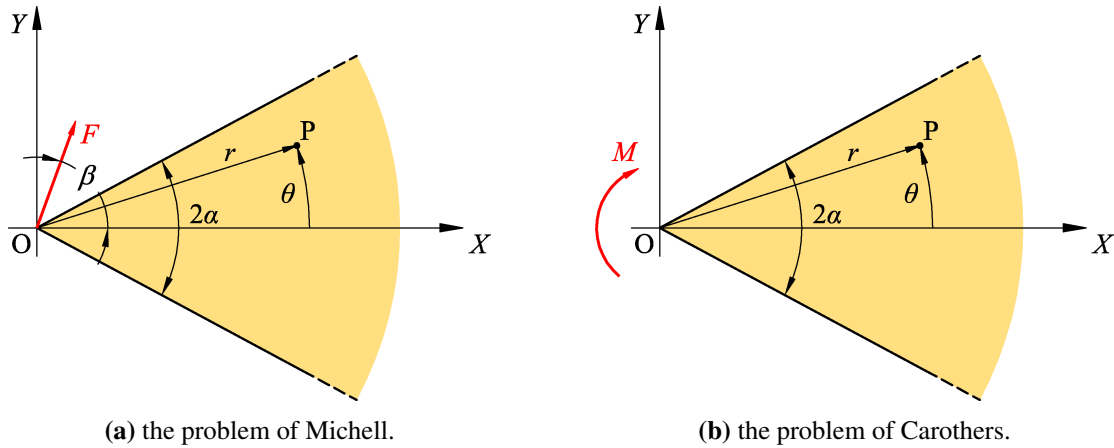


Figure 4.1: the infinite wedge studied in the two classical problems of Michell and Carothers.

Y -axes, respectively:

$$\begin{cases} F_X = F \cos \beta, \\ F_Y = F \sin \beta. \end{cases} \quad (4.1)$$

For the sake of clarity we show separately the solutions for the cases of normal force, F_X , and the case of shear force, F_Y . Looking forward to the application of the results to beams, those two different cases will somehow recall the pure extension, and part of the shear loading condition.

Pure extension

Let us suppose that a horizontal force F_X is applied at the vertex O . The stress field in such a case is:

$$\begin{cases} \sigma_{rr} = -\frac{F_X}{r} \frac{\cos \theta}{\alpha + \sin \alpha \cos \alpha}, \\ \sigma_{\theta\theta} = 0, \\ \sigma_{r\theta} = 0. \end{cases} \quad (4.2)$$

Shear loading

In the case that a vertical force F_Y is applied at the vertex O , the stress distribution is:

$$\begin{cases} \sigma_{rr} = -\frac{F_Y}{r} \frac{\sin \theta}{\alpha - \sin \alpha \cos \alpha}, \\ \sigma_{\theta\theta} = 0, \\ \sigma_{r\theta} = 0. \end{cases} \quad (4.3)$$

4.1.2 Problem of Carothers

Let us consider an infinite wedge loaded at its vertex by a concentrated couple, M_Z (Figure 4.1b). The stress field in polar coordinate system is given by Timoshenko and Goodier [1951] and is due to Carothers [1914].

$$\begin{cases} \sigma_{rr} = \frac{M_Z}{r^2} \frac{2 \sin 2\theta}{\sin 2\alpha - 2\alpha \cos 2\alpha}, \\ \sigma_{\theta\theta} = 0, \\ \sigma_{r\theta} = \frac{M_0}{r^2} \frac{\cos 2\alpha - \cos 2\theta}{\sin 2\alpha - 2\alpha \cos 2\alpha}. \end{cases} \quad (4.4)$$

This solution is not applicable in the case of

$$\sin 2\alpha = 2\alpha \cos 2\alpha, \quad (4.5)$$

for which the denominators in Equations 4.4 vanish. Such condition gives rise to the well known *Carothers' paradox* [Villaggio, 1997], but it is noteworthy that Equation 4.5 is verified for values of α far from the cases of interest for slender tapered beams: in particular, Equation 4.5 is satisfied for $\alpha = 0$ and $\alpha \approx 2.2467$ ($= 128.73^\circ$) (in the range $[0, \pi]$) (Figure 4.2). In our study we assume that the effects of the Carothers' paradox do not have influence and will not be taken into account.

It can be easily verified that the stress fields defined in Equations 4.2, 4.3 and 4.4, satisfy the equilibrium equations [Timoshenko and Goodier, 1951],

$$\begin{cases} \frac{\partial \sigma_{rr}}{\partial r} + \frac{\sigma_{rr}}{r} + \frac{1}{r} \frac{\partial \sigma_{r\theta}}{\partial \theta} - \frac{\sigma_{\theta\theta}}{r} = 0, \\ \frac{1}{r} \frac{\partial \sigma_{\theta\theta}}{\partial \theta} + \frac{\partial \sigma_{r\theta}}{\partial r} + 2 \frac{\sigma_{r\theta}}{r} = 0, \end{cases} \quad (4.6)$$

under the hypothesis that the body forces are negligible.

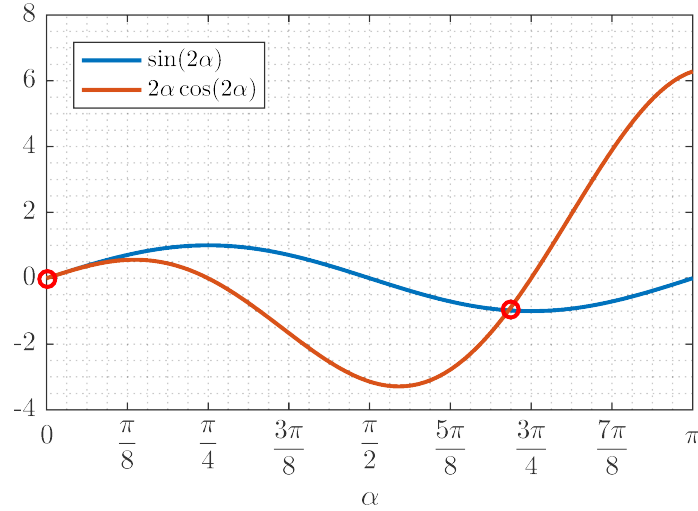


Figure 4.2: the red circles highlight the conditions for which the Carothers' Paradox takes place.

4.1.3 Finite wedge clamped at one end

Let us consider a triangular sheet of unitary width clamped at the base. The angle between the two faces of the wedge is 2α . The length of the wedge is L_0 . The base is $2h_0$.

Based on the exact solutions for the infinite wedge exposed in Paragraph 4.1, we determine the solution in terms of stresses, strains, and displacements in three simple cases (extension, shear and bending).

Clamped wedge in extension

In the case of pure extension, when the load N_0 is applied at the vertex (Figure 4.3), the stress distribution can be easily obtained by substituting $F_x = -N_0$ in Equation 4.2. Such stresses are defined with respect to a polar coordinate system located at the vertex, and described in Paragraph 4.1.1.

We introduce a new Cartesian reference system, $\{O : y, z\}$, more consistent with the classical approach to beams based on the *De Saint-Venant Problem* [Timoshenko and Goodier, 1951]. The new system is shown in Figure 4.3: the origin, O, is located at the root of the wedge. The z -axis is oriented along the mid-line of the wedge, and the y -axis is oriented downwards. The x -axis is oriented consistently with respect to the other axes to form a right-handed reference frame.

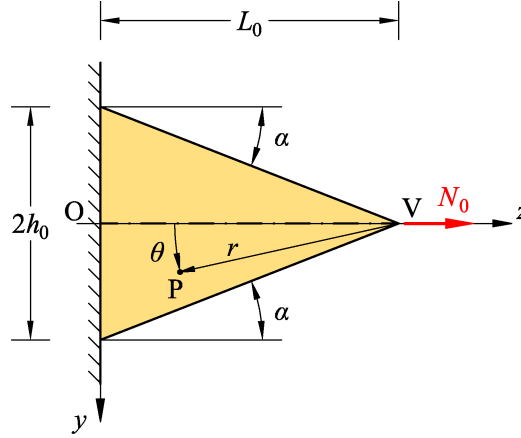


Figure 4.3: the finite wedge loaded at its vertex by a concentrated axial force.

To obtain the expressions of the stresses in the new coordinates, it is necessary to apply a rotation of the reference.

The components of the stress tensor in polar coordinates can be collected into the following matrix

$$\mathbf{T}_{\text{pol}} = \begin{bmatrix} \sigma_{rr} & \sigma_{r\theta} \\ \sigma_{r\theta} & \sigma_{\theta\theta} \end{bmatrix}. \quad (4.7)$$

The rotation matrix of the reference system is, in this case,

$$\mathbf{R}(\theta) = \begin{bmatrix} \sin \theta & -\cos \theta \\ \cos \theta & \sin \theta \end{bmatrix}. \quad (4.8)$$

Thus, the stress tensor in the Cartesian system is

$$\mathbf{T}_{\text{Cart}} = \mathbf{R}(\theta)^T \mathbf{T}_{\text{pol}} \mathbf{R}(\theta), \quad (4.9)$$

where it is also necessary to add a proper translation: in particular we have

$$\begin{cases} r^2 = (L_0 - z)^2 + y^2, \\ \tan \theta = \frac{y}{L_0 - z}. \end{cases} \quad (4.10)$$

At the end, we get the stress field of Equation 4.3 in Cartesian coordinates:

$$\begin{cases} \sigma_{zz} = \frac{N_0}{\alpha + \sin \alpha \cos \alpha} \frac{(L_0 - z)^3}{[y^2 + (L_0 - z)^2]^2}, \\ \sigma_{yy} = \frac{N_0}{\alpha + \sin \alpha \cos \alpha} \frac{y^2 (L_0 - z)}{[y^2 + (L_0 - z)^2]^2}, \\ \sigma_{zy} = -\frac{N_0}{\alpha + \sin \alpha \cos \alpha} \frac{y (L_0 - z)^2}{[y^2 + (L_0 - z)^2]^2}. \end{cases} \quad (4.11)$$

Assuming that the material is isotropic, with E , G and ν as the moduli of elasticity.

The constitutive equations are [Timoshenko and Goodier, 1951]

$$\begin{cases} \varepsilon_{zz} = \frac{\sigma_{zz}}{E} - \nu \frac{\sigma_{yy}}{E}, \\ \varepsilon_{yy} = \frac{\sigma_{yy}}{E} - \nu \frac{\sigma_{zz}}{E}, \\ \varepsilon_{zy} = \frac{\sigma_{zy}}{2G}, \end{cases} \quad (4.12)$$

By substituting Equations 4.11 into 4.12 and simplifying, the following expressions for the strain field are obtained:

$$\begin{cases} \varepsilon_{zz} = -\frac{N_0}{E(\alpha + \sin \alpha \cos \alpha)} \frac{(L_0 - z) [v y^2 - (L_0 - z)^2]}{[y^2 + (L_0 - z)^2]^2}, \\ \varepsilon_{yy} = \frac{N_0}{E(\alpha + \sin \alpha \cos \alpha)} \frac{(L_0 - z) [y^2 - v(L_0 - z)^2]}{[y^2 + (L_0 - z)^2]^2}, \\ \varepsilon_{zy} = -\frac{(1 + \nu) N_0}{E(\alpha + \sin \alpha \cos \alpha)} \frac{y(L_0 - z)^2}{[y^2 + (L_0 - z)^2]^2}, \end{cases} \quad (4.13)$$

where we have substituted

$$G = \frac{E}{2(1 + \nu)}. \quad (4.14)$$

The strain field is defined as a function of the displacement field [Timoshenko and Goodier, 1951]:

$$\begin{cases} \varepsilon_{zz} = \frac{\partial w}{\partial z}, \\ \varepsilon_{yy} = \frac{\partial v}{\partial y}, \\ \varepsilon_{zy} = \frac{1}{2} \left(\frac{\partial v}{\partial z} + \frac{\partial w}{\partial y} \right). \end{cases} \quad (4.15)$$

The displacement field can be determined inverting Equations 4.15 [Love, 1944]:

$$\begin{aligned} v &= \int \varepsilon_{yy} dy \\ &= f(z) - \frac{N_0}{2E(\alpha + \sin \alpha \cos \alpha)} \left[\frac{(1 + \nu)y(L_0 - z)}{y^2 + (L_0 - z)^2} - (1 - \nu) \arctan \left(\frac{y}{L_0 - z} \right) \right], \end{aligned} \quad (4.16)$$

and, similarly,

$$\begin{aligned} w &= \int \varepsilon_{zz} dz \\ &= g(y) - \frac{N_0}{2E(\alpha + \sin \alpha \cos \alpha)} \left[\frac{(1 + \nu)y^2}{y^2 + (L_0 - z)^2} + \log(y^2 + (L_0 - z)^2) \right]. \end{aligned} \quad (4.17)$$

In the above expressions, $f(z)$ and $g(y)$ are arbitrary functions which have to be determined.

We substitute v and w into the definition of ε_{zy} (Equation 4.15) and we obtain that the following relation has to be verified:

$$\frac{df(z)}{dz} + \frac{dg(y)}{dy} = 0. \quad (4.18)$$

Equation 4.18 can be satisfied only if the derivatives of $f(z)$ and $g(y)$ are equal to a constant value. In other words, this also means that $f(z)$ and $g(y)$ must be linear functions of their arguments. We introduce then four parameters (v_0, v_1, w_0 and w_1) such that

$$\begin{cases} f(z) = v_1 z + v_0, \\ g(y) = w_1 y + w_0. \end{cases} \quad (4.19)$$

By substituting Equation 4.19 into Equation 4.18 we immediately find that

$$v_1 = -w_1. \quad (4.20)$$

We observe that v_0 and w_0 represent a rigid-body translation in the yz -plane. Likewise, w_1 represents a rigid-body rotation about the x -axis. Therefore, we can define the rotation at any point (y, z)

$$w_1 = -\varphi \quad (4.21)$$

The displacements of the wedge can be determined by imposing only three suitable boundary conditions. In particular, it is possible to impose the clamping of the mid-line ($y = 0$) at the section $z = 0$:

$$\begin{cases} w|_{y,z=0} = 0, \\ v|_{y,z=0} = 0, \\ \frac{dv}{dz}|_{y,z=0} = 0. \end{cases} \quad (4.22)$$

It has to be noted that those conditions are not exactly equivalent to the definition of “*clamped roof*”, which instead would require null displacements in both the z - and y -directions for all the points belonging to the clamped section. Applying those conditions will result in a distribution of stresses which is not affected by the local distortions that are induced by the effective kinematic constraints. Moreover, also the displacements on the root cross section will be affected by some faults. Nevertheless, under the hypothesis that the wedge is sufficiently slender (small angle α and big length L), the stress field far enough from the root is expected to be comparable in the two differently constrained cases.

Solving the linear system represented by Equations 4.22, we determine the values of v_0 , w_0 and w_1 , and finally the displacements of a clamped wedge loaded by an axial force at the vertex can be written as:

$$\begin{cases} v = -\frac{N_0}{E(\alpha + \sin \alpha \cos \alpha)} \left[\frac{1+v}{2} \frac{y(L_0-z)}{y^2 + (L_0-z)^2} - \frac{1-v}{2} \arctan\left(\frac{y}{L_0-z}\right) \right], \\ w = -\frac{N_0}{E(\alpha + \sin \alpha \cos \alpha)} \left[\frac{1+v}{2} \frac{y^2}{y^2 + (L_0-z)^2} - \frac{1}{2} \log\left(\frac{L_0^2}{y^2 + (L_0-z)^2}\right) \right]. \end{cases} \quad (4.23)$$

In particular, the displacements of the mid-line turn out to be:

$$\begin{cases} v|_{y=0} = 0, \\ w|_{y=0} = \frac{1}{2} \frac{N_0}{E(\alpha + \sin \alpha \cos \alpha)} \log\left(\frac{L_0^2}{y^2 + (L_0-z)^2}\right). \end{cases} \quad (4.24)$$

Clamped wedge in shear

Let us now consider the case shown in Figure 4.4. If only the force Q_0 is applied at the vertex V of the wedge, we suppose that the stress distribution is, with sufficient approximation, that shown for an infinite wedge in Equation 4.3 at Page 42.

Following the same solution strategy adopted in Paragraph 4.1.3, we apply a rotation (Equation 4.9) and subsequently a translation (Equation 4.10) to the coordinate reference system. Thus, we obtain:

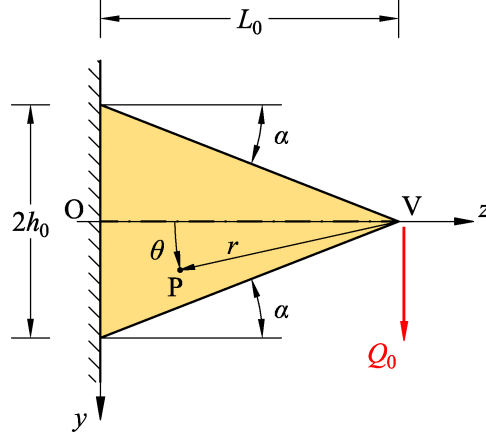


Figure 4.4: the finite wedge loaded at its vertex by a concentrated shear force.

$$\left\{ \begin{array}{l} \sigma_{zz} = -\frac{Q_0}{\alpha - \sin \alpha \cos \alpha} \frac{y(L_0 - z)^2}{[y^2 + (L_0 - z)^2]^2}, \\ \sigma_{yy} = -\frac{Q_0}{\alpha - \sin \alpha \cos \alpha} \frac{y^3}{[y^2 + (L_0 - z)^2]^2}, \\ \sigma_{zy} = \frac{Q_0}{\alpha - \sin \alpha \cos \alpha} \frac{y^2(L_0 - z)}{[y^2 + (L_0 - z)^2]^2}. \end{array} \right. \quad (4.25)$$

The associated strain field is (recalling Equation 4.14):

$$\left\{ \begin{array}{l} \varepsilon_{zz} = \frac{Q_0}{E(\alpha - \sin \alpha \cos \alpha)} \frac{\nu y^3 - y(L_0 - z)^2}{[y^2 + (L_0 - z)^2]^2}, \\ \varepsilon_{yy} = -\frac{Q_0}{E(\alpha - \sin \alpha \cos \alpha)} \frac{y^3 - \nu y(L_0 - z)^2}{[y^2 + (L_0 - z)^2]^2}, \\ \varepsilon_{zy} = \frac{(1 + \nu) Q_0}{E(\alpha - \sin \alpha \cos \alpha)} \frac{y^2(L_0 - z)}{[y^2 + (L_0 - z)^2]^2}. \end{array} \right. \quad (4.26)$$

Finally, by imposing that the mid-line at the root is fixed (Equation 4.22), as for the case of pure extension, we obtain the displacements:

$$\left\{ \begin{array}{l} v = -\frac{Q_0}{E(\alpha - \sin \alpha \cos \alpha)} \cdot \\ \left\{ \frac{z^3 - 2L_0 z^2 + (L_0^2 + y^2)z - L_0 y^2 \frac{1+\nu}{2}}{L_0 [y^2 + (L_0 - z)^2]} - \frac{1}{2} \log \left(\frac{L_0^2}{y^2 + (L_0 - z)^2} \right) \right\}, \\ w = \frac{Q_0}{E(\alpha - \sin \alpha \cos \alpha)} \cdot \\ \left\{ y^3 - y(L_0 - z) \left(z - L_0 \frac{1-\nu}{2} \right) - L_0 \frac{1-\nu}{2} [y^2 + (L_0 - z)^2] \arctan \left(\frac{y}{L_0 - z} \right) \right\}. \end{array} \right. \quad (4.27)$$

In particular, the displacements of the mid-line turn out to be:

$$\begin{cases} v|_{y=0} = \frac{Q_0}{E(\alpha - \sin \alpha \cos \alpha)} \left[\frac{1+\nu}{2} \frac{y^2}{L_0^2 + y^2} + \log \left(\frac{L_0^2}{L_0^2 + y^2} \right) \right], \\ w|_{y=0} = 0. \end{cases} \quad (4.28)$$

Clamped wedge in bending

When a couple M_0 is applied at the vertex (Figure 4.5), the stress distribution is given by Equation 4.4. Such stresses are defined with respect to a polar coordinate system located at the vertex, and described in Paragraph 4.1.1.

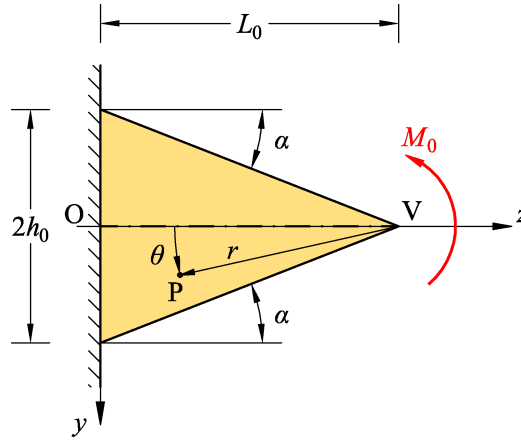


Figure 4.5: the finite wedge loaded at its vertex by a concentrated couple M_0 .

Following the solution strategy adopted in the above Paragraphs, we apply a rotation (Equation 4.9) and subsequently a translation (Equation 4.10) to the coordinate reference system. Thus, we obtain:

$$\begin{cases} \sigma_{zz} = -\frac{4M_0}{\sin 2\alpha - 2\alpha \cos 2\alpha} \frac{y(L_0 - z) \left\{ y^2 - (L_0 - z)^2 - [y^2 + (L_0 - z)^2] \sin^2 \alpha \right\}}{[y^2 + (L_0 - z)^2]^3}, \\ \sigma_{yy} = \frac{4M_0}{\sin 2\alpha - 2\alpha \cos 2\alpha} \frac{y(L_0 - z) \left\{ y^2 - (L_0 - z)^2 + [y^2 + (L_0 - z)^2] \cos^2 \alpha \right\}}{[y^2 + (L_0 - z)^2]^3}, \\ \sigma_{zy} = \frac{M_0}{\sin 2\alpha - 2\alpha \cos 2\alpha} \frac{[2y^2 - 4yz - (L_0 + y - z)^2] [2y^2 - 4yz - (L_0 - y + z)^2]}{[y^2 + (L_0 - z)^2]^3}. \end{cases} \quad (4.29)$$

The associated strain field is (recalling Equation 4.14):

$$\left\{ \begin{array}{l} \varepsilon_{zz} = -\frac{4M_0}{E(\sin 2\alpha - 2\alpha \cos 2\alpha)} \frac{y(L_0 - z)}{[y^2 + (L_0 - z)^2]^3} \cdot \\ \quad \left\{ (1 + 2\nu)y^2 - (L_0 - z)^2 - (1 + \nu)[y^2 + (L_0 - z)^2] \sin^2 \alpha \right\}, \\ \varepsilon_{yy} = -\frac{4M_0}{E(\sin 2\alpha - 2\alpha \cos 2\alpha)} \frac{y(L_0 - z)}{[y^2 + (L_0 - z)^2]^3} \cdot \\ \quad \left\{ (2 + \nu)y^2 - \nu(L_0 - z)^2 - (1 + \nu)[y^2 + (L_0 - z)^2] \sin^2 \alpha \right\}, \\ \varepsilon_{zy} = -\frac{(1 + \nu)M_0}{E(\sin 2\alpha - 2\alpha \cos 2\alpha)} \frac{y^4 - 6y^2(L_0 - z)^2 - 2[y^4 - (L_0 - z)^4] \sin^2 \alpha}{[y^2 + (L_0 - z)^2]^3}. \end{array} \right. \quad (4.30)$$

By imposing that the mid-line at the root is fixed (Equation 4.22), we obtain the displacement field:

$$\left\{ \begin{array}{l} v = -\frac{2M_0}{E(\sin 2\alpha - 2\alpha \cos 2\alpha)} \left(\frac{L_0 + z}{L_0^2} [\nu - (1 - \nu) \cos^2 \alpha] + \right. \\ \quad \left. \frac{L_0 - z}{[y^2 + (L_0 - z)^2]^2} \left\{ y^2 - \nu(L_0 - z)^2 + [y^2 + (L_0 - z)^2] (1 + \nu) \cos^2 \alpha \right\} \right), \\ w = -\frac{M_0}{E(\sin 2\alpha - 2\alpha \cos 2\alpha)} y \left\{ 2 \frac{\nu - (1 + \nu) \cos^2 \alpha}{L_0^2} + \right. \\ \quad \left. \frac{(1 - \nu)y^2 + (3 + \nu)(L_0 - z)^2}{[y^2 + (L_0 - z)^2]^2} - \frac{(1 + \nu) \cos 2\alpha}{y^2 + (L_0 - z)^2} \right\}. \end{array} \right. \quad (4.31)$$

In particular, the displacements of the mid-line turn out to be:

$$\left\{ \begin{array}{l} v|_{y=0} = \frac{2M_0}{E(\sin 2\alpha - 2\alpha \cos 2\alpha)} \frac{z^2 [\nu - (1 + \nu) \cos^2 \alpha]}{L_0^2 (L_0 - z)}, \\ w|_{y=0} = 0. \end{array} \right. \quad (4.32)$$

4.1.4 Non-dimensionalisation of the solution

In the following, we propose a non-dimensionalisation strategy to the aim of drastically simplifying the mathematical expressions and shed light on the effective dependency of the solution on the parameters involved.

In particular, we propose a transformation of the wedge into a rectangle whose length is 1 and the height is 2 (Figure 4.6).

Dimensionless parameters

We introduce the *dimensionless axial coordinate*

$$\zeta = \frac{z}{L_0}, \quad (4.33)$$

where L_0 is the length of the wedge. To each section of the wedge a value of ζ will be associated, ranging from $\zeta = 0$ at the root section, to $\zeta = 1$ at the wedge vertex.

We also introduce the *dimensionless transverse coordinate*, describing the relative vertical position of each point in the section,

$$\eta = \frac{y}{h(z)}, \quad (4.34)$$

where

$$h(z) = (L_0 - z) \tan \alpha. \quad (4.35)$$

As it can be easily verified (Figure 4.6), for each section the value of η will range from -1 (corresponding to the upper free surface) to 1 (corresponding to the lower free surface).

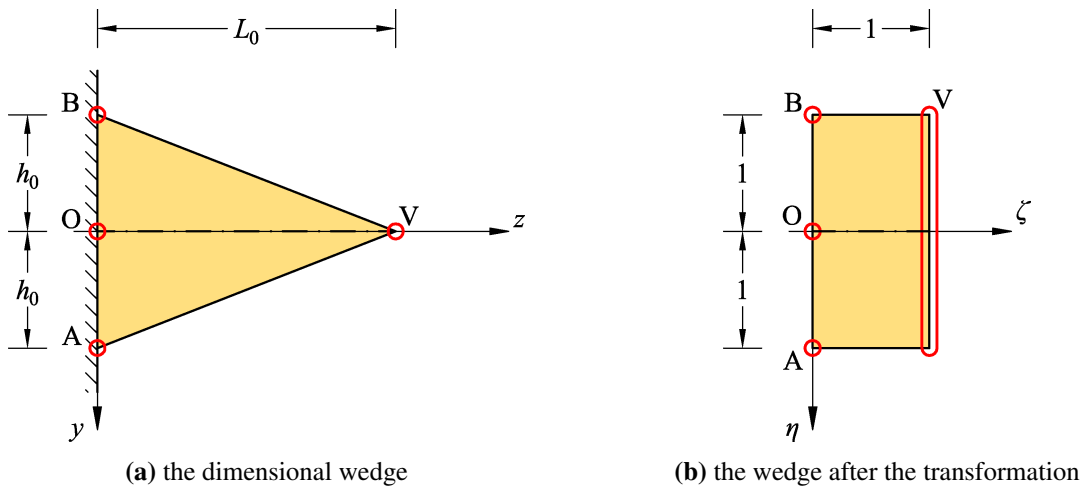


Figure 4.6: the non-dimensionalisation of the wedge.

We also introduce the *reference stress* $\bar{\sigma}_N$, which will be used as a reference for the state of stress in the wedge. In particular, it is the mean stress of an equivalent prismatic beam with the same root section of the wedge:

$$\bar{\sigma}_N = \frac{N_0}{2h_0 t}, \quad (4.36)$$

where, from Equation 4.35,

$$h_0 = h(0), \quad (4.37)$$

and where t is the width of the wedge. In the present case we are assuming that t is equal to the unity, being the classical solution for the wedge a two-dimensional problem.

We also define a *reference shear stress*,

$$\bar{\sigma}_Q = \frac{Q_0}{2h_0 t}. \quad (4.38)$$

As a reference for the case of the bending moment, we assume the stress at the lower surface of the root section for an equivalent prismatic beam

$$\bar{\sigma}_M = \frac{M_0 h_0}{\frac{1}{12} t (2h_0)^3}, = \frac{3M_0}{2th_0^2}. \quad (4.39)$$

Dimensionless solution for the pure extension

In the case of pure extension, the non-dimensionalisation gives

$$\begin{cases} \sigma_{zz} = \frac{2 \tan \alpha}{(\alpha + \sin \alpha \cos \alpha) (1 - \zeta) (1 + \eta^2 \tan^2 \alpha)^2} \bar{\sigma}_N, \\ \sigma_{yy} = \frac{2 \eta^2 \tan^3 \alpha}{(\alpha + \sin \alpha \cos \alpha) (1 - \zeta) (1 + \eta^2 \tan^2 \alpha)^2} \bar{\sigma}_N, \\ \sigma_{zy} = -\frac{2 \eta \tan^2 \alpha}{(\alpha + \sin \alpha \cos \alpha) (1 - \zeta) (1 + \eta^2 \tan^2 \alpha)^2} \bar{\sigma}_N. \end{cases} \quad (4.40)$$

Dimensionless solution for the shear force

In the case of shear, the non-dimensionalisation gives

$$\begin{cases} \sigma_{zz} = -\frac{2 \eta \tan^2 \alpha}{(\alpha - \sin \alpha \cos \alpha) (1 - \zeta) (1 + \eta^2 \tan^2 \alpha)^2} \bar{\sigma}_Q, \\ \sigma_{yy} = -\frac{2 \eta^3 \tan^4 \alpha}{(\alpha - \sin \alpha \cos \alpha) (1 - \zeta) (1 + \eta^2 \tan^2 \alpha)^2} \bar{\sigma}_Q, \\ \sigma_{zy} = \frac{2 \eta^2 \tan^3 \alpha}{(\alpha - \sin \alpha \cos \alpha) (1 - \zeta) (1 + \eta^2 \tan^2 \alpha)^2} \bar{\sigma}_Q. \end{cases} \quad (4.41)$$

Dimensionless solution for the bending moment

In case of bending, the non-dimensionalisation gives

$$\begin{cases} \sigma_{zz} = \frac{4 \eta [3 - \eta^2 - (1 - \eta^2) \cos 2\alpha] \tan^3 \alpha}{3 (\sin 2\alpha - 2\alpha \cos 2\alpha) (1 - \zeta)^2 (1 + \eta^2 \tan^2 \alpha)^3} \bar{\sigma}_M, \\ \sigma_{yy} = -\frac{4 \eta [1 - 3\eta^2 + (1 - \eta^2) \cos 2\alpha] \tan^5 \alpha}{3 (\sin 2\alpha - 2\alpha \cos 2\alpha) (1 - \zeta)^2 (1 + \eta^2 \tan^2 \alpha)^3} \bar{\sigma}_M, \\ \sigma_{zy} = \frac{2 [1 - 6\eta^2 + \eta^4 + (1 - \eta^4) \cos 2\alpha] \tan^4 \alpha}{3 (\sin 2\alpha - 2\alpha \cos 2\alpha) (1 - \zeta)^2 (1 + \eta^2 \tan^2 \alpha)^3} \bar{\sigma}_M. \end{cases} \quad (4.42)$$

4.1.5 Dimensionless functions

It is noteworthy that all the stress components listed in Equations 4.40, 4.41 and 4.42 can be written as the product of a dimensionless function (which depends only on η , ζ , and α), and a dimensional term which depends on the loading condition and the sizes of the wedge.

In particular, for the cases of concentrated forces applied to the vertex, we have

$$\begin{aligned} \sigma_{ij}|_N &= \Delta_{0,ij}(\eta, \zeta, \alpha) \bar{\sigma}_N, \\ \sigma_{ij}|_Q &= \Gamma_{0,ij}(\eta, \zeta, \alpha) \bar{\sigma}_Q, \end{aligned} \quad (4.43)$$

where i and j can be y or z .

By substituting Equations 4.36 and 4.38 into Equation 4.43, we have:

$$\begin{aligned} \sigma_{ij}|_N &= \Delta_{0,ij}(\eta, \zeta, \alpha) \frac{N_0}{2h_0t}, \\ \sigma_{ij}|_Q &= \Gamma_{0,ij}(\eta, \zeta, \alpha) \frac{Q_0}{2h_0t}. \end{aligned} \quad (4.44)$$

As already mentioned, in our derivations we will assume a unit width ($t = 1$), to adapt to the two-dimensional problem of the wedge.

For the case of concentrated couple applied to the vertex, we have

$$\sigma_{ij}|_M = \Phi_{0,ij}(\eta, \zeta, \alpha) \frac{3M_0}{2th_0^2}. \quad (4.45)$$

$\Delta_{0,ij}$, $\Gamma_{0,ij}$, and $\Phi_{0,ij}$, are the dimensionless functions, while the dimensional quantities of the problem are included in the remaining terms.

Dimensionless functions $\Delta_{0,ij}$ (N_0 applied at vertex)

Thus, the functions Δ are defined as:

$$\Delta_{0,zz} = \frac{2 \tan \alpha}{(\alpha + \sin \alpha \cos \alpha) (1 - \zeta) (1 + \eta^2 \tan^2 \alpha)^2}. \quad (4.46)$$

$$\Delta_{0,yy} = \frac{2\eta^2 \tan^3 \alpha}{(\alpha + \sin \alpha \cos \alpha) (1 - \zeta) (1 + \eta^2 \tan^2 \alpha)^2}. \quad (4.47)$$

$$\Delta_{0,zy} = -\frac{2\eta \tan^2 \alpha}{(\alpha + \sin \alpha \cos \alpha) (1 - \zeta) (1 + \eta^2 \tan^2 \alpha)^2}. \quad (4.48)$$

In Figure 4.7, the behaviour of the dimensionless functions $\Delta_{0,ij}$ is shown for $\alpha = 2.5^\circ$. In those plots, and in the following ones, both a surface plot and the equivalent contour line plot are presented for the dimensionless functions, with the aim of easing the interpretation. The dimensionless axial coordinate ζ and the dimensionless transverse coordinate η are represented on the abscissa and the ordinate respectively, in accordance with their definitions and with the transformation shown in Figure 4.6. Also, the singularity in the vertex of the wedge is not shown, being $0 \leq \zeta \leq 0.9$. All the dimensionless functions shown increase in intensity for increasing values of ζ due to the associated reduction of the height of the section. Due to the relatively small values of α taken into account, $\Delta_{0,zz}$ is almost constant on each section of the wedge. $\Delta_{0,zy}$ shows an apparent linearity with respect to η , and $\Delta_{0,yy}$ can be approximated by a quadratic function for any given value of ζ .

Dimensionless functions $\Gamma_{0,ij}$ (Q_0 applied at vertex)

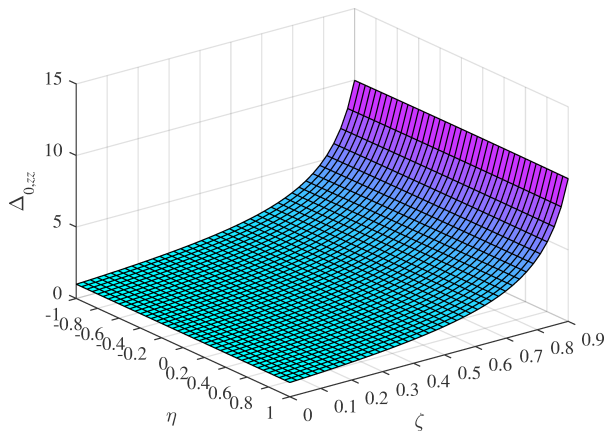
The functions $\Gamma_{0,ij}$ are defined as:

$$\Gamma_{0,zz} = -\frac{2\eta \tan^2 \alpha}{(\alpha - \sin \alpha \cos \alpha) (1 - \zeta) (1 + \eta^2 \tan^2 \alpha)^2}. \quad (4.49)$$

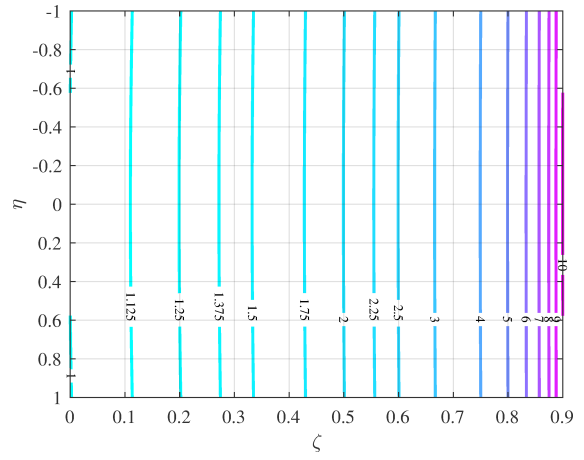
$$\Gamma_{0,yy} = -\frac{2\eta^3 \tan^4 \alpha}{(\alpha - \sin \alpha \cos \alpha) (1 - \zeta) (1 + \eta^2 \tan^2 \alpha)^2}. \quad (4.50)$$

$$\Gamma_{0,zy} = \frac{2\eta^2 \tan^3 \alpha}{(\alpha - \sin \alpha \cos \alpha) (1 - \zeta) (1 + \eta^2 \tan^2 \alpha)^2}. \quad (4.51)$$

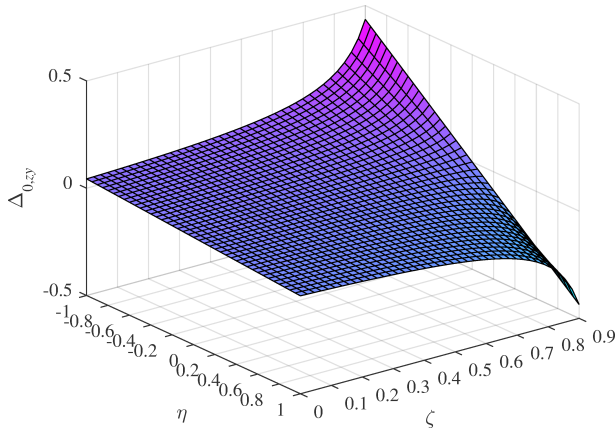
In Figure 4.8, the behaviour of the dimensionless functions $\Gamma_{0,ij}$ it is shown for $\alpha = 2.5^\circ$. For small values of α , $\Gamma_{0,zz}$ is an odd (almost) linearly distributed function with respect to the η -coordinate. On the other hand, $\Gamma_{0,zy}$ and $\Gamma_{0,yy}$ show approximately parabolic and cubic distributions, respectively.



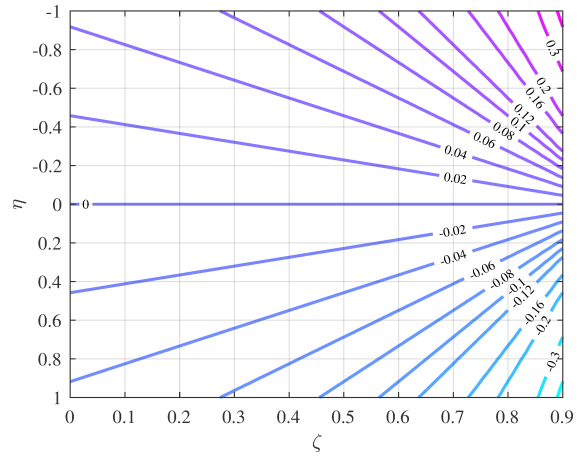
(a) $\Delta_{0,zz}$ (Equation 4.46)



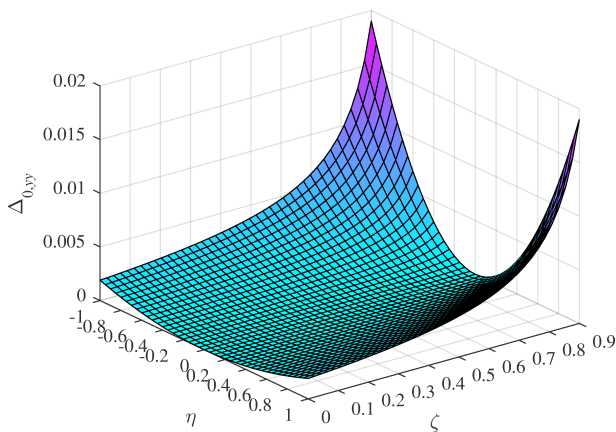
(b) plan view contour map of $\Delta_{0,zz}$



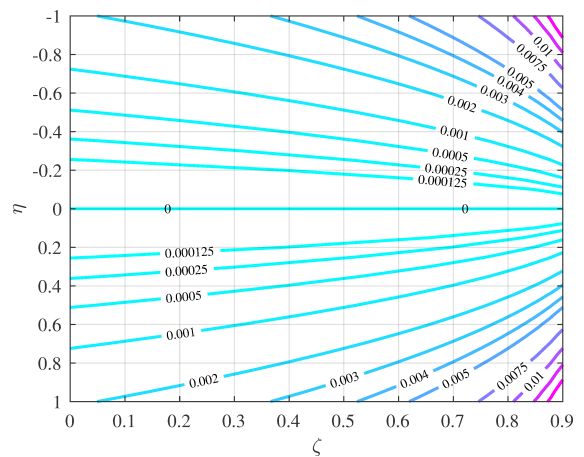
(c) $\Delta_{0,zy}$ (Equation 4.48)



(d) plan view contour map of $\Delta_{0,zy}$

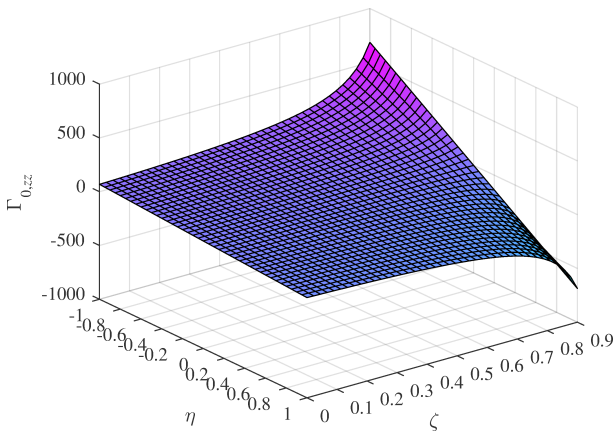


(e) $\Delta_{0,yy}$ (Equation 4.47)

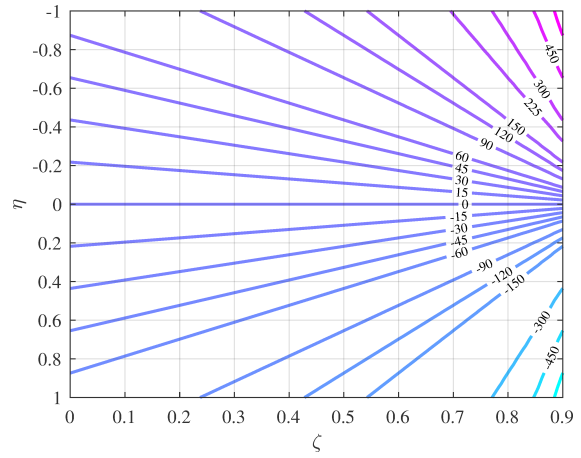


(f) plan view contour map of $\Delta_{0,yy}$

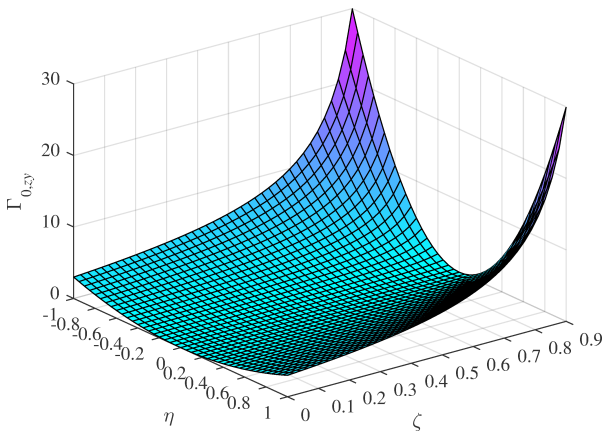
Figure 4.7: the dimensionless functions $\Delta_{0,ij}$ for $\alpha = 2.5^\circ$.



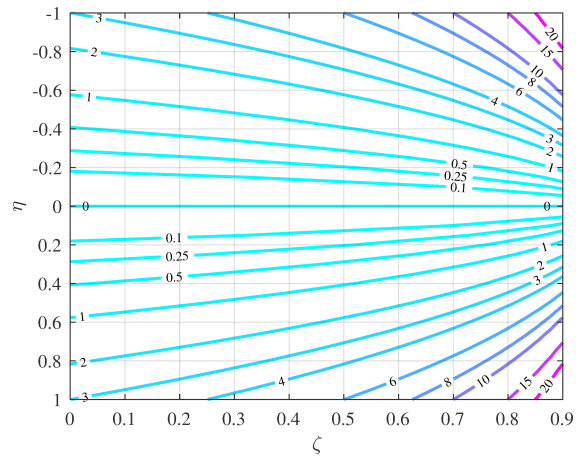
(a) $\Gamma_{0,zz}$ (Equation 4.49)



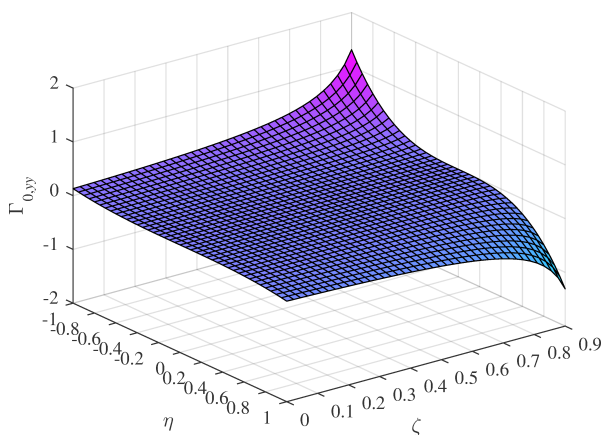
(b) plan view contour map of $\Gamma_{0,zz}$



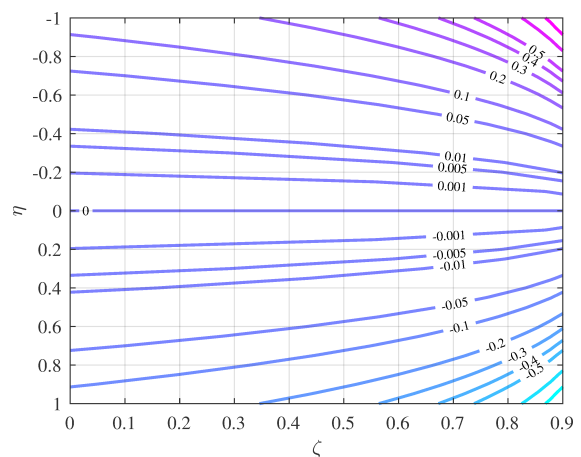
(c) $\Gamma_{0,zy}$ (Equation 4.51)



(d) plan view contour map of $\Gamma_{0,zy}$



(e) $\Gamma_{0,yy}$ (Equation 4.50)



(f) plan view contour map of $\Gamma_{0,yy}$

Figure 4.8: the dimensionless functions $\Gamma_{0,ij}$ for $\alpha = 2.5^\circ$.

Dimensionless functions $\Phi_{0,ij}$ (M_0 applied at vertex)

The functions Φ_0 are defined as:

$$\Phi_{0,zz} = \frac{4\eta [3 - \eta^2 - (1 - \eta^2) \cos 2\alpha] \tan^3 \alpha}{3 (\sin 2\alpha - 2\alpha \cos 2\alpha) (1 - \zeta)^2 (1 + \eta^2 \tan^2 \alpha)^3}. \quad (4.52)$$

$$\Phi_{0,yy} = -\frac{4\eta [1 - 3\eta^2 + (1 - \eta^2) \cos 2\alpha] \tan^5 \alpha}{3 (\sin 2\alpha - 2\alpha \cos 2\alpha) (1 - \zeta)^2 (1 + \eta^2 \tan^2 \alpha)^3}. \quad (4.53)$$

$$\Phi_{0,zy} = \frac{2 [1 - 6\eta^2 + \eta^4 + (1 - \eta^4) \cos 2\alpha] \tan^4 \alpha}{3 (\sin 2\alpha - 2\alpha \cos 2\alpha) (1 - \zeta)^2 (1 + \eta^2 \tan^2 \alpha)^3}. \quad (4.54)$$

In Figure 4.9, the shape is shown of the dimensionless functions $\Phi_{0,ij}$ for $\alpha = 2.5^\circ$. As shown for the dimensionless functions $\Gamma_{0,zz}$, also $\Phi_{0,zz}$ appear to be essentially linear with respect to the variable η . The function $\Phi_{0,zy}$ shows a particular trend with respect to the η variable: in particular it could be approximated by a parabolic function for very small angles α . $\Phi_{0,zy}$ is equal to zero only for $\eta = \hat{\eta}$ and $\eta = -\hat{\eta}$, where $\hat{\eta}$ depends on the angle α – for $-\hat{\eta} \leq \eta \leq \hat{\eta}$ this dimensionless function is positive, and outside this domain it is negative. Moreover, for any given ζ the integral with respect of η of $\Phi_{0,zy}$ is null.

Non-dimensional functions for the von Mises equivalent stresses

It is well known that the von Mises equivalent stress is

$$\sigma_{\text{vM}} = \sqrt{\sigma_{zz}^2 - \sigma_{zz}\sigma_{yy} + \sigma_{yy}^2 + 3\sigma_{zy}^2}. \quad (4.55)$$

Being each term a combination of the dimensionless functions and the dimensional one, it is possible to define non-dimensional functions associated to the von Mises equivalent stress. In particular, we have:

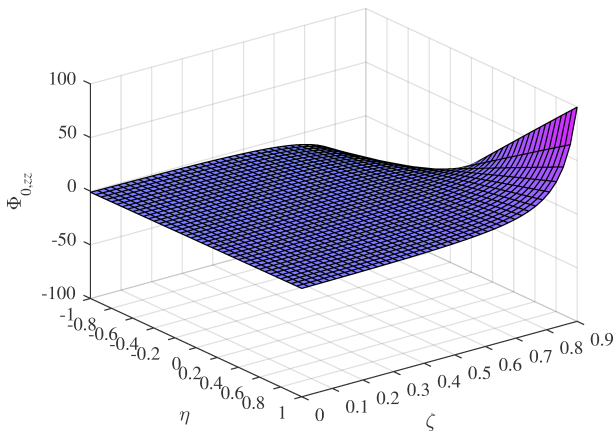
$$\begin{aligned} \sigma_{\text{vM}}|_N &= \Delta_{0,\text{vM}} \frac{N_0}{2h_0 t}, \\ \sigma_{\text{vM}}|_Q &= \Gamma_{0,\text{vM}} \frac{Q_0}{2h_0 t}, \\ \sigma_{\text{vM}}|_M &= \Phi_{0,\text{vM}} \frac{3M_0}{2th_0^2}. \end{aligned} \quad (4.56)$$

In Figure 4.10, the non-dimensional functions associated to the von Mises equivalent stresses in the three different load conditions in exam (pure extension, shear and bending moment applied to the vertex) are shown. It is evident that the predominant contribution to the equivalent stress is given by the normal stresses ($\Delta_{0,zz}$, $\Gamma_{0,zz}$, and $\Phi_{0,zz}$), being the plots on Figure 4.10 almost identical – except for small differences – almost identical to those presented in 4.7(b), 4.8(b), and 4.9(b), respectively. Nevertheless, even if not comparable in intensity with the normal stresses σ_{zz} , also shear stresses σ_{zy} – and even smaller normal stresses σ_{yy} – are present.

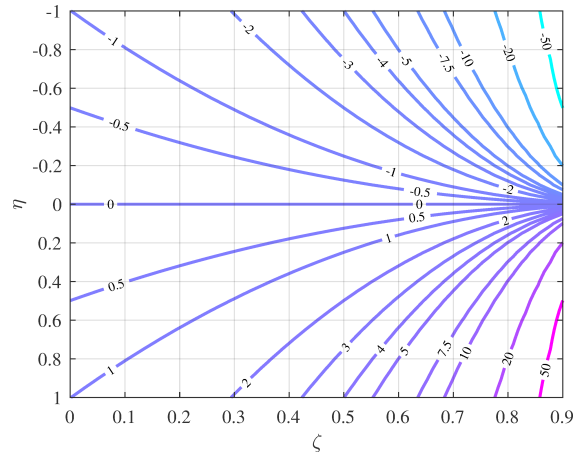
4.1.6 Discussion of results

Stresses at different sections

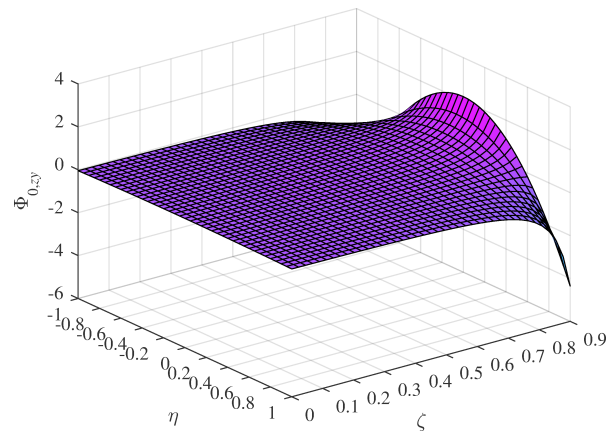
To highlight the variation of the stress distribution along the wedge, we focus our attention on five different sections (Figure 4.11). In particular, a specific color will be associated to each section: *cyan* for the root section ($\zeta = 0$), *green* for the section at one-quarter of the length of the wedge ($\zeta = \frac{1}{4}$), *yellow*



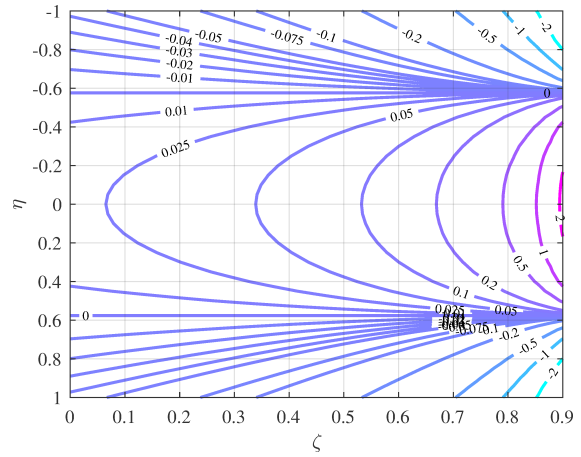
(a) $\Phi_{0,zz}$ (Equation 4.52)



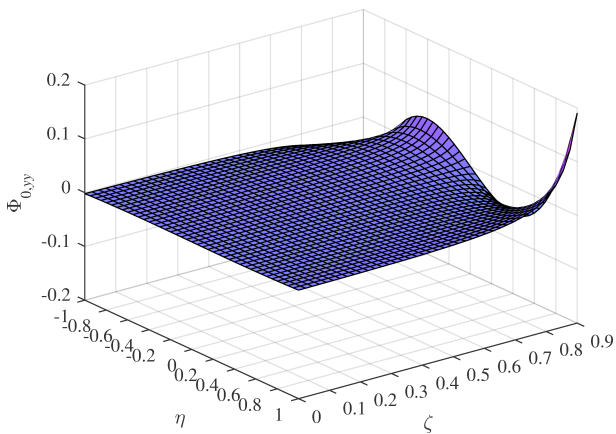
(b) plan view contour map of $\Phi_{0,zz}$



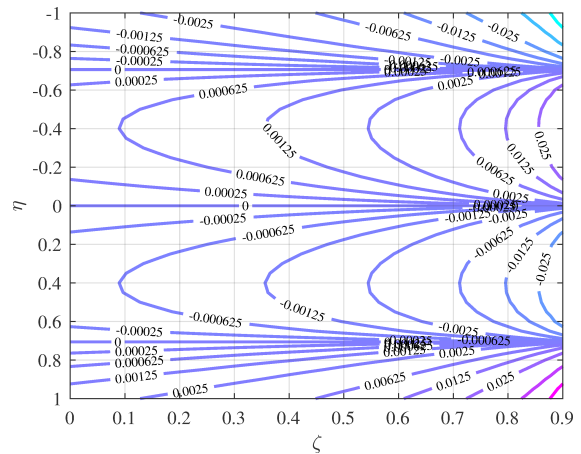
(c) $\Phi_{0,zy}$ (Equation 4.54)



(d) plan view contour map of $\Phi_{0,zy}$



(e) $\Phi_{0,yy}$ (Equation 4.53)



(f) plan view contour map of $\Phi_{0,yy}$

Figure 4.9: the dimensionless functions $\Phi_{0,ij}$ for $\alpha = 2.5^\circ$.

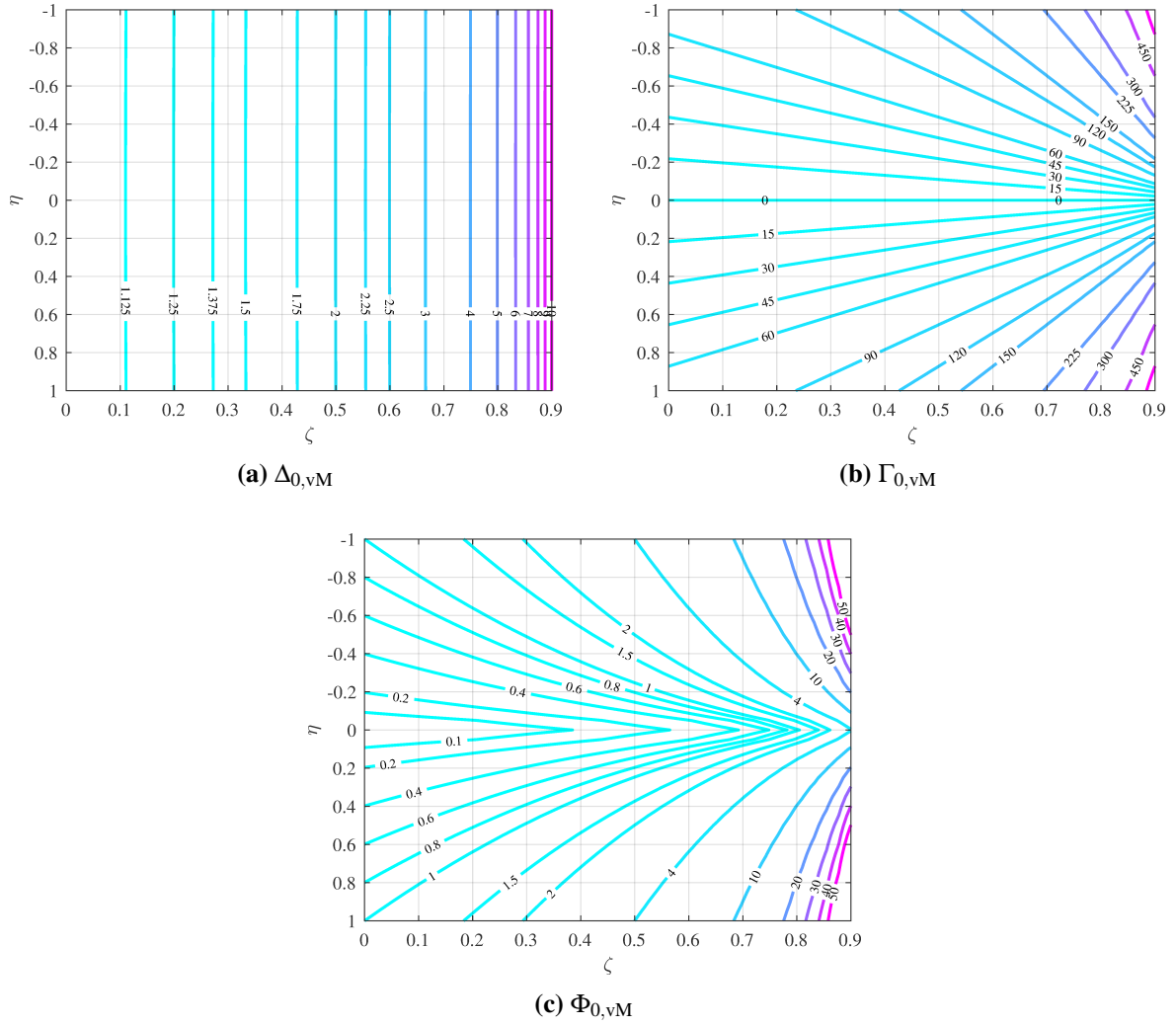


Figure 4.10: plan view contour maps of the dimensionless functions for the equivalent von Mises stresses (Equation 4.56) for $\alpha = 2.5^\circ$.

for the mid-span section ($\zeta = \frac{1}{2}$), *red* for the section at three-quarters of the length ($\zeta = \frac{3}{4}$), and *purple* for a section close to the vertex ($\zeta = \frac{9}{10}$). In this Section, the distributions of the dimensionless functions evaluated on those sections will be compared with each other.

Figure 4.12 shows the dimensionless functions $\Delta_{0,ij}$ (for the case of pure extension) for $\alpha = 2.5^\circ$. Likewise, Figures 4.13 and 4.14 show the $\Gamma_{0,ij}$ and $\Phi_{0,ij}$ functions for the same five sections. In those plots, the value of the dimensionless function and the η -coordinate are represented on the abscissa and on the ordinate, respectively.

In Figure 4.12(a), the nearly constant distribution of $\Delta_{0,zz}$ for a small angle α is evident, and the relative increase in the intensity on sections closer to the vertex is also shown. On the other hand, Figure 4.13(a) and 4.14(a) present the linearity of $\Gamma_{0,zz}$ and $\Phi_{0,zz}$.

The results presented in Figures 4.12(c), 4.13(c), and 4.14(c) show that shear stresses σ_{zy} arise in the wedge for each elementary loading condition, even if those stresses are consistently smaller in magnitude with respect to the normal stresses σ_{zz} – in particular smaller of an order of magnitude.

Dependence on alpha

The non-dimensionalisation of the solution allows us to highlight the dependency of the solution on the angle α .

In Figures 4.15, 4.16, and 4.16 the dimensionless functions at the mid-span section ($\zeta = 0.5$) are

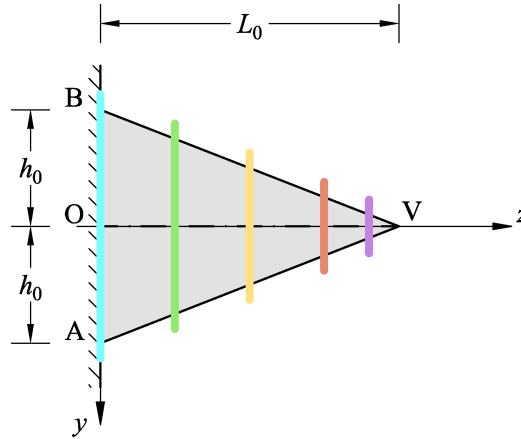


Figure 4.11: the five cross section considered for the wedge: *cyan* for the root section ($\zeta = 0$), *green* for the section at one-quarter of the length of the wedge ($\zeta = \frac{1}{4}$), *yellow* for the mid-span section ($\zeta = \frac{1}{2}$), *red* for the section at three-quarters of the length ($\zeta = \frac{3}{4}$), and *purple* for a section close to the vertex ($\zeta = \frac{9}{10}$).

shown for different values of the angle α . In particular, the values of α considered are 0.5° , 1° , 2.5° , 5° , and 10° .

First of all, it is noteworthy that the normal stresses do not show a relevant dependency on the variation of the angle α in the case of pure extension and pure bending (Figure 4.15(a) and 4.17(a)). However in Figure 4.16(a), the normal stresses σ_{zz} obtained for the shear case show an increase in the slope of the linear distribution as the value of the angle of the wedge decreases: such a variation can be justified recalling the nature of the non-dimensionalisation, and it is expected to vanish once dimensions are reintroduced as needed.

Moreover, $\Delta_{0,zy}$ shows an increase in the slope of the linear distribution with the increase of the angle α (Figure 4.15(b)). Also $\Phi_{0,zy}$ changes its distribution with respect to the increase of α : in particular, the zeros of the function are fixed along the ordinate (at $\eta = -\hat{\eta}$ and $\eta = \hat{\eta}$) but the maximum and the minimum values of $\Phi_{0,zy}$ increase linearly (Figure 4.17). $\Gamma_{0,zy}$ shows evident independence from the values of the angle of the wedge.

In Figures 4.15(d), 4.16(d), and 4.17(d), it is shown that the predominant stress component contributing to the general state of stress in a wedge is σ_{zz} . Nevertheless, all the other stress components are present, even though those may be significantly smaller than the normal stresses.

4.1.7 Final remarks

The solutions of Michell and Carothers are solutions for two classic plane problems defined on an infinite plane wedge. Thus, it could not be rigorously possible to compare the stresses predicted by those two solutions with the stresses which arise in a real physical problems such as, i.e. a tapered beam.

Nevertheless, it is interesting to make some general considerations. First of all, it is evident that in all the three cases considered (extension, shear, and bending) the predominant stress component is the σ_{zz} . We can conclude this from a comparison between the intensities of the stress components and from the analysis of the von Mises stresses. But even more noteworthy, all the stress components are present in each load condition. The distribution of shear stress is not trivial, and quite different from what the classical theory of beams could predict. In Section 4.2 we will superimpose the wedge solutions to obtain the solution of a truncated wedge: we expect that even in that case all the stress components will be different from zero, in contrast with the classical theory of beams.

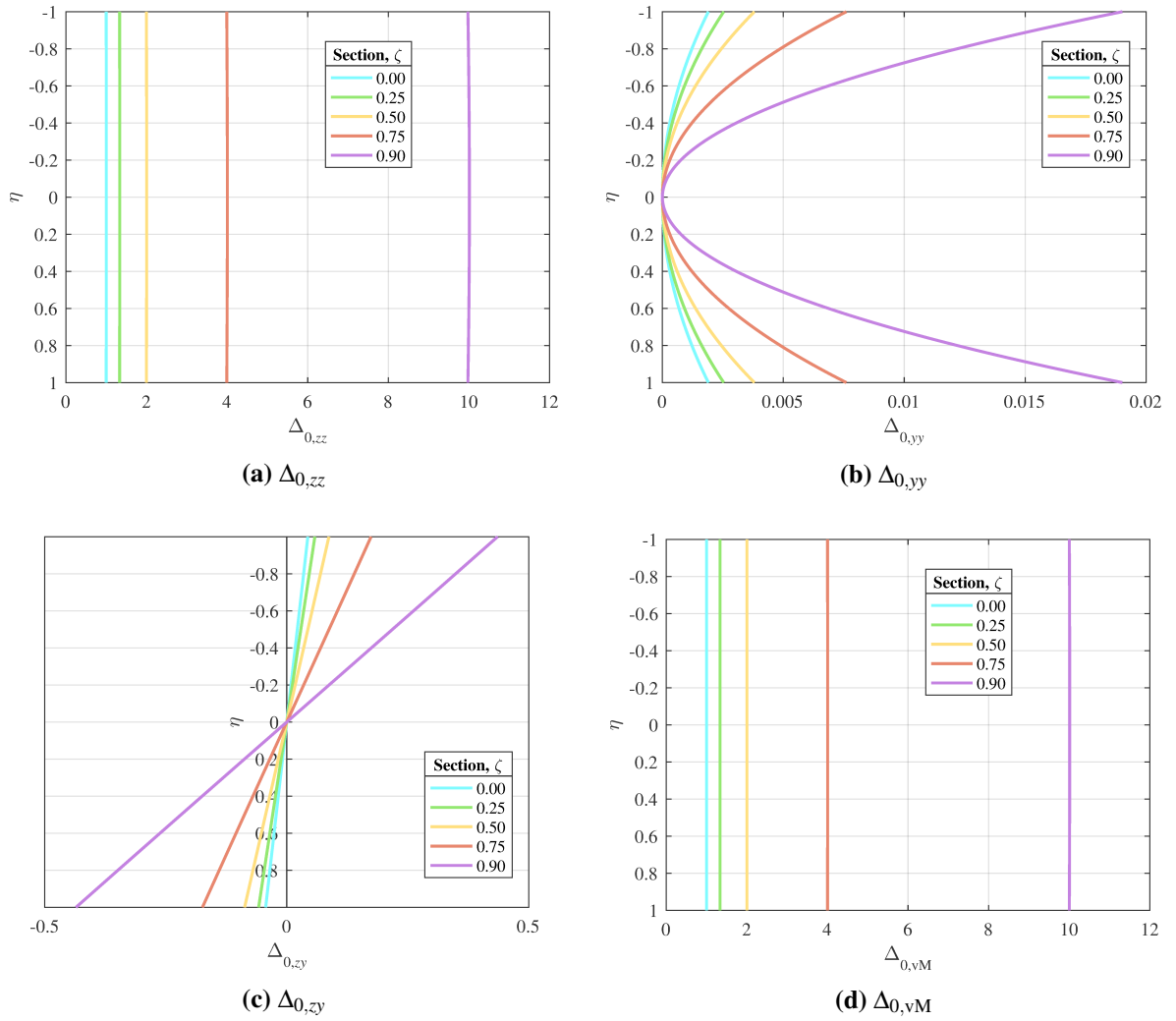


Figure 4.12: stress distribution at different sections in the case of simple extension.

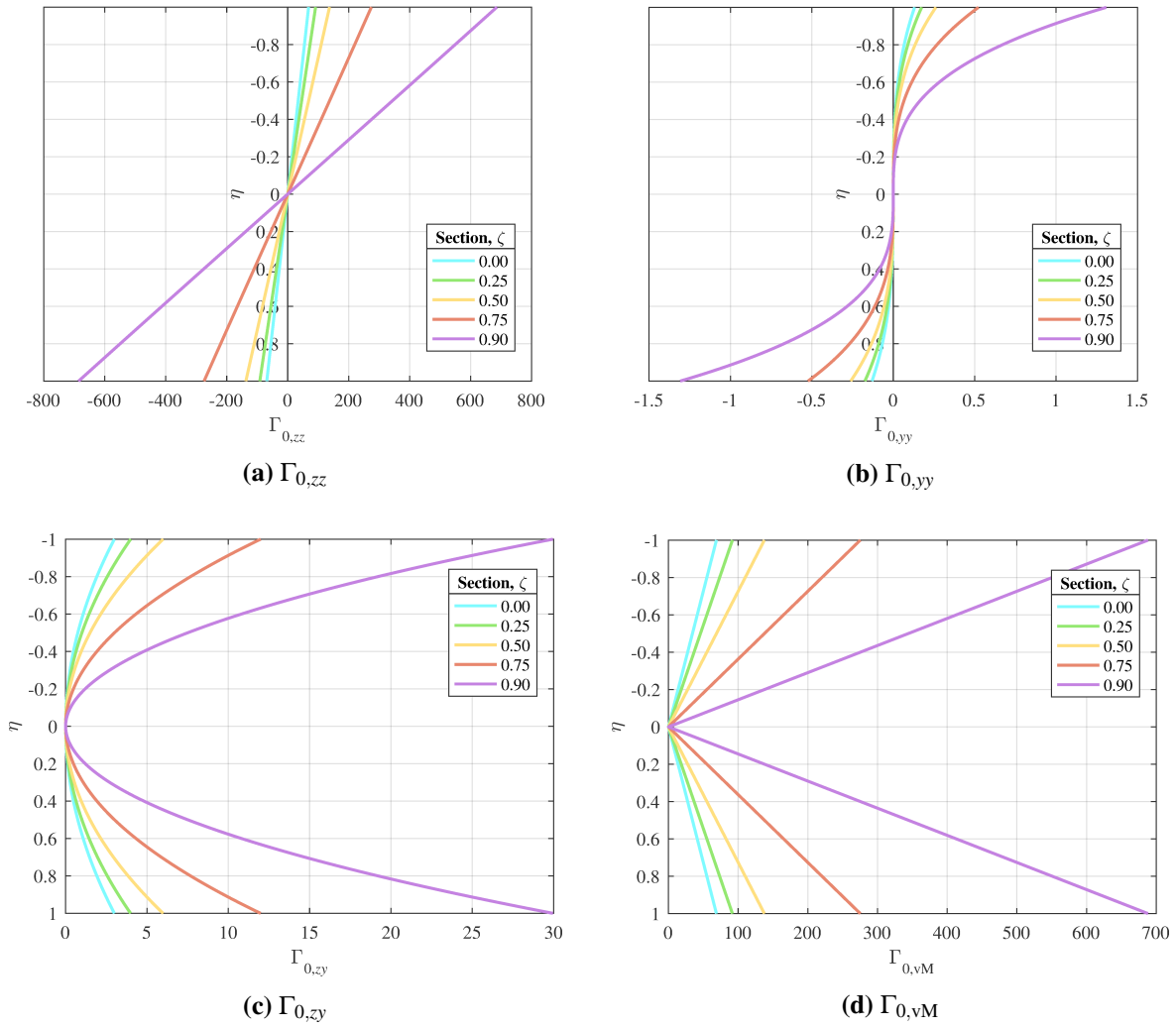


Figure 4.13: stress distribution at different sections in the case of shear force applied at the vertex.

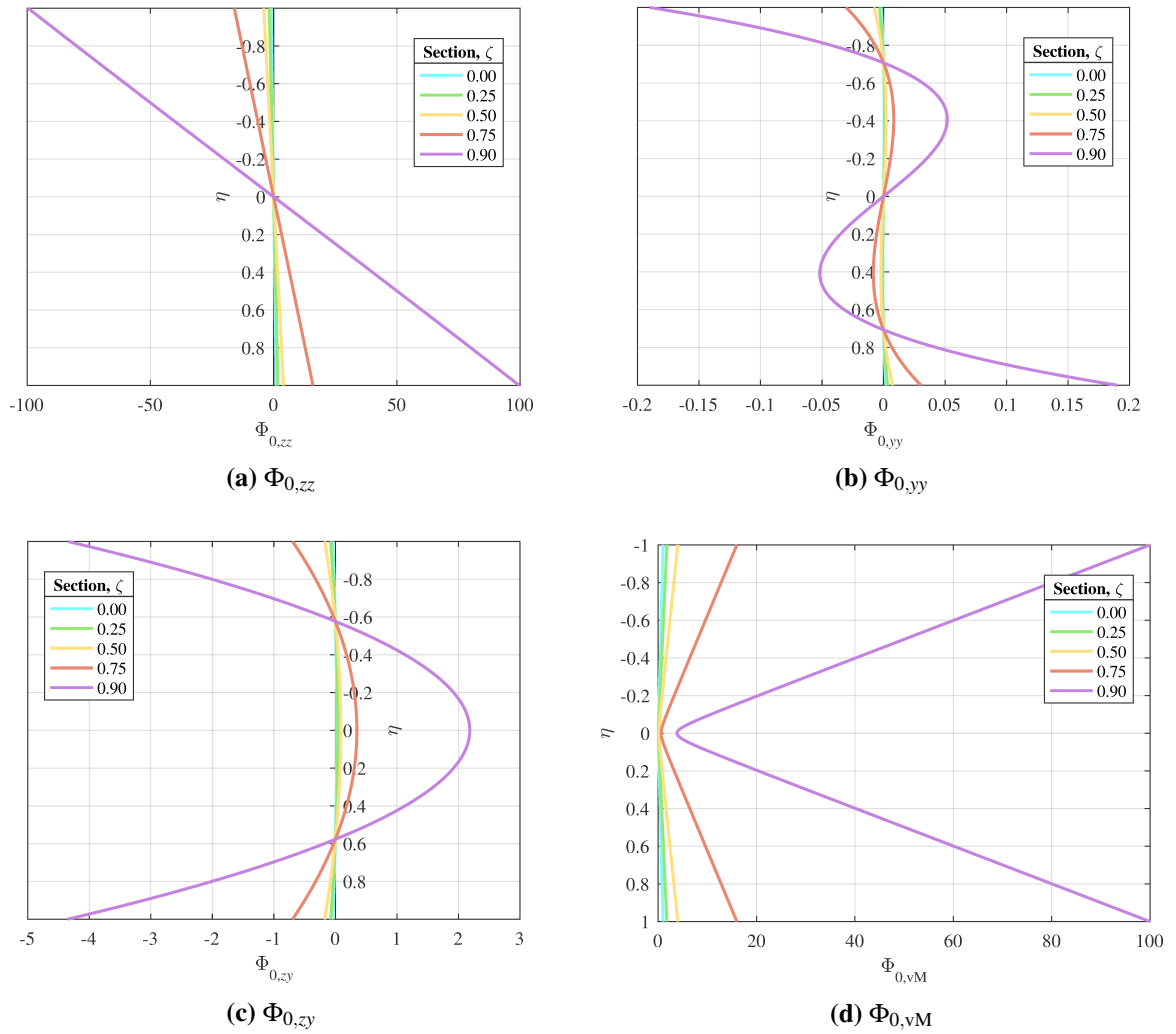


Figure 4.14: stress distribution at different sections in the case of concentrated couple at the vertex.

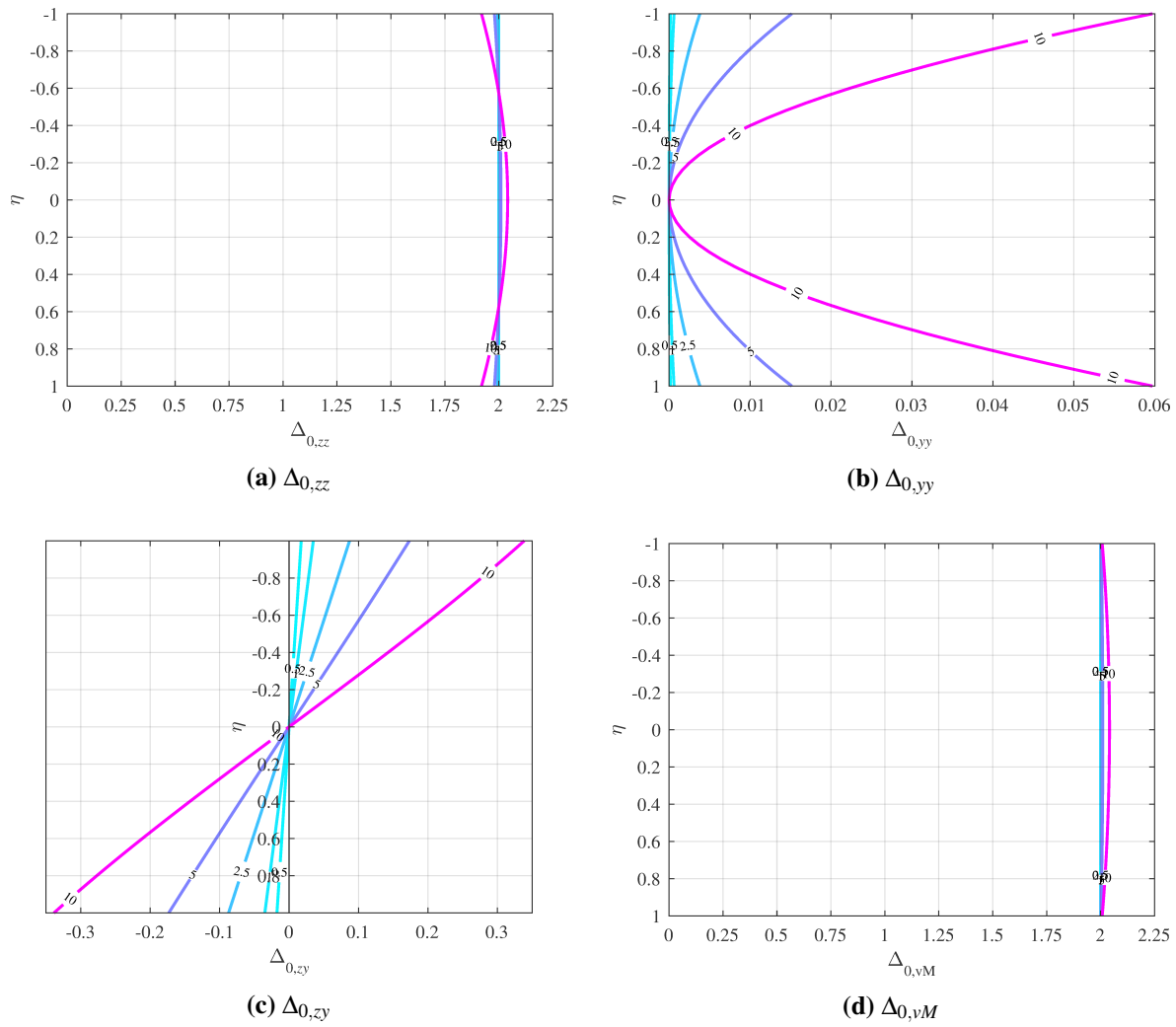


Figure 4.15: the dimensionless functions Δ_0 at the mid-span section ($\zeta = 0.5$) for the pure extension case.

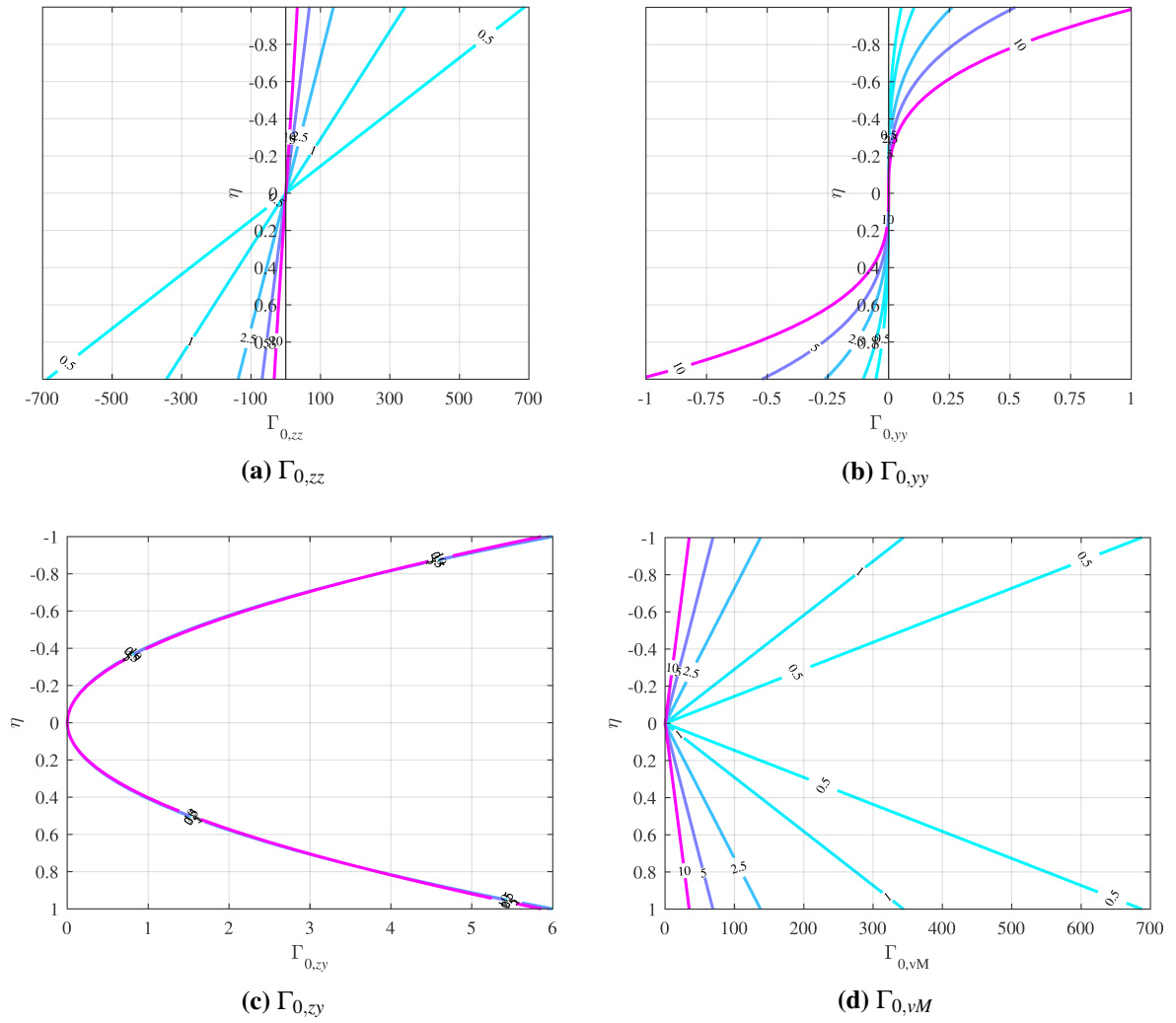


Figure 4.16: the dimensionless functions Γ_0 at the mid-span section ($\zeta = 0.5$) for the shear case.

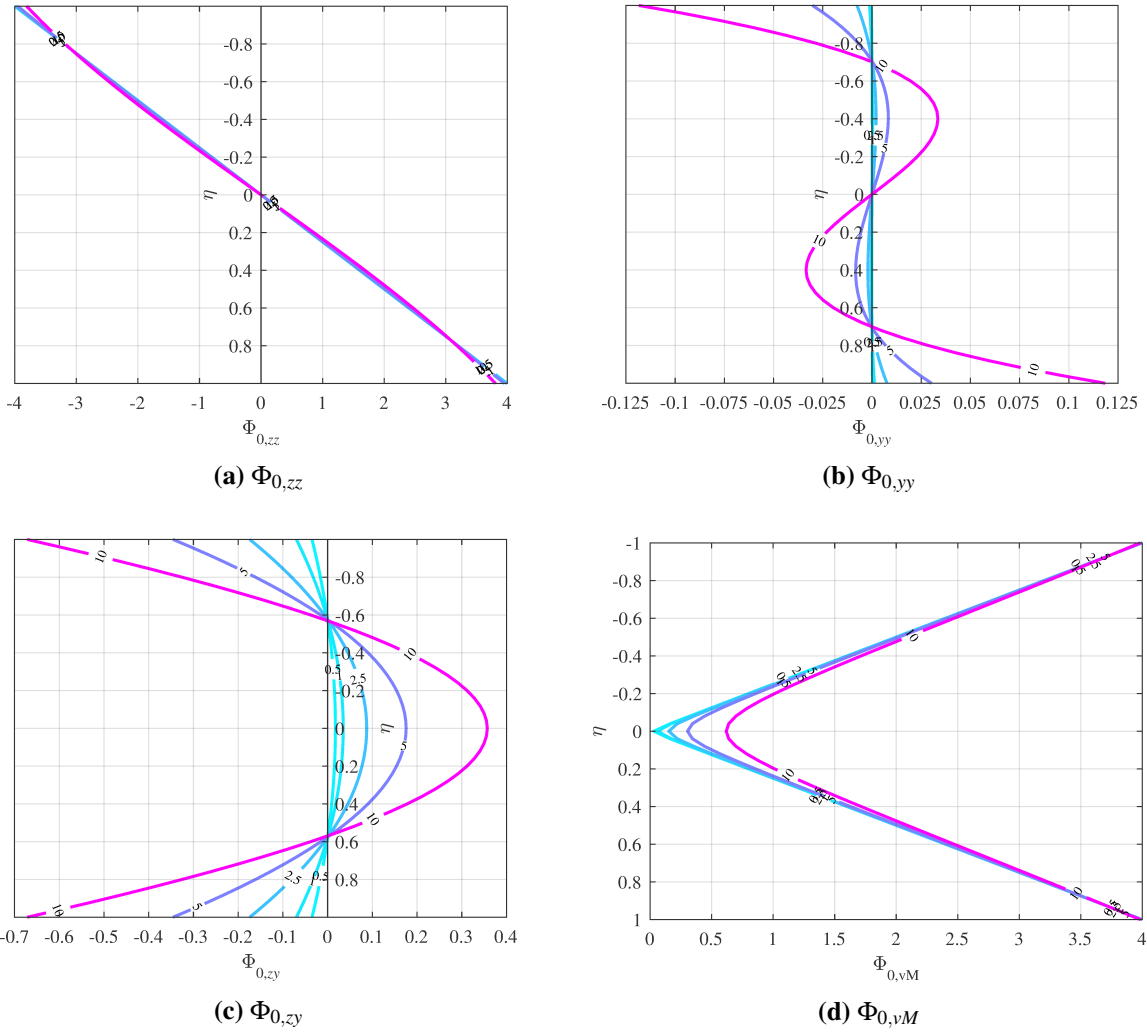


Figure 4.17: the dimensionless functions Φ_0 at the mid-span section ($\zeta = 0.5$) for the pure bending case.

4.2 Truncated wedge

4.2.1 Definition of the problem

Let us consider a truncated wedge of length L , clamped at the root section. The height of the root cross section and of the tip are $2h_0$ and $2h_t$, respectively. In the present case, we are assuming that the width of the truncated wedge, t , is equal to the unity.

The truncated wedge is loaded at the tip by a system of concentrated forces, \bar{N} and \bar{Q} , and bending moment, \bar{M} (Figure 4.18).

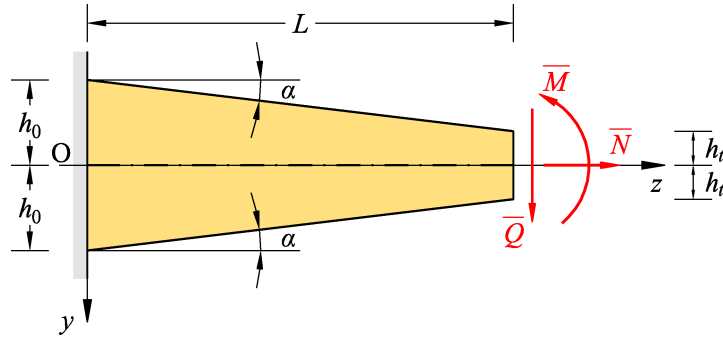


Figure 4.18: the truncated wedge.

Within the Theory of elasticity and by means of the *Superposition Principle*, the solution to the problem of such truncated wedge can be obtained by properly summing together various solutions of the infinite elastic wedge (Figure 4.19) [Galerkin, 1929; Knops and Villaggio, 1999]. Moreover, Knops and Villaggio [1999] suggest that the plane elasticity solution for the truncated wedge could adequately resemble also the plane stresses acting on a linearly tapered beam of thin rectangular cross section.

In fact, the *De Saint-Venant Principle* assures that – in regions of the body far away from the bases (so neglecting the boundary effects) and under the assumption that the body is sufficiently slender and thin – the stress distribution in the general problem shown in Figure 4.18, in which the tip of the truncated wedge is loaded by the concentrated forces \bar{N} and \bar{Q} , and the couple \bar{M} , is equivalent to that of a clamped wedge loaded at its vertex by the following loading system:

$$\begin{cases} N_0 = \bar{N}, \\ Q_0 = \bar{Q}, \\ M_0 = \bar{M} + \bar{Q}b, \end{cases} \quad (4.57)$$

where b is the distance between the vertex and the equivalent section in which the forces \bar{N} , \bar{Q} , and the couple \bar{M} , are applied. Our final purpose is to study a beam, which is a structural element characterised by having a dimension (the length) which is much larger than the other two (the cross section sizes). Then, using the solutions of an infinite wedge sufficiently slender is in line with our objectives, and we expect that the boundary effects will influence the solution only in a reasonably small fraction.

Stresses, strains, and displacements are then obtained by properly summing up together those of the elementary solutions of Michell and Carothers. As an example,

$$\underbrace{\sigma_{zz}}_{\text{Truncated wedge}} = \underbrace{\sigma_{zz}}_{\text{Wedge, } N_0 \text{ (from Eq. 4.11)}} + \underbrace{\sigma_{zz}}_{\text{Wedge, } Q_0 \text{ (from Eq. 4.25)}} + \underbrace{\sigma_{zz}}_{\text{Wedge, } M_0 \text{ (from Eq. 4.29)}}. \quad (4.58)$$

It is easy to note that the analytical expressions of the stresses for the truncated wedge may be extremely complicated. This awkwardness is even more so for the strains and displacements.

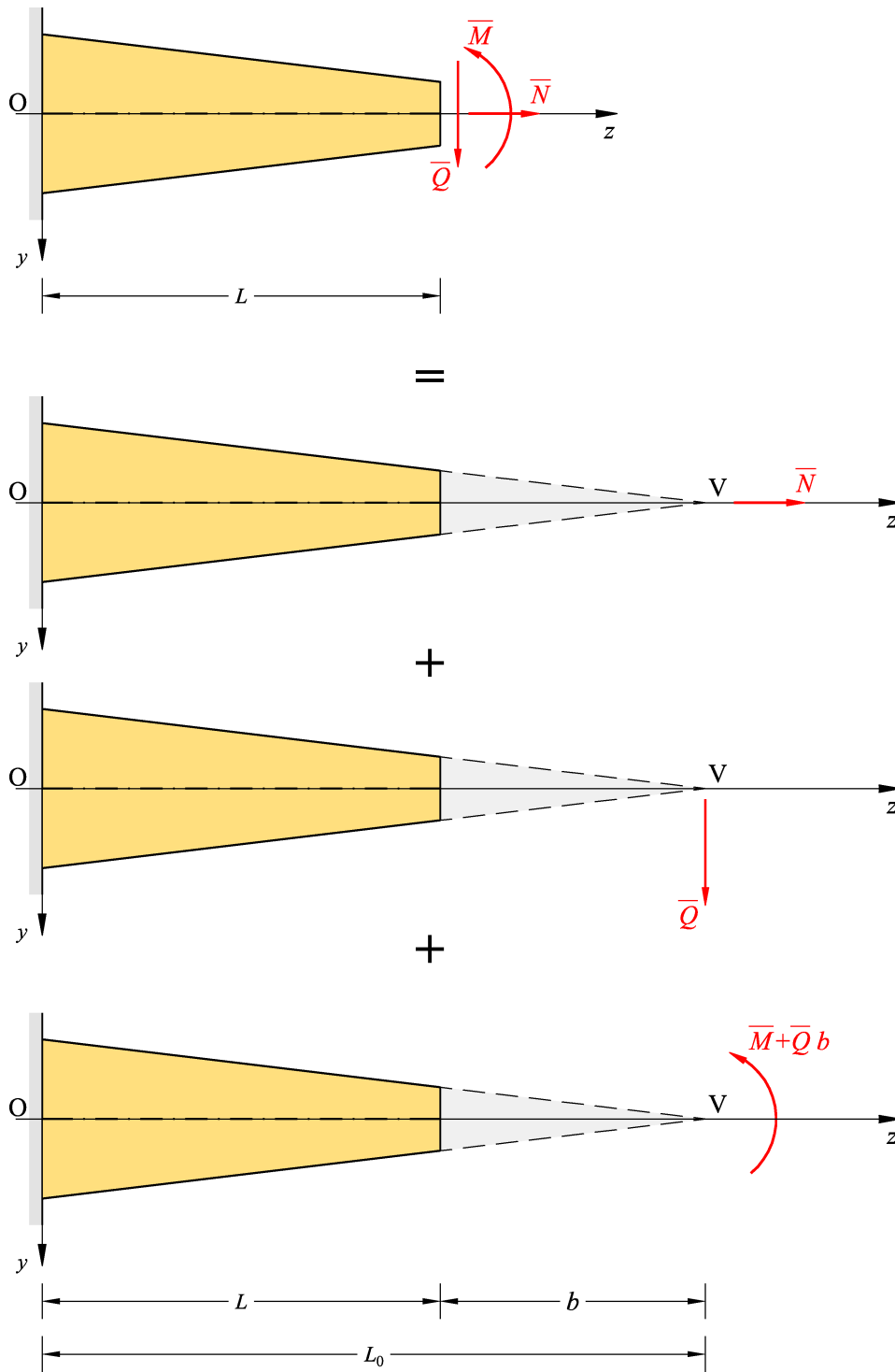


Figure 4.19: schematic application of the *Superposition Principle*.

4.2.2 Non-dimensionalisation of the solution

We propose a non-dimensionalisation strategy to the aim of slightly simplify the mathematical expressions. For such non-dimensionalisation, the strategy adopted in Section 4.1.4 has been adopted also in what follows.

In particular, we propose a transformation of the truncated wedge into a rectangle whose length is 1 and height is 2 (Figure 4.21).

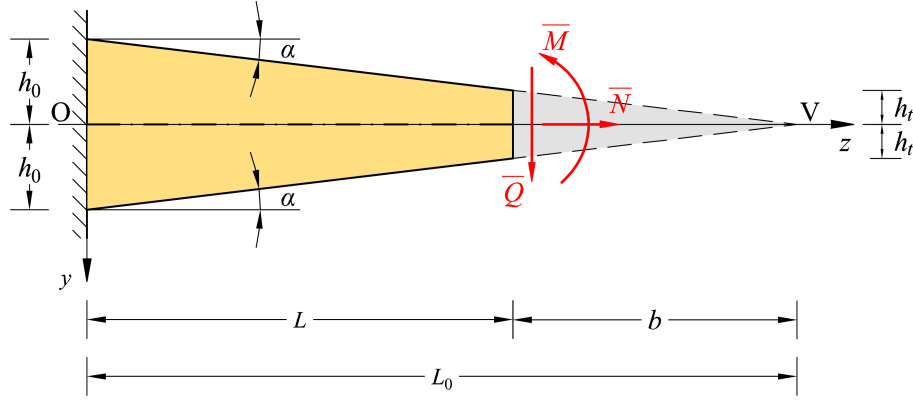


Figure 4.20: definition of the geometric parameters

Dimensionless parameters

To unequivocally define the geometry of the truncated wedge (Figure 4.20) we need to introduce the geometric parameter β , which is the distance between the tip cross section and the vertex of a wedge with the same height at the root cross section and same taper angle α . Normalizing with the length L , it is possible to define the equivalent *dimensionless vertex distance*,

$$\beta = \frac{b}{L}. \quad (4.59)$$

For $\beta = 0$ the truncated wedge becomes a pure wedge. Conversely, for $\beta \rightarrow \infty$ the truncated wedge tends to become a rectangle. β is somehow related to the slenderness of the truncated wedge.

We also introduce the *dimensionless axial coordinate*,

$$\zeta = \frac{z}{L}, \quad (4.60)$$

where L is the length of the truncated wedge. To each cross section a value of ζ will be associated, ranging from $\zeta = 0$ for the root section, to $\zeta = 1$ for the tip.

We also introduce the *dimensionless transverse coordinate* η , individualising the relative vertical position of each point in the section,

$$\eta = \frac{y}{h(z)}, \quad (4.61)$$

where

$$h(z) = h_0 - z \tan \alpha, \quad (4.62)$$

where h_0 is the mid-length of the root section. As it can be easily verified (for example from Figure 4.21), for each section the value of η will range from -1 (corresponding to the upper free surface) to 1 (corresponding to the lower free surface).

To easily determine the value of β for a given truncated wedge, we notice that

$$\beta = \frac{\lambda}{1 - \lambda}, \quad (4.63)$$

where the *taper ratio* has been defined as

$$\lambda = \frac{h_t}{h_0}. \quad (4.64)$$

It can be easily verified that, being L_0 the length of the wedge, we have

$$L_0 = L(1 + \beta). \quad (4.65)$$

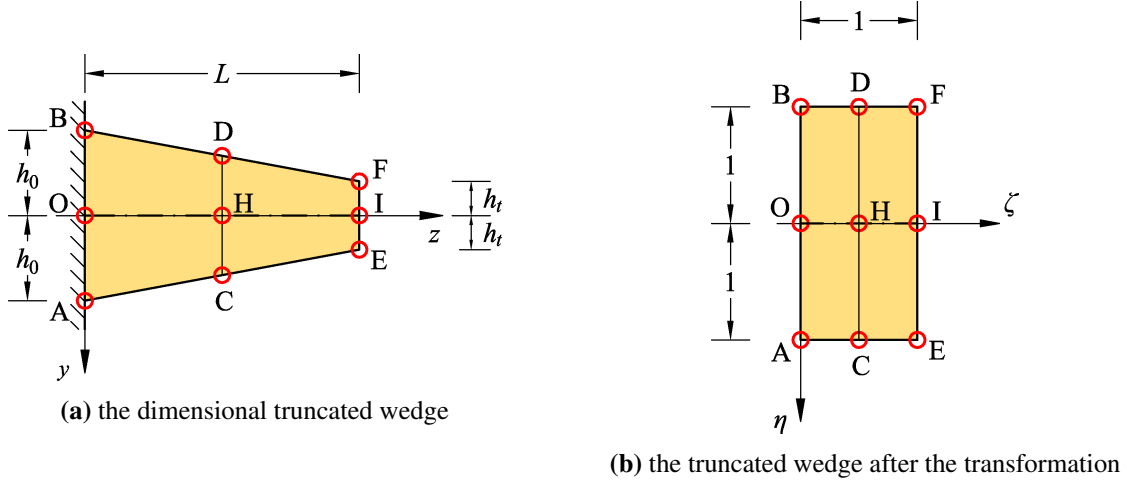


Figure 4.21: the non-dimensionalisation of the truncated wedge.

As done for the wedge in Section 4.1.4, we also introduce the *reference stress*,

$$\bar{\sigma}_N = \frac{\bar{N}}{2h_0t}, \quad (4.66)$$

equal to the mean stress of an equivalent prismatic beam with the same root section of the tapered beam under consideration.

We also define the *reference shear stress*,

$$\bar{\sigma}_Q = \frac{\bar{Q}}{2h_0t}, \quad (4.67)$$

and the *reference stress for bending*,

$$\bar{\sigma}_M = \frac{\bar{M}h_0}{\frac{1}{12}t(2h_0)^3}, = \frac{3\bar{M}}{2th_0^2}. \quad (4.68)$$

Under the above-mentioned hypothesis, it is possible to write the following Equations for the stress state of the truncated wedge.

4.2.3 Solution for stresses

Normal stress σ_{zz}

$$\sigma_{zz} = \Delta_{zz}\bar{\sigma}_N + \Gamma_{zz}\bar{\sigma}_Q + \Phi_{zz}\bar{\sigma}_M, \quad (4.69)$$

where

$$\Delta_{zz} = \frac{2(1+\beta)\tan\alpha}{(1+\beta-\zeta)(\alpha+\cos\alpha\sin\alpha)(1+\eta^2\tan^2\alpha)^2}, \quad (4.70)$$

$$\Gamma_{zz} = \frac{2(1+\beta)\tan\alpha}{3(1+\beta-\zeta)^2(1+\eta^2\tan^2\alpha)^3} \left\{ \frac{6\beta\eta[3-\eta^2-(1-\eta^2)\cos 2\alpha]\tan\alpha}{\sin 2\alpha-2\alpha\cos 2\alpha} - \frac{3(1+\beta-\zeta)\eta(1+\eta^2\tan^2\alpha)\tan\alpha}{\alpha-\cos\alpha\sin\alpha} \right\}, \quad (4.71)$$

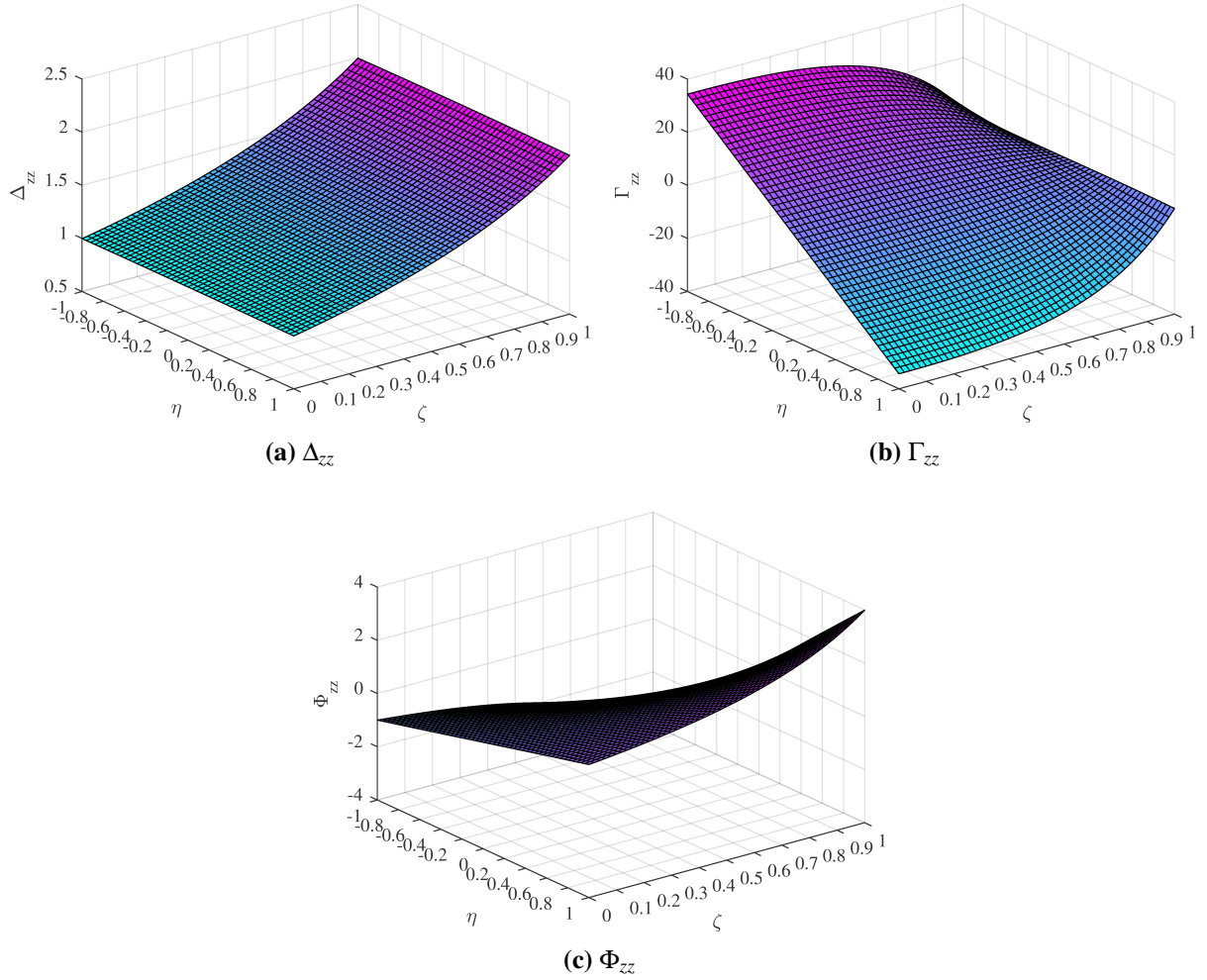


Figure 4.22: distribution of the dimensionless functions whose combination gives σ_{zz} , for $\alpha = 2.5^\circ$ and $\beta = 1$.

and

$$\Phi_{zz} = \frac{4(1+\beta)^2 \eta [3 - \eta^2 - (1 - \eta^2) \cos 2\alpha] \tan^3 \alpha}{3(1+\beta - \zeta)^2 (\sin 2\alpha - 2\alpha \cos 2\alpha) (1 + \eta^2 \tan^2 \alpha)^3}. \quad (4.72)$$

Figure 4.22 shows the surface plots of the dimensionless functions that, properly summed together (Equation 4.69), give the value of σ_{zz} . In particular, those plots – and those that follows for the other dimensionless functions – are obtained for $\alpha = 2.5^\circ$ and $\beta = 1$. The dimensionless axial coordinate ζ and the dimensionless transverse coordinate η are represented on the abscissa and the ordinate respectively.

In Figure 4.22(a) the contribution of the pure extension is shown: it increase with the increase of the abscissa ζ due to the relative reduction of the height of the sections, on which the σ_{zz} are approximately constant. In Figure 4.22(c) the analogous contribution of the bending is shown: such contribution is linear with respect to the η -coordinate and its maximum values – in correspondence of the upper and lower edges of the truncated wedge – increase with the increase of the ζ -coordinate. Conversely, the contribution to the σ_{zz} due to the shear force applied at the tip section – linear with the η -coordinate – intensifies with the increase of the distance from the tip (4.22(b)).

Shear stress σ_{zy}

$$\sigma_{zy} = \Delta_{zy} \bar{\sigma}_N + \Gamma_{zy} \bar{\sigma}_Q + \Phi_{zy} \bar{\sigma}_M, \quad (4.73)$$

where

$$\Delta_{zy} = -\frac{2(1+\beta)\eta \tan^2 \alpha}{(1+\beta-\zeta)(\alpha + \cos \alpha \sin \alpha)(1+\eta^2 \tan^2 \alpha)^2}, \quad (4.74)$$

$$\Gamma_{zy} = \frac{2(1+\beta) \tan^2 \alpha}{3(1+\beta-\zeta)^2(1+\eta^2 \tan^2 \alpha)^3} \left\{ \frac{3\beta [1-6\eta^2 + \eta^4 + (1-\eta^4) \cos 2\alpha] \tan \alpha}{\sin 2\alpha - 2\alpha \cos 2\alpha} + \frac{3(1+\beta-\zeta)\eta^2 \tan \alpha (1+\eta^2 \tan^2 \alpha)}{\alpha - \cos \alpha \sin \alpha} \right\}, \quad (4.75)$$

and

$$\Phi_{zy} = \frac{2(1+\beta)^2 [1-6\eta^2 + \eta^4 + (1-\eta^4) \cos 2\alpha] \tan^4 \alpha}{3(1+\beta-\zeta)^2 (\sin 2\alpha - 2\alpha \cos 2\alpha) (1+\eta^2 \tan^2 \alpha)^3}. \quad (4.76)$$

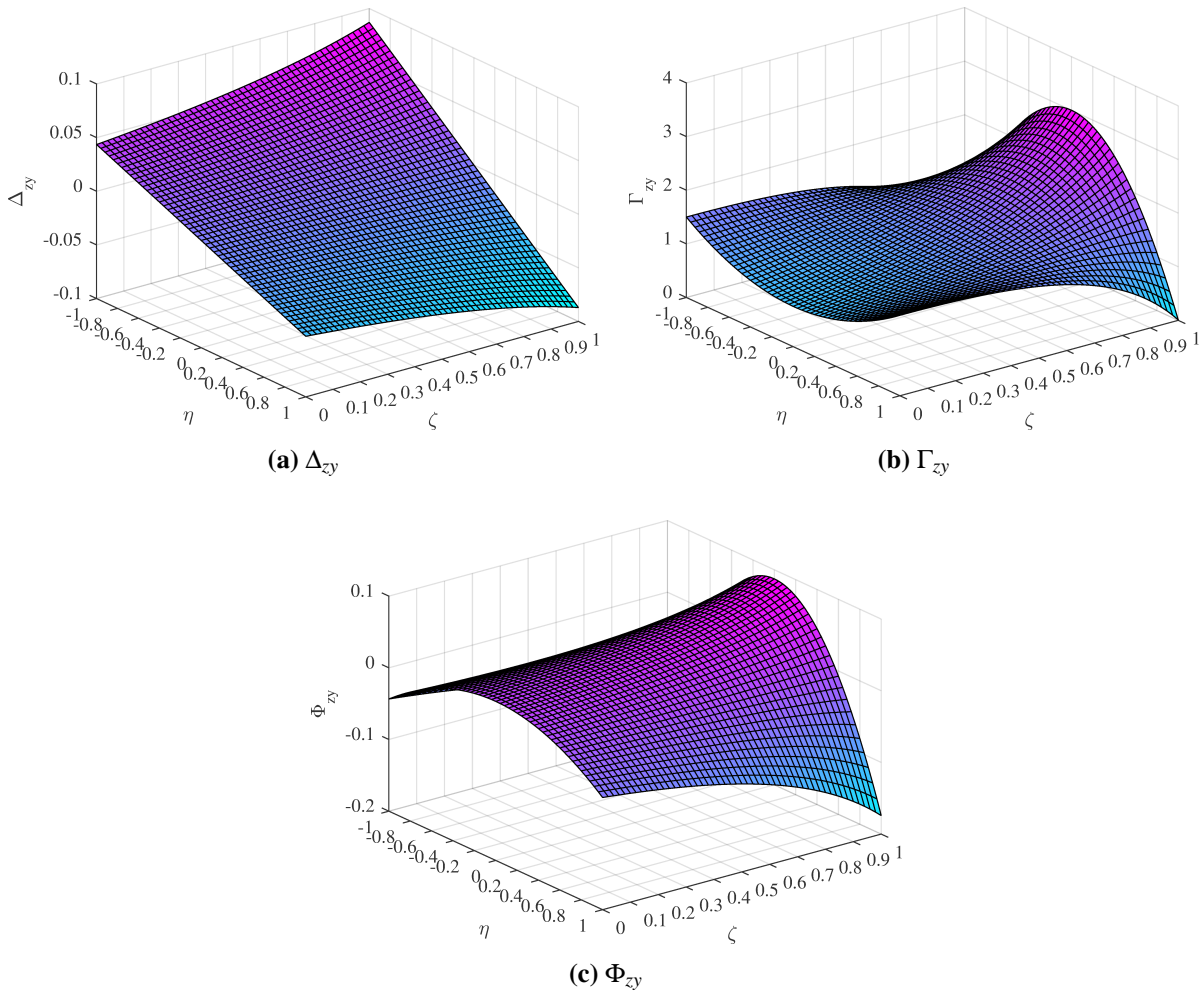


Figure 4.23: distribution of the dimensionless functions whose combination gives σ_{zy} , for $\alpha = 2.5^\circ$ and $\beta = 1$.

In Figure 4.23, plots are presented of the dimensionless functions which properly summed together give the shear stress σ_{zy} – for $\alpha = 2.5^\circ$ and $\beta = 1$, in analogy to those shown in Figure 4.22 for the σ_{zz} .

All the load conditions considered give a contribution to the final value of the shear stress: in particular, for the angle taken into account ($\alpha = 2.5^\circ$), it is evident that the contribution of the pure extension is almost linear with respect to the η -coordinate. Instead, the contributions of the shear force and bending are quadratic with respect to the η -coordinate.

Probably the most interesting result is shown in Figure 4.23(b), where the distribution of Γ_{zy} is shown. At the tip section ($\zeta = 1$), the dimensionless function is parabolic, with the maximum on the centreline and zeros on the edges of the truncated wedge. Moving from the tip to the root, the curvature of the function gradually changes sign, and the location of the maximum value on the section migrates from the centreline to the edges – on which Γ_{zy} is different from zero. The area underlying the plot of Γ_{zy} for each section is kept constant and its value is 2.

Summarising, in a truncated wedge we witness a drastic change in the distribution of Γ_{zy} from the root section to the tip section. This will be of great interest for our study, being the dimensionless function Γ_{zy} strictly related (Equation 4.73) to the shear stresses σ_{zy} induced by a shear force.

Normal stress σ_{yy}

$$\sigma_{yy} = \Delta_{yy} \bar{\sigma}_N + \Gamma_{yy} \bar{\sigma}_Q + \Phi_{yy} \bar{\sigma}_M, \quad (4.77)$$

where

$$\Delta_{yy} = \frac{2(1 + \beta)\eta^2 \tan^3 \alpha}{(1 + \beta - \zeta)(\alpha + \cos \alpha \sin \alpha)(1 + \eta^2 \tan^2 \alpha)^2}, \quad (4.78)$$

$$\Gamma_{yy} = \frac{2(1 + \beta)\eta \tan^3 \alpha}{3(1 + \beta - \zeta)^2 (1 + \eta^2 \tan^2 \alpha)^3} \left\{ \frac{6\beta [-1 + 3\eta^2 - (1 - \eta^2) \cos 2\alpha] \tan \alpha}{\sin 2\alpha - 2\alpha \cos 2\alpha} - \frac{3(1 + \beta - \zeta)\eta^2 \tan \alpha (1 + \eta^2 \tan^2 \alpha)}{\alpha - \cos \alpha \sin \alpha} \right\}, \quad (4.79)$$

and

$$\Phi_{yy} = -\frac{4(1 + \beta)^2 \eta [1 - 3\eta^2 + (1 - \eta^2) \cos 2\alpha] \tan^5 \alpha}{3(1 + \beta - \zeta)^2 (\sin 2\alpha - 2\alpha \cos 2\alpha) (1 + \eta^2 \tan^2 \alpha)^3}. \quad (4.80)$$

It is noteworthy that these dimensionless functions depend not only on α (as in the case of the wedge), but also on β . Moreover, for $\beta = 0$ it can be proven that all the dimensionless functions (Equations 4.70-4.72, 4.74-4.76 and 4.78-4.80) give the same results obtained for the wedge (Equations from 4.46 to 4.54).

Figure 4.24 shows the distribution of the dimensionless functions Δ_{yy} , Γ_{yy} , and Φ_{yy} for $\alpha = 2.5^\circ$ and $\beta = 1$. Those functions appear to have a small impact on the state of stress in the truncated wedge. Infact, those appear to be approximately two and one order of magnitude lower if compared with the functions related to σ_{zz} and σ_{zy} , respectively, and which are shown in Figures 4.22 and 4.23.

4.2.4 Discussion of results

Stresses at different sections

As already shown for the wedge (in Section 4.1.6), we focus on five reference sections (Figure 4.25), corresponding to the root section ($\zeta = 0$, cyan curve), the mid-span section ($\zeta = 0.5$, yellow curve), and the tip section ($\zeta = 1$, purple curve), as well as other two intermediate quarter cross sections ($\zeta = 0.25$, green curve, and $\zeta = 0.75$, red curve).

In Figure 4.26, the dimensionless functions which gives the stress σ_{zz} are shown. Even if not rigorous due to the fact that the proposed solution for the truncated wedge is relative to a plane problem and not to a physical beam, the typical constant and linear Navier's distributions due, respectively, to the extension and to the bending moment can be recognised in Figures 4.26(a) and 4.26(c). Those distributions are not equal for the different sections, and the intensity is higher approaching to the tip. In Figure 4.26(b) it is highlighted that also the shear force \bar{Q} induces linearly distributed normal stresses in the sections, whose intensity increase approaching to the tip: this contribution has to be strictly connected to the shear-induced bending.

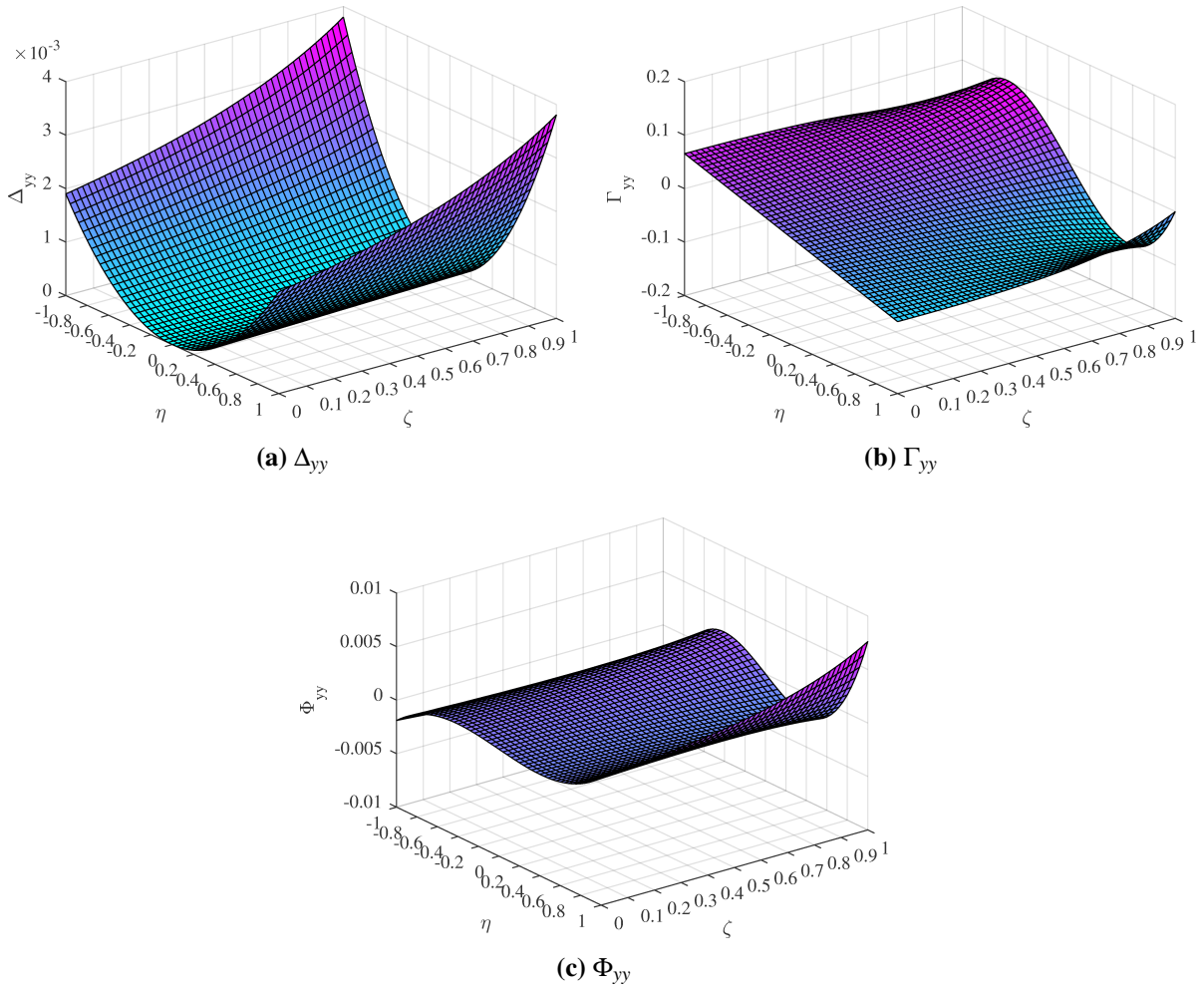


Figure 4.24: distribution of the dimensionless functions whose combination gives σ_{yy} , for $\alpha = 2.5^\circ$ and $\beta = 1$.

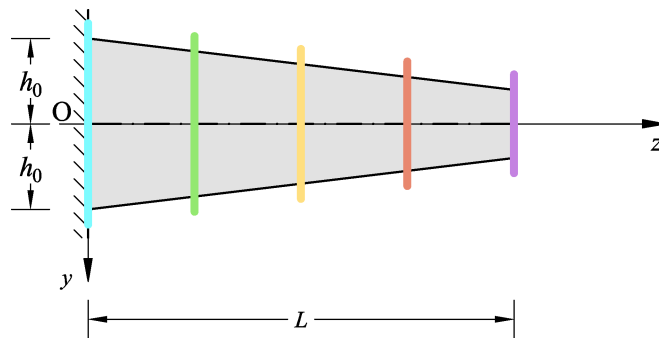


Figure 4.25: the five section considered in the truncated wedge: the root section ($\zeta = 0$, cyan section), the mid-span section ($\zeta = 0.5$, yellow section), and the tip section ($\zeta = 1$, purple section), and the other two intermediate quarter cross sections ($\zeta = 0.25$, green section, and $\zeta = 0.75$, red section).

Figure 4.27 shows the dimensionless functions which give the stress σ_{zy} . As well known, in prismatic beams only the shear force induce shear stresses in the sections. In the truncated wedge, the normal and shear force, and the bending moment induce shear stresses.

In particular, the pure extension introduce linearly distributed shear stresses whose resultant is null (Figure 4.27(a)).

In Figure 4.27(c), the parabolic distribution of shear stresses connected to the bending moment is

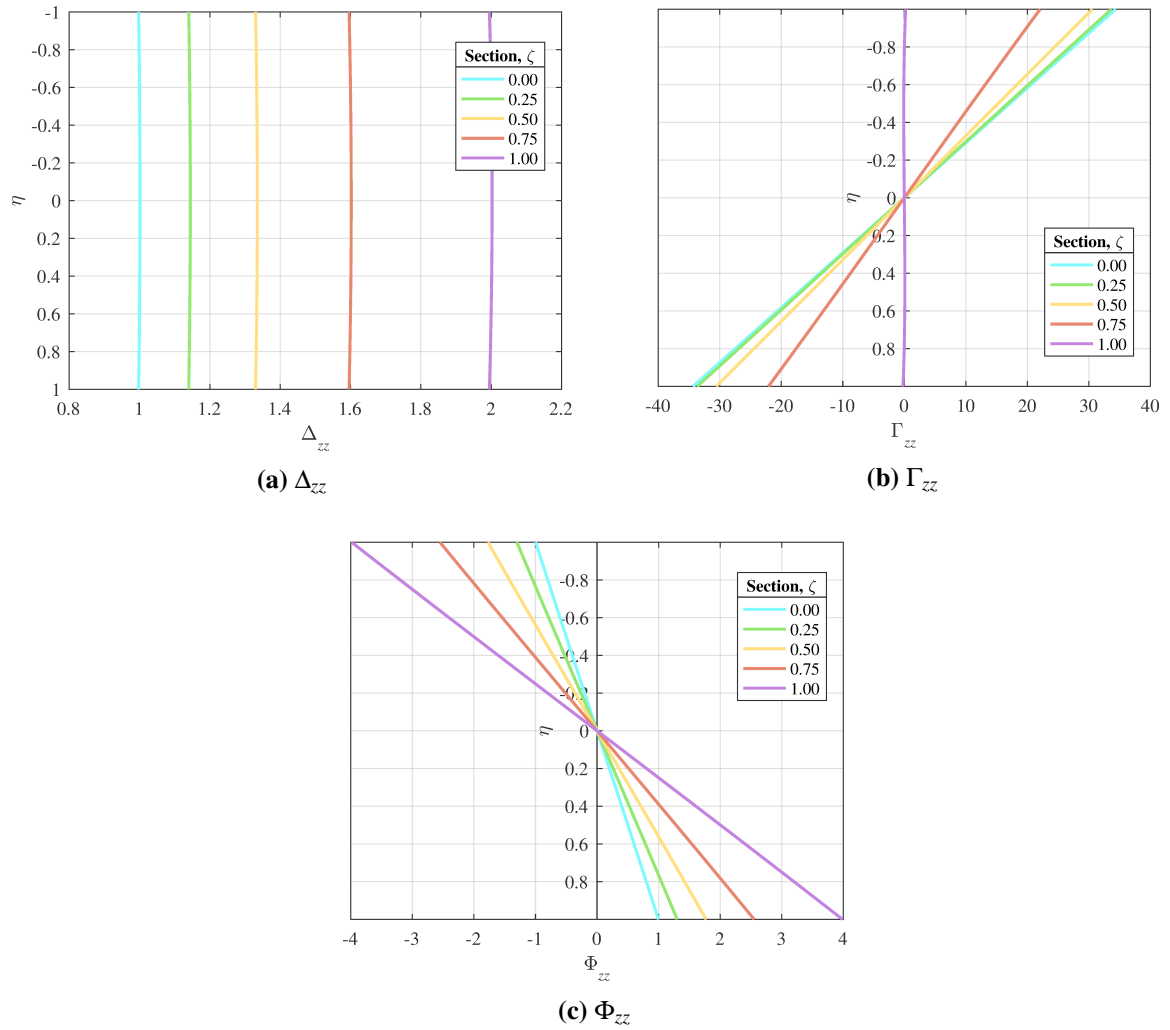


Figure 4.26: distribution at different sections of the dimensionless functions whose combination gives σ_{zz} (for $\alpha = 2.5^\circ$ and $\beta = 1$).

shown. The integral on the section of such distribution is null. For positive values of the bending moment (Figure 4.18), highest negative values on the free surfaces and the maximum positive value on the mid-line are reached.

Figure 4.27(b) shows the influence of the shear force on the shear stresses. At the tip section, the parabolic distribution of the shear stresses typical of prismatic beams is evident: the only force acting on that particular section is the shear \bar{Q} , and the distribution is equivalent to that given by the Jourawski shear stress formula. From the tip to the root, the contribution of the shear-induced bending moment to the shear stresses changes the intensity of the maximum shear location (and also the values at the outer edges), reaching an almost constant distribution at the mid-span section (for the particular β chosen as an example). Moving closer to the root, also the curvature of the distribution changes, and the maximum is no more located on the mid-line of the truncated wedge, but moves to the outer and inner surface.

In Figure 4.28, the dimensionless functions which give the stress σ_{yy} are shown: all the three loading conditions induce such stresses in the truncated wedge, even though the intensity is much smaller, and somehow negligible, with respect to the normal stresses σ_{zz} , and the shear stresses σ_{zy} .

The mid-span section: variation with α

The dimensionless functions show a dependency on both the parameters α and β . To the aim of investigating further those dependencies, we focus our attention to the mid-span section ($\zeta = 0.5$). Such a section is equally distant from the tip and the root sections, and then it will be the less affected by boundary effects, under the assumption that the truncated wedge is sufficiently slender.

In Figures 4.29, 4.31, and 4.30, the distributions of the dimensionless functions along the section are shown for different values of the angle α and for $\beta = 1$. In particular, the values of α which have been taken into account are: 0.5° , 1° , 2.5° , 5° and 10° .

Δ_{zz} (Figure 4.29(a)) and Φ_{zz} (Figure 4.29(c)) show a very small dependency on the variation of the angle α , as well as Γ_{zy} (Figure 4.30(b)).

All the other dimensionless functions present a relevant variation in respect of α . For example, the normal stresses σ_{zz} induced by a shear force \bar{Q} reach high levels on the free edges for smaller angles of taper (Figure 4.29(b)).

It is interesting to highlight the behaviour of the dimensionless functions Δ_{zy} and Φ_{zy} in the truncated wedge (Figure 4.30), because those functions show differences in respect to what could be expected on a rectangle loaded in a similar manner. In fact in the case of a rectangle loaded on one section, the axial force and the bending moment do not introduce shear stresses.

Also, Δ_{zy} and Φ_{zy} appear to be sensitive to the variation of angles of taper. It is noteworthy that for the limit of $\alpha \rightarrow 0$, the solution of the truncated wedge converges to that of a rectangle.

The mid-span section: variation with β

In Figures 4.32, 4.34 and 4.33, the distributions of the dimensionless functions along the section are shown for different values of the parameter β and for $\alpha = 2.5^\circ$. In particular, the values of β which have been taken into account are: 0, 0.5, 1, 1.5, 2 and 5° .

For $\beta = 0$ the truncated wedge becomes a pure wedge, and the solution converges to that given in Section 4.1. On the other hand, for β greater than 5 the solution approaches that of the rectangle. This is evident in Figure 4.33(b): the light cyan curve corresponding to $\beta = 0$ is exactly comparable to $\Gamma_{0,zy}$ shown in Figure 4.16(c). As the value of β increases, the curve gradually changes in curvature, and, exceeding the value of $\beta = 1$ the location of the maximum moves from the edges to the centreline, and gradually converges to the parabolic distribution typical of the Jourawski shear stress formula.

In Figures 4.33(a) and 4.33(c) is also evident that for the limit of $\beta \rightarrow \infty$ (so that the truncated wedge can be approximated by a rectangle), $\Delta_{0,zy}$ and $\Phi_{0,zy}$ gradually become a constant null function with respect to the η -coordinate.

All the dimensionless functions show a dependency on β .

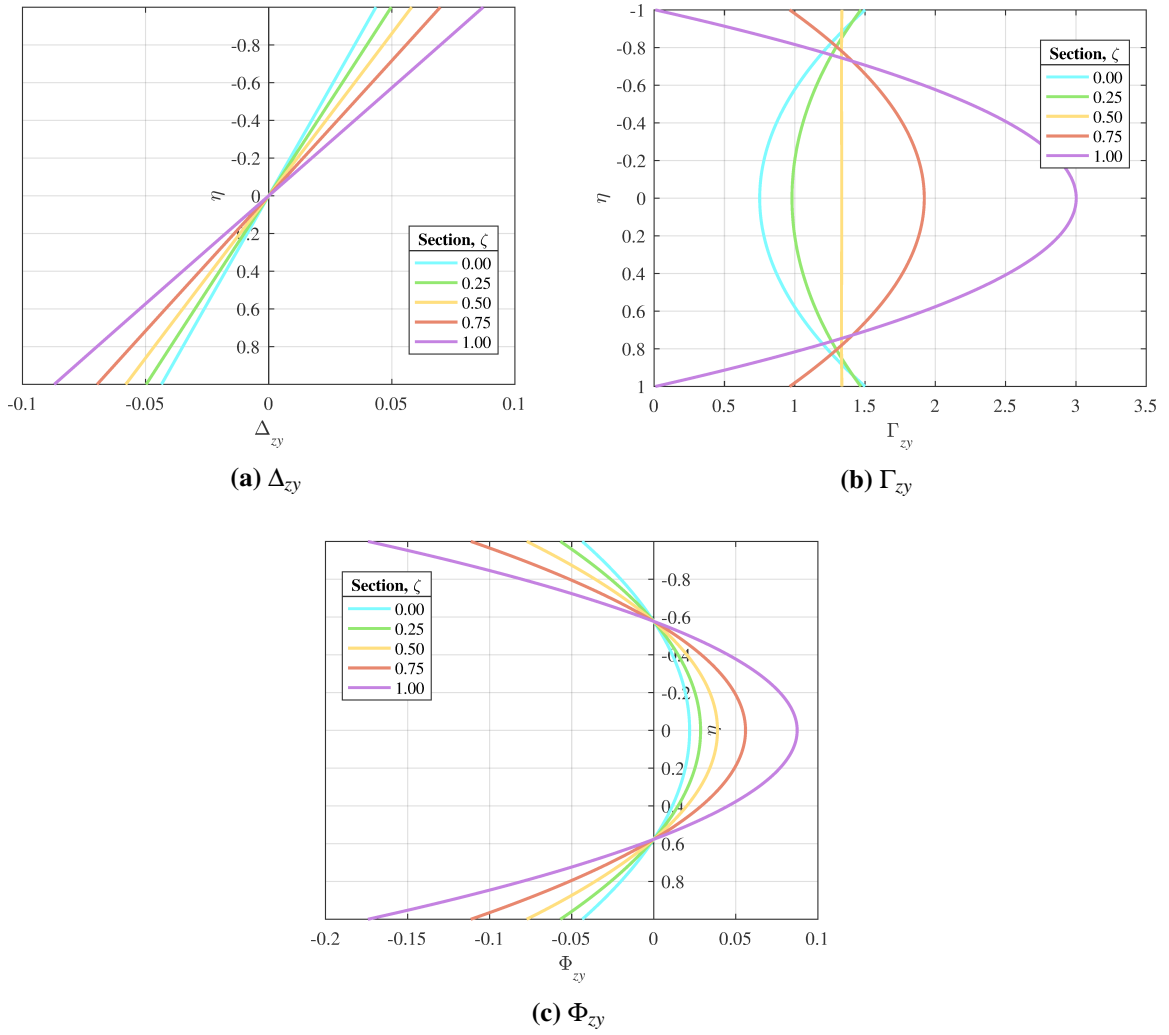


Figure 4.27: distribution at different sections of the dimensionless functions whose combination gives σ_{zy} (for $\alpha = 2.5^\circ$ and $\beta = 1$).

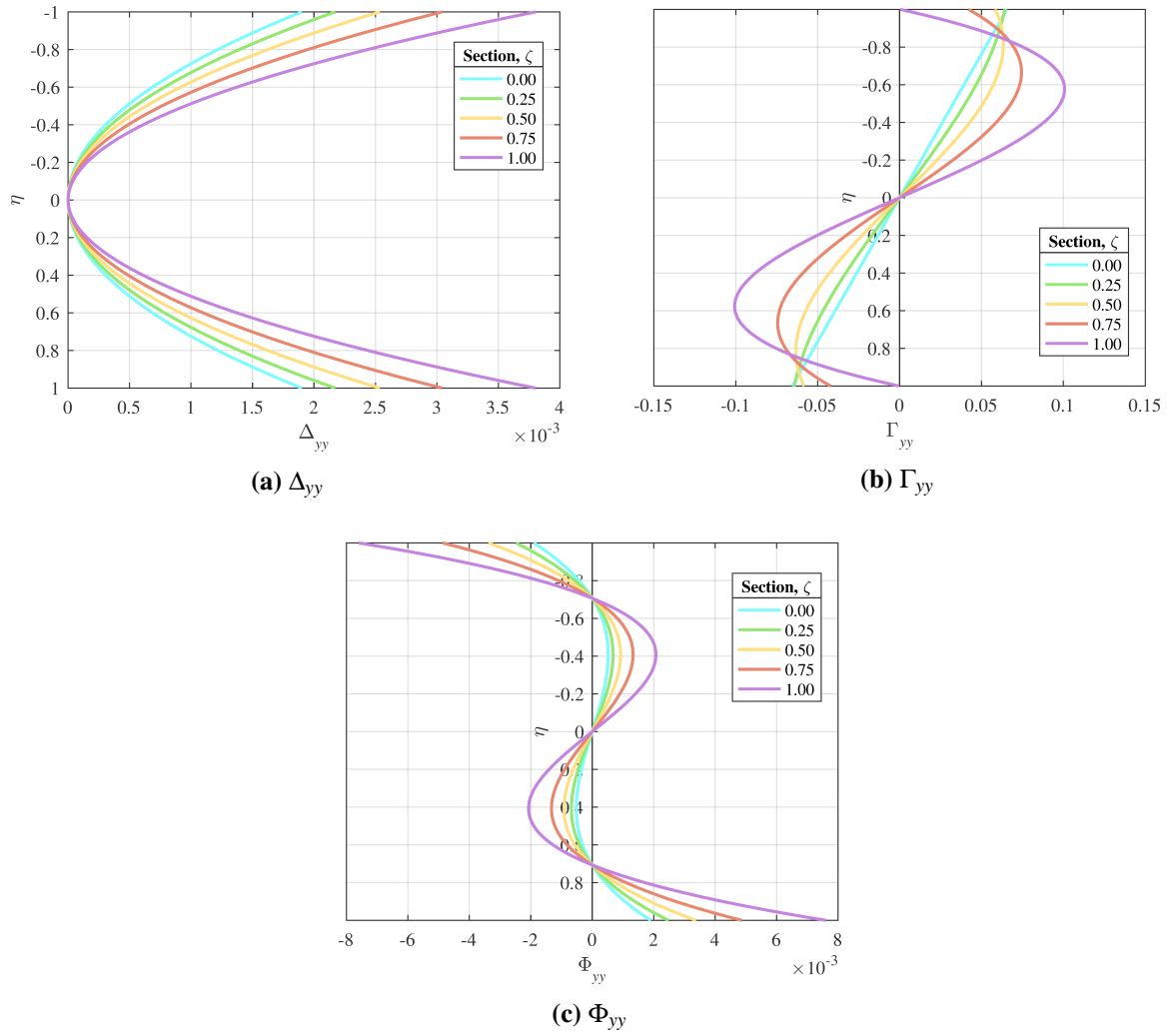


Figure 4.28: distribution at different sections of the dimensionless functions whose combination gives σ_{yy} (for $\alpha = 2.5^\circ$ and $\beta = 1$).

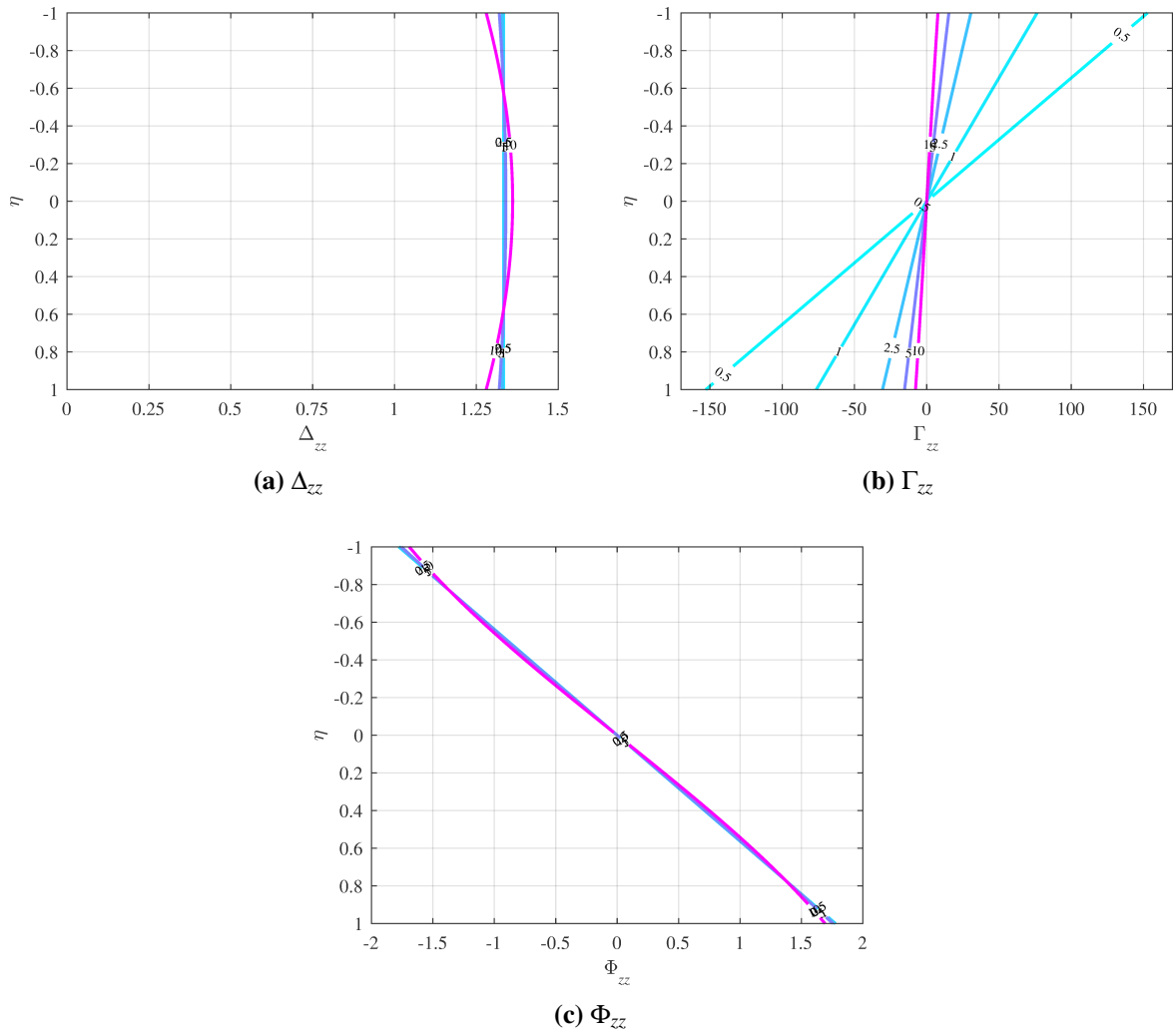


Figure 4.29: distribution at the mid-span section ($\zeta = 0.5$) of the dimensionless functions whose combination gives σ_{zz} for different values of α .

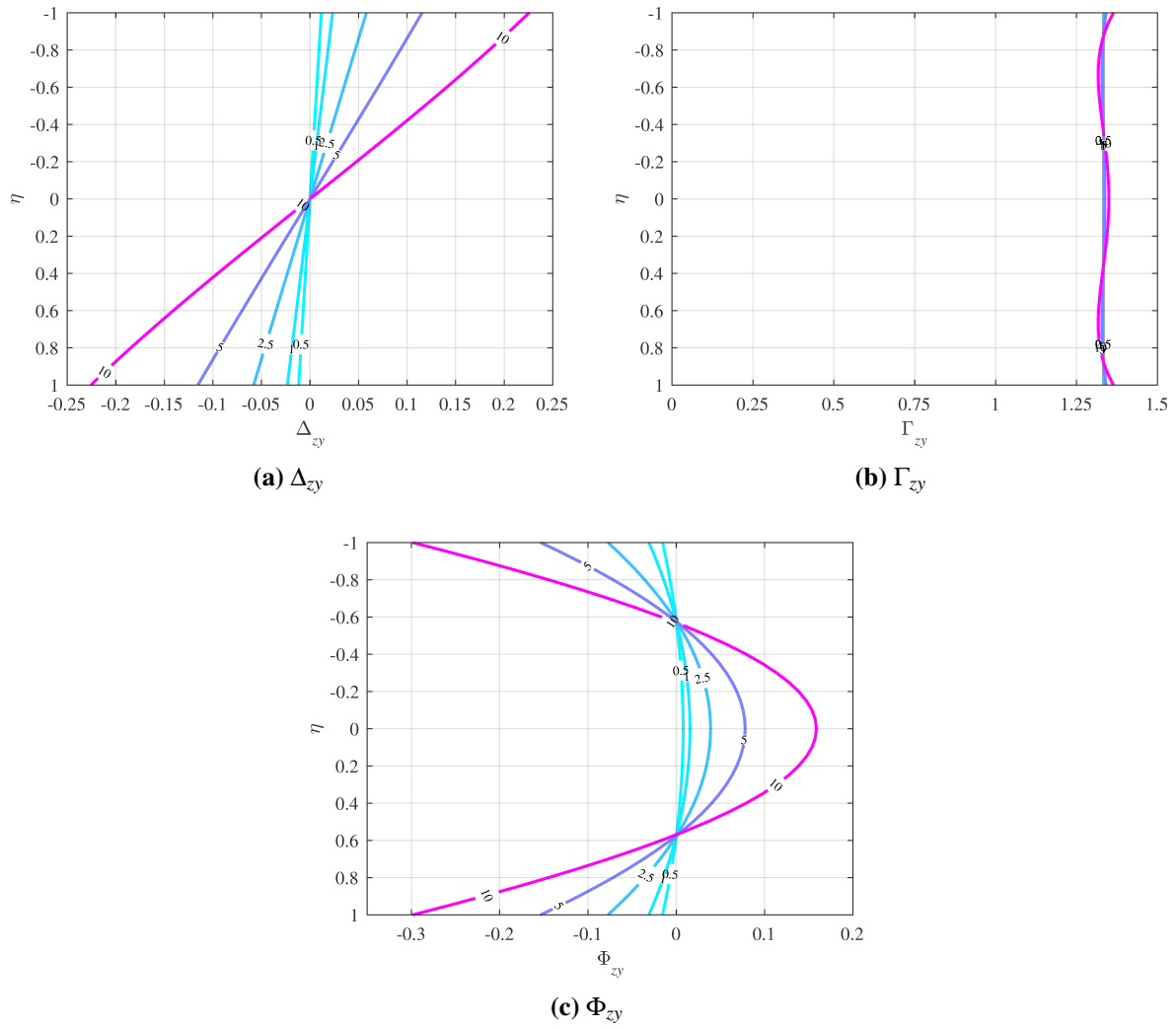


Figure 4.30: distribution at the mid-span section ($\zeta = 0.5$) of the dimensionless functions whose combination gives σ_{zy} for different values of α .

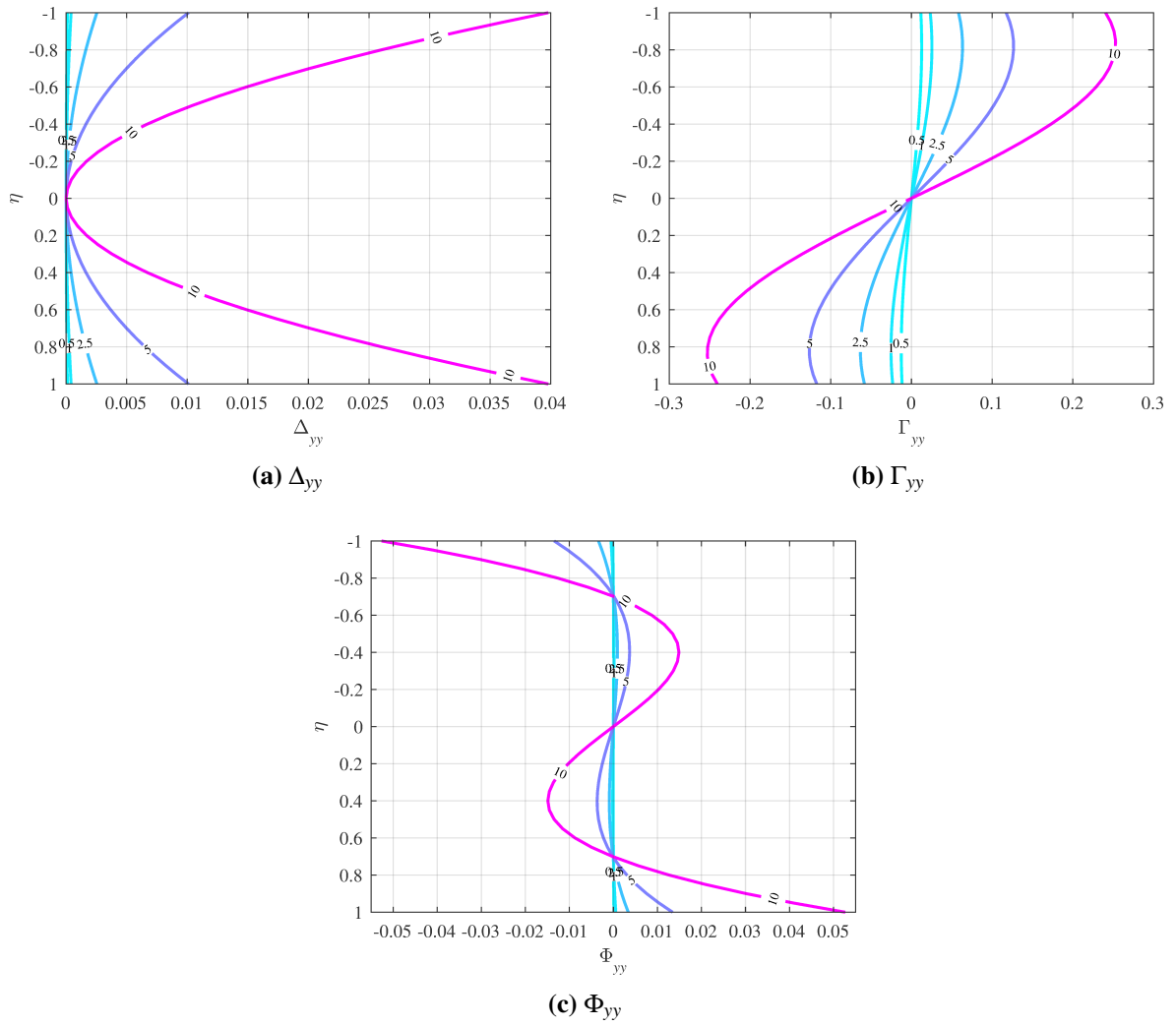


Figure 4.31: distribution at the mid-span section ($\zeta = 0.5$) of the dimensionless functions whose combination gives σ_{yy} for different values of α .

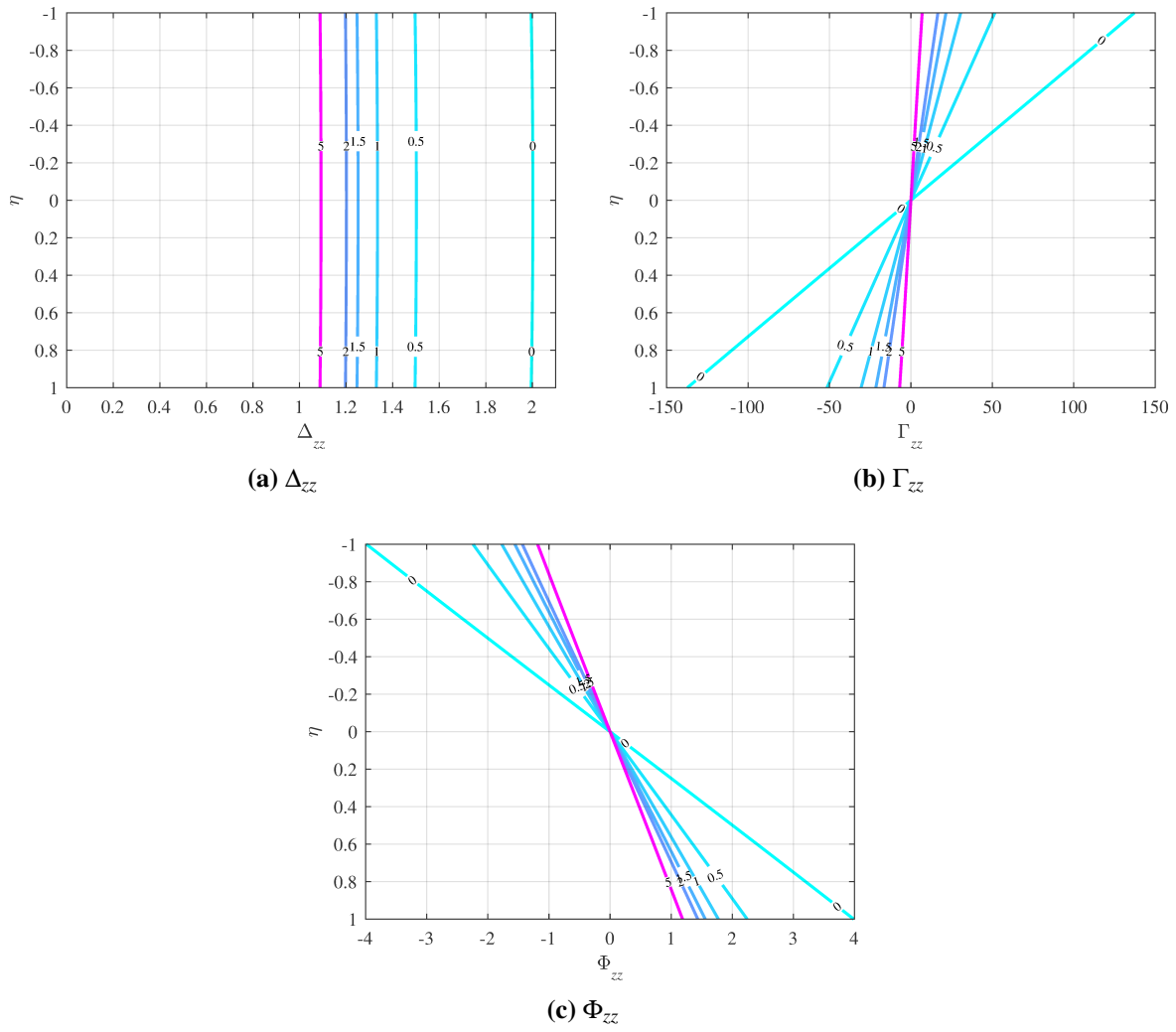


Figure 4.32: distribution at the mid-span section ($\zeta = 0.5$) of the dimensionless functions whose combination gives σ_{zz} for different values of β .

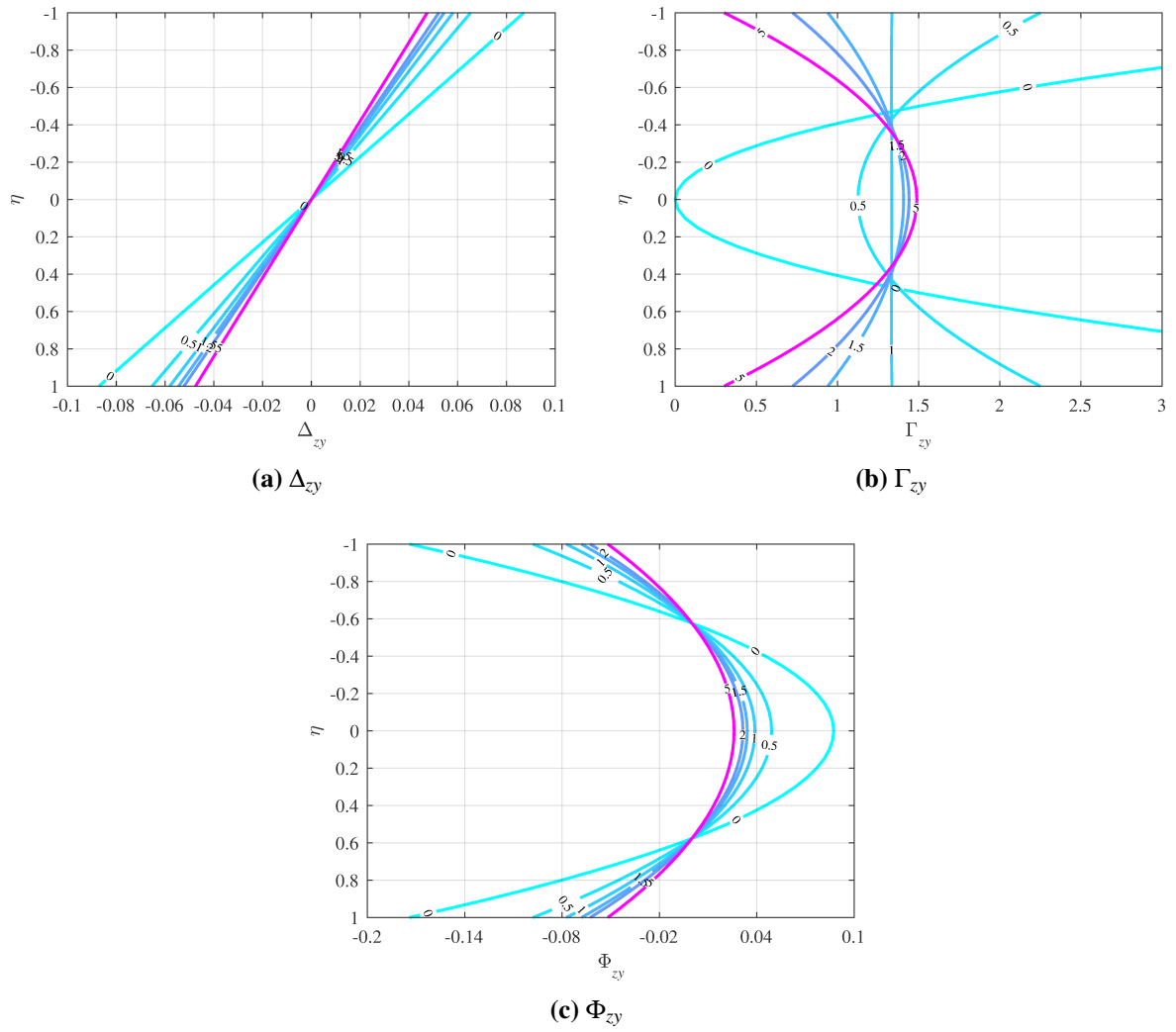


Figure 4.33: distribution at the mid-span section ($\zeta = 0.5$) of the dimensionless functions whose combination gives σ_{zy} for different values of β .

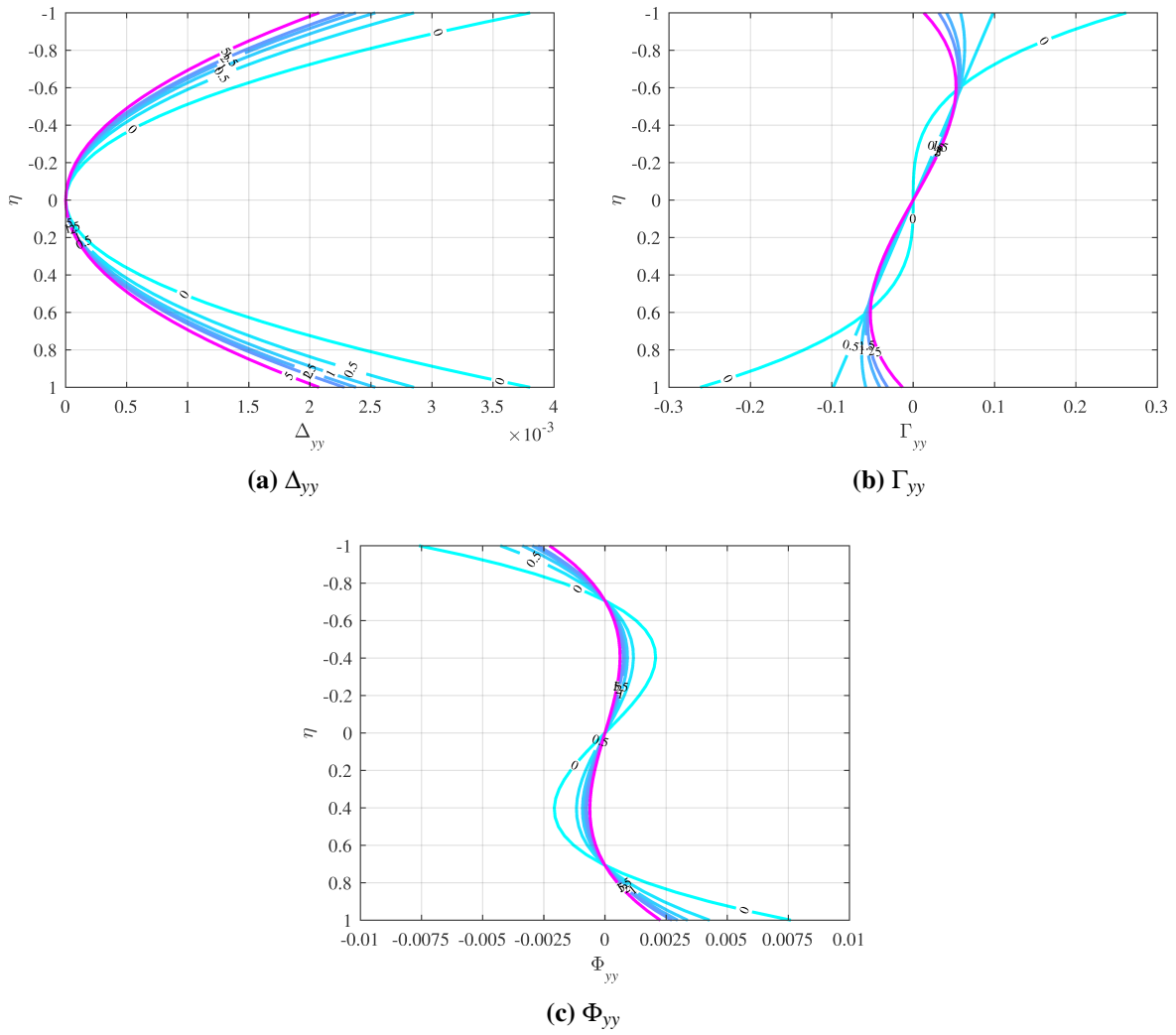


Figure 4.34: distribution at the mid-span section ($\zeta = 0.5$) of the dimensionless functions whose combination gives σ_{yy} for different values of β .

Dependence on α and β

Let us focus on two specific reference points belonging to the mid-span section ($\zeta = 0.5$). The first point is located on the mid-line of the truncated wedge ($\eta = 0$) and will be associated to a purple colour; meanwhile the second point is located on the outer edge ($\eta = -1$) and will be associated to the dark green colour (Figure 4.35 and following, where the variations of the dimensionless functions Δ_{ij} , Γ_{ij} , and Φ_{ij} with respect to the angle α and the parameter β are show).

In the surface plots shown in the Figures 4.35, 4.36, and 4.37, the parameter β is drawn on the abscissa, meanwhile the angle α is associated to the ordinate, so that those plots show how differently the two reference point considered are stressed as the values of the parameters change.

A contour plot is also associated to each surface plot. The parameter β and the corresponding dimensionless function are drawn on the abscissa and on the ordinate, respectively. Specific curves corresponds to different values of the angle α and to the two reference points (the one on the mid-line and the one on the outer edge).

It is evident that Δ_{zz} (Figure 4.35(a)), Φ_{zz} (Figure 4.35(c)), and Γ_{zy} (Figure 4.36(b)) are substantially independent of the variation of α .

All the dimensionless functions which are not constantly null, strongly depend on β .

With the only exception of Δ_{zz} and Γ_{zy} , the reference point which is more stressed appear to be the one located on the free edge, independently on the value of the parameters α and β .

In particular, Γ_{zy} shows an abrupt variation: for low values of β the higher stress is located on the mid-line. For $\beta = 1$ the point on the mid-line and on the free edge are equally stressed (this can be seen also on Figure 4.23(b) and Figure 4.27(b), where it is evident that the stresses are substantially equally distributed on the section). For β greater than 1 the most loaded point is the one located on the outer surface. Figures 4.36(c) and 4.36(d) show in a different way the behaviour of σ_{zy} already highlighted in Figure 4.33(b).

4.2.5 Final remarks

The superposition of the solutions of the wedge allowed us to determine the exact solution for a truncated wedge. The domain of both those solutions (discussed in the present Chapter) is Plane Elasticity. Even though the extension to physical three dimensional problems should not be granted for free, under limited conditions the truncated wedge solution could resemble a preliminary approximation of a plane stress distribution in tapered beams of rectangular section and with small width. Among the 10/5000 aforementioned limitations there is the assumption that the beam is loaded in its plane, and no second order effects are taken into account. Moreover, the beam should be sufficiently slender and long, so that the boundary effects could be negligible in the large majority of the beam itself.

That said, the stress distribution shows substantial differences with respect to the classical solution for prismatic beams: each loading condition (extension, shear, and bending) introduce all of the three components (σ_{zz} , σ_{yy} , and σ_{zy}) of the stress tensor in plane stress conditions. Moreover, the shear stresses appear to be the most affected by the taper angle, α .

It has been shown that the shear stresses σ_{zy} are at least of an order of magnitude lower than the normal stresses σ_{zz} . The general state of stress in the beam could then be described with sufficient accuracy by the normal stresses (which are predominant in the von Mises equivalent stress). However, if for example adhesively bonded joints are present in the design, also extreme care has to be given to the shear stresses.

For what concern the solution of the truncated wedge, the shear stresses are affected by all the loading conditions considered, and not only by the shear force. Moreover, the distribution of σ_{zy} may result to be extremely different to that predicted by the classical solution for prismatic beams, in particular if bending moment and bending moment associated to the shear force are present. In fact, shear stresses induced by bending are of a magnitude comparable to those induced by the sole shear force. This results in a distribution of shear stresses which may be counter-intuitive if the approach to the design is based on the classical solution for prismatic beams.

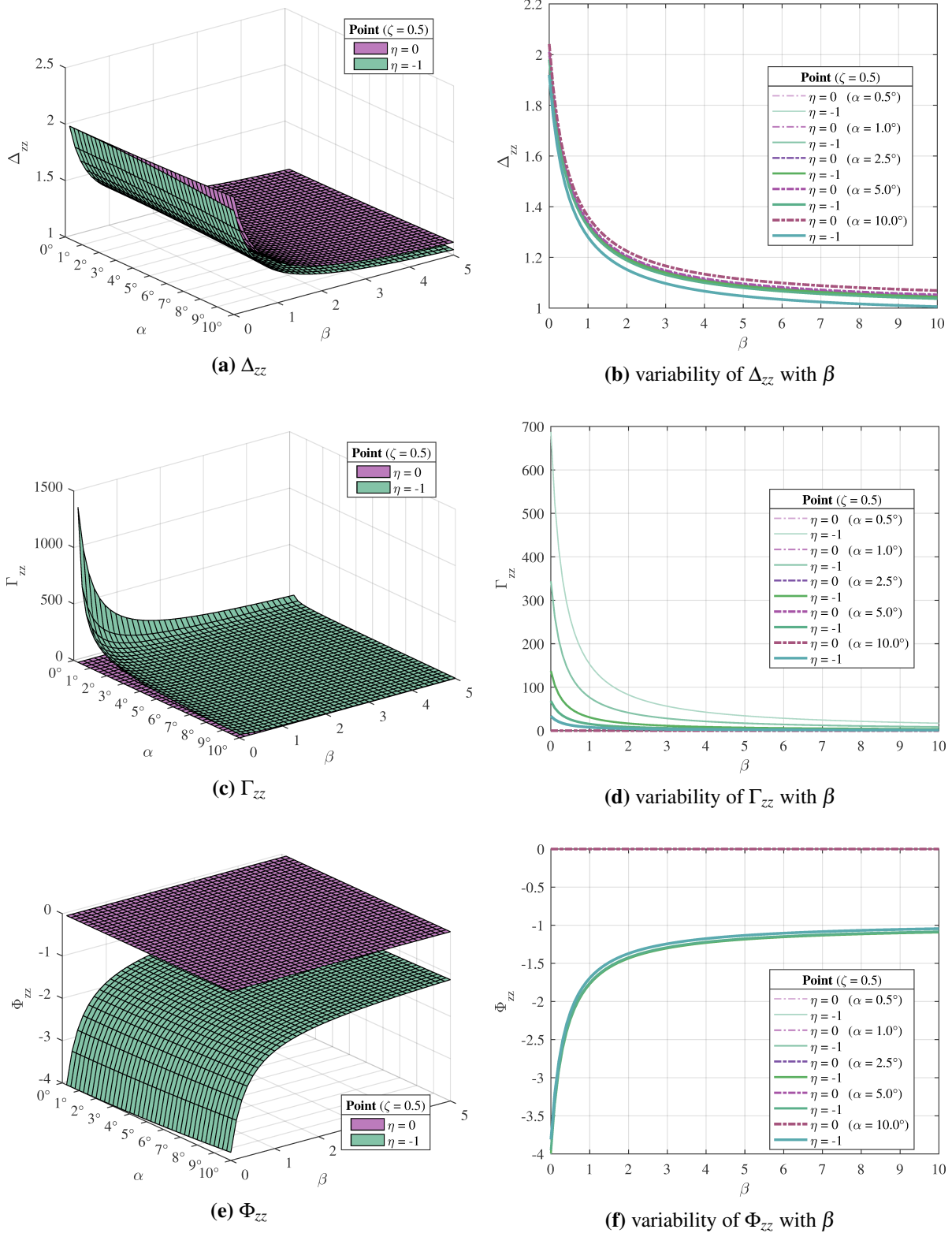


Figure 4.35: the dimensionless functions whose combination gives σ_{zz} calculated in two specific points of the mid-span section.

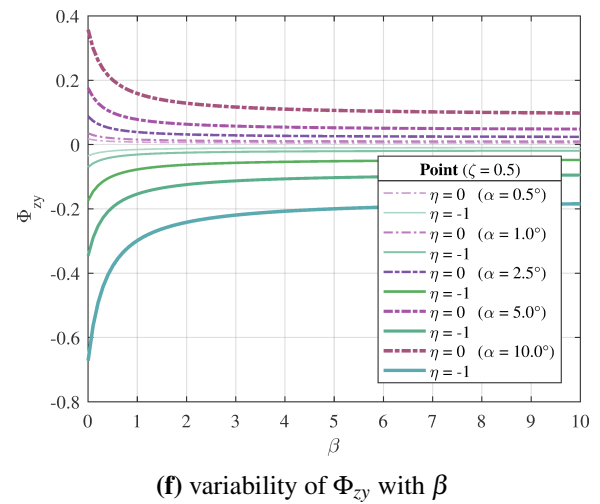
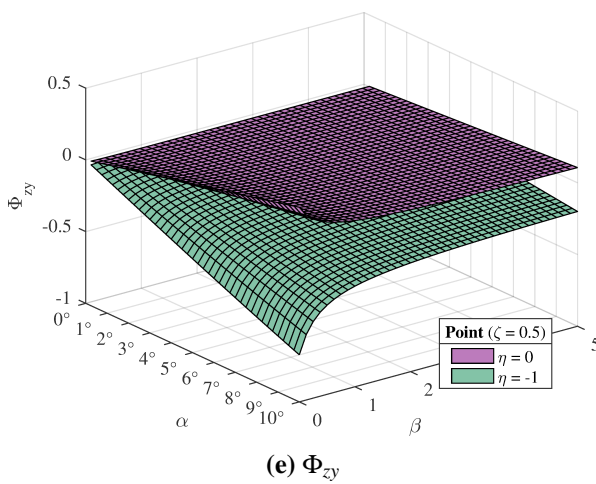
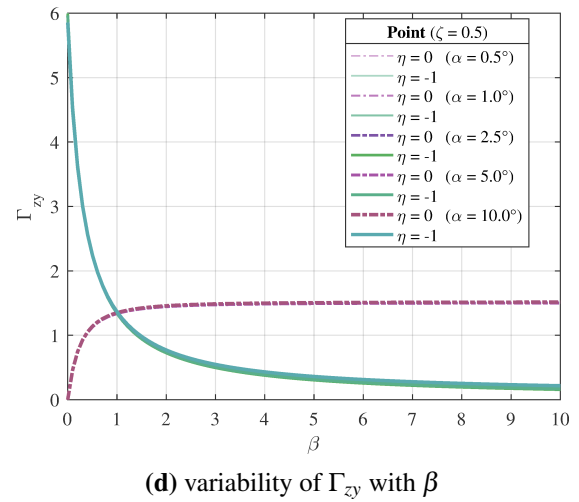
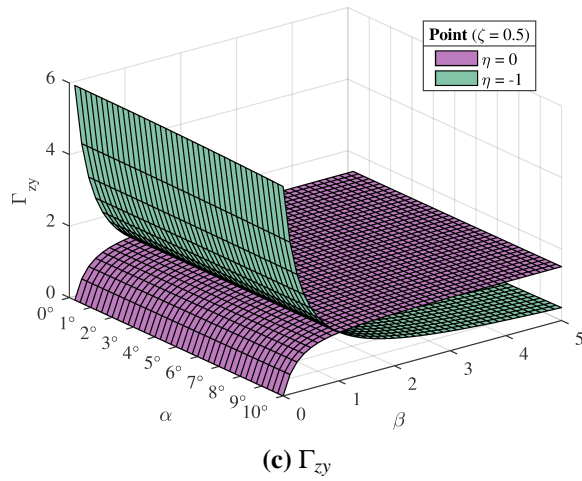
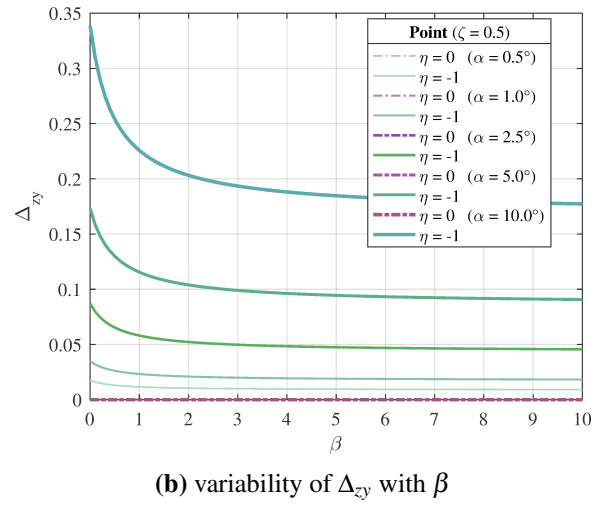
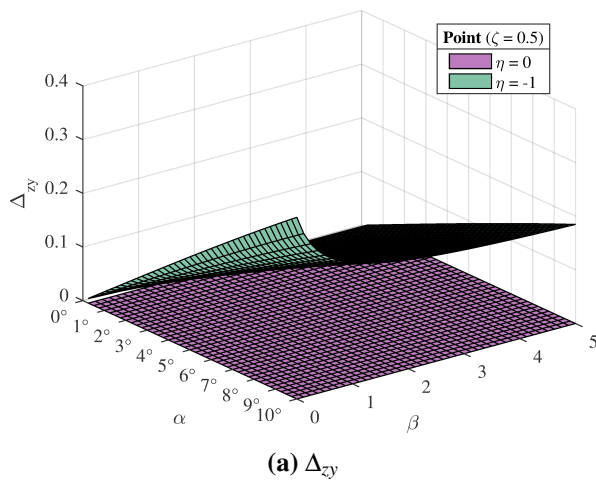


Figure 4.36: the dimensionless functions whose combination gives σ_{zy} calculated in two specific points of the mid-span section.

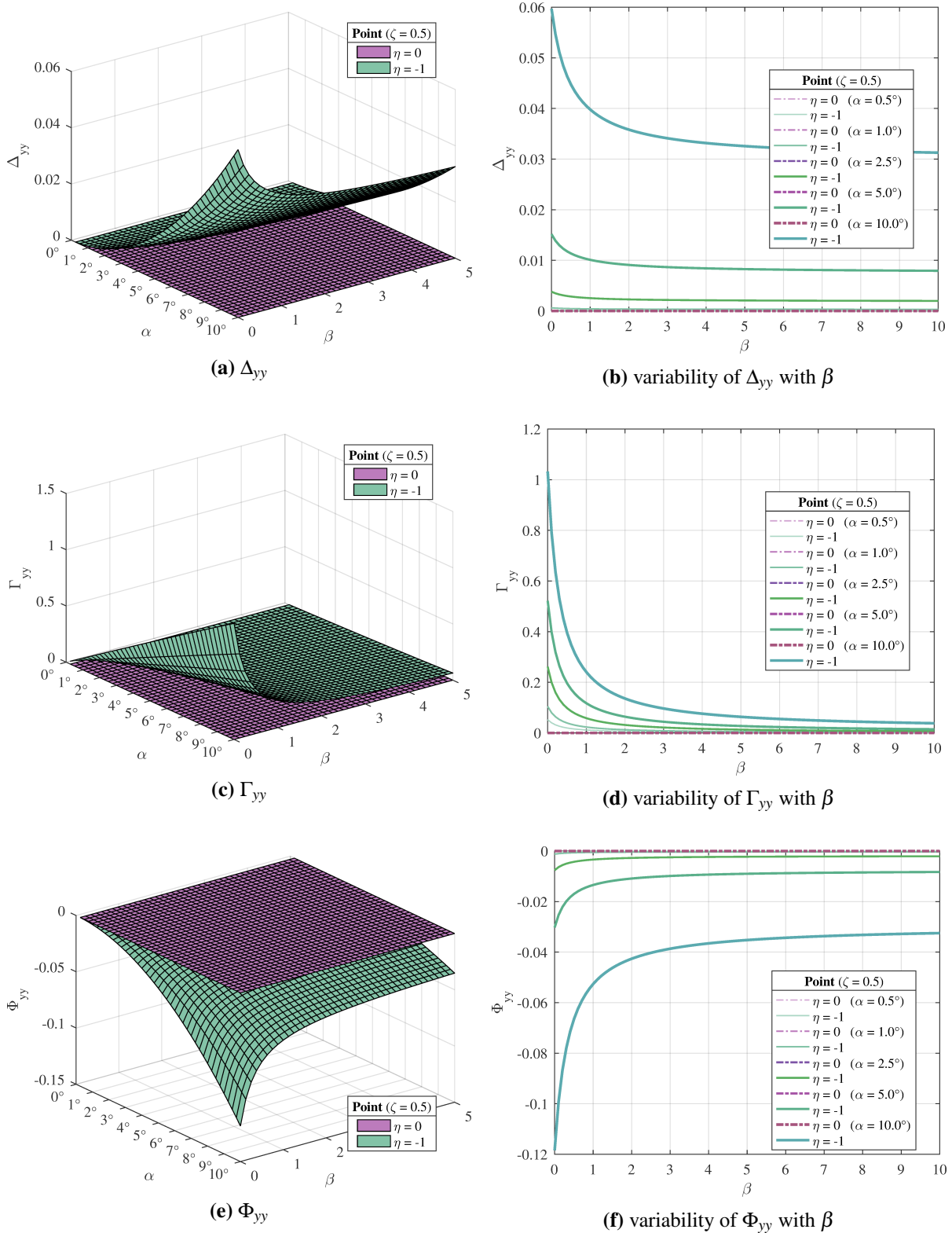


Figure 4.37: the dimensionless functions whose combination gives σ_{yy} calculated in two specific points of the mid-span section.

Also, to properly describe the geometry of the truncated wedge, we introduced a novel independent dimensionless parameter β . This new parameter is related to the taper ratio λ as illustrated for a number of values in Table 4.1. The solution appears to greatly depend on both α and β (or λ).

β	0	0.5	1	3/2	2	5	10	∞
λ	0	1/3	1/2	3/5	2/3	5/6	10/11	1

Table 4.1: conversions from β to λ

Chapter 5

Extended shear stress formula

Summary. In this Chapter, an extended shear stress formula is derived for tapered beams with generic cross section and subjected to distributed loads. The particular case in which no distributed loads are present is also discussed, confirming the validity of the approach followed by Bleich [1932].

5.1 The need for a different approach

In Sections 4.1 and 4.2, the solutions to two plane problems – a wedge and a truncated wedge – were presented in terms of the classical Theory of Elasticity. Such solutions are valuable because under certain conditions they can be considered exact. Furthermore, the obtained results shed light on the stress distribution in tapered beams. Nevertheless, direct application of those analytical solutions to practical problems appears questionable.

In particular, such solutions could be suitable to describe only plane stress problems – also neglecting the out-of-plane strains, and the related displacements. Moreover, even if derived for very particular and simple geometries, the formulae of the stresses appear to be extremely complicated and unpractical. The latter statement is even more appropriate for what concerns strains and displacements.

That said, the solutions presented in Chapter 4 proved to be of remarkable importance, helping us to highlight some fundamental results. The shear stresses induced by taper are of the same order of magnitude of those calculated with the classical shear stress formula for the same problem, but the distribution changes significantly. In addition, the analysis of the exact solution confirmed that the normal stresses, due to bending, show an almost linear distribution over the height of the cross section which is substantially equivalent to that described by the Navier equation [Timoshenko and Goodier, 1951].

Therefore, we turned to search for a more user-friendly, yet approximated, solution. Under the assumption that Navier's equation still holds for tapered beams – as already said, hypothesis confirmed by the solution for the truncated wedge (Section 4.2) – we derived a solution based on the equilibrium of a portion of an elementary segment of the beam. The result is an extended shear stress formula which extends the well-known Jourawski formula for shear stresses due to shear force in a beam [Timoshenko, 1940, 1953]. The obtained formula can be considered as a further extension and correction of the formula by Bleich [1932] (Equation 2.1), which takes into account the variation along the length of the beam of the section area and of the first and second moments of area. The extended shear stress formula also takes into account the possible presence of distributed loads, which were neglected in all previous formulations.

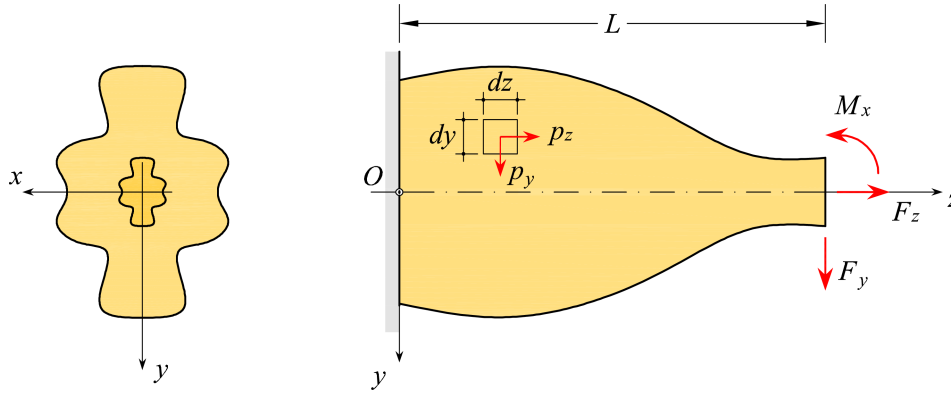


Figure 5.1: a tapered beam of generic cross section.

5.2 Extended shear stress formula for tapered beams

5.2.1 Derivation of the extended shear stress formula

Let us consider a tapered beam of length L with generic cross section, but straight centre-line (Figure 5.1).

For simplicity, we assume that the cross section has two axes of symmetry and the loads act only in the yz -plane. The variation in size of the cross sections is supposed smooth, but not necessarily linear.

The beam may be subjected to distributed (per unit length) axial loads, p , transverse loads, q , and couples, m , applied to the centreline. Those distributed loads are obtained by properly summing the body force components per unit volume, $p_z(x, y, z)$ and $p_y(x, y, z)$:

$$\begin{cases} p(z) = \int_A p_z(x, y, z) dA \\ q(z) = \int_A p_y(x, y, z) dA \\ m(z) = \int_A y p_z(x, y, z) dA \end{cases} \quad (5.1)$$

where $A = A(z)$ is the area of the cross section of the tapered beam.

In the notation that follows, we will omit the dependency of the functions upon the z -coordinate, if not strictly necessary.

Being N , Q and M the internal forces acting on the cross sections of the beam, the equilibrium equations are:

$$\begin{cases} \frac{dN}{dz} + p = 0 \\ \frac{dQ}{dz} + q = 0 \\ \frac{dM}{dz} + m - Q = 0 \end{cases} \quad (5.2)$$

Let us consider an elementary beam segment included between the sections at z and $z + dz$ (Figure 5.2).

We also define a unit vector $\boldsymbol{\eta}$ lying on the xy -plane (not necessarily parallel to the reference axes). Associated with the properly defined abscissa $\boldsymbol{\eta}$, such unit vector $\boldsymbol{\eta}$ identify an orthogonal plane parallel to the z -axis. Such plane cuts the elementary beam segment into two complementary parts. On the cross section at z , the projection of the cross section on the plane forms a chord of length b which divides the

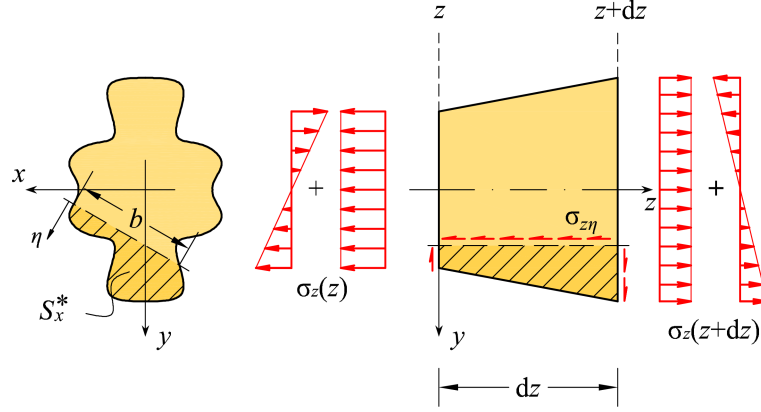


Figure 5.2: equilibrium of a portion of an element of the tapered beam.

cross section into two parts with areas $A^*(z)$ and $\bar{A}^*(z)$, respectively. Also the first moments of area, S_x^* and \bar{S}_x^* can be defined for the parts of the section. Here and in what follows each quantity related to the portion of area $A^*(z)$ will be denoted by the * symbol.

We impose the equilibrium along the z -axis of the portion of beam with positive values of η , and we get

$$\int_{A^*(z)} \sigma_{zz} dA + \sigma_{z\eta} \frac{b + (b + db)}{2} dz - \int_z^{z+dz} \int_{A^*(z)} \frac{p}{A} dA dz = \int_{A^*(z+dz)} (\sigma_{zz} + d\sigma_{zz}) dA \quad (5.3)$$

Assuming that the increment of area $A^*(z + dz) -$ due to the taper – could be written as

$$A^*(z + dz) = A^*(z) + dA^*, \quad (5.4)$$

Equation 5.3 can be manipulated as follows, by dividing both members for dz and simplifying by neglecting high-order infinitesimal quantities:

$$b \sigma_{z\eta} = \int_{A^*(z)} \frac{d\sigma_{zz}}{dz} dA + \frac{pA^*(z)}{A} + \sigma_{zz}|_{dA^*} \frac{dA^*}{dz}, \quad (5.5)$$

where $\sigma_{zz}|_{dA^*}$ denotes the (average) value of the normal stress evaluated in correspondence of the increment of the area due to the taper, dA^* .

We observe that

$$\begin{aligned} \frac{d}{dz} \int_{A^*(z)} \sigma_{zz} dA &= \frac{1}{dz} \left[\int_{A^*(z+dz)} \sigma_{zz}(z + dz) dA - \int_{A^*(z)} \sigma_{zz}(z) dA \right] \\ &= \frac{1}{dz} \left[\int_{A^*(z)} (\sigma_{zz}(z) + d\sigma_{zz}) dA + \int_{dA^*} (\sigma_{zz}(z) + d\sigma_{zz}) dA - \int_{A^*(z)} \sigma_{zz}(z) dA \right] \\ &= \frac{1}{dz} \left[\int_{A^*(z)} d\sigma_{zz} dA + \int_{dA^*} \sigma_{zz} dA + \int_{dA^*} d\sigma_{zz} dA \right] \\ &\cong \int_{A^*(z)} \frac{d\sigma_{zz}}{dz} dA + \sigma_{zz}|_{dA^*} \frac{dA^*}{dz}, \end{aligned} \quad (5.6)$$

where we have neglected high-order infinitesimal quantities.

Thus, substituting Equation 5.6 into 5.5, and manipulating, we obtain

$$\sigma_{z\eta} = \frac{1}{b} \frac{d}{dz} \int_{A^*(z)} \sigma_{zz} dA + \frac{1}{b} \frac{pA^*}{A}. \quad (5.7)$$

We recall Navier's formula,

$$\sigma_{zz} = \frac{N}{A} + \frac{M}{I_x} y, \quad (5.8)$$

where I_x is the second moment of area of the cross section of the beam. We assume that Equation 5.8 is valid also for non-prismatic beams. Such an hypothesis has been widely adopted by many authors in the literature ([Krahula, 1975; Timoshenko and Gere, 1972]), and in the following its consistency will be confirmed by means of a comparison between the analytical solution for the truncated wedge and FE analyses of beams with different geometries.

Under the latter hypotheses, we can write Equation 5.7 as

$$\sigma_{z\eta} = \frac{1}{b} \frac{d}{dz} \left(\frac{N}{A} \int_{A^*} dA \right) + \frac{1}{b} \frac{d}{dz} \left(\frac{M}{I_x} \int_{A^*} y dA \right) + \frac{1}{b} \frac{pA^*}{A}. \quad (5.9)$$

Calculating the integrals, and recalling the first of Equations 5.2, we have

$$\sigma_{z\eta} = \frac{1}{b} \frac{d}{dz} \left(\frac{NA^*}{A} \right) + \frac{1}{b} \frac{d}{dz} \left(\frac{MS_x^*}{I_x} \right) - \frac{1}{b} \frac{A^*}{A} \frac{dN}{dz}. \quad (5.10)$$

Applying the chain rule to the first term of 5.10, we get

$$\sigma_{z\eta} = \frac{1}{b} \frac{dNA^*}{dz} \frac{1}{A} + \frac{1}{b} N \frac{d}{dz} \left(\frac{A^*}{A} \right) + \frac{1}{b} \frac{d}{dz} \left(\frac{MS_x^*}{I_x} \right) - \frac{1}{b} \frac{A^*}{A} \frac{dN}{dz}. \quad (5.11)$$

In Equation 5.11, the contributions of the derivative of the axial force cancel each other, leading to the following Equation:

$$\sigma_{z\eta} = \frac{1}{b} N \frac{d}{dz} \left(\frac{A^*}{A} \right) + \frac{1}{b} \frac{d}{dz} \left(\frac{MS_x^*}{I_x} \right). \quad (5.12)$$

By applying the chain rule also to the second term and recalling Equations 5.2, the formula of the shear stresses can also be written as

$$\sigma_{z\eta} = \frac{1}{b} N \frac{d}{dz} \left(\frac{A^*}{A} \right) + \frac{1}{b} (Q - m) \frac{S_x^*}{I_x} + \frac{1}{b} M \frac{d}{dz} \left(\frac{S_x^*}{I_x} \right). \quad (5.13)$$

5.2.2 Linearly tapered rectangular cross section beam

Let us assume a linearly tapered beam with rectangular cross section of constant width b and height

$$h(z) = h_0 - z \tan \alpha. \quad (5.14)$$

Substitution of

$$\frac{dA^*}{dz} = b \tan \alpha \quad (5.15)$$

and

$$\frac{dS_x^*}{dz} = A \tan \alpha \quad (5.16)$$

into the derivatives of Equation 5.13 proofs many similarities with Equation 2.1. In his book, Bleich assumes with no apparently justification that

$$\frac{dN}{dz} = 0, \quad (5.17)$$

which anyway leads to a shear stress formula similar to ours. It is noteworthy that taking into account also the distributed loads allows us to substitute Equation 5.9 with Equation 5.10. The latter substitution introduces the two terms $\frac{1}{b} \frac{A^*}{A} \frac{dN}{dz}$ which cancel each other, giving a better explanation of Bleich's assumption in Equation 5.17.

5.2.3 Negligible distributed loads

If distributed loads are not present or negligible, Equation 5.9 cannot be substituted by Equation 5.10. However Equation 5.11 becomes

$$\sigma_{z\eta} = \frac{1}{b} \frac{d}{dz} \left(\frac{A^*}{A} N + \frac{S_x^*}{I_x} M_x \right). \quad (5.18)$$

If the axial force N is also negligible, Equation 5.18 turns out to be identical to the equation adopted by Krahula [1975] (Equation 2.2).

5.3 Final remarks

Equation 5.13 is an extension of the well known Jourawski formula to tapered beams subjected to distributed loads. It is evident that not only the shear force, Q , but also the bending moment, M , and axial force, N , introduce shear stresses on the cross section of a tapered beam. In particular, the contribution of the axial force, N , depends on the derivative with respect to z of the ratio of the area of a portion of section delimited by the chord of length b , A^* over the area of the cross section, A . The contribution of the bending moment, M , is proportional to the derivative with respect to z of the ratio of the first moment of area, S_x^* , over the second moment of area of the cross section, I_x . Summarizing, the contributions of bending moment and axial force are proportional to the change in size of the cross section along the length of the beam which is due to the taper.

The contribution of the shear force, Q , to the shear stresses is not directly affected by the change in size of the cross section (Equation 5.13). Conversely, shear stresses appear to be influenced also by the bending moment induced by the shear force, depending on the size and sign of the derivative $\frac{d}{dz} \left(\frac{S_x^*}{I_x} \right)$. In the limit case of a null angle of taper α , the contribution of the bending induced by the shear force vanishes, and the extended shear stress formula is equivalent to Jourawski's one.

Also, the distributed loads – with the exception of the distributed couples m – do not have direct influence on the distribution of shear stresses.

The request of the cross section having two axes of symmetry is the only strict requirement made in the derivation of the extended shear stress formula, and it is needed to allow the use of Navier's formula. Thus, there are not theoretical restrictions on the applicability of the extended shear stress formula to beams of both thick- and thin-walled cross sections. Equation 5.13 – and in the case of negligible distributed loads Equation 5.18 – can be applied to many two-dimensional (i.e. the web panel) and three-dimensional problems (i.e. the box girder), and in Part III the results from the extended shear stress formula are compared with FE analysis for different case studies.

Part III
Results

Chapter 6

Linearly tapered beams

Summary. In the present Chapter, the different solutions proposed in Part II are discussed and compared, also with the aid of numerical examples.

The stress field in a thin rectangular cross section beam is shown at first. Both the elastic solution and the application of the extended shear stress formula are presented, supported by the comparison with FE analysis.

The complete stress field in linearly tapered hollow-section beams is also determined. As an example, the cases of the box girder and of the conical hollow-section beam are investigated. Under the hypothesis that the Navier equation and the extended shear stress formula are valid, all the remaining stress components are determined under the hypothesis of plane stress state for thin-walled beams.

In all the cases presented, the analytical results and FE analysis give comparable results, reassuring on the validity of the approach proposed.

6.1 Thin rectangular cross section beam

In what follows, we will specialise the approach discussed in Section 5.2 to a linearly tapered beam with a rectangular cross section. Such cross section will be characterized by a variable height, $h = h(z)$, and a much smaller constant thickness, t . Thus in such case, we will assume a plane state of stress, and consequently

$$\sigma_{zx} = \sigma_{zy} = \sigma_{xy} = 0. \quad (6.1)$$

Moreover, we will attempt to compare such solution with the stress field obtained with the elastic solution for a truncated wedge of comparable size (Section 4.2).

Let us consider the tapered beam of length L shown in Figure 6.1.

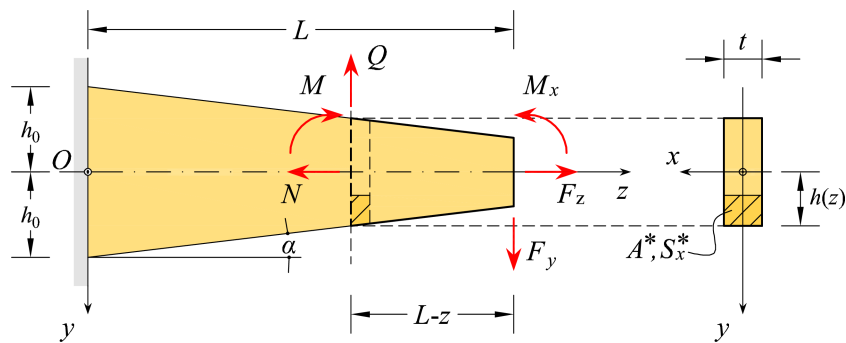


Figure 6.1: equilibrium of the elementary beam segment of a linearly tapered beam.

The beam is clamped at the root cross section and loaded by the forces F_z and F_y and by the bending moment M_x at the tip cross section.

The internal forces in the beam are functions of z and can be calculated as

$$\begin{cases} N = F_z \\ Q = F_y \\ M = M_x - F_y(L - z) \end{cases} \quad (6.2)$$

Applying the extended shear stress formula strategy to the beam under consideration, we get an approximated representation of the full stress field. In particular, from Navier's formula we get

$$\sigma_{zz} = \frac{F_z}{2th(z)} - \frac{3y(L-z)F_y}{2th(z)^3} + \frac{3yM_x}{2th(z)^3}. \quad (6.3)$$

Applying the extended shear stress formula (Equation 5.18) we can also deduce the shear stresses in the cross section:

$$\begin{aligned} \sigma_{zy} = & -\frac{y \tan \alpha F_z}{2th(z)^2} - \frac{3[h(z)(y^2 - h(z)^2) - (L-z)(3y^2 - h(z)^2) \tan \alpha] F_y}{4th(z)^4} \\ & - \frac{3(3y^2 - h(z)^2) \tan \alpha M_x}{4th(z)^4}. \end{aligned} \quad (6.4)$$

Finally, by integrating the second Cauchy equilibrium equation [Timoshenko and Goodier, 1951]

$$\frac{\partial \sigma_{xy}}{\partial x} + \frac{\partial \sigma_{yy}}{\partial y} + \frac{\partial \sigma_{zy}}{\partial z} = 0, \quad (6.5)$$

where $\sigma_{xy} = 0$ for the hypothesis of plane stress. we can determine the last stress component:

$$\begin{aligned} \sigma_{yy} = & \frac{y^2 \tan^2 \alpha F_z}{2th(z)^3} + \frac{3y \tan \alpha [h(z)(y^2 - h(z)^2) - (L-z)(2y^2 - h(z)^2) \tan \alpha] F_y}{2th(z)^5} \\ & - \frac{3y(2y^2 - h(z)^2) \tan^2 \alpha M_x}{2th(z)^5}. \end{aligned} \quad (6.6)$$

6.1.1 Numerical example: geometry and loads

We define a numerical example with the aim of compare the different solution strategies proposed.

Let us consider a tapered cantilever beam of length $L = 10000$ mm (Figure 6.1).

The rectangular cross section has width $t = 1$ mm. The root cross section has height $H_0 = 1000$ mm, while the tip cross section has height $H_t = 500$ mm. The angle of taper can than be deduced and is

$$\alpha = \arctan \frac{H_0 - H_t}{2L} = 2.8624^\circ.$$

Recalling Equation 4.59, for the example chosen we have

$$\beta = 1.$$

Thus, the fictitious length of the equivalent wedge is $L_0 = 10000$ mm (see Page 67).

We define three different loading conditions. In particular, we will analyse the case of *simple extension* (applying at the tip cross section a force in the z direction, $F_z = 1000$ N), the case of *shear* (applying at the tip cross section a force in the y direction, $F_y = 1000$ N), and finally the case of *bending* (applying at the tip cross section a bending moment, $M_x = 10000$ N mm).

For our analysis we will consider the material to be isotropic and linearly elastic, such as an Aluminium alloy with Young's modulus $E = 72$ GPa and Poisson's ratio $\nu = 0.35$. Even though such material properties are not strictly necessary to determine the stress distribution using both the elasticity theory solution and the solution based on the extended shear stress formula, they were used to conduct a FE analysis of the stated problem with the Abaqus software.

The internal forces in the different loading cases are summarized in Table 6.1.

	Extension	Shear	Bending
$N(z)$	F_z	0	0
$Q(z)$	0	F_y	0
$M(z)$	0	$-F_y(L-z)$	M_x

Table 6.1: internal forces for the different loading cases.

6.1.2 Discussion of the results

Extended shear stress formula

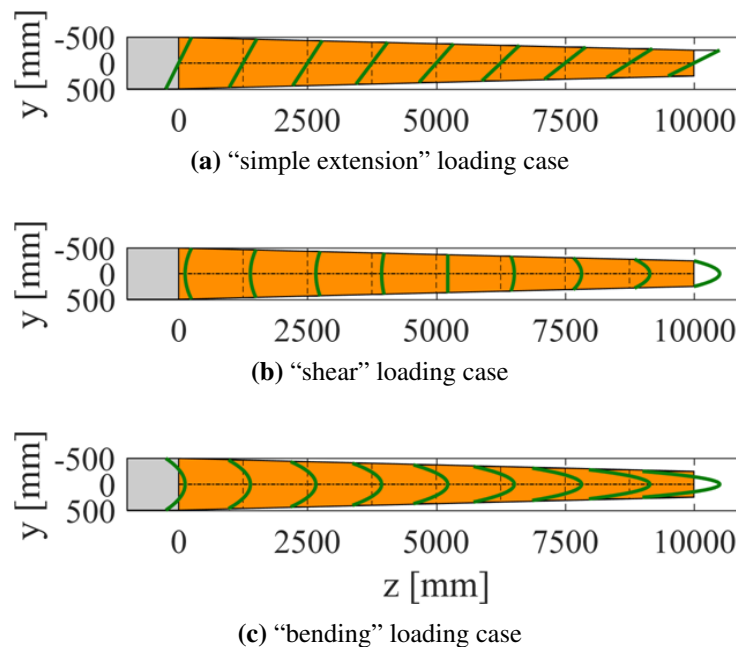
According to the classical Jourawski formula for prismatic beams, the shear stresses are produced only by shear forces. On the other hand, the extended shear stress formula predicts shear stresses also associated with the axial force and the bending moment.

In Figure 6.2, the shear stresses σ_{zy} on different cross sections are shown for each elementary loading case considered.

In Figure 6.2(a), the shear stresses for the simple extension loading case are plotted, and an odd linear distribution on the cross section is evident.

The shear stresses induced by bending are shown in Figure 6.2(c): such distribution is parabolic. A maximum is present for $y = 0$ and the stresses are negative on the outer surfaces, so that the integral of the σ_{zy} on each section is null.

The shear stresses induced by a shear force applied at the tip section are plotted in Figure 6.2(b). In particular, on the tip section the typical Jourawski's parabolic distribution is shown. On such cross section the stress on the outer surfaces is null. Following the evolution of the shear stresses from the tip to the root sections, the increasing contribution of the shear-induced bending moment gradually modify the stresses summing a parabolic distribution of null resultant to the Jourawski parabola. This results in the gradual change of the curvature of the stress distribution – and even its inversion in sign.

**Figure 6.2:** shear stresses in the linearly tapered beam for the "simple" loading cases obtained with extended shear stress formula.

Classical Elasticity solution

The elastic solution discussed in Section 4.2 is applied to a truncated wedge which has the same sizes that the beam described in Section 6.1.1.

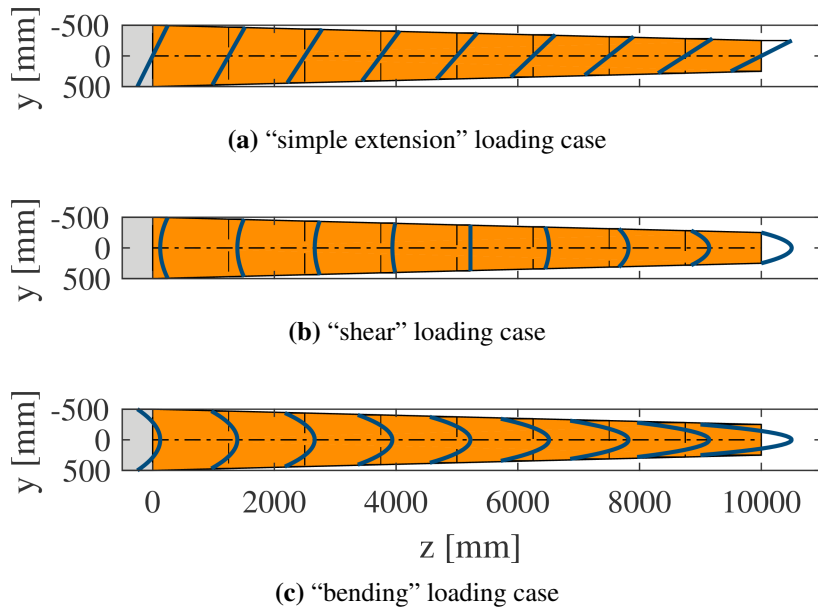


Figure 6.3: distribution of shear stresses on the truncated wedge for the “simple” loading cases.

In the Figure 6.3, the shear stresses evaluated using the classical elasticity approach show the exact same trend shown by the shear stresses calculated using the extended shear stress formula (Figure 6.2).

Finite element model

Also a FE analysis has been performed to compare and validate the previously shown results: we defined a 2D model (shown in Figure 6.4), meshed with quadrilateral plane stress elements with 4 nodes (CPS4R).

At the root section the nodal displacements are inhibited in all directions.

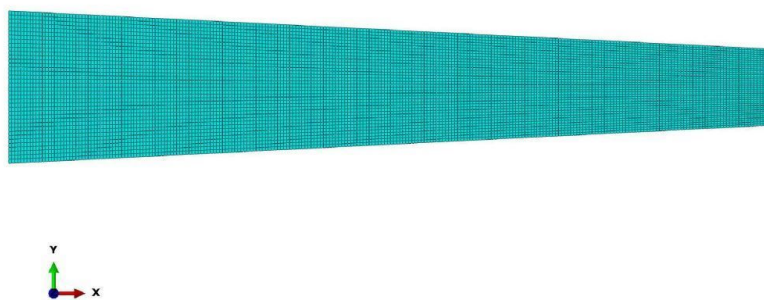


Figure 6.4: FE model of the tapered beam (Abaqus software).

Comparison of the results on the linearly tapered beam In Figure 6.5, plots are shown where the three different solution strategies have been drawn, analogously to those presented in Figures 6.2 and 6.3.

The perfect matching between approaches so different from each other is somehow astonishing. The green line, representing the extended shear stress formula, is perfectly overlaid by the red line, which is the only one clearly visible. Also the FE results are practically indistinguishable from the other two

methods, with only the exception of the tip and cross sections, where locally different boundary conditions were given (as stated by the De Saint-Venant Principle, the boundary effects become negligible in a very short portion of the body).

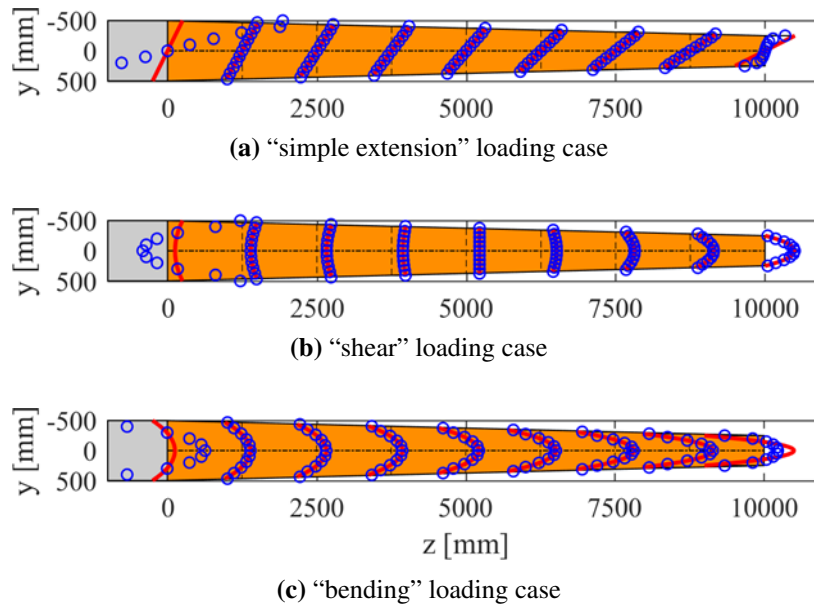


Figure 6.5: comparison of the shear stresses calculated with the elastic solution (red line), the extended shear stress formula (green line), and FE analysis (blue circles), on the linearly tapered beam and for the "simple" loading cases.

Comparison of the results at the mid-span section To the aim of more carefully compare the three solution methods proposed (classical elasticity, extended shear stress formula, and FE analysis), let us focus on the mid-span section of the tapered beam.

A perfect agreement is shown between the classical elasticity solution, the extended shear stress formula, and the FE analysis.

In particular, the solution in terms of classical elasticity shows a perfect agreement with the FE analysis for each loading case and each stress component (Figures 6.6, 6.7, and 6.8).

On the other hand, a perfect matching is not always shown between the FE analysis and the extended shear stress formula. In particular, σ_{zz} for the "simple extension" (Figure 6.6(a)), and σ_{zy} for the "shear" case (Figure 6.7(b)), appears to be constant on the section despite the fact that the effective distribution is quite different.

That said, we can also note that the extended shear stress formula gives the mean value of the total distribution. Also, the maximum and minimum values of the effective distribution (FE analysis) appear to be close to each other if compared with the overall order of magnitude. The mean value could be then considered a good approximation of the distribution itself.

The extended shear stress formula, obtained by generalising the Jourawski formula, appears to give an effective approximation of the stress distribution from an engineering point of view.

It is evident that the predominant stress component is σ_{zz} , which can be effectively predicted via the classical Navier formula. But if an accurate description of the behaviour of the shear stresses is required (i.e. if adhesive joints have to be designed) then taper appears to affect the overall distribution of stresses, making the use of the classical formulas for prismatic beams at least unwise, and potentially ruinous.

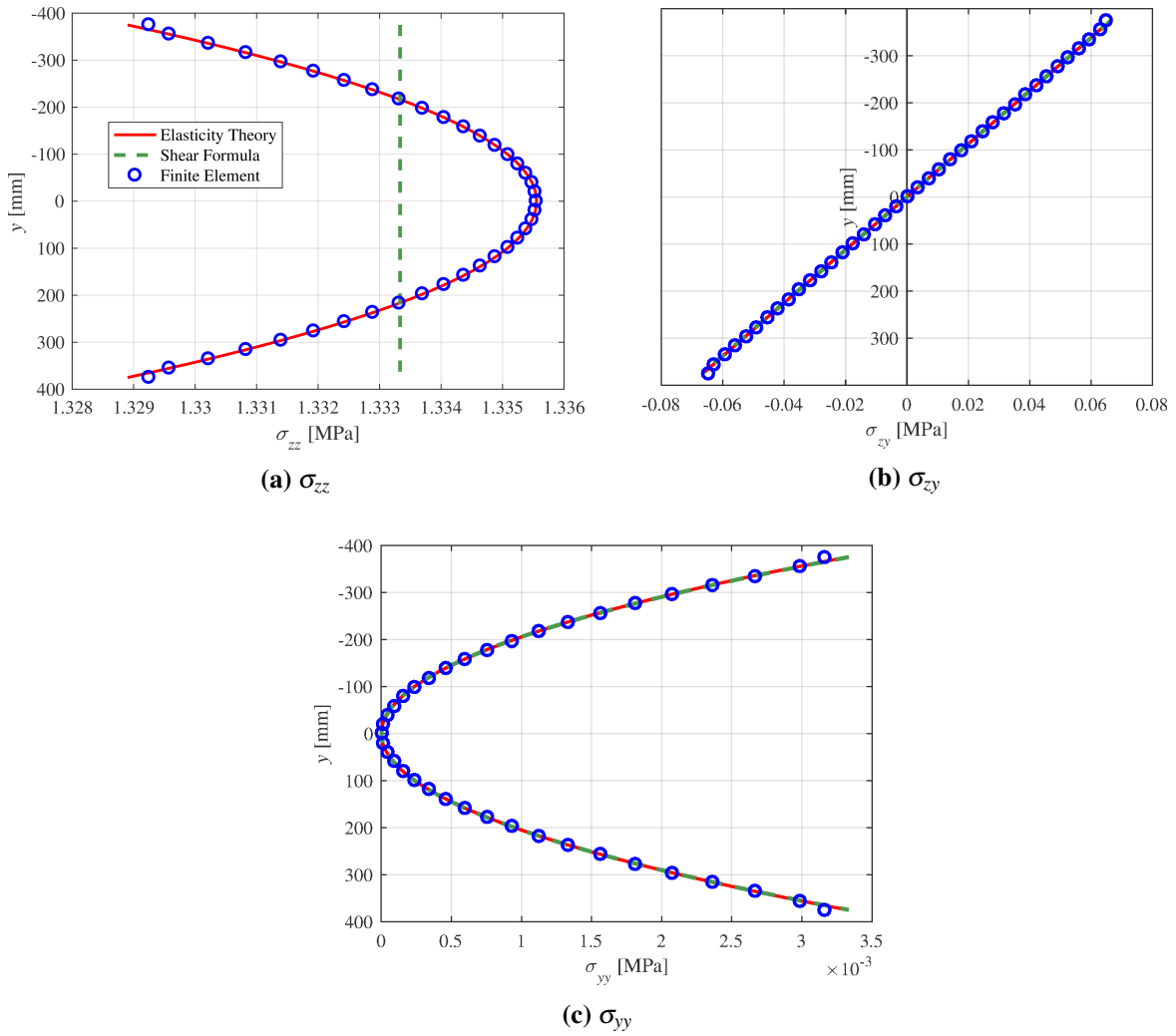


Figure 6.6: distribution of stresses on the mid-span section for the “simple extension” loading case.

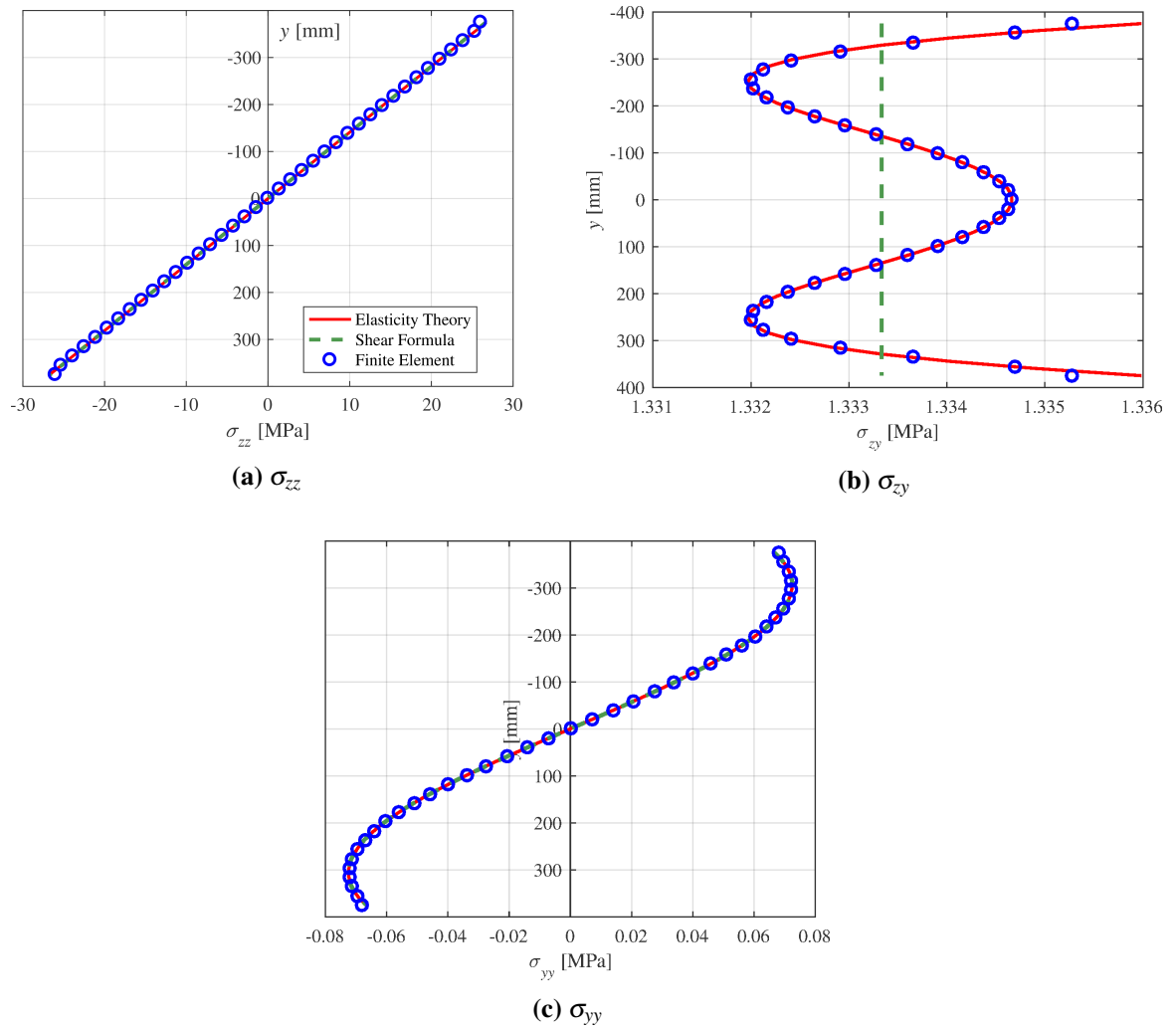


Figure 6.7: distribution of stresses on the mid-span section for the “shear” loading case.

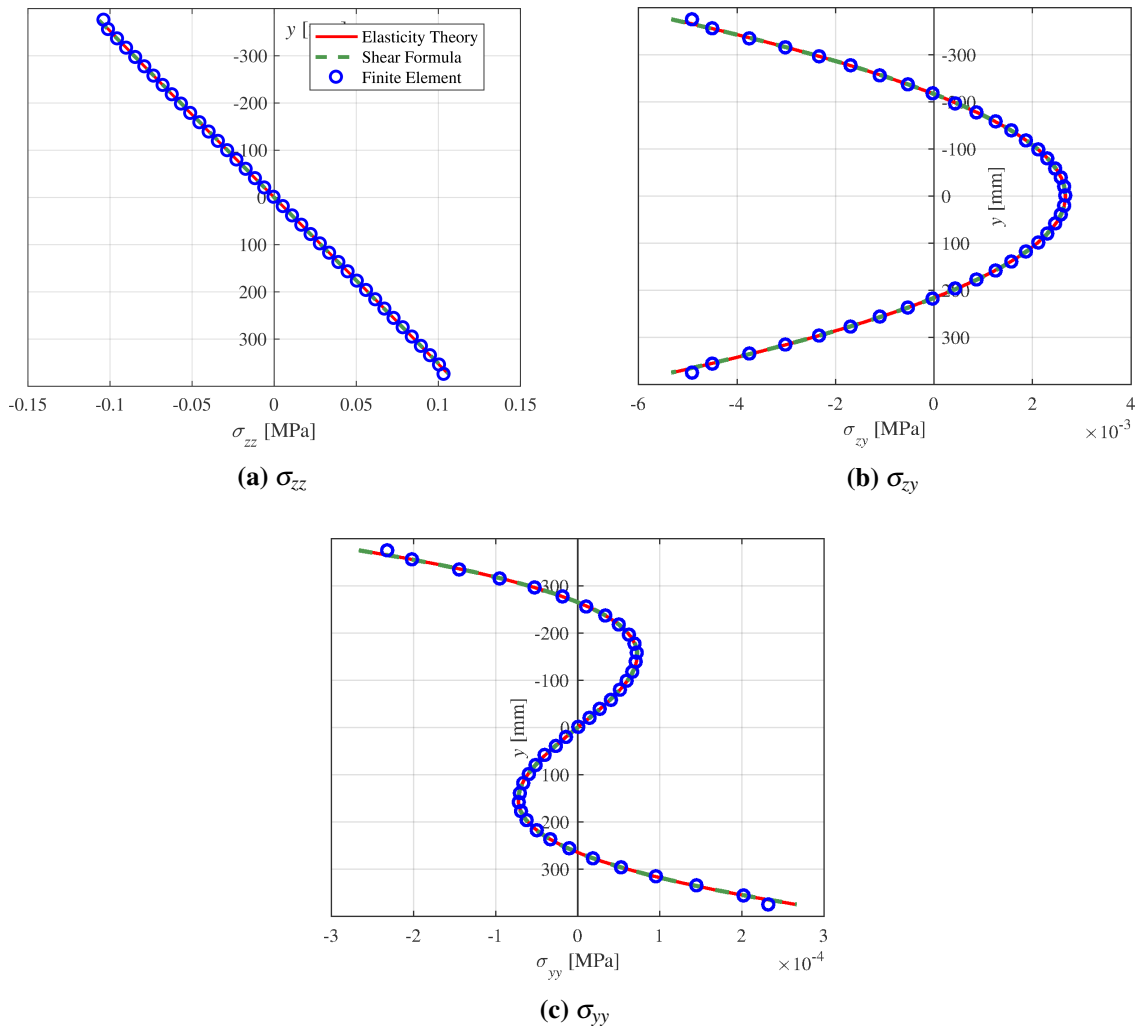


Figure 6.8: distribution of stresses on the mid-span section for the “bending” loading case.

6.2 Box girder

A box girder is a thin-walled tapered cantilever beam with rectangular cross section (Figure 6.9). In particular, and for simplicity, we will take into account only symmetric cross sections: this will allow us to use symmetry in the derivation of the stress field. A more general approach for not-symmetric cross sections, or multicellular thin-walled beams, will be the subject of future developments.

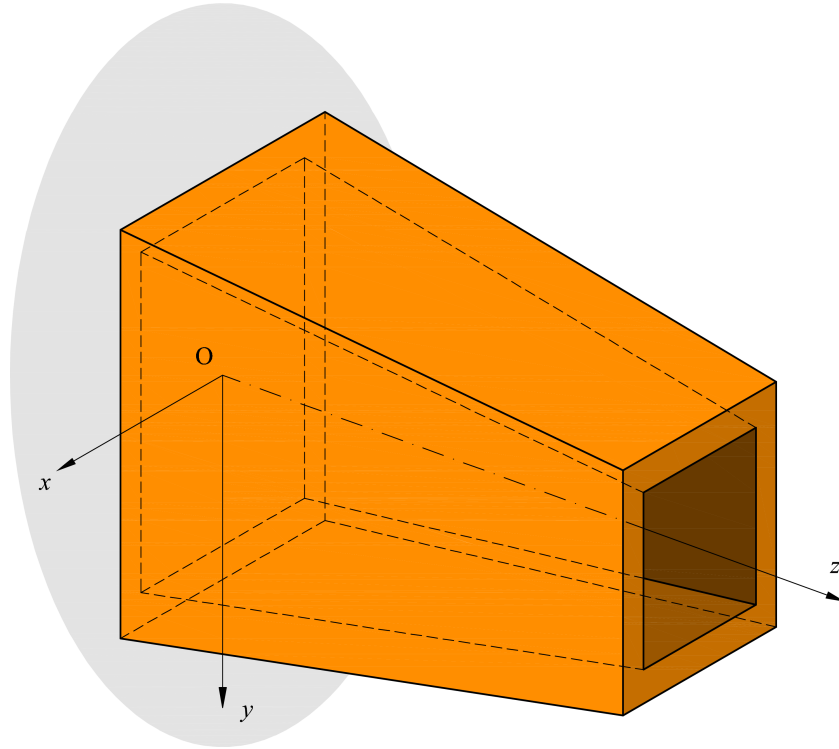


Figure 6.9: doubly tapered box girder.

We fix a Cartesian reference system $(O; x, y, z)$ origin O fixed in the centre of the root cross section, and the z -axis coincides with the mid-line of the beam. The x -axis and y -axis coincide with the principal axes of inertia of the root cross section.

The length of the box girder is L . Also, let $B(z)$ and $b(z)$ be the width and the half width of the section, and let $H(z)$ and $h(z)$ the height and the half height of the cross section, respectively. We introduce the angles of taper α_x and α_y , which are the angles that the webs and the flanges form with respect to the z -axis (Figure 6.10).

Different configurations can be identified:

- doubly tapered box girder (if α_x and α_y are both different from zero);
- a box girder linearly tapered in the vertical direction (if $\alpha_y = 0$);
- a box girder linearly tapered in the horizontal direction (if $\alpha_x = 0$);
- cylindrical rectangular thin-walled beam (if both α_x and α_y are zero).

For the latter case, the classical beam theory is applied.

In the most general case, we have

$$h(z) = h_0 - z \tan \alpha_x, \quad (6.7)$$

where h_0 is the half-height of the root cross section (at $z = 0$), and

$$b(z) = b_0 - z \tan \alpha_y, \quad (6.8)$$

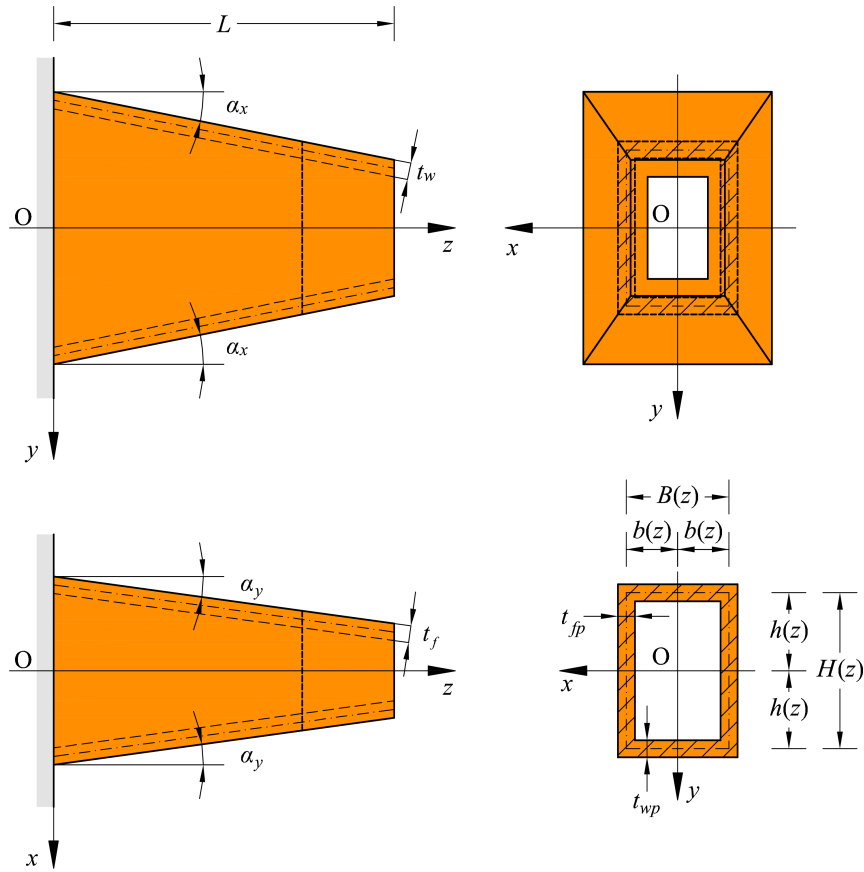


Figure 6.10: geometry of a doubly tapered box girder.

where b_0 is the half-width of the root cross section. The thickness of flanges, t_f , and webs, t_w , do not depends upon z .

As shown in Figure 6.11, the flange thickness projected onto the cross-sectional plane is

$$t_{fp} = \frac{t_f}{\cos \alpha_x}. \tag{6.9}$$

Also, the web thickness projected onto the same cross-sectional plane is

$$t_{wp} = \frac{t_w}{\cos \alpha_y}. \tag{6.10}$$

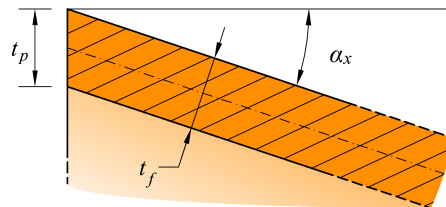


Figure 6.11: projection of the thickness of the cross section in function of the angle of taper.

The cross-sectional area of a generic section at a given z -coordinate is

$$A(z) = 4(h(z)t_{wp} + b(z)t_{fp}), \tag{6.11}$$

while the second moment of area is

$$I_x(z) = 4 \left(b(z)t_{fp}h(z)^2 + \frac{t_{wp}h(z)^3}{3} \right). \tag{6.12}$$

For the sake of simplicity, in what follows we will omit the dependency on z for the cross-sectional properties A and I_x .

The tip is supposed to be loaded by a concentrated force, whose components are an axial force \bar{N} (parallel to the z -axis) and a shear force \bar{Q} (parallel to the y -axis), and a concentrated couple \bar{M} (orthogonal to the x -axis). Consequently, the internal forces induced by those external loads into the box girder are the axial force N , the shear force Q , and the bending moment M .

Here and in what follows, we will suppose that the body forces, b_x , b_y and b_z are negligible.

To apply the extended shear stress formula, the area of a part of the section have to be computed. In particular, we define the area included between the yz -plane and the location at which the shear stresses have to be computed as

$$A^* = \begin{cases} xt_{fp} & \text{on the flange, } y = h(z) \\ b(z)t_{fp} + (h(z) - y)t_{wp} & \text{on the web, } x = b(z) \end{cases} \quad (6.13)$$

Also, the first moment of area with respect to the x -axis can be computed for the same part of section:

$$S_x^* = \begin{cases} xt_{fp}h(z) & \text{on the flange, } y = h(z) \\ b(z)t_{fp}h(z) + t_{wp}\frac{(h(z)^2 - y^2)}{2} & \text{on the web, } x = b(z) \end{cases} \quad (6.14)$$

In what follows, the extended shear stress formula derived in Chapter 5 is applied to tapered box beams.

In Paragraph 6.2.1 and in Paragraph 6.2.2, the solution is first given for a box girder linearly tapered in the vertical direction and in the horizontal one is given, respectively. Subsequently, in Paragraph 6.2.3 the problem of a double tapered box girder is shown. The solution for a generic element of beam is derived, and lastly the application to the simple cantilever box girder loaded at the tip is proposed.

6.2.1 Vertically tapered box girder

Let us consider an element of a vertically tapered box girder whose length is dz (Figure 6.12). Thus, in this case we have $\alpha_y = 0$. In Figure 6.13 the cross section at a given z -coordinate is shown.

As stated in Section 5.2.1, we assume that Navier's equation (Equation 5.8) is valid also for tapered beams. Thus

$$\sigma_{zz} = \frac{N}{A} + \frac{M}{I_x}h. \quad (6.15)$$

Stress components in the bottom flange

We define the *bottom flange*: the flange which is located in the half-space $y > 0$. On the other hand, the *top flange* will be the flange on the side of the half-space $y < 0$. The solution for the top flange will be deduced from the symmetry of the problem. Figure 6.14 shows an element of the bottom flange.

Substituting Equations 6.11 and 6.12 into Equation 6.15, we get the normal stress in the flange,

$$\sigma_{zz}^f = \frac{1}{4} \left(\frac{N}{ht_w + \frac{bt_f}{\cos \alpha_x}} + \frac{3M}{3h\frac{bt_f}{\cos \alpha_x} + h^2t_w} \right). \quad (6.16)$$

The shear stress component σ_{zx}^f can be obtained from Equation 5.13.

$$\sigma_{zx}^f = \frac{1}{b} \frac{d}{dz} \left(\frac{A^f}{A}N + \frac{S_x^*}{I_x}M \right). \quad (6.17)$$

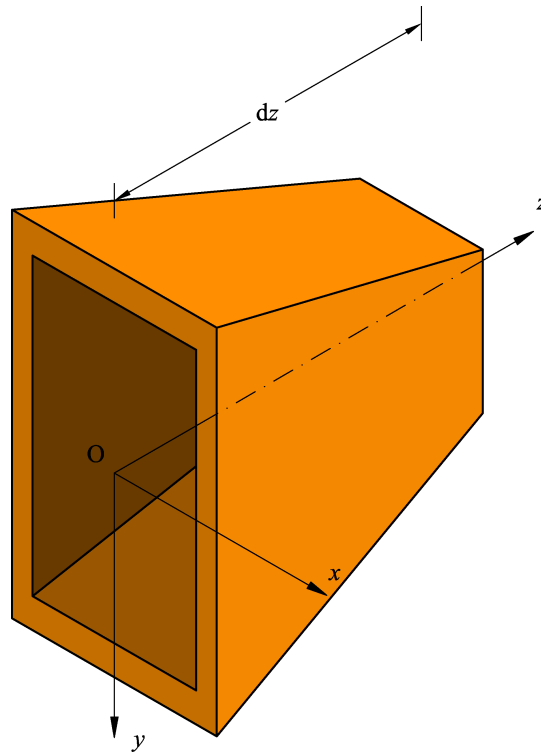


Figure 6.12: vertically tapered box beam.

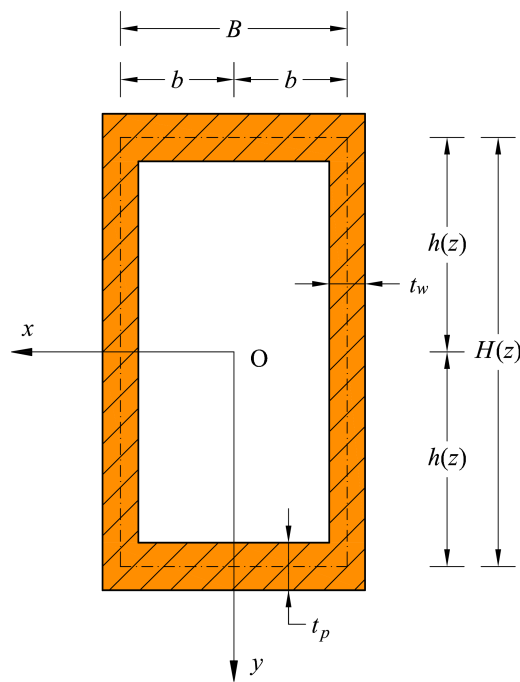


Figure 6.13: cross section of the vertically tapered box girder.

Substituting Equations 6.13, 6.14, 6.11 and 6.12 into Equation 6.17, this equation can be written as

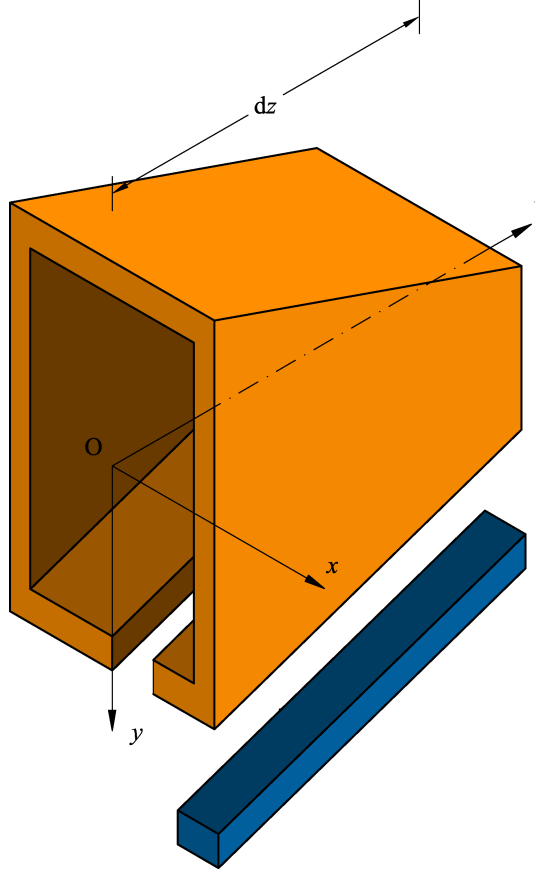


Figure 6.14: portion of flange of the element of the tapered box girder.

follows

$$\sigma_{zx}^f = \frac{x \cos \alpha_x}{4} \left[\frac{t_w \sin \alpha_x N}{(bt_f + t_w h \cos \alpha_x)^2} + \frac{3Q}{3bt_f h + t_w h^2 \cos \alpha_x} + \frac{3(3bt_f + 2t_w h \cos \alpha_x) \tan \alpha_x M}{h^2 (3bt_f + t_w h \cos \alpha_x)^2} \right] \quad (6.18)$$

The box girder is supposed to be a thin-walled beam. Such hypothesis allows us to determine the three other stress component. In fact, we state that the flange is in a plane stress state. σ_{yy}^f , σ_{xy}^f , and σ_{yz}^f can be obtained by rotating the global stress tensor into a local flange reference system, where the 1-axis is aligned with the flange, the 2-axis is aligned with the x -axis and the 3-axis is normal to the flange plane (Figure 6.15). Here and in what follows, the subscript numbers denote the corresponding local coordinate axes: i.e. σ_{12} will be the projection in the direction of the 2-axis of the stress acting on a plane orthogonal to the 1-axis. In particular, the stress components in the local reference can be written,

$$\sigma_{1,2,3} = \mathbf{R}^T \sigma_{x,y,z}^f \mathbf{R}, \quad (6.19)$$

where the rotation matrix is introduced

$$\mathbf{R} = \begin{bmatrix} 0 & 1 & 0 \\ -\sin \alpha_x & 0 & \cos \alpha_x \\ \cos \alpha_x & 0 & \sin \alpha_x \end{bmatrix}. \quad (6.20)$$

Thus, substituting we get:

$$\begin{bmatrix} \sigma_{11}^f & \sigma_{12}^f & \sigma_{13}^f \\ \sigma_{12}^f & \sigma_{22}^f & \sigma_{23}^f \\ \sigma_{13}^f & \sigma_{23}^f & \sigma_{33}^f \end{bmatrix} = \begin{bmatrix} 0 & -\sin \alpha_x & \cos \alpha_x \\ 1 & 0 & 0 \\ 0 & \cos \alpha_x & \sin \alpha_x \end{bmatrix} \begin{bmatrix} \sigma_{xx}^f & \sigma_{xy}^f & \sigma_{zx}^f \\ \sigma_{xy}^f & \sigma_{yy}^f & \sigma_{zy}^f \\ \sigma_{zx}^f & \sigma_{zy}^f & \sigma_{zz}^f \end{bmatrix} \begin{bmatrix} 0 & 1 & 0 \\ -\sin \alpha_x & 0 & \cos \alpha_x \\ \cos \alpha_x & 0 & \sin \alpha_x \end{bmatrix}. \quad (6.21)$$

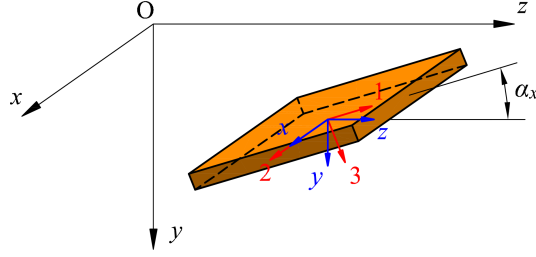


Figure 6.15: reference systems on an element of the bottom flange.

Converting Equation 6.21 to the notation in the single stress components, a set of 6 linearly independent equations is obtained. In particular

$$\begin{cases} \sigma_{11} = \sigma_{yy}^f \sin^2 \alpha_x - 2\sigma_{zy}^f \sin \alpha_x \cos \alpha_x + \sigma_{zz}^f \cos^2 \alpha_x, \\ \sigma_{22} = \sigma_{xx}^f, \\ \sigma_{33} = \sigma_{yy}^f \cos^2 \alpha_x + \sigma_{zz}^f \sin^2 \alpha_x + \sigma_{zy}^f \sin 2\alpha_x, \\ \sigma_{12} = \sigma_{zx}^f \cos \alpha_x - \sigma_{xy}^f \sin \alpha_x, \\ \sigma_{13} = \sigma_{zy}^f \cos 2\alpha_x + (\sigma_{zz}^f - \sigma_{yy}^f) \frac{\sin 2\alpha_x}{2}, \\ \sigma_{23} = \sigma_{xy}^f \cos \alpha_x + \sigma_{zx}^f \sin \alpha_x. \end{cases} \quad (6.22)$$

For the plane stress hypothesis, we have

$$\begin{cases} \sigma_{33} = 0, \\ \sigma_{13} = 0, \\ \sigma_{23} = 0. \end{cases} \quad (6.23)$$

Substituting Equations 6.23 into the third, fifth, and sixth of 6.22, we obtain a set of three linear equations in the three unknowns σ_{yy}^f , σ_{xy}^f , and σ_{zy}^f . Once solved, such set of equations gives

$$\begin{cases} \sigma_{yy}^f = \tan^2 \alpha_x \sigma_{zz}^f, \\ \sigma_{xy}^f = -\tan \alpha_x \sigma_{zx}^f, \\ \sigma_{zy}^f = -\tan \alpha_x \sigma_{zz}^f. \end{cases} \quad (6.24)$$

Where, recalling Equation 6.7, $\tan \alpha_x = \frac{dh}{dz}$.

The last unknown stress component, σ_{xx}^f , can be obtained by integrating the first Cauchy equilibrium equation [Timoshenko and Goodier, 1951]:

$$\frac{\partial \sigma_{xx}}{\partial x} + \frac{\partial \sigma_{xy}}{\partial y} + \frac{\partial \sigma_{zx}}{\partial z} = 0. \quad (6.25)$$

Thus,

$$\sigma_{xx}^f = - \int_0^x \frac{\partial \sigma_{zx}^f}{\partial z} dx + \sigma_{xx}^f|_{x=0} = \int_x^b \frac{\partial \sigma_{zx}^f}{\partial z} dx + \sigma_{xx}^f|_{x=b}. \quad (6.26)$$

$\sigma_{xx}^f|_{x=0}$ and $\sigma_{xx}^f|_{x=b}$ are the values of the stress σ_{xx} calculated in $x=0$ and $x=b$, respectively. This is due to the fact that at a given cross section, the dependency on z and y of the stress can be neglected on the flanges.

Stress components in the right-hand web

The web located in the half-space $x > 0$ will be referred to as the *right-hand web*. The solution for the *left-hand web* will be deduce from the symmetry of the problem.

From Equations 6.13 and 6.14, we recall the cross sectional properties of one half of the flange and part of the web, i.e. the part included between the yz -plane and a plane $y = \text{const}$ (Figure 6.16).

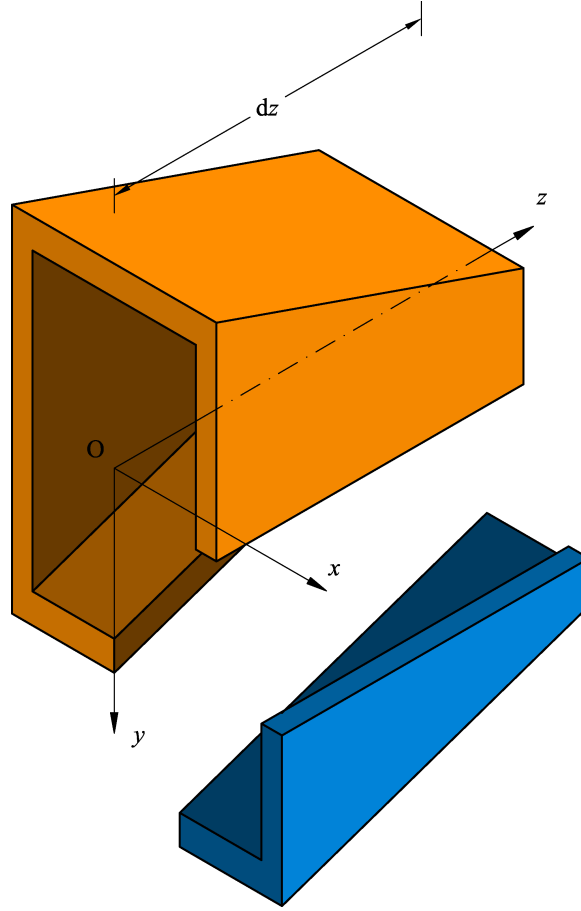


Figure 6.16: portion of web of the element of the tapered box girder.

Again, the stress component σ_{zz}^w can be obtained by Navier's equation. By substituting Equations 6.11 and 6.12 into Equation 6.15, we get

$$\sigma_{zz}^w = \frac{1}{4} \left(\frac{N}{ht_w + \frac{bt_f}{\cos \alpha_x}} + \frac{3yM}{3h^2 \frac{bt_f}{\cos \alpha_x} + h^3 t_w} \right). \quad (6.27)$$

The shear stress component σ_{zy}^w can be obtained from Equation 5.13. Substituting the values of the cross-sectional properties, it can be written as follows

$$\begin{aligned} \sigma_{zy}^w = \frac{1}{8t_w} \left\{ -\frac{2yt_w^2 \cos^2 \alpha_x \tan \alpha_x N}{(t_w h \cos \alpha_x + bt_f)^2} + \frac{3[t_w \cos \alpha_x (h^2 - y^2) + 2bt_f h] Q}{h^2 (ht_w \cos \alpha_x + 3bt_f)} \right. \\ \left. + 3M \tan \alpha_x \left[\frac{(t_w^2 h (h^2 - 3y^2) \cos^2 \alpha_x}{h^3 (ht_w \cos \alpha_x + 3bt_f)^2} \right. \right. \\ \left. \left. + \frac{4t_w t_f b (h^2 - \frac{3y^2}{2}) \cos \alpha_x + 6b^2 t_f^2 h}{h^3 (ht_w \cos \alpha_x + 3bt_f)^2} \right] \right\}. \quad (6.28) \end{aligned}$$

The stress components σ_{xx}^w , σ_{xy}^w and σ_{zx}^w in the web are zero for the hypothesis of thin-walled beam.

The last stress component of the web can be calculated by integration of the second Cauchy equation (Equation 6.5).

$$\sigma_{yy}^w = - \int_0^y \frac{\partial \sigma_{zy}^w}{\partial z} dy + \sigma_{yy}^w|_{y=0} = \int_y^h \frac{\partial \sigma_{zy}^w}{\partial z} dy + \sigma_{yy}^w|_{y=h}. \tag{6.29}$$

As already seen for the stress distribution on the flange, any function on the web will be constant with respect to x for each cross section.

Equilibrium conditions on edges

We have completely defined the stress distributions in the box girder, except for the two integration constants, $\sigma_{xx}^f|_{x=0}$ and $\sigma_{yy}^w|_{y=0}$ introduced in σ_{xx}^f and σ_{yy}^w respectively. Those constants can be calculated for each cross-section $z = \text{const}$, by imposing two equilibrium conditions for the edge of a box girder segment of length dz (Figure 6.17). In particular, we will write the equilibrium equations for the edge which connect the bottom flange and the right-hand web.

The equilibrium in the x -direction gives

$$t_f \sigma_{xx}^f|_{x=b} \frac{dz}{\cos \alpha_x} + t_w \sigma_{xy}^w|_{y=h} dz + t_w \sigma_{zx}^w|_{y=h} \tan \alpha_x dz = 0, \tag{6.30}$$

and the equilibrium in the y -direction gives

$$t_f \sigma_{xy}^f|_{x=b} \frac{dz}{\cos \alpha_x} + t_w \sigma_{yy}^w|_{y=h} dz + t_w \sigma_{zy}^w|_{y=h} \tan \alpha_x dz = 0. \tag{6.31}$$

The unknowns in Equations 6.30 and 6.31 are the two integration constants $f \sigma_{xx}^f|_{x=0}$ and $\sigma_{yy}^w|_{y=0}$. Due to the complexity of the mathematical expressions involved in this algebraic system, the integrals in Equations 6.30 and 6.31 can be numerically evaluated with the Matlab software [The MathWorks, Inc., 2016] at each given z -coordinate.

Those two equilibrium conditions merge together the two separate solutions for the flange and for the web, and complete the stress field assessment in the box girder.

By substituting Equations 6.26 and 6.29 into Equations 6.30 and 6.31, respectively, we get

$$\sigma_{xx}^f|_{x=0} = \int_0^b \frac{\partial \sigma_{zx}^f}{\partial z} dx - \frac{t_w}{t_f} \left(\cos \alpha_x \sigma_{xy}^w|_{y=h} + \sin \alpha_x \sigma_{zx}^w|_{y=h} \right), \tag{6.32}$$

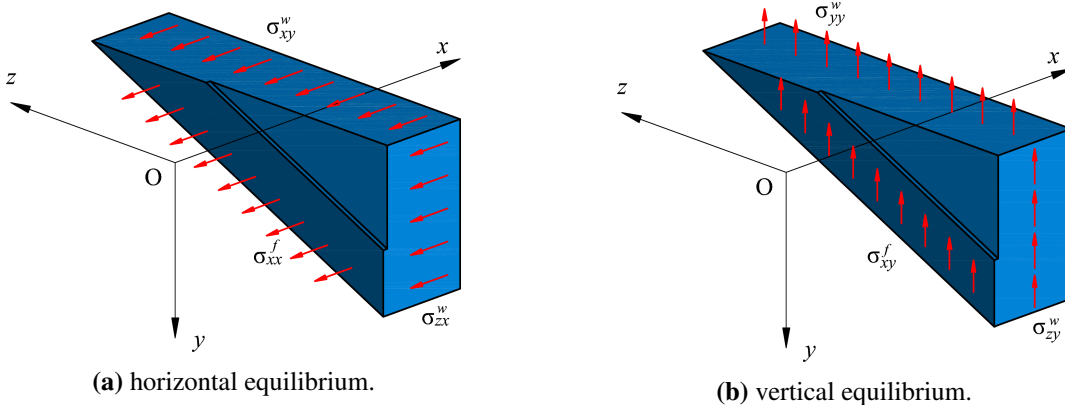


Figure 6.17: connection wedge between flange and web.

and

$$\sigma_{yy}^w|_{y=0} = \int_0^h \frac{\partial \sigma_{zy}^w}{\partial z} dy - \tan \alpha_x \sigma_{zy}^w|_{y=h} - \frac{t_f}{t_w \cos \alpha_x} \sigma_{xy}^f|_{x=b}. \quad (6.33)$$

Numerical example and comparison with FE

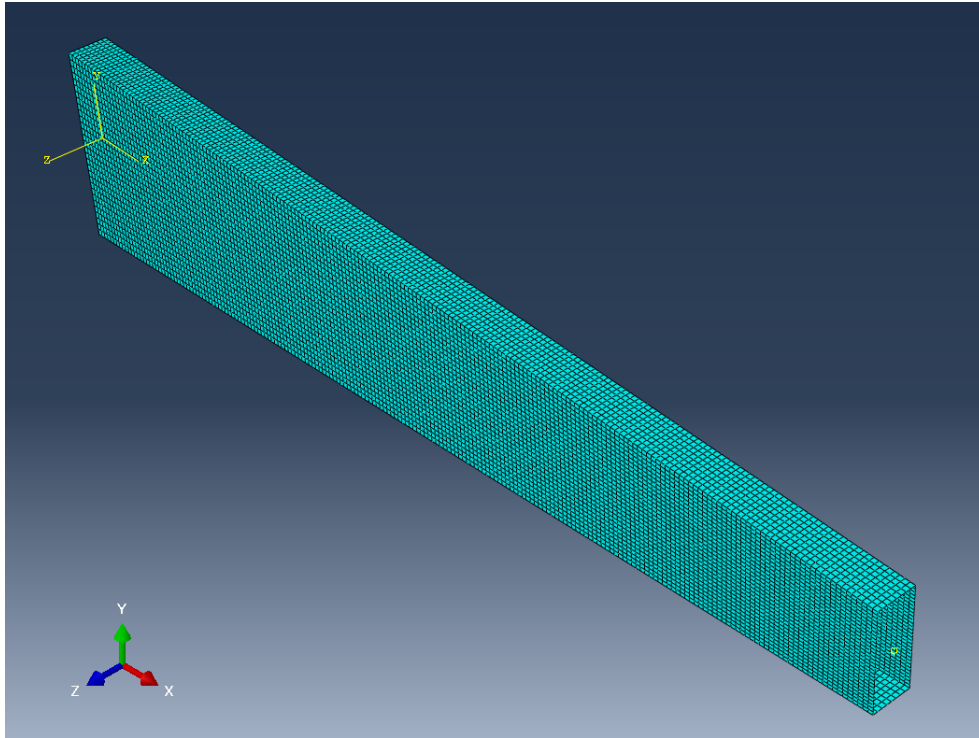


Figure 6.18: shell model of the box girder.

Let us consider a vertically tapered box-girder of length $L = 5000$ mm. The width of the cross section is $W = 200$ mm and the height of the section changes linearly from the root cross section ($H_0 = 1000$ mm) to the tip cross section ($H_t = 500$ mm.)

The angle of taper can then be deduced and is

$$\alpha_x = \arctan \frac{H_0 - H_t}{2L} = 2.8624^\circ.$$

We also suppose that the thickness of the wall of the box girder is equal between the flange and the web, and is $t_w = t_f = 10$ mm.

We define three different loading conditions. In particular, we will analyse the case of *simple extension* (applying at the tip cross section a force in the z direction, $F_z = 1000$ N), the case of *shear* (applying at the tip cross section a force in the y direction, $F_y = 1000$ N), and finally the case of *bending* (applying at the tip cross section a bending moment, $M_x = 10000$ N mm). The forces are applied at the centre of the cross section ($x = 0$ and $y = 0$)

For our analysis we will consider an isotropic linear elastic material, in particular a generic aluminium alloy, whose Young's modulus is $E = 72$ GPa and the Poisson ratio is $\nu = 0.35$. Even though such material properties are not strictly necessary to determine the "approximate" stress distribution, we have also conducted a FE analyses to compare the results.

The internal forces in the different loading cases are summarised in Table 6.2.

We focus on the stresses on the mid-span section.

	Extension	Shear	Bending
$N(z)$	F_z	0	0
$Q(z)$	0	F_y	0
$M(z)$	0	$-F_y(L-z)$	M_x

Table 6.2: internal forces for the different loading cases.

In Figure 6.19, a comparison between the well-known Jourawski formula (red line) and the extended shear stress formula (blue line) is given. In particular, the shear stresses on the mid-span section are presented. The intensity of the stress is referred to the mid-line of the thin-walled cross section. The influence of the shear-induced bending on the shear stresses is here evident: being the maximum of the shear stress σ_{zy} consistently smaller of that predicted by the classical Jourawski approach, and meanwhile being the values on the edges almost doubled. Moreover, on the flanges the bending effect appears to be even advantageous, lowering the shear stresses σ_{zx} .

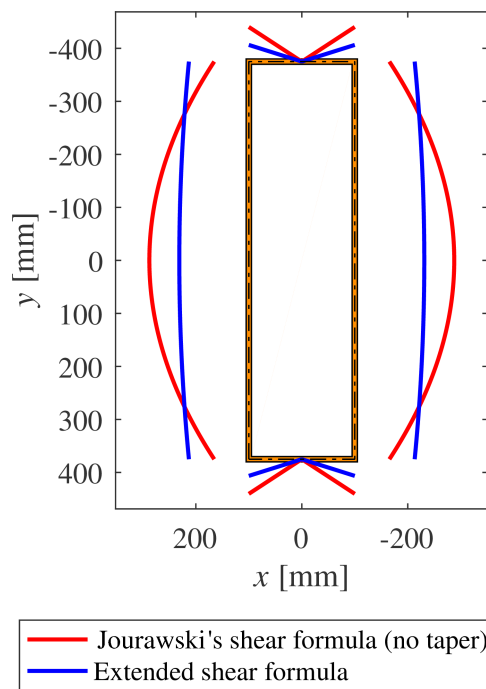
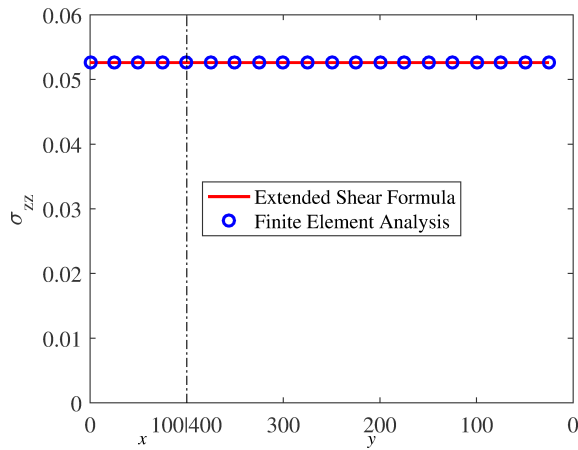


Figure 6.19: comparison between the Jourawski formula (red line) and the extended shear stress formula (blue line) on the mid-span cross section in the “shear” loading case.

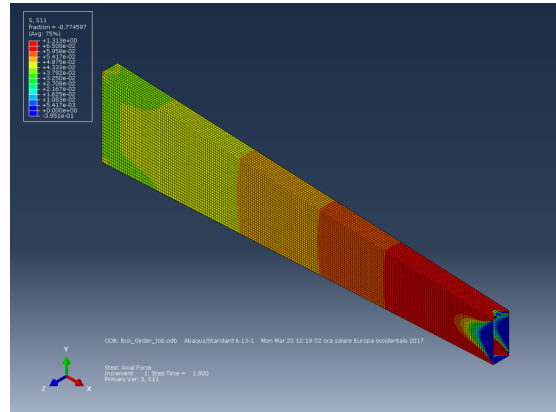
A FE model has also been prepared using shell quadrilateral elements of 4 nodes, and is shown in Figure 6.18.

In Figure 6.20, the stresses of a quarter of section are presented: in particular, the part of the section under exam is characterised by $x \geq 0$ and $y \geq 0$. In each of the plots both the distribution of stresses on half of the flange (left-hand side) and on half of the web (right-hand side) are shown. In Figure 6.21 and Figure 6.22, the analogous results for the other two loading cases presented here are shown. In those Figures, the results of the FE analyses of the corresponding loading cases are also shown.

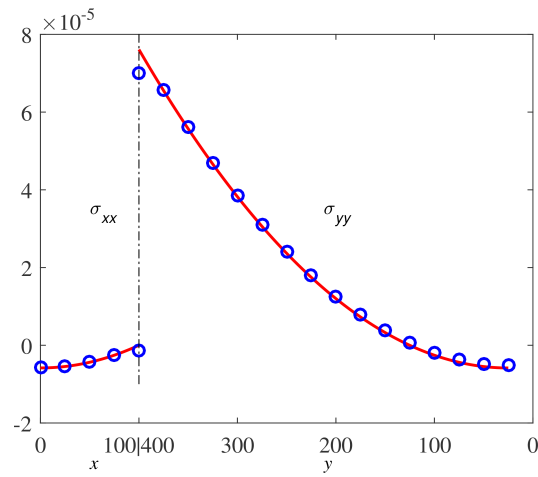
In Figures 6.21(e) and 6.21(f), the change of the curvature of the distribution of shear stresses closing from the tip to the root is evident. For cross sections closes to the root than the mid-span one the maximum migrates from the mid-plane (the zx -plane) to the lower and upper edges, where the joint with the flange is present. Recalling how wind turbine blades are usually designed (Figure 3.1 at Page 33), higher-than-expected shear stresses in proximity of the adhesively joints could jeopardize the safety of the structure.



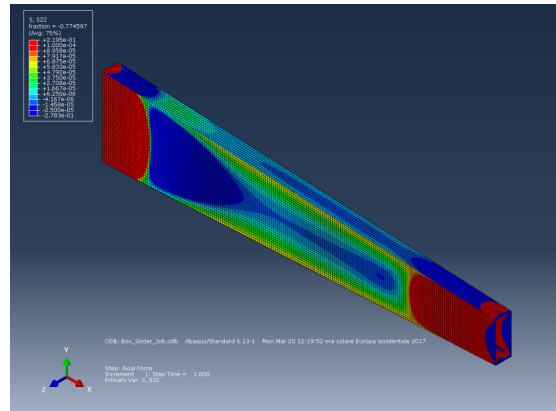
(a) σ_{zz}



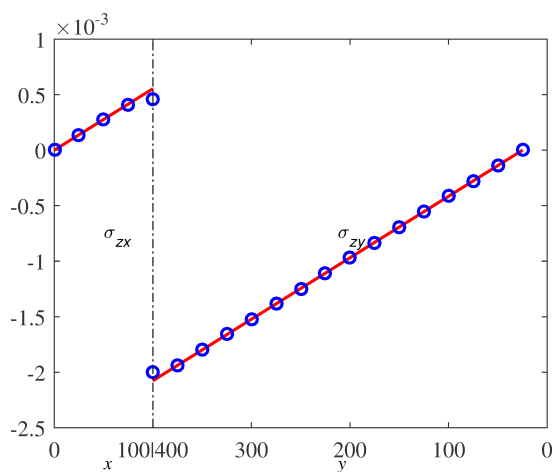
(b) σ_{zz}



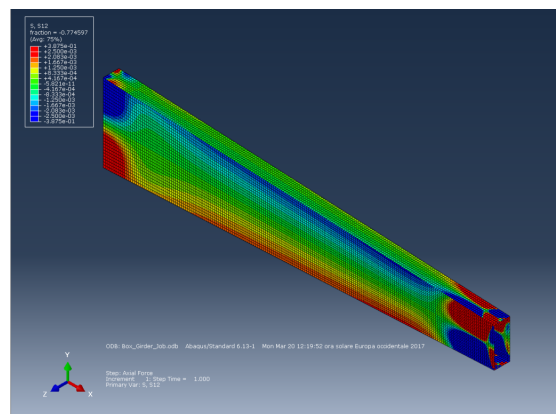
(c) σ_{xx} (in the flange) and σ_{yy} (in the web)



(d) σ_{xx} (in the flange) and σ_{yy} (in the web)



(e) σ_{zx} (in the flange) and σ_{zy} (in the web)



(f) σ_{zx} (in the flange) and σ_{zy} (in the web)

Figure 6.20: distribution of stresses on a quarter of the mid-span section for the “extension” loading case.

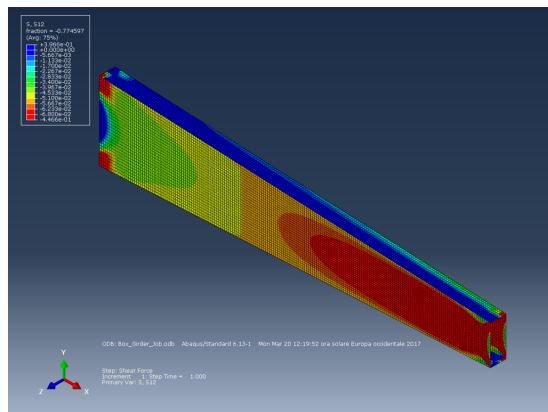
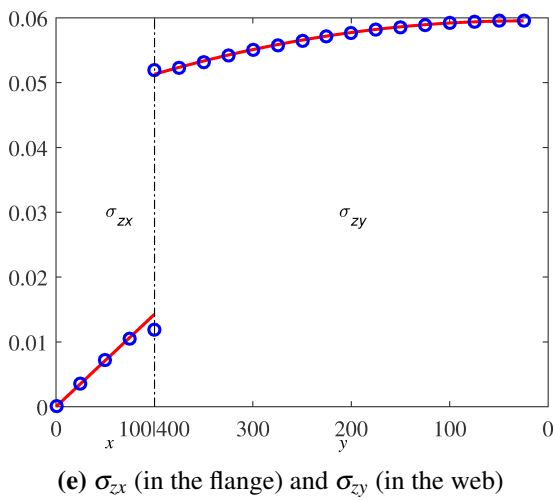
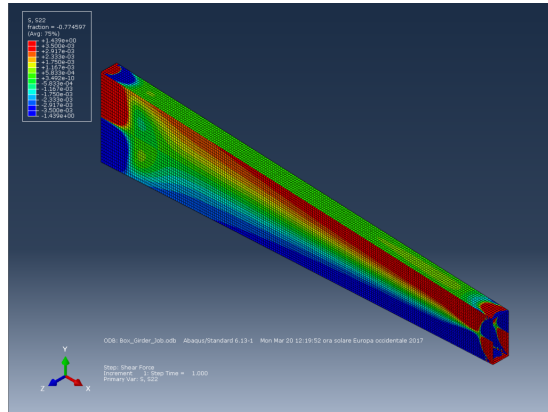
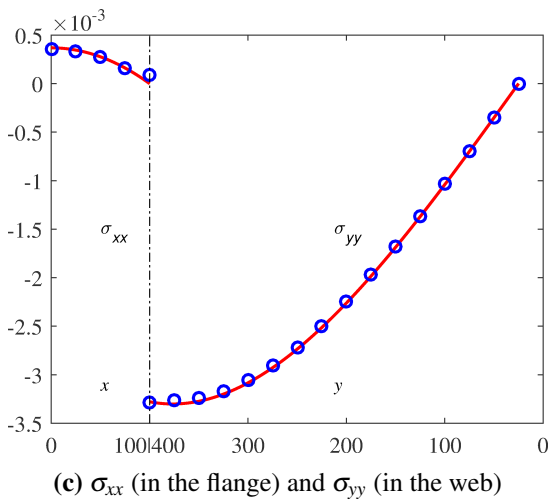
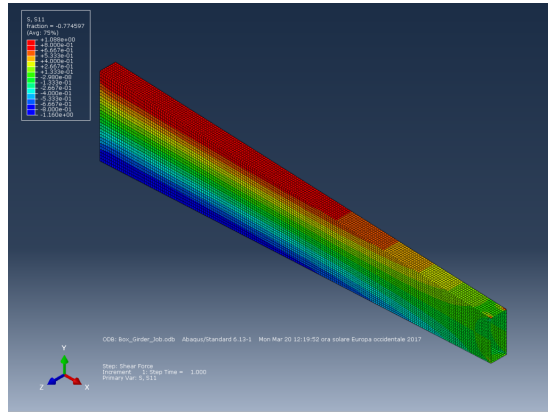
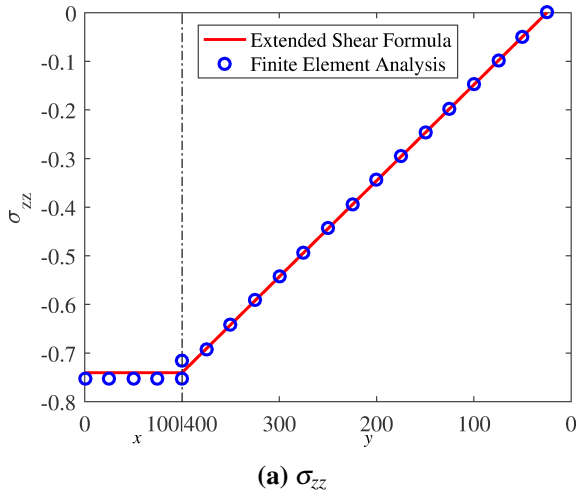
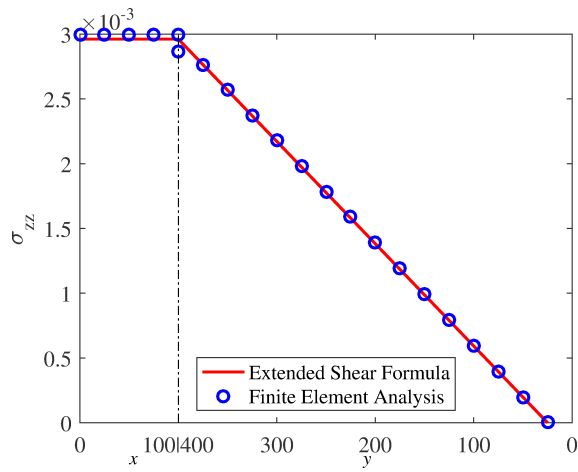
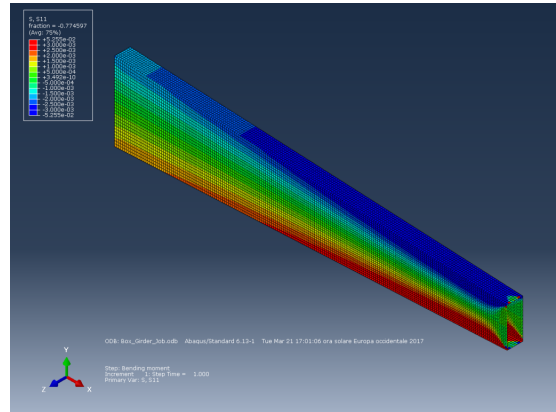


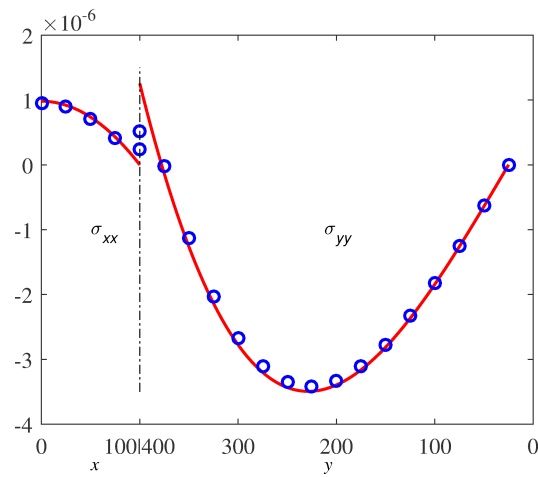
Figure 6.21: distribution of stresses on a quarter of the mid-span section for the “shear” loading case.



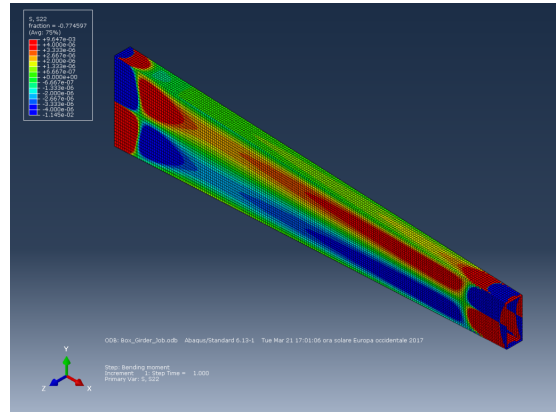
(a) σ_{zz}



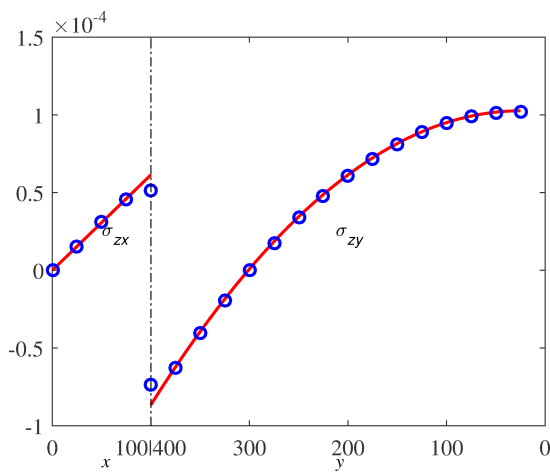
(b) σ_{zz}



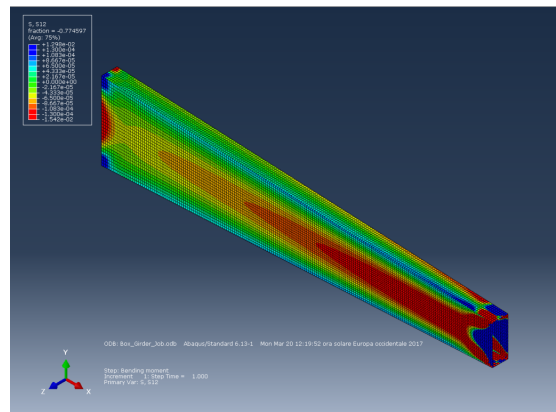
(c) σ_{xx} (in the flange) and σ_{yy} (in the web)



(d) σ_{xx} (in the flange) and σ_{yy} (in the web)



(e) σ_{zx} (in the flange) and σ_{zy} (in the web)



(f) σ_{zx} (in the flange) and σ_{zy} (in the web)

Figure 6.22: distribution of stresses on a quarter of the mid-span section for the “bending” loading case.

6.2.2 Horizontally tapered box girder

In the following it is briefly summarised the derivation of the stress tensor (in the flanges and in the webs) of a horizontally tapered box girder whose length is dz (Figure 6.23). In such a case, the angle of taper α_x is null. Figure 6.24 shows a cross section of such horizontally tapered box girder.

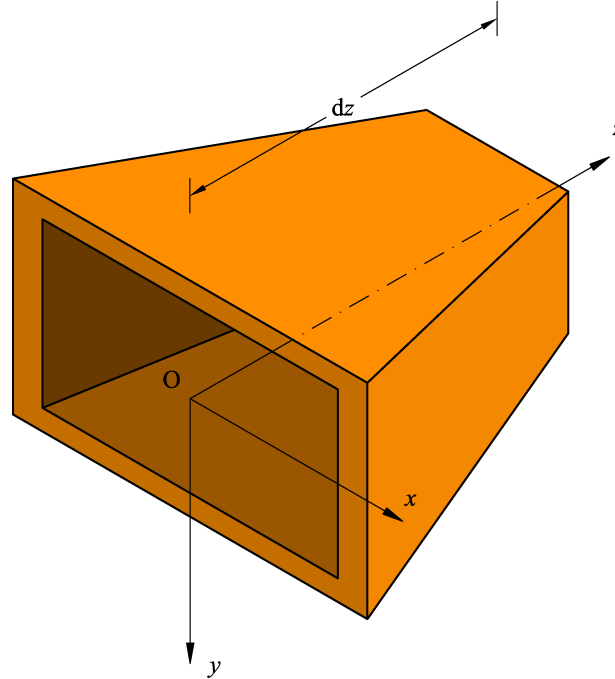


Figure 6.23: horizontally tapered box beam.

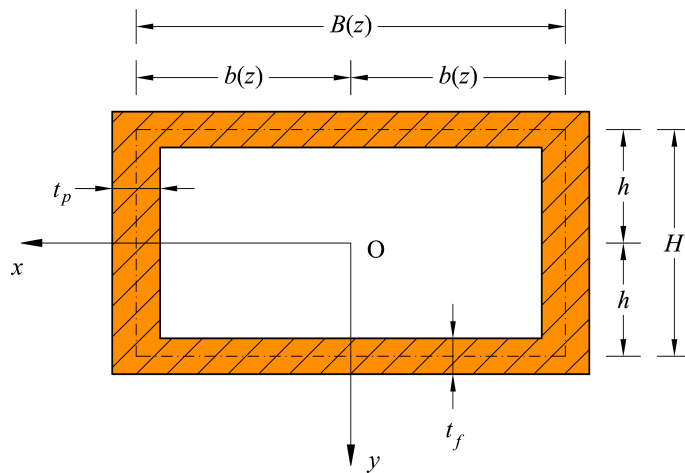


Figure 6.24: cross section of a horizontally tapered box girder.

Stress components in the bottom flange

Under the hypothesis of plane stress in the thin walls of the box girder, the tension components σ_{yy}^f , σ_{zy}^f and σ_{xy}^f have to be null.

The stress component σ_{zz}^f can be derived directly from the Navier equation: by substituting Equations

6.11 and 6.12 into Equation 6.15, we get

$$\sigma_{zz}^f = \frac{1}{4} \left(\frac{N}{t_f b + \frac{t_w h}{\cos \alpha_y}} + \frac{3M}{3t_f h b + \frac{t_w h^2}{\cos \alpha_y}} \right). \quad (6.34)$$

The stress component σ_{zx}^f comes from Equation 5.13. Thus, substituting Equations 6.13, 6.14, 6.11 and 6.12 into Equation 6.17, we get:

$$\sigma_{zx}^f = \frac{x}{4} \left[\frac{t_f \tan \alpha_y N}{(t_f b + \frac{h t_w}{\cos \alpha_y})^2} + \frac{3Q}{3t_f h b + \frac{t_w h^2}{\cos \alpha_y}} + \frac{9t_f \tan \alpha_y M}{\left(3t_f h b + \frac{t_w h^2}{\cos \alpha_y}\right)^2} \right]. \quad (6.35)$$

Following the same strategy adopted for the vertically tapered beam, by integrating the first equilibrium equation (Equation 6.25), we obtain the stress component σ_{xx}^f :

$$\sigma_{xx}^f = - \int_0^x \frac{d\sigma_{zx}^f}{dz} dx + \sigma_{xx}^f|_{x=0}. \quad (6.36)$$

We have here introduced the integration constant $\sigma_{xx}^f|_{x=0}$. The same considerations which we have already discussed in the Section 6.2.1 are also valid for $\sigma_{xx}^f|_{x=0}$.

Stress components in the right-hand web

The stress component σ_{zz}^w can be determined by substituting Equations 6.11 and 6.12 into Equation 6.15:

$$\sigma_{zz}^w = \frac{1}{4} \left(\frac{N}{\frac{h t_w}{\cos \alpha_y} + t_f b(z)} + \frac{3M y}{3h^2 t_f b + \frac{h^3 t_w}{\cos \alpha_y}} \right). \quad (6.37)$$

Applying the extended shear stress formula (Equation 5.13) we get the stress component σ_{zy}^w . In particular:

$$\sigma_{zy}^w = - \frac{\cos \alpha_y}{8t_w} \left[\frac{2N y t_f t_w \sin \alpha_y}{(h t_w + t_f b \cos \alpha_y)^2} - \frac{3Q [t_w (h^2 - y^2) + 2h t_f b \cos \alpha_y]}{h^2 (h t_w + 3t_f b \cos \alpha_y)} - \frac{3M (h^2 - 3y^2) t_f t_w \sin \alpha_y}{h^2 (h t_w + 3t_f b \cos \alpha_y)^2} \right]. \quad (6.38)$$

Under the hypothesis that the web is in a plane stress state, and by rotating the global stress tensor into a local web reference where the 1-axis is aligned with the web, the 2-axis is reversed with respect to the y-axis, and the 3-axis is normal to the web plane, three equations for σ_{xx} , σ_{xy} , and σ_{zx} can be obtained (Figure 6.25). In particular,

$$\boldsymbol{\sigma}_{1,2,3} = \mathbf{R}^T \boldsymbol{\sigma}_{x,y,z} \mathbf{R}, \quad (6.39)$$

where

$$\mathbf{R} = \begin{bmatrix} -\sin \alpha_y & 0 & \cos \alpha_y \\ 0 & -1 & 0 \\ \cos \alpha_y & 0 & \sin \alpha_y \end{bmatrix}. \quad (6.40)$$

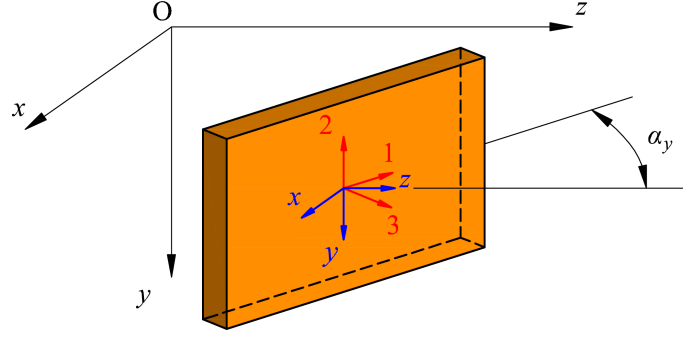


Figure 6.25: reference systems on an element of the web.

Passing to the stress components, we obtain the following set of linear equations

$$\begin{cases} \sigma_{11} = \sigma_{xx}^w \sin^2 \alpha_x - 2\sigma_{zx}^w \sin \alpha_x \cos \alpha_x + \sigma_{zz}^w \cos^2 \alpha_x, \\ \sigma_{22} = \sigma_{yy}^w, \\ \sigma_{33} = \sigma_{xx}^w \cos^2 \alpha_x + \sigma_{zz}^w \sin^2 \alpha_x + \sigma_{zx}^w \sin 2\alpha_x, \\ \sigma_{12} = \sigma_{xy}^w \sin \alpha_x - \sigma_{zy}^w \cos \alpha_x, \\ \sigma_{13} = \sigma_{zx}^w \cos 2\alpha_x + (\sigma_{zz}^w - \sigma_{xx}^w) \frac{\sin 2\alpha_x}{2}, \\ \sigma_{23} = -\sigma_{xy}^w \cos \alpha_x - \sigma_{zy}^w \sin \alpha_x. \end{cases} \quad (6.41)$$

For the plane stress hypothesis, we have

$$\begin{cases} \sigma_{33} = 0, \\ \sigma_{13} = 0, \\ \sigma_{23} = 0. \end{cases} \quad (6.42)$$

Substituting Equations 6.42 into the third, fifth, and sixth of 6.41, we obtain a set of three linear equations in the unknowns σ_{xx}^w , σ_{xy}^w , and σ_{zx}^w . Once solved this set of equations, we get

$$\begin{cases} \sigma_{xx}^w = \tan^2 \alpha_y \sigma_{zz}^w, \\ \sigma_{xy}^w = -\tan \alpha_y \sigma_{zy}^w, \\ \sigma_{zx}^w = -\tan \alpha_y \sigma_{zz}^w, \end{cases} \quad (6.43)$$

were, recalling Equation 6.8, we have $\tan \alpha_y = \frac{db}{dz}$.

The last stress component of the web can be calculated by integration of the second Cauchy equation (Equation 6.5 at Page 110).

$$\sigma_{yy}^w = - \int_0^y \frac{d\sigma_{zy}^w}{dz} dy + \sigma_{yy}^w|_{y=0}. \quad (6.44)$$

As already seen for the case of the vertically tapered box girder, we need to introduce integration constant $\sigma_{yy}^w|_{y=0}$.

Equilibrium conditions on edges

The stress distribution in the box girder has been unveiled, except for the two integration constants $\sigma_{xx}^f|_{x=0}$ and $\sigma_{yy}^w|_{y=0}$. Those two unknown can be numerically calculated for each cross-section z , by

imposing two equilibrium conditions at one corner of the corresponding cross-section. In particular, the equilibrium in the x -direction gives

$$t_f \sigma_{xx}^f|_{x=b} dz + t_w \sigma_{xy}^w|_{y=h} \frac{dz}{\cos \alpha_y} + t_f \sigma_{zx}^f|_{x=b} \tan \alpha_y dz = 0, \quad (6.45)$$

and the equilibrium in the y -direction gives

$$t_f \sigma_{xy}^f|_{x=b} dz + t_w \sigma_{yy}^w|_{y=h} \frac{dz}{\cos \alpha_y} + t_f \sigma_{zy}^f|_{x=b} \tan \alpha_y dz = 0. \quad (6.46)$$

With simple manipulations, we get

$$\sigma_{xx}^f|_{x=0} = \int_0^b \frac{d\sigma_{zx}^f}{dz} dx - \tan \alpha_y \sigma_{zx}^f|_{x=b} - \frac{t_w}{t_f \cos \alpha_y} \sigma_{xy}^w|_{y=b}, \quad (6.47)$$

and

$$\sigma_{yy}^w|_{y=0} = \int_0^h \frac{d\sigma_{zy}^w}{dz} dy - \frac{t_f}{t_w} \left(\cos \alpha_y \sigma_{xy}^f|_{x=b} + \sin \alpha_y \sigma_{zy}^f|_{x=b} \right). \quad (6.48)$$

This concludes the determination of the distributions of the stresses in the horizontally tapered box girder.

6.2.3 Doubly tapered box girder

Once the solution strategy has been settled down for the horizontal and vertical taper cases, it is immediate to extend such a solution also to a doubly tapered box girder (Figure 6.9).

Stress components in the bottom flange

The cross-sectional properties of the portion of flange (Figure 6.14) are shown in Equations 6.13 and 6.14 at Page 107.

As stated in Section 5.2.1, we assume that Navier's equation (Equation 5.8) is valid also for tapered beams. Thus

$$\sigma_{zz}^f = \frac{N}{A} + \frac{M}{I_x} h. \quad (6.49)$$

The shear stress component σ_{zx} can be obtained from Equation 5.13.

$$\sigma_{zx}^f = \frac{1}{b} \frac{d}{dz} \left(\frac{A^*}{A} N + \frac{S_x^*}{I_x} M \right). \quad (6.50)$$

The thin-walled section hypothesis allows us to determine also the three remaining stress components. In fact, we state that the flange is in a plane stress state. With a procedure used for the flange in the case of vertical taper, we obtain

$$\begin{cases} \sigma_{yy}^f = \tan^2 \alpha_x \sigma_{zz}^f, \\ \sigma_{xy}^f = -\tan \alpha_x \sigma_{zx}^f, \\ \sigma_{zy}^f = -\tan \alpha_x \sigma_{zz}^f. \end{cases} \quad (6.51)$$

The last unknown stress components, σ_{xx}^f , can be obtained by integrating the first Cauchy equilibrium equations (Equations 6.25 at Page 110). As before, we obtain:

$$\sigma_{xx}^f = - \int_0^x \frac{d\sigma_{zx}^f}{dz} dx + \sigma_{xx}^f|_{x=0}. \quad (6.52)$$

As usual, to complete the integration of Equation 6.26, we need to introduce the integration constant $\sigma_{xx}^f|_{x=0}$.

Stress components in the right-hand web

The stress component σ_{zz}^w can be obtained by Navier's equation, and the shear stress component σ_{zy}^w can be obtained from Equation 5.13.

Being the web in a plane stress state, we can identify three equations for σ_{xx}^w , σ_{xy}^w , and σ_{zx}^w . Thus, we have:

$$\begin{cases} \sigma_{xx}^w = \tan^2 \alpha_y \sigma_{zz}^w, \\ \sigma_{xy}^w = -\tan \alpha_y \sigma_{zy}^w, \\ \sigma_{zx}^w = -\tan \alpha_y \sigma_{zz}^w. \end{cases} \quad (6.53)$$

The last stress component of the web can be calculated by integration of the second Cauchy equation (Equation 6.5).

$$\sigma_{yy}^w = -\int_0^y \frac{d\sigma_{zy}^w}{dz} dy + \sigma_{yy}^w|_{y=0}. \quad (6.54)$$

where we have introduced the integration constant $\sigma_{yy}^w|_{y=0}$.

Equilibrium conditions on edges

We have completely defined the stress distributions in the box girder, except for the two integration constants $\sigma_{xx}^f|_{x=0}$ and $\sigma_{yy}^w|_{y=0}$ introduced above. Those constants can be evaluated numerically (using the Matlab software [The MathWorks, Inc., 2016]) for each cross-section z , by solving two equilibrium conditions at one edge of an element of box girder of length dz . In particular, the equilibrium in the x -direction gives

$$t_{fp} \sigma_{xx}^f|_{x=b} dz + t_{fp} \sigma_{zx}^f|_{x=b} \tan \alpha_y dz + t_{wp} \sigma_{xy}^w|_{y=h} dz + t_{wp} \sigma_{zx}^w|_{y=h} \tan \alpha_x dz = 0, \quad (6.55)$$

and the equilibrium in the y -direction gives

$$t_{fp} \sigma_{xy}^f|_{x=b} dz + t_{fp} \sigma_{zy}^f|_{x=b} \tan \alpha_y dz + t_{wp} \sigma_{yy}^w|_{y=h} dz + t_{wp} \sigma_{zy}^w|_{y=h} \tan \alpha_x dz = 0. \quad (6.56)$$

By manipulating those two equations, we can completely define the stress distribution in a doubly tapered box girder. In fact, we have

$$\sigma_{xx}^f|_{x=0} = \int_0^b \frac{d\sigma_{zx}^f}{dz} dx - \tan \alpha_y \sigma_{zx}^f|_{x=b} - \frac{t_{wp}}{t_{fp}} \left(\sigma_{xy}^w|_{y=h} + \tan \alpha_x \sigma_{zx}^w|_{y=h} \right) \quad (6.57)$$

and

$$\sigma_{yy}^w|_{y=0} = \int_0^h \frac{d\sigma_{zy}^w}{dz} dy - \tan \alpha_x \sigma_{zy}^w|_{y=h} - \frac{t_{fp}}{t_{wp}} \left(\sigma_{xy}^f|_{x=b} + \tan \alpha_y \sigma_{zy}^f|_{x=b} \right). \quad (6.58)$$

6.3 Conical beam

We consider a conical thin-walled hollow beam, for which the radius defining as a function of z the mid-surface of the wall can be written as

$$r(z) = r_0 - z \tan \alpha \quad (6.59)$$

The wall of the cone has constant thickness t . The projected wall thickness in the cross-sectional plane

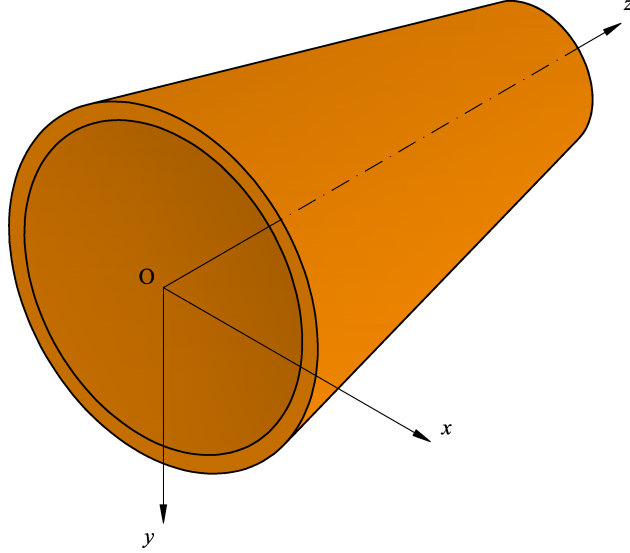


Figure 6.26: a conical thin-walled hollow beam.

is given by $t_p = \frac{t}{\cos \alpha}$, and the cross-sectional properties in cylinder coordinates can be written as:

$$A = \frac{2\pi t r(z)}{\cos \alpha}, \quad (6.60)$$

and

$$I_x = \frac{\pi t r(z)^3}{\cos \alpha} \quad (6.61)$$

The axial stress component σ_{zz} can be obtained by Equation (5.8), substituting Equation 6.60 and Equation 6.61.

$$\sigma_{zz} = \frac{\cos \alpha N}{2\pi t r(z)} + \frac{\cos \alpha \sin \theta M}{\pi t r(z)^2} \quad (6.62)$$

We introduce the area of a portion of section between the yz -plane and the location where the stresses have to be calculated,

$$A^* = 2 \int_{\theta}^{\pi/2} r(z) t_p d\theta = \frac{2r(z)t(\pi - \theta)}{\cos \alpha} \quad (6.63)$$

and the first moment of area of the same portion,

$$S_x^* = 2 \int_{\theta}^{\pi/2} r(z)^2 t_p \sin \theta d\theta = \frac{2r(z)^2 t \cos \theta}{\cos \alpha} \quad (6.64)$$

The circumferential shear stress component $\sigma_{z\theta}$ can be obtained from Equation 5.13, under the assumption that $b = 2t_p$. We get

$$\sigma_{z\theta} = \frac{\cos \alpha \cos \theta Q}{\pi t r(z)} + \frac{\sin \alpha \cos \theta M}{\pi t r(z)^2} \quad (6.65)$$

We recall the third Cauchy equilibrium equation in cylindrical coordinates [Timoshenko and Goodier, 1951]

$$\frac{\partial \sigma_{zr}}{\partial r} + \frac{1}{r} \frac{\partial \sigma_{z\theta}}{\partial \theta} + \frac{\partial \sigma_{zz}}{\partial z} + \frac{1}{r} \sigma_{zr} = 0, \quad (6.66)$$

and we assume that, under the hypothesis of thin-walled beam, $\partial/\partial r = 0$. The radial shear stress component σ_{zr} can be obtained substituting Equations 6.62 and 6.65 into 6.66.

$$\sigma_{zr} = -\frac{\sin \alpha N}{2\pi t r(z)} - \frac{\sin \alpha \sin \theta M}{\pi t r(z)^2}. \quad (6.67)$$

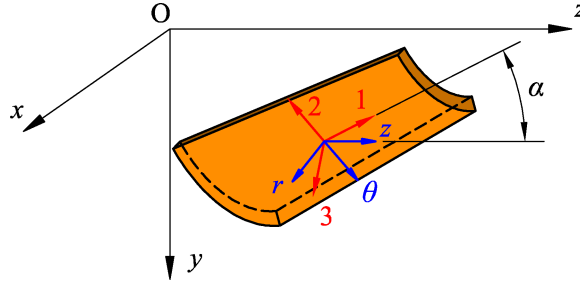


Figure 6.27: projection of the stresses consistent to the thin-walled beam hypothesis.

Analogously to what has been done for the box girder, we consider the following relationship between the local reference systems (the global stress tensor $\sigma_{r,z,\theta}$, and the local stress tensor $\sigma_{1,2,3}$):

$$\sigma_{1,2,3} = \mathbf{R}^T \sigma_{r,\theta,z} \mathbf{R}, \quad (6.68)$$

where

$$\mathbf{R} = \begin{bmatrix} -\sin \alpha & 0 & \cos \alpha \\ 0 & -1 & 0 \\ \cos \alpha & 0 & \sin \alpha \end{bmatrix}. \quad (6.69)$$

Thus, substituting we get:

$$\begin{bmatrix} \sigma_{rr} & \sigma_{r\theta} & \sigma_{zr} \\ \sigma_{r\theta} & \sigma_{\theta\theta} & \sigma_{z\theta} \\ \sigma_{zr} & \sigma_{z\theta} & \sigma_{zz} \end{bmatrix} = \begin{bmatrix} -\sin \alpha & 0 & \cos \alpha \\ 0 & -1 & 0 \\ \cos \alpha & 0 & \sin \alpha \end{bmatrix} \begin{bmatrix} \sigma_{11} & \sigma_{12} & \sigma_{13} \\ \sigma_{12} & \sigma_{22} & \sigma_{23} \\ \sigma_{13} & \sigma_{23} & \sigma_{33} \end{bmatrix} \begin{bmatrix} -\sin \alpha & 0 & \cos \alpha \\ 0 & -1 & 0 \\ \cos \alpha & 0 & \sin \alpha \end{bmatrix}^T \quad (6.70)$$

Assuming a plane stress state in the wall, the local stress components σ_{13} , σ_{23} , and σ_{33} are identically null. Consequently, Equation 6.70 give a set of three linear equations for the unknowns σ_{rr} , $\sigma_{r\theta}$, and σ_{zr} :

$$\begin{cases} \sigma_{31} = 2\sigma_{zr} \cos 2\alpha - (\sigma_{rr} - \sigma_{zz}) \sin 2\alpha = 0 \\ \sigma_{32} = \sigma_{r\theta} \cos \alpha + \sigma_{z\theta} \sin \alpha = 0 \\ \sigma_{33} = \sigma_{rr} \cos^2 \alpha + \sigma_{zr} \sin 2\alpha + \sigma_{zz} \sin^2 \alpha = 0 \end{cases} \quad (6.71)$$

The solution of the linear set of equations is:

$$\sigma_{rr} = \sigma_{zz} \tan^2 \alpha \quad (6.72)$$

$$\sigma_{r\theta} = -\sigma_{z\theta} \tan \alpha \quad (6.73)$$

$$\sigma_{zr} = -\sigma_{zz} \tan \alpha \quad (6.74)$$

Finally, $\sigma_{\theta\theta}$ can be immediately derived from the equilibrium equation in the radial direction for a portion of an element of the thin-walled conical beam, recalling that $R = R(z)$ (Figure 6.28). Such equilibrium equation can be written as

$$\begin{aligned} & \frac{t}{\cos \alpha} [(R + dR)(\sigma_{zr} + d\sigma_{zr}) - R\sigma_{zr}] d\theta + t \cos \frac{d\theta}{2} [(\sigma_{r\theta} + d\sigma_{r\theta}) - \sigma_{r\theta}] \frac{dz}{\cos \alpha} \\ & - t \sin \frac{d\theta}{2} [(\sigma_{\theta\theta} + d\sigma_{\theta\theta}) - \sigma_{\theta\theta}] \frac{dz}{\cos \alpha} = 0 \end{aligned} \quad (6.75)$$

where α is the angle of taper and t is the thickness of the thin wall of the beam. Dividing for Rdz and neglecting the higher order terms, we get:

$$\frac{1}{R} \sigma_{zr} \frac{dR}{dz} + \frac{d\sigma_{zr}}{dz} - \frac{\sigma_{\theta\theta}}{R} + \frac{1}{R} \frac{d\sigma_{r\theta}}{d\theta} = 0, \quad (6.76)$$

In particular, substituting Equations 6.74 and 6.73 into 6.76, we obtain $\sigma_{\theta\theta} = 0$ for all the loading conditions considered.

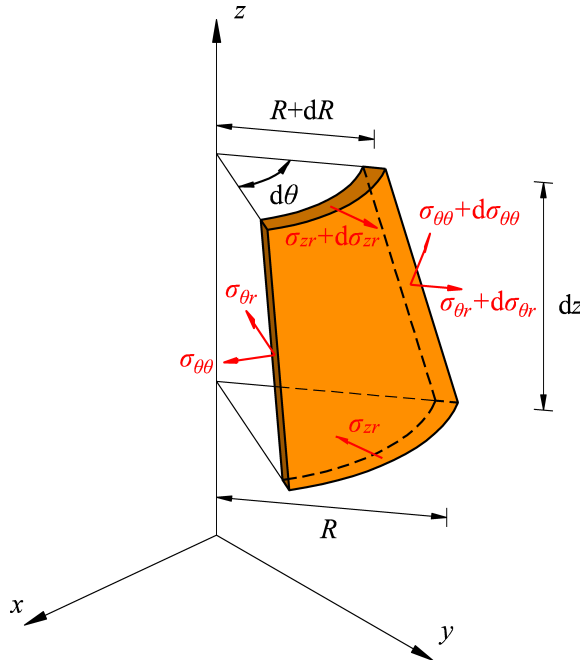


Figure 6.28: portion of an element of a thin-walled conical beam; only the stress components having a role in the radial equilibrium are shown.

6.3.1 Numerical results

Let us consider a hollow conical beam of length $L = 5000$ mm. The diameter of the root cross section is $2R_0 = 1000$ mm. The radius of the cross sections changes linearly from the root to the tip ($R_t = 500$ mm.)

The angle of taper is

$$\alpha = \arctan \frac{R_0 - R_t}{L} = 2.8624^\circ.$$

We also suppose that the thickness of the wall of the conical beam is constant on the entire beam and which it is $t = 10$ mm.

As already shown in Paragraph 6.2.1, we define three different loading conditions. In particular, we will analyse the case of *simple extension* (applying at the tip cross section a force in the z direction,

$F_z = 1000\text{N}$), the case of *shear* (applying at the tip cross section a force in the y direction, $F_y = 1000\text{N}$), and finally the case of *bending* (applying at the tip cross section a bending moment, $M_x = 10000\text{Nmm}$).

For our analysis, we will consider an isotropic linear elastic material, and in particular a generic aluminium alloy – whose Young’s modulus is $E = 72\text{GPa}$ and Poisson’s ratio is $\nu = 0.35$. Even though the knowledge of the material properties is not necessary when applying the extended shear stress formula, those data will be an input for the FE analysis (with the Abaqus software) whose results will be used to validate the analytical model.

The internal forces in the different loading cases are summarized in Table 6.3.

	Extension	Shear	Bending
$N(z)$	F_z	0	0
$Q(z)$	0	F_y	0
$M(z)$	0	$-F_y(L-z)$	M_x

Table 6.3: internal forces for the different loading cases.

We will focus on the distribution of stresses on the mid-span section.

In Figure 6.29, a comparison between the well-known Jourawski formula (red line) and the extended shear stress formula (blue line) is given. In particular, the shear stresses on the mid-span section are presented in the case of the “shear” loading condition. The intensity of the stress is referred to the mid-line of the hollow conical beam cross section. From Table 6.3, in this case the shear-induced bending has a negative contribution, which lowers the overall shear stresses on the considered cross section. Unlike what happens for prismatic beams, in tapered beams the shear stress distribution is strongly affected by the intensity and the sign of the bending moment. For the same structure and depending on the particular loading condition, the effect of taper could be advantageous or unfavourable, lowering or increasing the shear stress respectively.

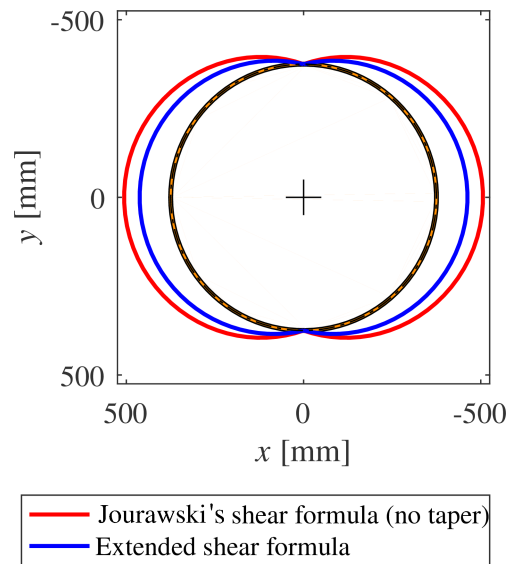


Figure 6.29: comparison

A FE model has been prepared using shell quadrilateral elements of 4 nodes, as shown in Figure 6.30.

Let us consider the quarter of the cross section characterized by $0 \leq \theta \leq \pi/2$. In Figure 6.31, the stress distribution for the extension loading case is shown. Meanwhile in Figure 6.32 and Figure 6.33, the analogous results for the other two loading cases presented here are shown.

The normal stresses σ_{zz} are predominant on all the other stress components, and the hoop stresses $\sigma_{\theta\theta}$ are null for all the loading cases. The shear stresses $\sigma_{z\theta}$ are null for the “extension” loading case,

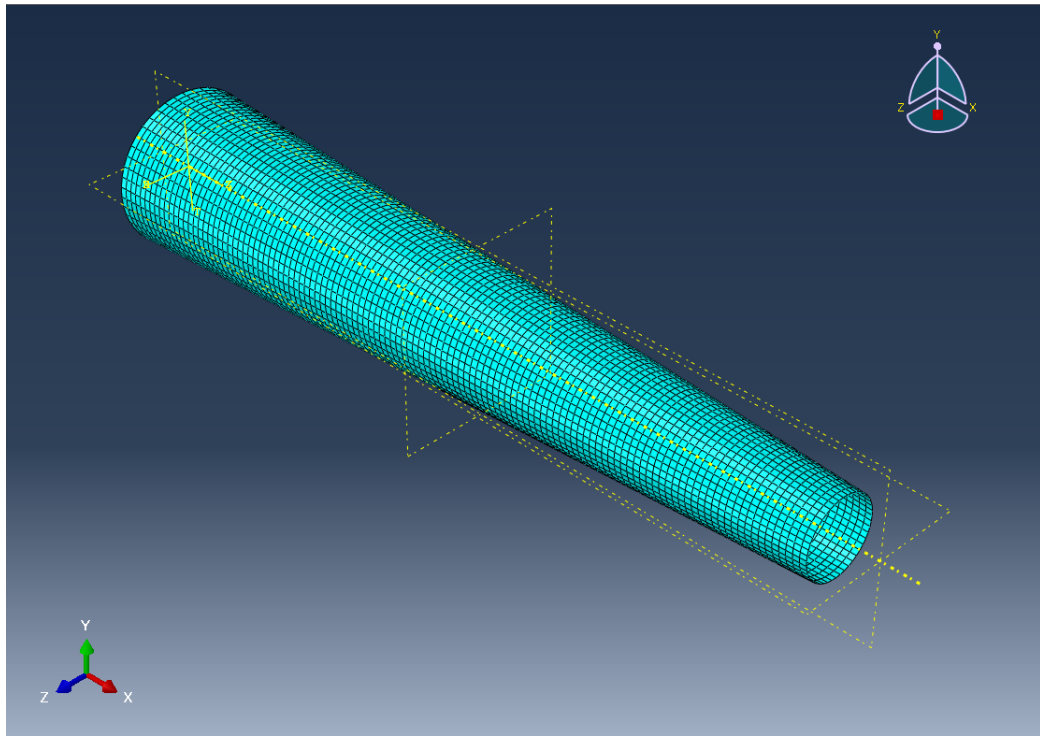


Figure 6.30: shell model of the hollow conical beam.

but are non-zero under the shear force and the bending moment loading cases. However, the intensity of such shear stresses is an order of magnitude smaller with respect to the normal stresses.

Again, it is evident the contribution of the shear-induced bending on the shear stresses in the “shear” loading case (Figure 6.32(f)). Starting from the tip, where no bending moment is present, the shear stresses $\sigma_{z\theta}$ can be calculated with the classical Jourawski formula. But moving along the beam, with the increase of the intensity of the shear-induced bending, the contribution of such component of the shear stresses arises and may become predominant.

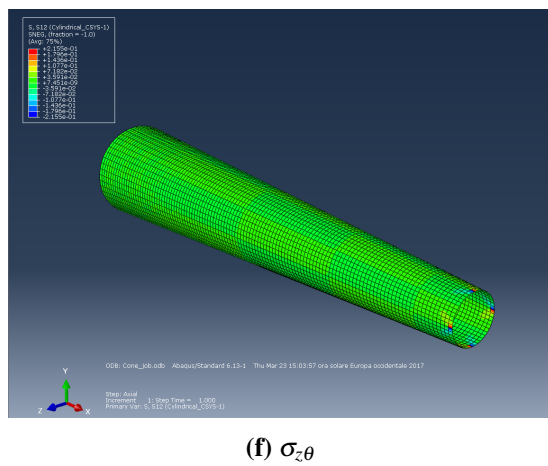
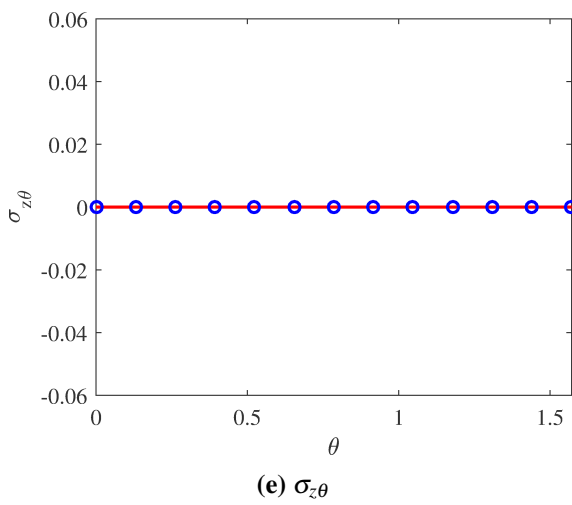
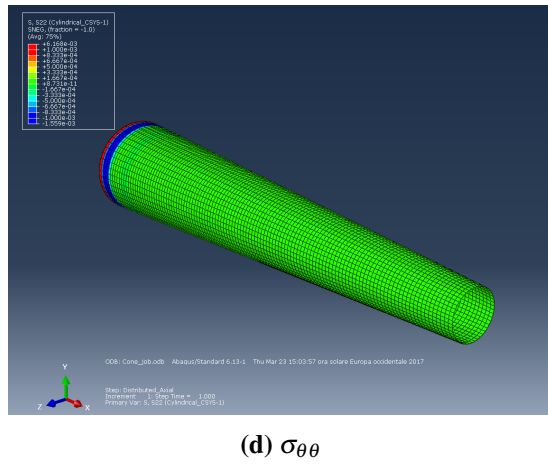
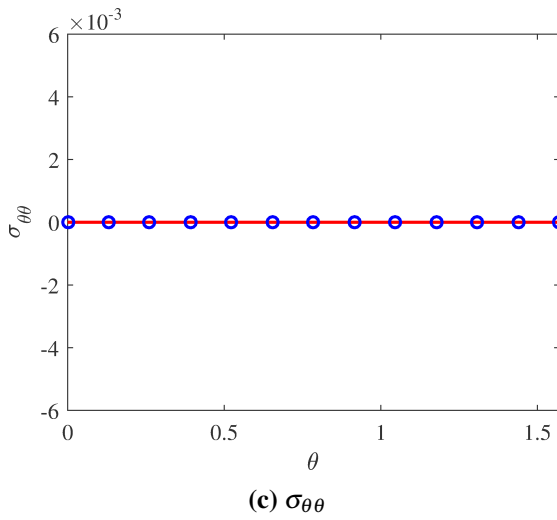
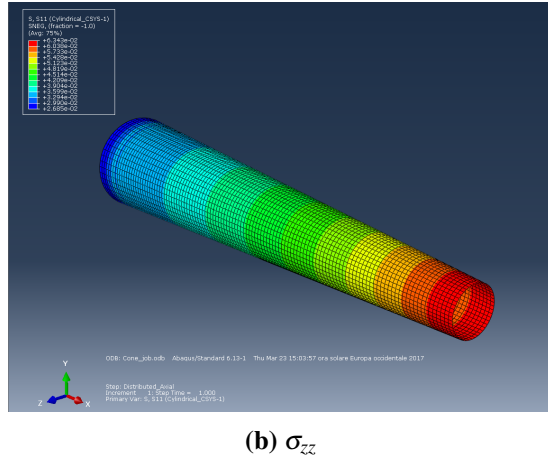
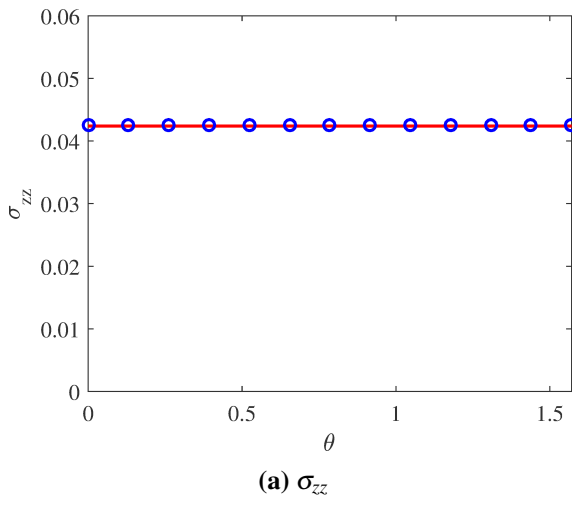
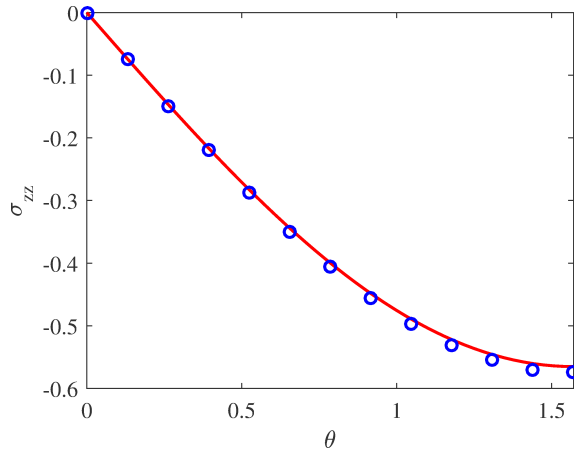
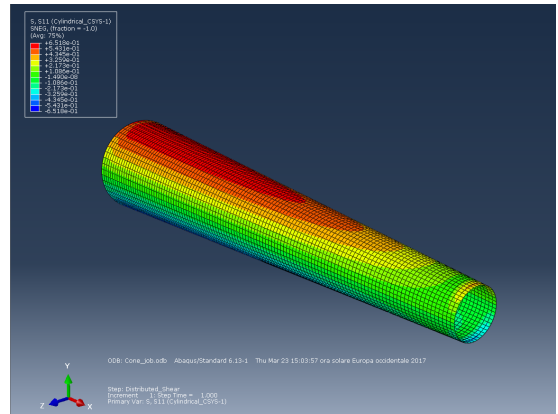


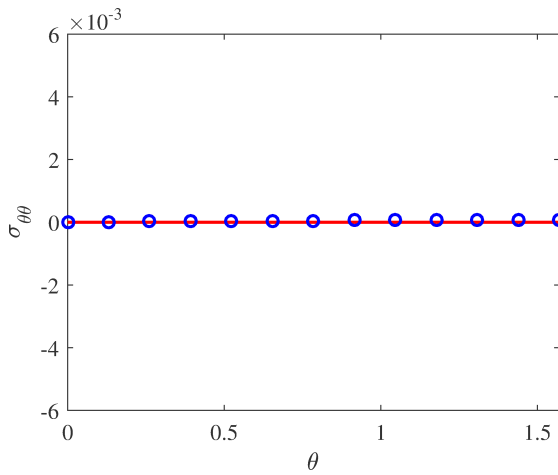
Figure 6.31: distribution of stresses on a quarter of the mid-span section for the “extension” loading case.



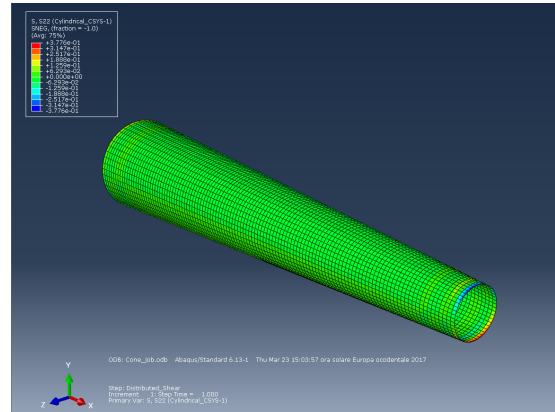
(a) σ_{zz}



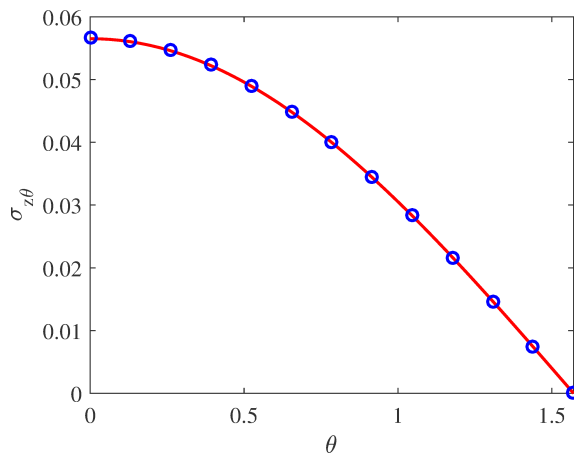
(b) σ_{zz}



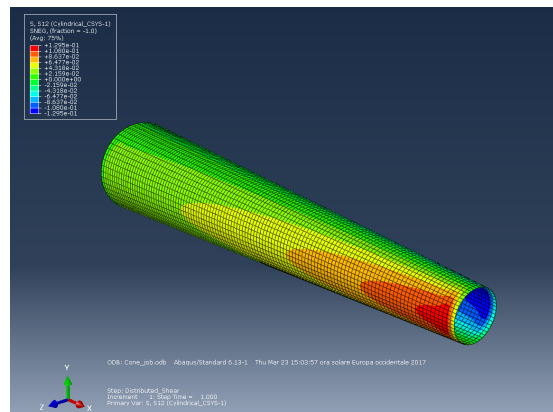
(c) $\sigma_{\theta\theta}$



(d) $\sigma_{\theta\theta}$



(e) $\sigma_{z\theta}$



(f) $\sigma_{z\theta}$

Figure 6.32: distribution of stresses on a quarter of the mid-span section for the “shear” loading case.

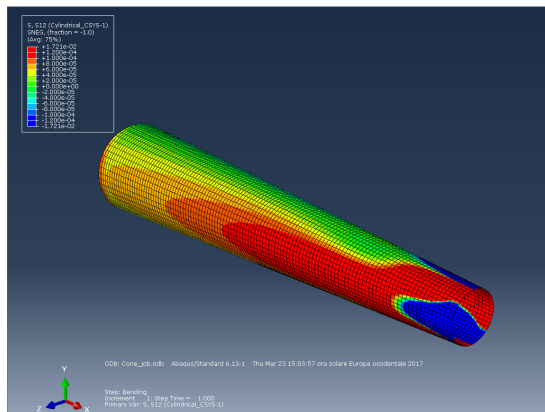
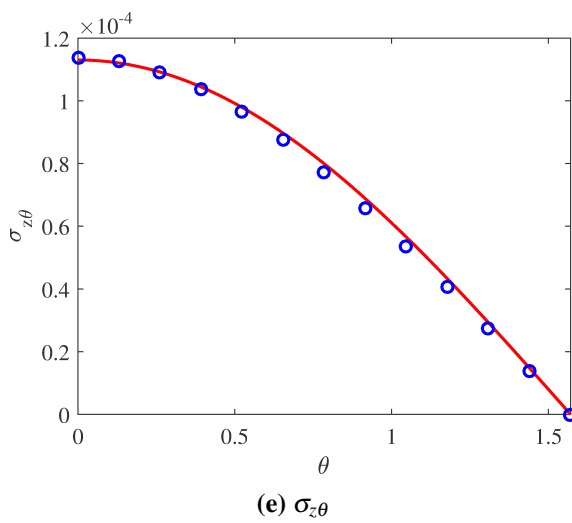
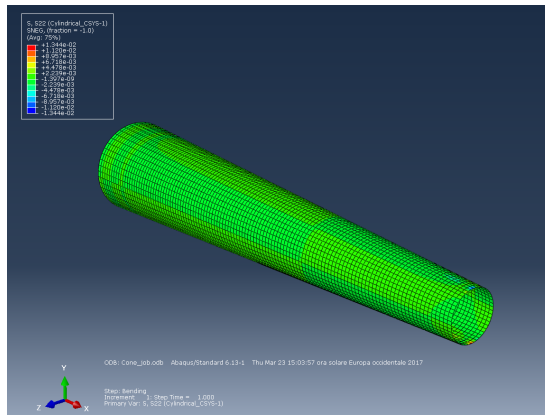
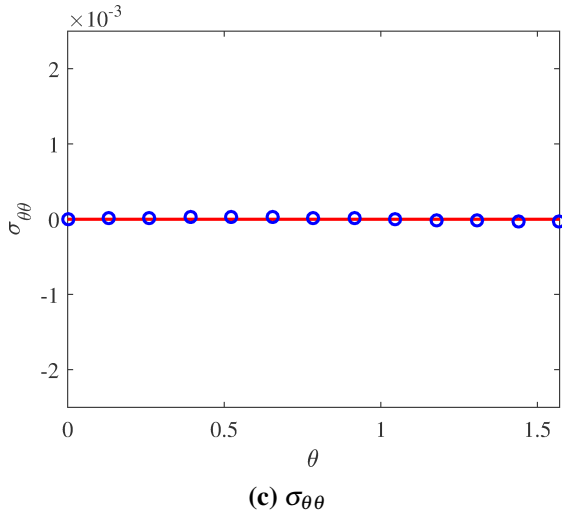
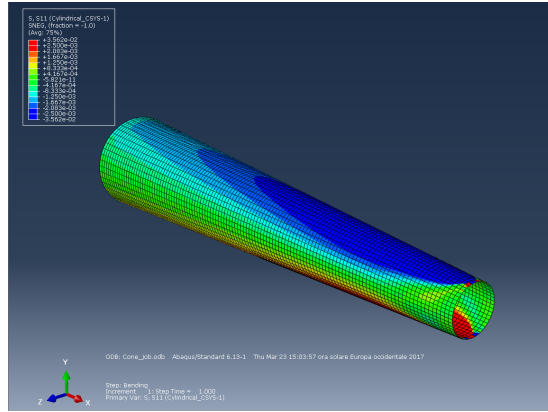
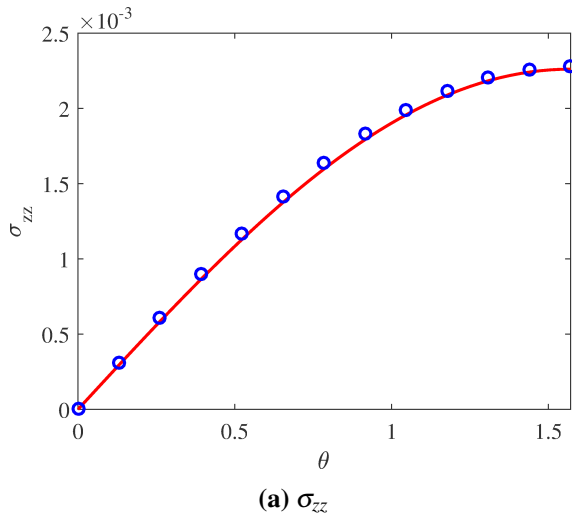


Figure 6.33: distribution of stresses on a quarter of the mid-span section for the “bending” loading case.

Chapter 7

10MW DTU wind turbine blade

Summary. In the present Chapter, a brief introduction to the 10MW DTU wind turbine blade is given, with a focus on the box girder of the blade. Such box girder is a non-linearly double tapered beam with curved centreline. A strategy to apply the extended shear stress formula to such a complex structural element is proposed here, and a comparison between the classical and extended shear stress formula, and the FE analysis results is shown.

7.1 DTU 10MW Reference Wind Turbine

The DTU 10MW Reference Wind Turbine was designed as part of the Light Rotor project, which was a cooperation between the Danish Technical University (DTU), and the industrial partner Vestas Wind Systems [Bak, Zahle, Bitsche, Kim, Yde, Henriksen, Natarajan, and Hansen, 2013a]. The need for such a reference was driven by the idea that it could have served as a comparison benchmark for future developments of the project itself. The turbine was designed with the most up-to-date yet conventional methods and techniques.

The main objective of the Light Rotor project was to suggest changes to the design of the blades to increase the stiffness and overall performance of the rotor, taking into account aerodynamic, aero-servo-elastic, and structural considerations. New airfoils and new aero-elastic as well as structural methods were developed. A great contribution of the project was the proposal for a systematic approach in the overall design process [Bak et al., 2013b].

Although the focus of the project was the rotor design, also the behaviour of the entire wind turbine, and the performance of the rotor in its interaction with the entire system had to be understood – including the structural dynamics of blades, tower and drive-train.

As the outcome of the design of such a reference turbine, a publicly available representative design was published, with the intent of being a basis for the next generation of rotors. A large amount of the public data available in Bak et al. [2013a] were of invaluable help in our research activity.

In Table 7.1, some of the key parameters of the DTU Reference Turbine are shown.

The blade is 89 m long and is reported to weigh about 41 tons [Bak et al., 2013a]. For our purposes, we will neglect the influence of the different materials, and will only focus on the geometry.

A model of the geometry of the blade in the form of an ABAQUS [Dassault Systèmes, 2013] FE shell model has been recovered from the data available. 8-node layered shell elements (ABAQUS element type S8R) were used (Figure 7.2). Unfortunately, it was possible to recover only the mesh of the model (*orphan mesh* of 95151 nodes and 32768 elements), and as a result the editing of the model with the ABAQUS software was somewhat limited.

In Figure 7.3 a representative section of the model is shown. The structural design is based on a classical approach of a load carrying box girder with two shear webs, adhesively bonded to the aerodynamic airfoil section.

In Figure 7.4, the thickness distributions along the length of the beam in the caps (or flanges) and in

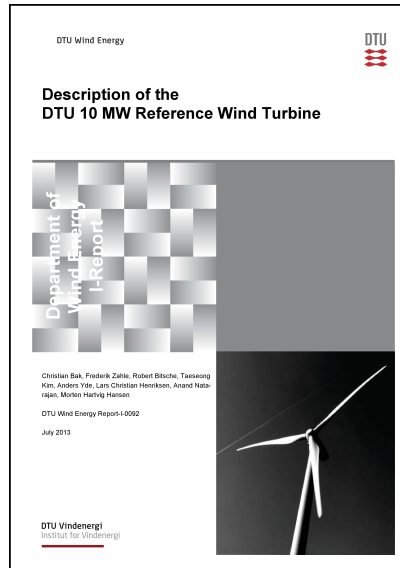


Figure 7.1: the front page of Bak et al. [2013a].

Parameter	Value
Number of blades	3
Rotor diameter	178.3 m
Hub height	119.0 m
Cut in wind speed	4.0 m/s
Cut out wind speed	25.0 m/s
Rated wind speed	11.4 m/s
Minimum rotor speed	6.0 rpm
Maximum rotor speed	9.6 rpm
Maximum tip speed	90.0 m/s
Rotor mass	227962 kg
Nacelle mass	446036 kg
Tower mass	628442 kg

Table 7.1: Key parameters of the DTU 10MW Reference Wind Turbine (from Bak et al. [2013a]).

the webs are shown, and two differed design approaches can be highlighted. In Figure 7.4(a), a smooth variation of the thickness characterise the flanges. Otherwise, the taper in thickness is often obtained by gradually adding, or removing, a small number of layers of material, so that steps are visible (Figure 7.4(b)). Despite being an important aspect of the design, which could introduce some sorta of weakness in the structure, this local aspect of the taper on thickness will be neglected in this thesis, and the investigation of the effect of a discontinuous thickness on the stresses could be the subject of future works.

To ease the structural analysis, the blade is subdivided in 27 cross sections. The software BECAS was used to identify the cross-sectional properties (mass, stiffnesses, location of the elastic and shear centres) of each cross section, and then to asses the stress distributions in 14 different load cases. In Figure 7.5 the list of those loading cases is shown. For each cross section, a detailed table listing the extreme internal forces – obtained by running the aeroelastic code HAWAC2 [Wang et al., 2016] – is given. Those values corresponds to the peak value of the three cross section force components and the three cross section moment components of a 600s time history simulation, and are given in the same row together with all the remaining component values at the same instant in time. In Figure 7.6, the table for the cross section 6 is shown as an example [Bak et al., 2013a].

A more detailed description of the geometry of the blade and of the design loading conditions is given

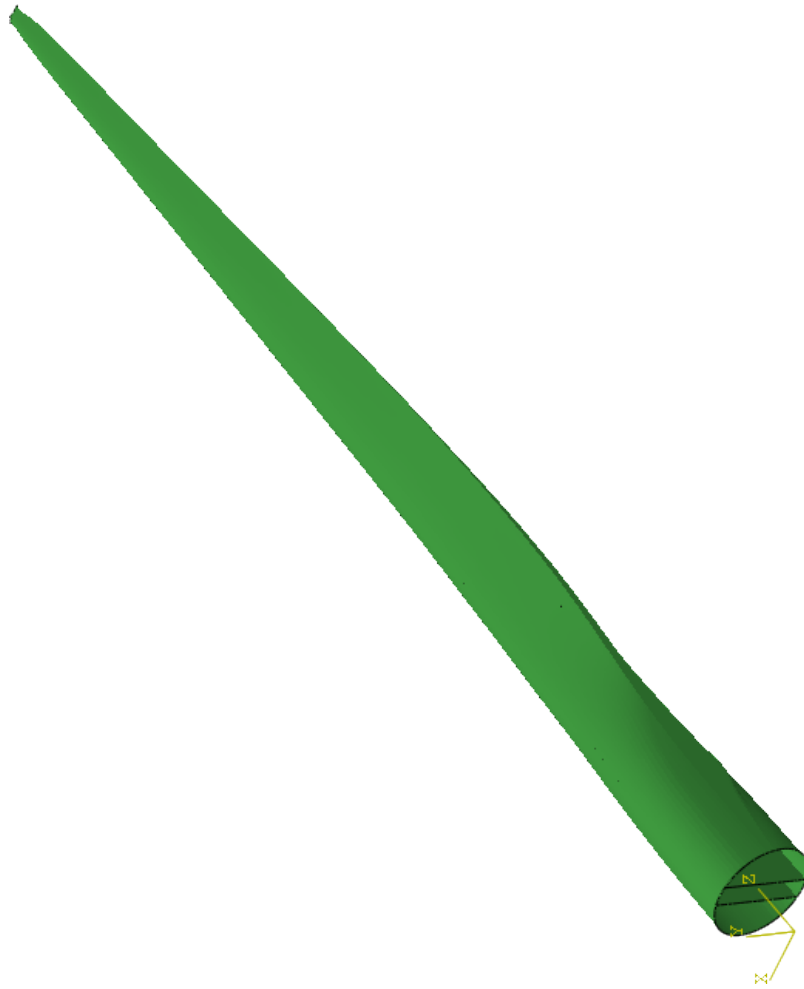


Figure 7.2: finite element shell model of the reference blade.

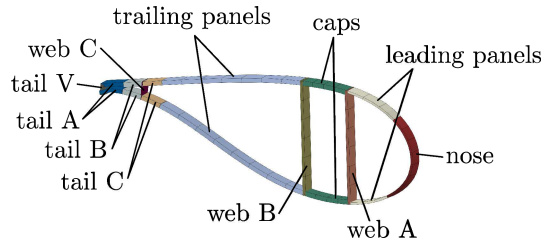


Figure 7.3: a representative section of the finite element model [Bak et al., 2013a].

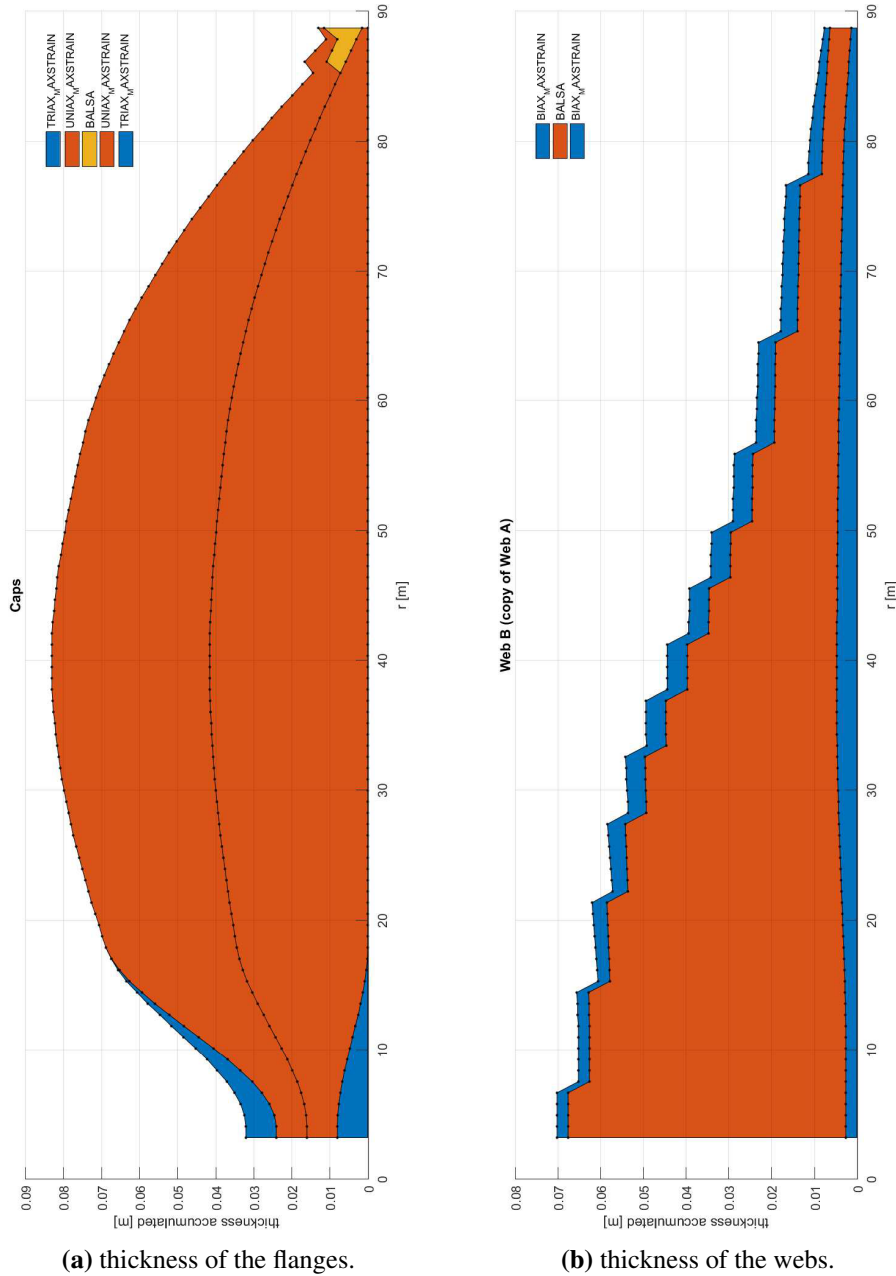


Figure 7.4: thickness distributions in flanges and webs [Bak et al., 2013a].

in Bak et al. [2013a], and here will be omitted.

Load case	DLC	Wind condition	Time (sec)	num. of turb. seed	Type of analysis	Safety factor	Other conditions
Power production	1.1	Normal Turbulence Model (NTM)	600	6	Ultimate	1.35	Extrapolation scheme is not applied. Therefore 1.35 as a safety factor is considered instead of 1.25.
	1.2	Normal Turbulence Model (NTM)	600	6	Fatigue	-	
	1.3	Extreme Turbulence Model (ETM)	600	6	Ultimate	1.35	
	1.4	Extreme coherent gust with direction change (ECD)	100	-	Ultimate	1.35	ECD is applied after transient period.
	1.5	Extreme Wind Shear (EWS)	100	-	Ultimate	1.35	EWS is applied after transient period.
Power production with fault	2.1	Normal Turbulence Model (NTM)	300	12	Ultimate	1.35	Electrical network is loss 10s after transient period.
	2.3	Extreme Operating Gust (EOG)	100	-	Ultimate	1.1	Electrical network is loss from 52s to 60s after transient period and EOG is applied just after transient period.
	2.4	Normal Turbulence Model (NTM)	600	6	Fatigue	-	$\pm 20^\circ$ are considered as the electrical system faults.
Start up	3.1	Normal Wind Profile Model (NWP)	300	-	Fatigue	-	Starting up the turbine 0.1s after transient period.
	3.2	Extreme Operating Gust (EOG)	100	-	Ultimate	1.35	Starting up the turbine 0.1s after transient period and EOG is applied 1s after transient period.
	3.3	Extreme Direction Change (EDC)	100	-	Ultimate	1.35	Starting up the turbine 0.1s after transient period and EDC is applied 1s after transient period.
Normal shut down	4.1	Normal Wind Profile Model (NWP)	100	-	Fatigue	-	Shutting down the turbine 10s after transient period.
	4.2	Extreme Operating Gust (EOG)	100	-	Ultimate	1.35	Shutting down the turbine 20s after transient period and EOG is applied just after transient period.
Emergency shut down	5.1	Normal Turbulence Model (NTM)	600	12	Ultimate	1.35	Shutting down the turbine 20s after transient period.
Parked (Idling)	6.1	Extreme Wind Speed Model (EWM), 50year recurrence period	600	6	Ultimate	1.35	$\pm 8^\circ$ with the turbulent extreme wind model are considered.
	6.2	Extreme Wind Speed Model (EWM), 50year recurrence period	600	6	Ultimate	1.1	It is assumed that the power for the control and yaw system is able to be back-up within 6 hours.
	6.3	Extreme Wind Speed Model (EWM), 1year recurrence period	600	6	Ultimate	1.35	$\pm 20^\circ$ with the turbulent extreme wind model are considered.
	6.4	Normal Turbulence Model (NTM)	600	6	Fatigue	-	Considered wind speed range is $5m/s \leq V_{hub} \leq 35m/s$.
Parked and fault condition	7.1	Extreme Wind Speed Model (EWM), 1year recurrence period	600	6	Ultimate	1.1	Wind direction is an equally increase of 30° .

where 100s is considered as a transient period.

Figure 7.5: the 14 load cases [Bak et al., 2013a].

	Load case	γ_F [-]	F_x [MN]	F_y [MN]	F_z [MN]	F_{res} [MN]	M_x [MNm]	M_y [MNm]	M_z [MNm]	M_{res} [Nm]	
F_x	max	dlc1.3	1.35	0.8121	0.7456	1.6027	1.1024	-13.6126	19.6475	0.2472	23.9025
	min	dlc1.3	1.35	-0.7267	0.0074	1.5903	0.7268	2.0122	-21.5182	-0.6676	21.6120
F_y	max	dlc1.3	1.35	0.6090	1.6115	1.2317	1.7228	-49.6688	13.8267	0.1799	51.5574
	min	dlc6.2	1.1	-0.0027	-1.3241	-0.4548	1.3241	37.9742	1.4133	0.6422	38.0005
F_z	max	dlc2.1	1.35	-0.3041	0.5581	2.6109	0.6356	-20.9757	-8.6780	-0.1767	22.6999
	min	dlc6.2	1.1	-0.0611	-0.6252	-0.6952	0.6282	26.5666	-0.9441	0.3448	26.5834
F_{res}	max	dlc1.3	1.35	0.7492	1.5656	1.5220	1.7357	-38.4433	18.0696	0.2588	42.4782
M_x	max	dlc6.2	1.1	0.1017	-1.3103	0.1660	1.3143	38.8238	4.7536	0.7679	39.1138
	min	dlc1.3	1.35	0.1745	1.3840	1.0163	1.3949	-55.3232	7.0217	0.3944	55.7670
M_y	max	dlc2.1	1.35	0.7552	-0.0095	1.5056	0.7553	13.1137	23.6727	0.6577	27.0623
	min	dlc1.3	1.35	-0.7227	-0.0101	1.5954	0.7227	3.0724	-21.5404	-0.6843	21.7584
M_z	max	dlc2.3	1.1	0.6201	-0.4436	1.5459	0.7624	25.2079	20.4328	1.0317	32.4490
	min	dlc1.3	1.35	-0.4601	0.0173	1.8237	0.4604	6.7589	-17.3205	-0.9567	18.5925
M_{res}	max	dlc1.3	1.35	0.1792	1.3878	1.0163	1.3993	-55.3232	7.1420	0.4202	55.7823

Figure 7.6: result of the extreme load evaluation for section 6 ($z = 13.2$ m) [Bak et al., 2013a].

7.2 Simplification of the geometry

In order to apply the proposed approach for the assessment of the influence of taper on the stress distribution (Chapter 5), we were forced to extract from the complex blade geometry the sole box girder shape with the aim of applying the results discussed in Chapter 6 (and in particular in Section 6.2.3).

Moreover, in the following we will focus our attention on the two cross sections of the box girder which show the higher vertical and horizontal taper – cross section 6 ($z = 13.2$ m) and cross section 25 ($z = 86.3$ m) respectively – and on one of the reference cross sections which is close to the mid-span of the blade – cross section 16 ($z = 43.0$ m).

In order to extract the box girder geometry, the leading and trailing panels have been removed from the finite element model. This was made under the hypothesis that the relative stiffness of those elements in the cross section is much smaller than the stiffness of flanges and webs, and consequently their contribution to the distribution of stresses is relatively small when compared to that of the box girder under the loading cases which will be investigated. Figure 7.7 shows the FE model of the tapered box girder of the 10MW wind turbine blade, as it has been obtained after the aerodynamic shell “removal”. There the reference cross sections are also highlighted.

In Figure 7.8, all the cross sections of the blade are depicted, as well as the corresponding box girder cross sections. The small inverted L-shaped symbols locate the position of the global z -axis with respect to each cross section. It is evident that the centreline of such box girder is not a straight line. We expect that this will greatly affect the results of the current extended shear stress formula. In fact, among the hypotheses made while deriving the extended shear stress formula there is the assumption that the centreline of the beam must be straight. Even for the simple loading cases that will be analysed later on, we expect that the stress distribution in the box girder modelled with the FE may even show significant differences with those derived analytically from the extended shear stress formula.

Moreover, the cross sections of the box girder – which are obtained by simply removing the leading and trailing panels – are still not suitable for attempting the application of the shear stress formula, being that they are not straight but slightly curved (in particular, the flanges of a real box girder show a slight curvature). For that reason, we decided to further simplify the geometry, taking into account equivalent thin-walled rectangular cross sections inscribed in those of the box girder. We expect that this difference will also bring some variations in the comparison between the FE analysis of the box girder and the approximated analytical solution.

Once the dimensions of the rectangular cross sections are determined, the taper angles should be evaluated.

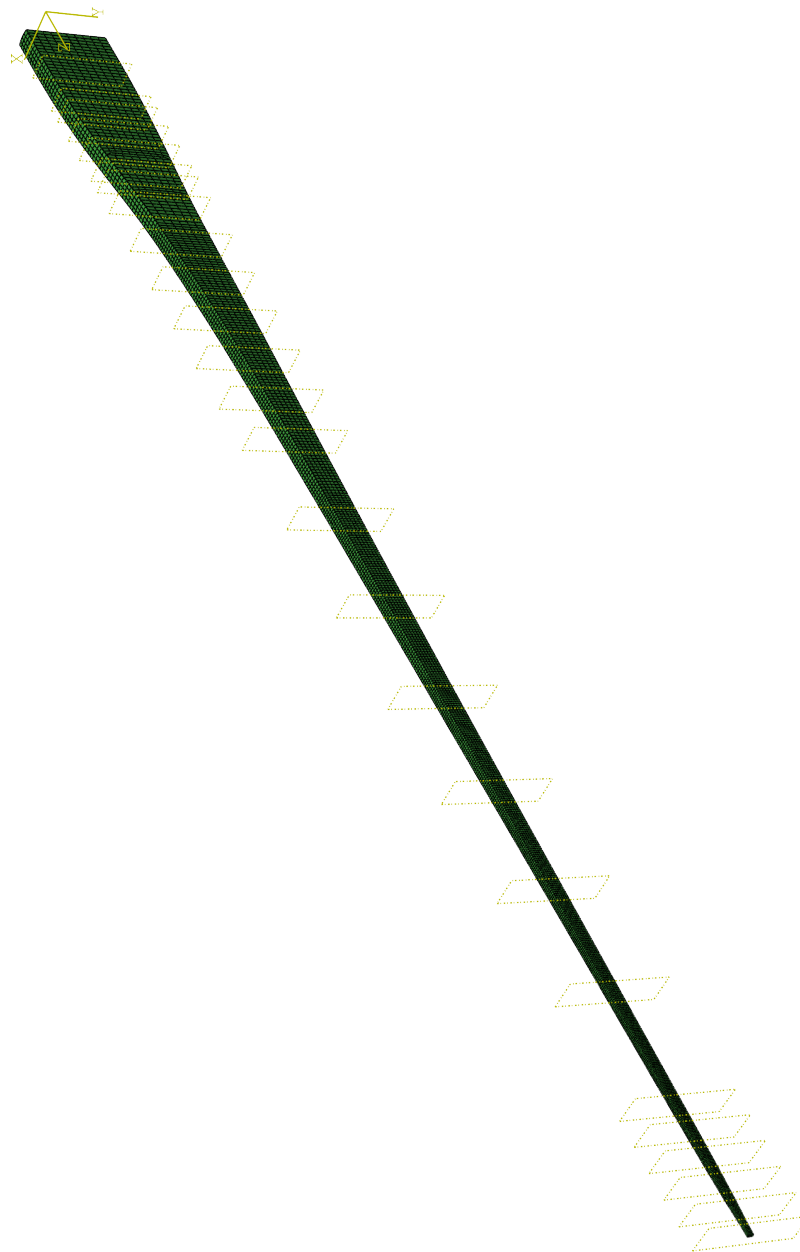


Figure 7.7: the FE model of the box girder has it has been analysed. The boxes in yellow dashed line identify the position of the cross sections.

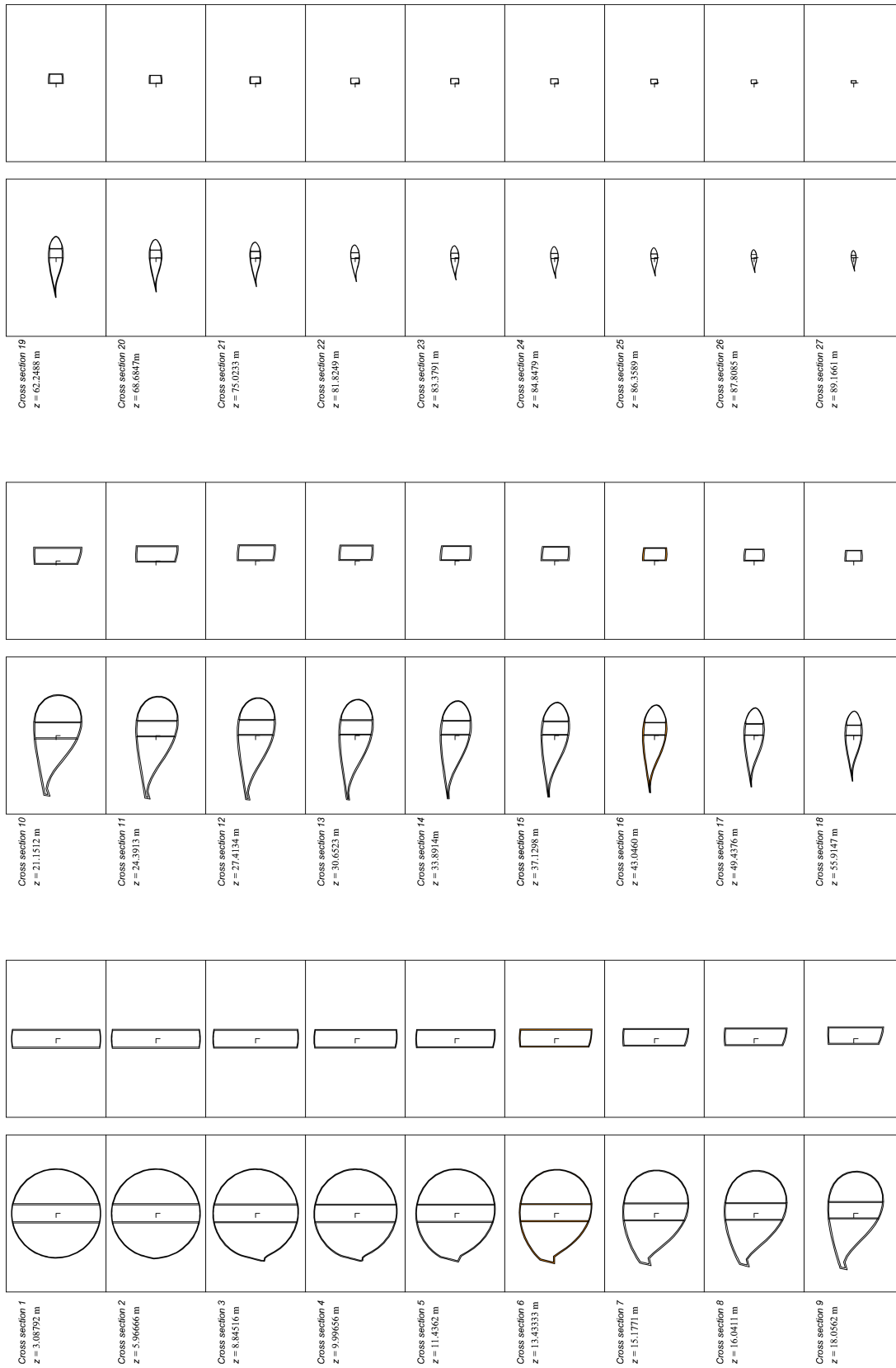


Figure 7.8: the finite element model of the box girder.

It is noteworthy that adopting cross sections normal to the global z -axis for a curved beam is not theoretically acceptable. Euler-Bernoulli's cross sections must be orthogonal to the centreline of the beam, where the centreline is defined as the locus of the centres of mass of the cross sections themselves [Timoshenko and Goodier, 1951]. Thus, once the centreline and the cross sections are given, the definition of *beam* is an easy task (see Section 2.2). On the contrary, to unequivocally identify the centreline and the cross sections of a given curved beam is not trivial as well, if not even impossible [Boley, 1963]. Thus, from a particular point of view, adopting globally parallel cross sections eases various aspects in the theoretical development [Balduzzi et al., 2016], design, and production [Hau, 2013].

The curvature of the beam we are analysing is not extremely significant, and when dealing with the assessment of the normal stresses, not assuming Euler-Bernoulli's cross sections could appear to be a reasonable choice. However, the shear stresses introduced by taper (whose intensity may be significantly lower in comparison with the normal stresses) may be more easily affected by such an error, and further investigations will be necessary in the future.

Thus, here we will assume that the centreline is the locus of the centres of the cross sections normal to the global z -axis.

We can now define the angles of taper as those angles that the local upper and lower surfaces of the beam form with the centreline. In particular, we state that, for i -th section of the discretised beam,

$$\alpha_x = \frac{\alpha_{x1} - \alpha_{x2}}{2}, \quad (7.1)$$

where α_{x1} and α_{x2} are defined as follows:

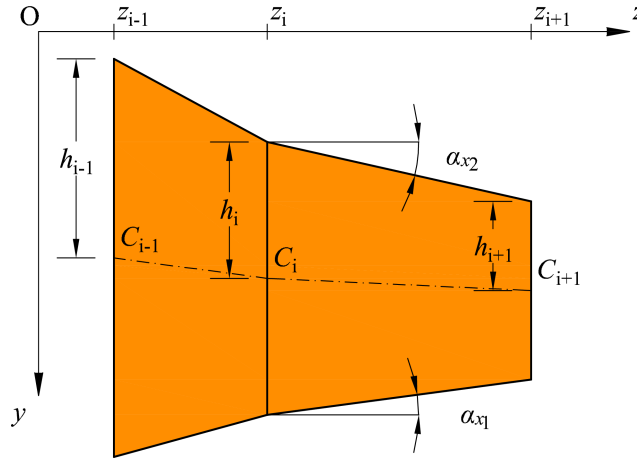


Figure 7.9: taper angles of a discretised tapered beam.

$$\alpha_{x1} = \frac{1}{2} \left[\arctan \left(\frac{(Y_{C_{i+1}} - h_{i+1}) - (Y_{C_i} - h_i)}{z_{i+1} - z_i} \right) + \arctan \left(\frac{(Y_{C_i} - h_i) - (Y_{C_{i-1}} - h_{i-1})}{z_i - z_{i-1}} \right) \right], \quad (7.2)$$

and

$$\alpha_{x2} = \frac{1}{2} \left[\arctan \left(\frac{(Y_{C_{i+1}} + h_{i+1}) - (Y_{C_i} + h_i)}{z_{i+1} - z_i} \right) + \arctan \left(\frac{(Y_{C_i} + h_i) - (Y_{C_{i-1}} + h_{i-1})}{z_i - z_{i-1}} \right) \right]. \quad (7.3)$$

All this asserts that the centreline of each element of beam between two cross sections is the bisector of the the upper and lower surfaces. At each cross section, the upper and lower surface angles are given by the mean of the angles of the surface preceding and following the section (Figure 7.9). Analogous considerations are also made for the angle of horizontal taper.

In Table 7.2, the geometrical values of the three sections which have been taken into account are shown. The position of the centre of the sections refers to a global coordinate system located at the root, and with respect of which the cross section 1 (circular) is centred. The centre of the tip cross section has the following coordinates: $X_C = -67.8$ mm and $Y_C = 14.3$ mm.

	Section 6	Section 16	Section 25
z position	13.2 m	43 m	86.3 m
Width, B	1025.3 mm	744.1 mm	279.8 mm
Height, H	4395.9 mm	1389.6 mm	396.9 mm
Web thickness, t_w	64.6 mm	40.6 mm	6.1 mm
Flange thickness, t_f	56.2 mm	81.8 mm	9.7 mm
Centre of mass, X_C	-35.6 mm	-403.6 mm	-88.3 mm
Y_C	71.8 mm	43.9 mm	-20.8 mm
Angle of vertical taper, α_x	5.96°	1.1°	1.22°
Angle of horizontal taper, α_y	0.26°	0.29°	0.83°

Table 7.2: geometry of the equivalent rectangular cross sections

7.3 Numerical results

7.3.1 Definition of the load cases

We introduce three load cases:

- a concentrated force F_z applied at the centre of the tip cross section in the z -direction (“axial force” loading condition);
- a concentrated force F_y applied at the centre of the tip cross section in the y -direction (“shear force” loading condition);
- a couple \bar{M} applied at the tip cross section in the x -direction (“bending moment” loading condition).

It is noteworthy that the initial curvature of the beam complicates the distribution of the internal forces in the blade, and that even if we are applying apparently simple loading conditions, the behaviour of the beam will not be in any case “pure”. For example, applying the F_z force at the tip will result in an eccentric normal force on the cross sections (due to the relative position of the respective centres of mass). Thus, in this case both axial force and bending moments will result on the cross sections. For the same reason, a load applied to the centre of mass of the tip cross section may introduce a certain amount of torsional moment on the other sections, and this could affect the results to a certain extent.

In Figure 7.10, the plots of the internal forces along the length of the beam in the “axial force” loading condition are shown. In Figures 7.11 and 7.12 the analogous plots are shown for the other two loading conditions. All these plots have been drawn under the hypothesis that the centreline of the beam is straight and parallel to the z -axis. In the plots, the reference cross sections z -coordinate have been highlighted with vertical dashed lines.

	Q_x	Q_y	N	M_x	M_y	M_z
Generic section	0	0	F_z	$F_z(Y_{C_{27}} - Y_{C_6})$	$F_z(X_{C_{27}} - X_{C_6})$	0
Section 6	0	0	1000 N	-86094 N mm	-32293 N mm	0
Section 16	0	0	1000 N	-58177 N mm	335796 N mm	0
Section 25	0	0	1000 N	6485 N mm	20485 N mm	0

Table 7.3: “axial force” loading condition.

In Table 7.3, Table 7.4, and Table 7.5 the details of the internal forces acting on the Sections 6, 16, and 25 for the different loading cases presented are listed.

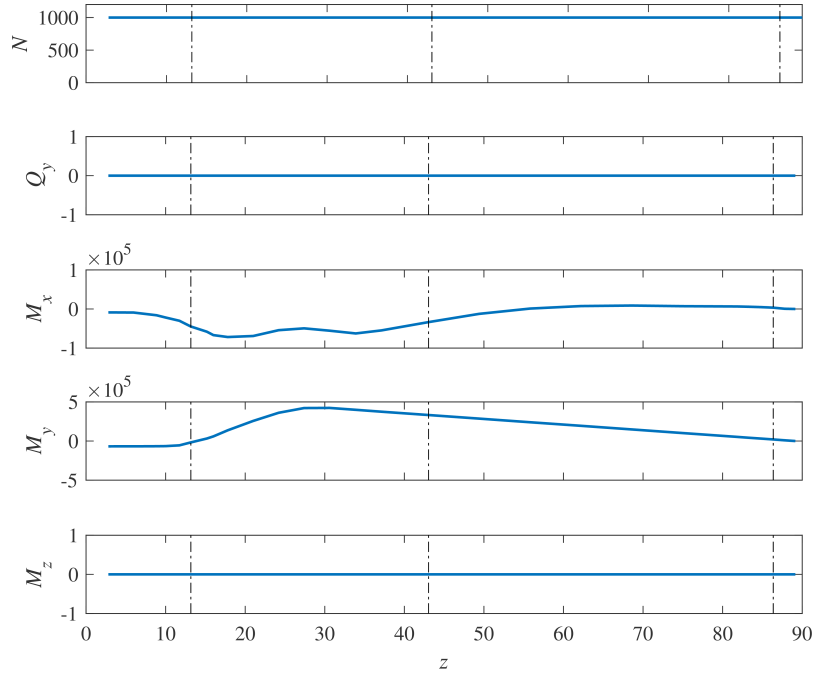


Figure 7.10: internal forces for the “axial force” loading condition.

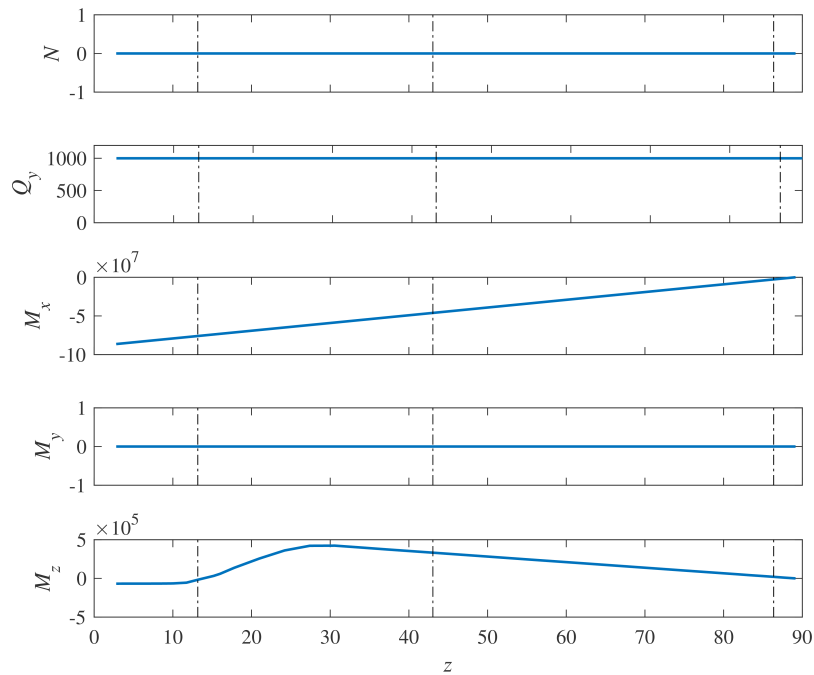


Figure 7.11: internal forces for the “shear force” loading condition.

7.3.2 Finite element analysis

The model shown in Figure 7.7 has been subjected to the three load cases discussed above. In Figure 7.13, Figure 7.14 and Figure 7.15 the results of the linear analysis are shown.

The “axial force” loading condition shows some unexpected results. In particular, a linear distribution of the normal stresses σ_{zz} is evident on the web, and close to Section 6 a slight deviation from linearity is also present (Figure 7.13(a)). This anomaly, most likely induced by the curvature of the centreline and the relative position of the centres of mass of the section, also induce unexpected normal stresses σ_{yy} (Figure 7.13(b)) and shear stresses (Figure 7.13(b)) when an axial force in the z -direction is applied at

	Q_x	Q_y	N	M_x	M_y	M_z
Generic section	0	F_y	0	$-Q_y(z_{27} - z_6)$	0	$Q_y(X_{C_{27}} - X_{C_6})$
Section 6	0	1000N	0	-75972000N mm	0	-32293 N mm
Section 16	0	1000N	0	-46090000N mm	0	335796 N mm
Section 25	0	1000N	0	-2777000N mm	0	20485 N mm

Table 7.4: “shear force” loading condition.

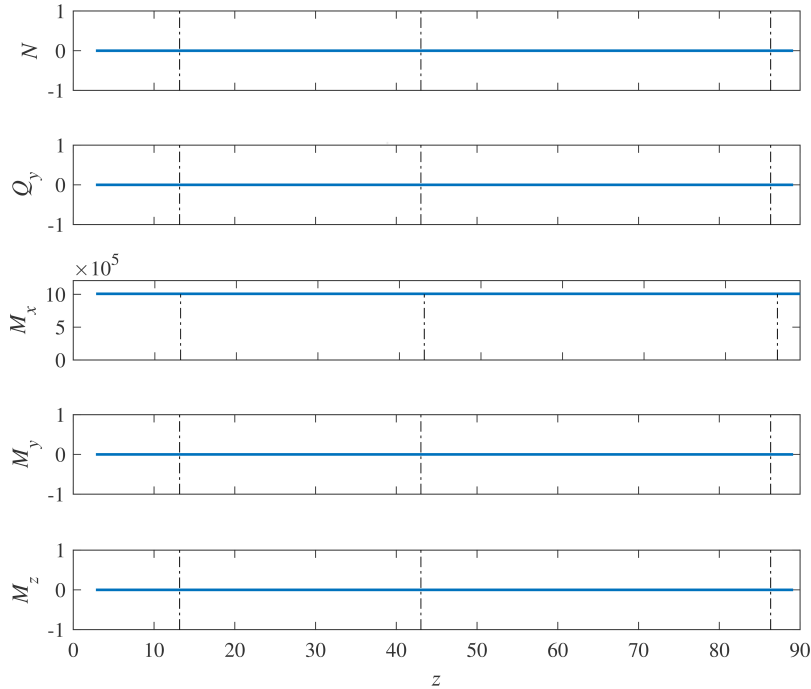


Figure 7.12: internal forces for the “bending moment” loading condition.

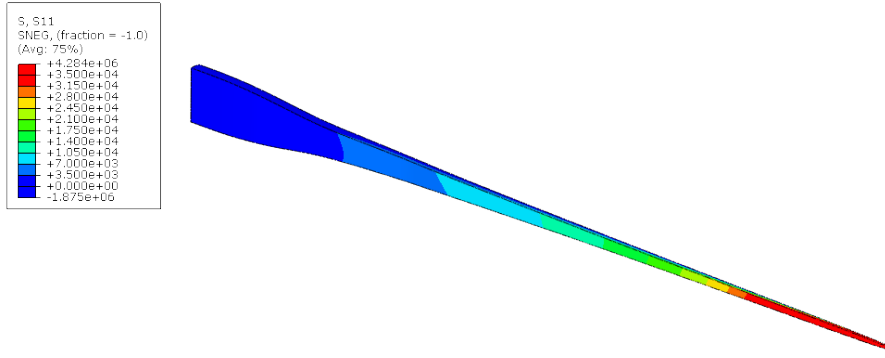
the tip.

Less unexpected are the other results (Figures 7.14 and 7.15), concerning the “shear force” and the “bending moment” loading conditions. In particular, in Figure 7.14(c), the shear stresses σ_{zy} on the web show an interesting changing distribution on the cross sections, which appear to also depend on the local angle of taper.

Moreover, by comparing Figure 7.14(c) with Figure 7.15(c), the increasing contribution of the shear-induced bending on the shear stresses – of the “shear force” loading condition – is also appreciable. In fact on the different plots – even if the values are of course different – the same trend is noticeable for the σ_{zy} .

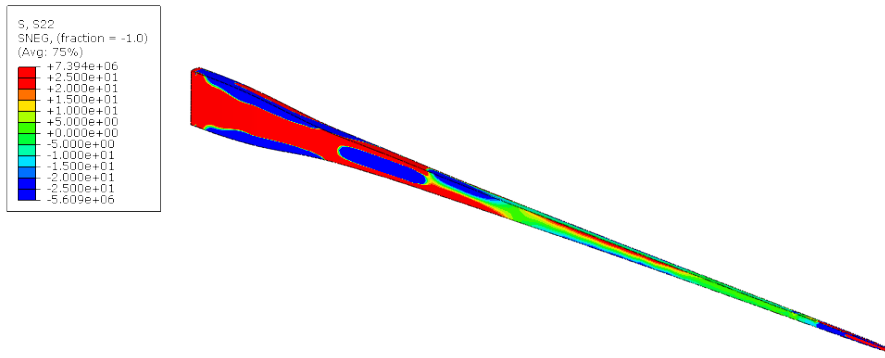
	Q_x	Q_y	N	M_x	M_y	M_z
Generic section	0	0	0	\bar{M}	0	0
Section 6	0	0	0	1007900N mm	0	0
Section 16	0	0	0	1007900N mm	0	0
Section 25	0	0	0	1007900N mm	0	0

Table 7.5: “bending moment” loading condition.



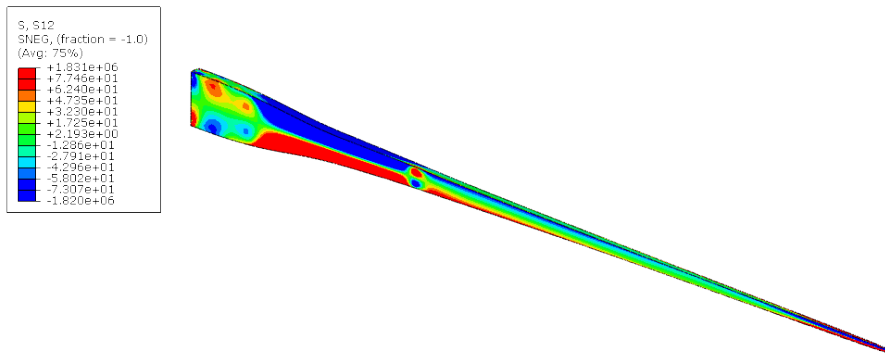
Y ODB: Blade_job.odb Abaqus/Standard 6.13-1 Thu Nov 23 15:57:10 ora solare Europa occidentale 2017
 X Step: Axial_perturbation
 Z Increment: 1; Step Time = 2.2200E-16
 Primary Var: S, S11

(a) σ_{zz}



Y ODB: Blade_job.odb Abaqus/Standard 6.13-1 Thu Nov 23 15:57:10 ora solare Europa occidentale 2017
 X Step: Axial_perturbation
 Z Increment: 1; Step Time = 2.2200E-16
 Primary Var: S, S22

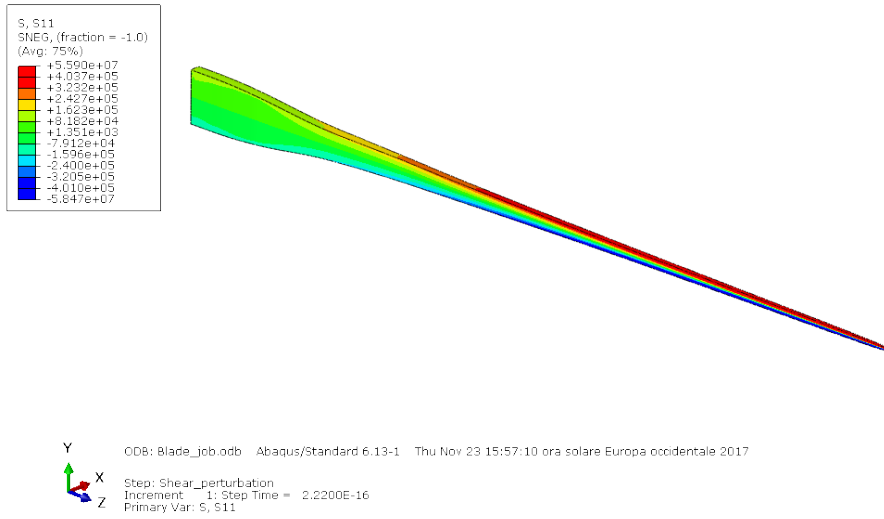
(b) σ_{yy} in the webs and σ_{xx} in the flanges



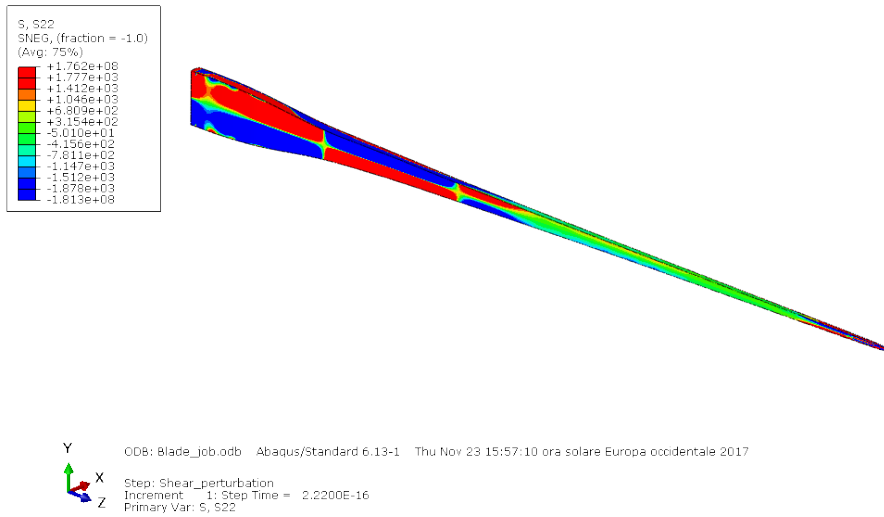
Y ODB: Blade_job.odb Abaqus/Standard 6.13-1 Thu Nov 23 15:57:10 ora solare Europa occidentale 2017
 X Step: Axial_perturbation
 Z Increment: 1; Step Time = 2.2200E-16
 Primary Var: S, S12

(c) σ_{zx} in the webs and σ_{zy} in the flanges

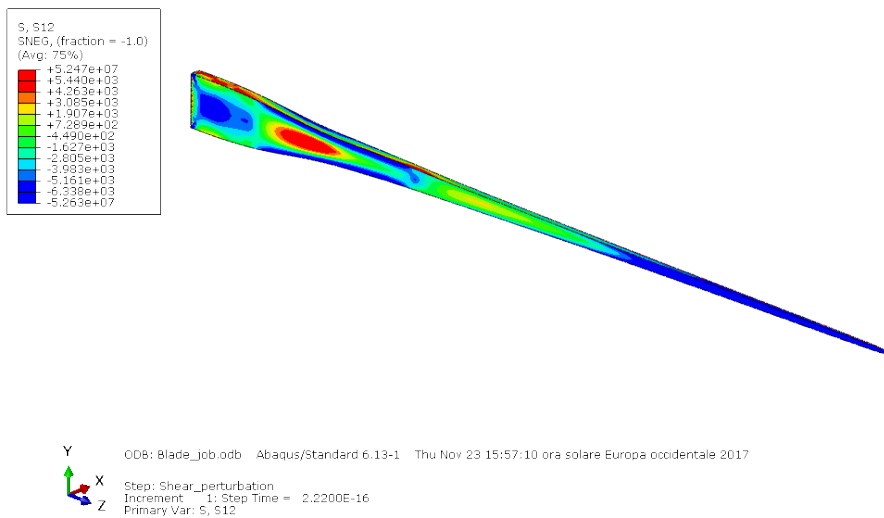
Figure 7.13: FE analysis results for the “axial force” loading condition.



(a) σ_{zz}

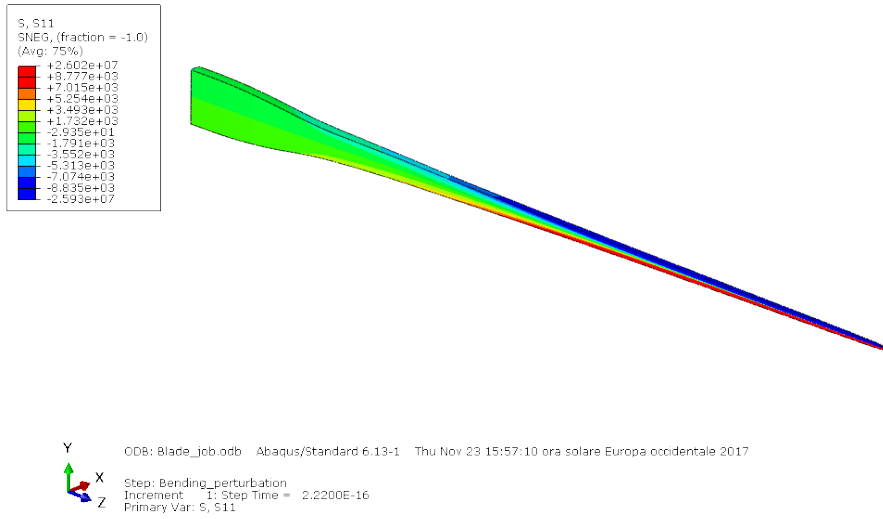


(b) σ_{yy} in the webs and σ_{xx} in the flanges

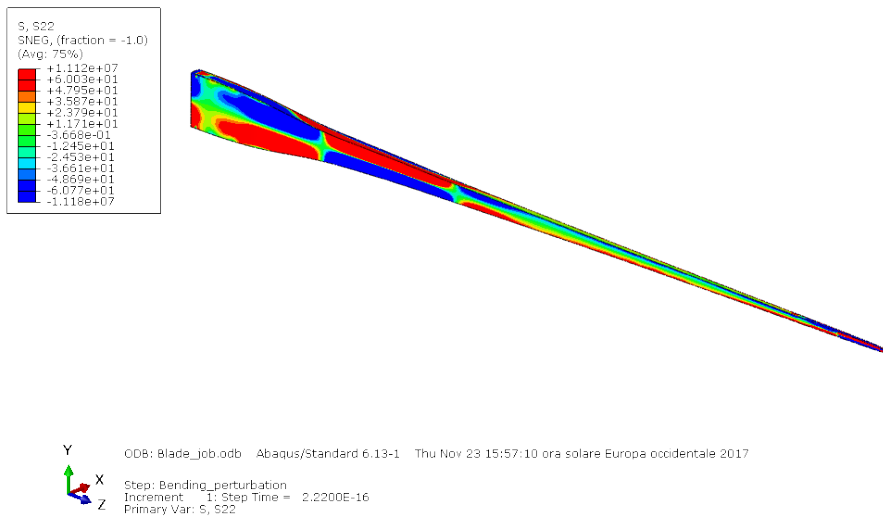


(c) σ_{xx} in the webs and σ_{yy} in the flanges

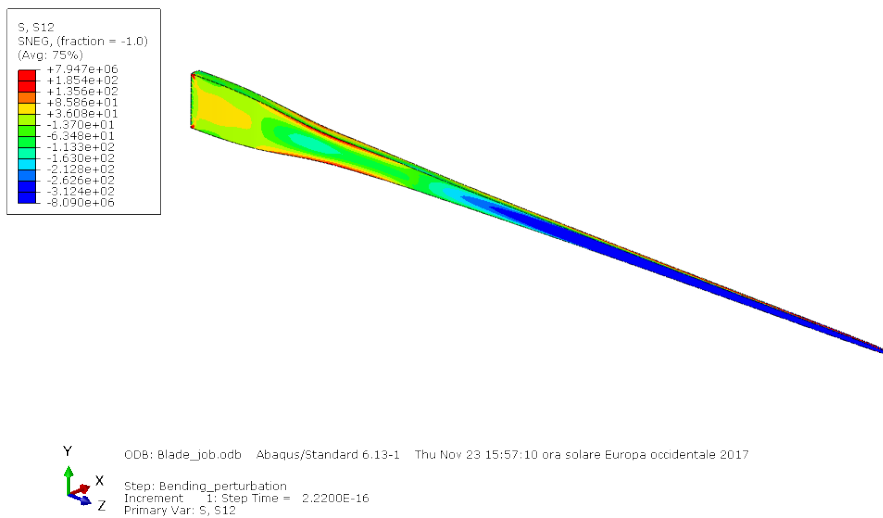
Figure 7.14: FE analysis results for the “shear force” loading condition.



(a) σ_{zz}



(b) σ_{yy} in the webs and σ_{xx} in the flanges



(c) σ_{zx} in the webs and σ_{yy} in the flanges

Figure 7.15: FE analysis results for the “bending moment” loading condition.

“Axial force” loading condition

With regard to the “axial force” loading condition, the results of the linear analysis are shown in Figure 7.17 (Section 6), Figure 7.18 (Section 16) and Figure 7.19 (Section 25). Here the FE analysis of the box girder (blue hollow dots), the application of the extended shear stress formula (red continuous line), and the results predicted by the classical Jourawski formula (dashed green line) are compared. In the plots of the present Figure, and in those that follow, the abscissa s (see Figure 7.16) has been used.

Again, the “axial force” loading condition (Figures 7.17, 7.18 and 7.19) shows some anomalies that could be justified by the hypotheses made on the centreline of the beam. In particular, the axial force applied to the tip cross section could have introduced small torsional contributions that are not taken into account by the analytical derivation of the extended shear stress formula. Also, it is to be noted that the shear stresses induced by an axial force have usually proven to be extremely small, and could be easily surmounted by those torsional contributions). More investigations in the future will be necessary.

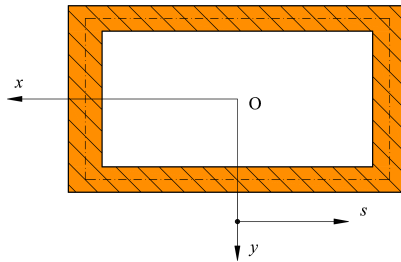


Figure 7.16: definition of an abscissa that follows the mid-line of the cross section and that rotates anticlockwise.

“Shear force” loading condition

With regard to the “shear force” loading condition, the results of the analysis are shown in Figure 7.20 (Section 6), Figure 7.21 (Section 16) and Figure 7.22 (Section 25).

These results show a very good agreement between the FE and the analytical extended shear stress formula. The small discrepancies are imputable to the slight differences in the sizes and shape of the cross section used for the analytical computations.

Moreover, the classical approach to prismatic beams (dashed green line) clearly leads to erroneous prediction of the shear stresses for the cases presented here (Figure 7.20(b), 7.21(b) and 7.22(b)).

“Bending moment” loading condition

With regard to the “bending moment” loading condition, the results of the analysis are shown in Figure 7.23 (Section 6), Figure 7.24 (Section 16) and Figure 7.25 (Section 25).

The classical approach to prismatic beams (dashed green line) predicts that no shear stresses are present when a bending moment is applied. For the cases presented here, this is evidently not the case in tapered beams (Figure 7.23(b), 7.24(b) and 7.25(b)).

7.3.3 Comments on the results

The extended shear stress formula proposed in Chapter 5 has been tested on a very complex geometry like the one shown in Figure 7.7 at 137. In order to allow us to do so, some important approximations had to be carried out.

First, the cross section of the beam must be symmetric but this is not the case in the tapered box girder of the DTU 10MW Reference Wind Turbine, as well as for general wind turbine blades. Despite the fact that we regularised the shape of the cross section and found a reasonable equivalent thin walled rectangular section, many differences are evident. First of all, the flanges of the box girder of the blade are

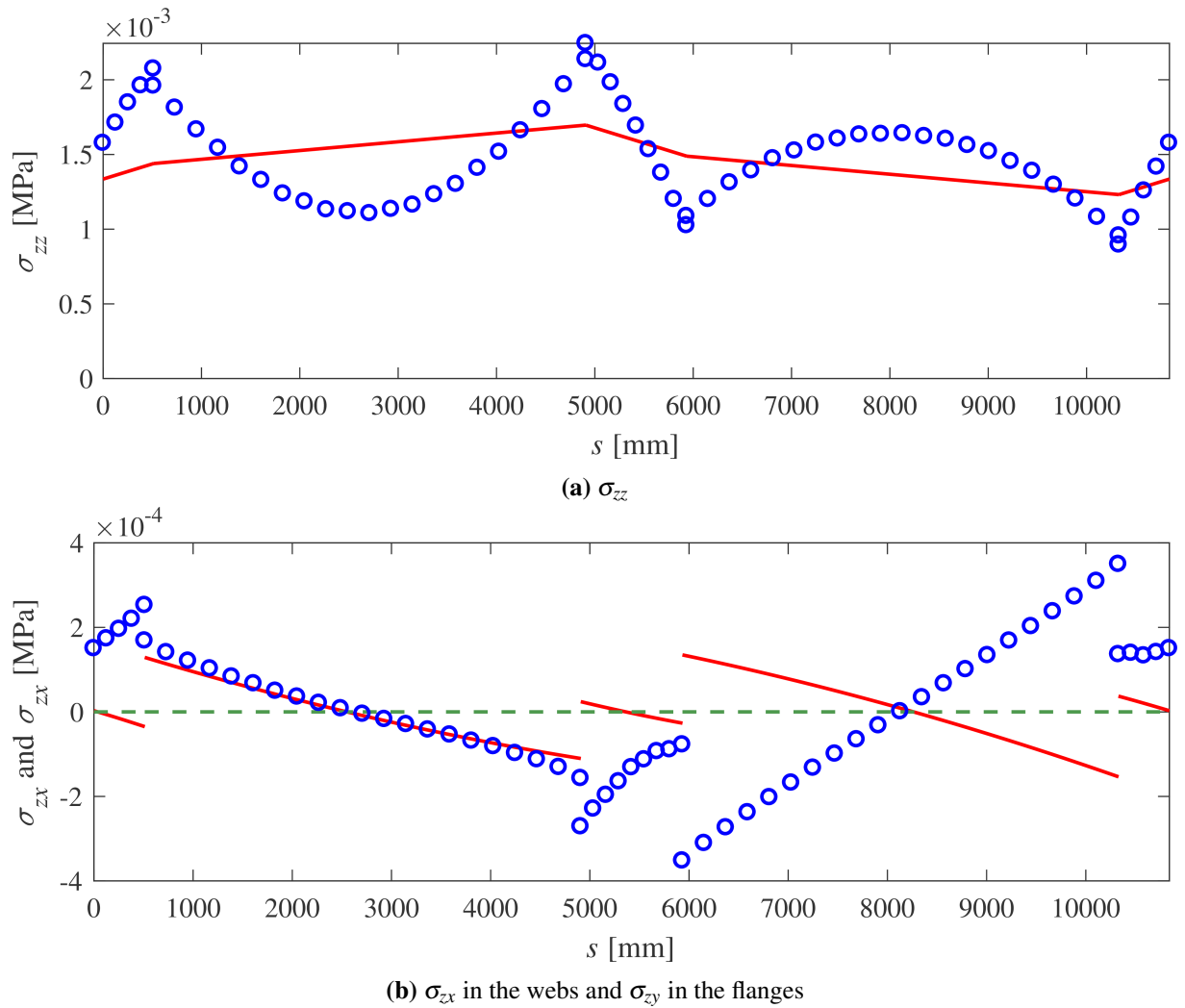


Figure 7.17: stresses in Section 6 for the “axial force” loading condition: extended shear stress formula (red line); FE analysis (blue dots); Jourawski’s shear stress formula (green dashed line).

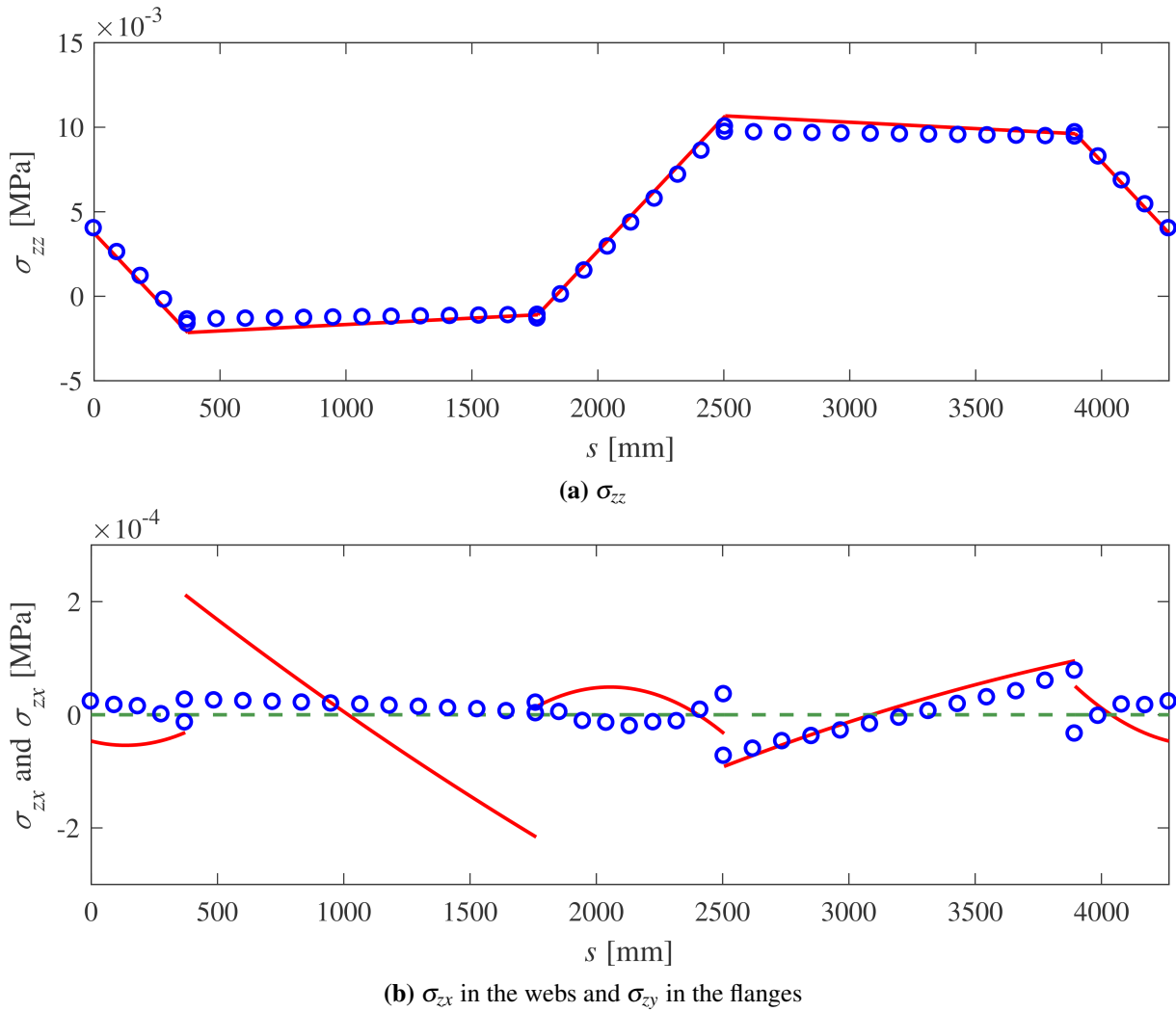


Figure 7.18: stresses in Section 16 for the “axial force” loading condition: extended shear stress formula (red line); FE analysis (blue dots); Jourawski’s shear stress formula (green dashed line).

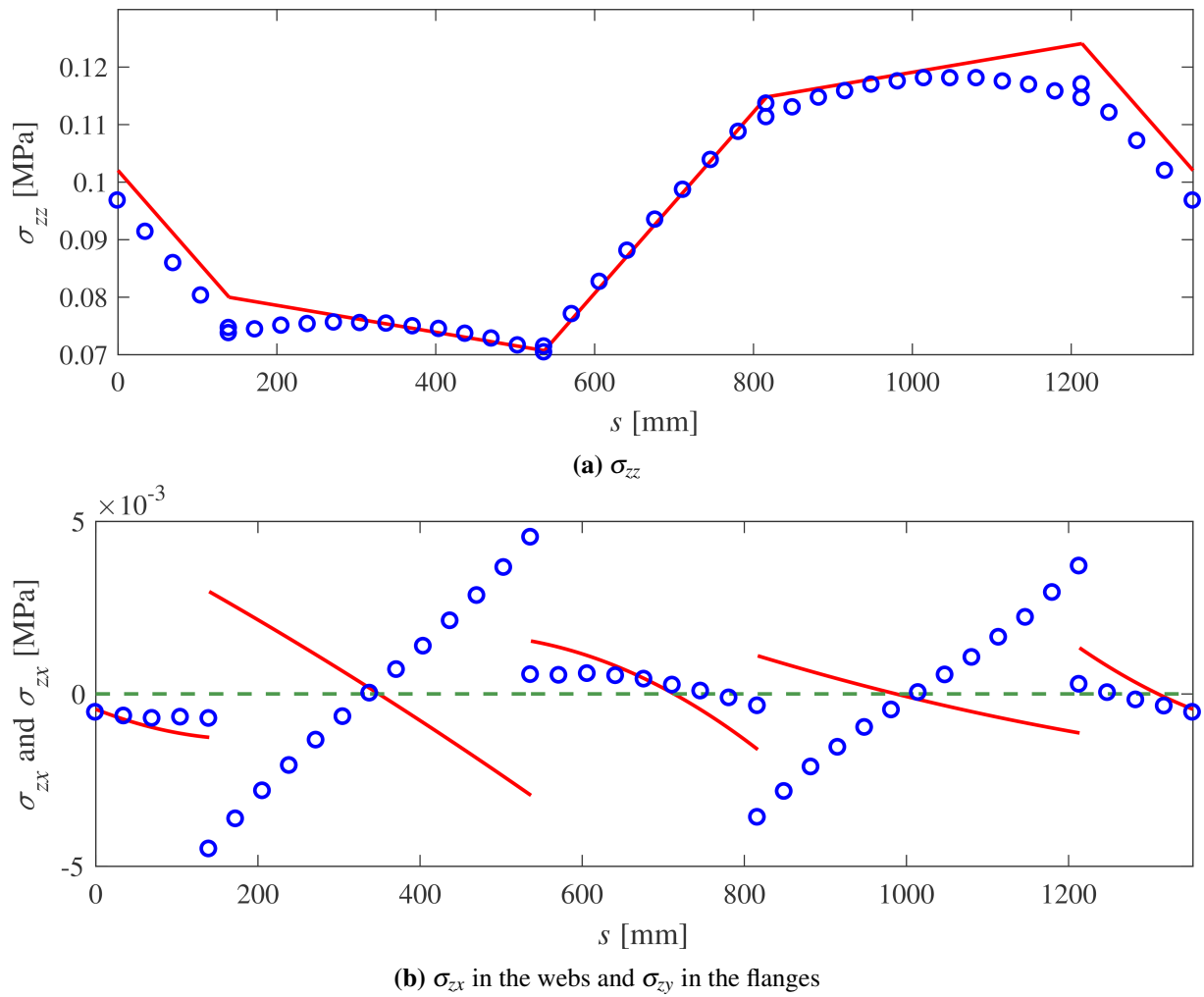


Figure 7.19: stresses in Section 25 for the “axial force” loading condition: extended shear stress formula (red line); FE analysis (blue dots); Jourawski’s shear stress formula (green dashed line).

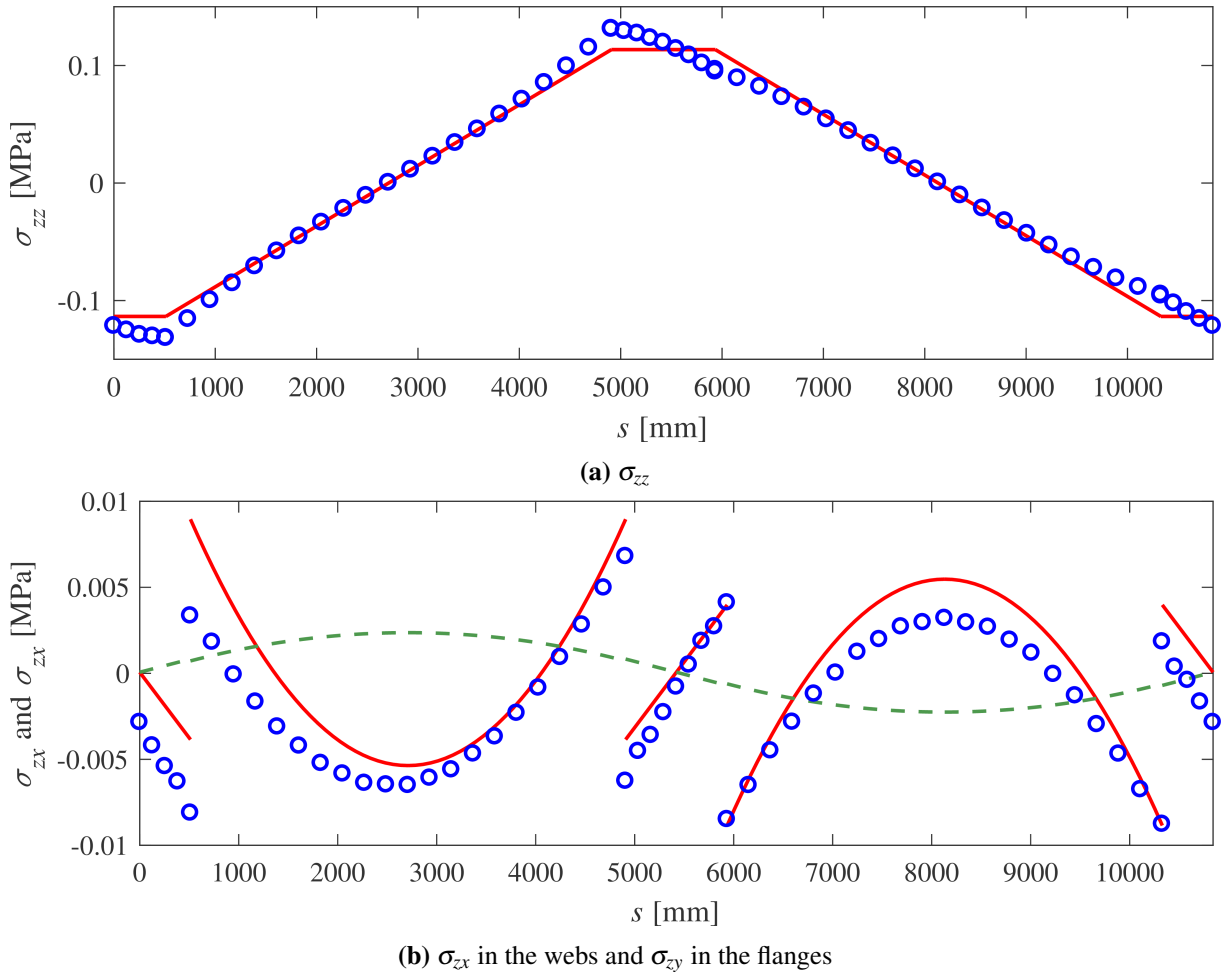


Figure 7.20: stresses in Section 6 for the “shear force” loading condition: extended shear stress formula (red line); FE analysis (blue dots); Jourawski’s shear stress formula (green dashed line).

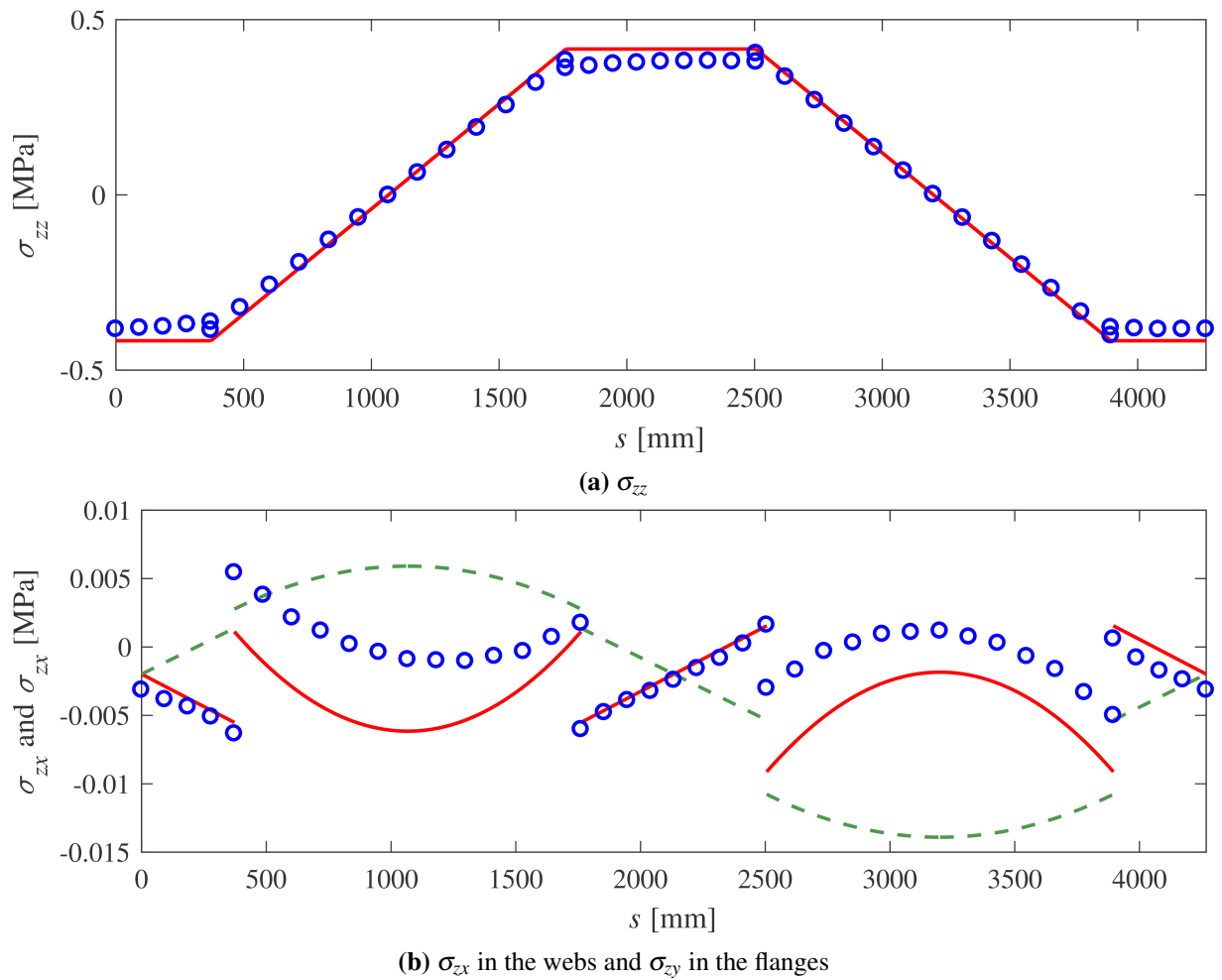


Figure 7.21: stresses in Section 16 for the “shear force” loading condition: extended shear stress formula (red line); FE analysis (blue dots); Jourawski’s shear stress formula (green dashed line).

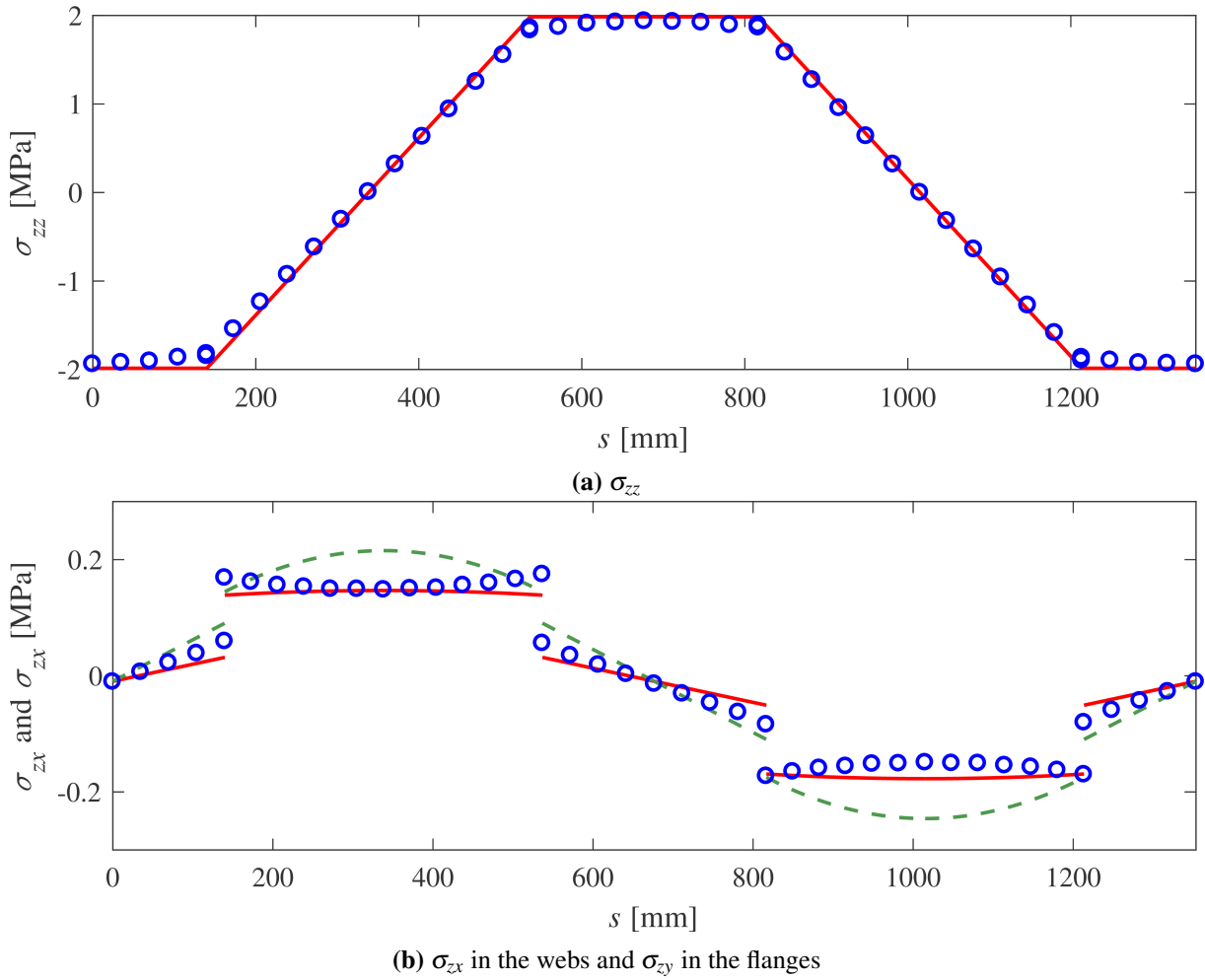


Figure 7.22: stresses in Section 25 for the “shear force” loading condition: extended shear stress formula (red line); FE analysis (blue dots); Jourawski’s shear stress formula (green dashed line).

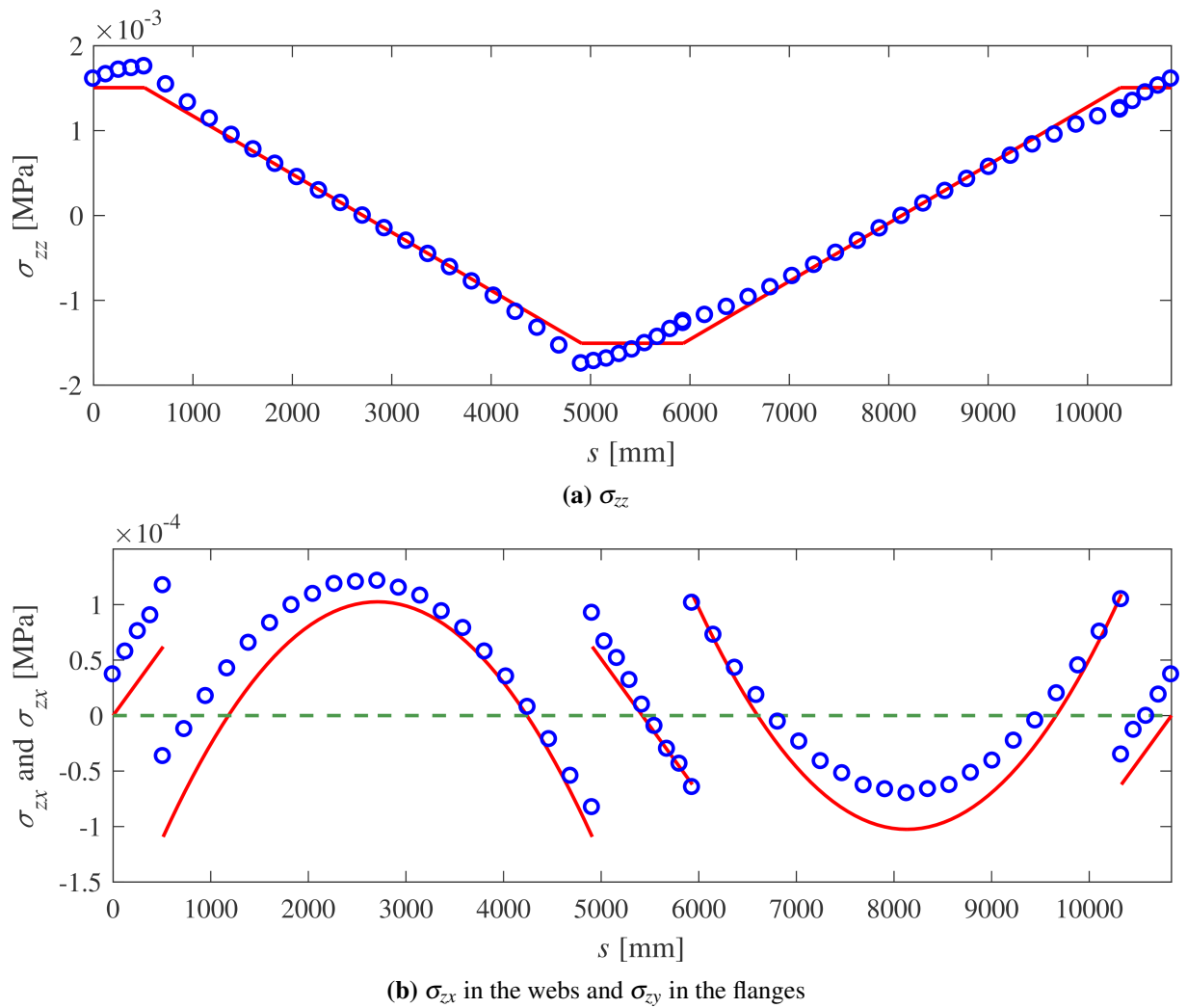


Figure 7.23: stresses in Section 6 for the “bending moment” loading condition: extended shear stress formula (red line); FE analysis (blue dots); Jourawski’s shear stress formula (green dashed line).

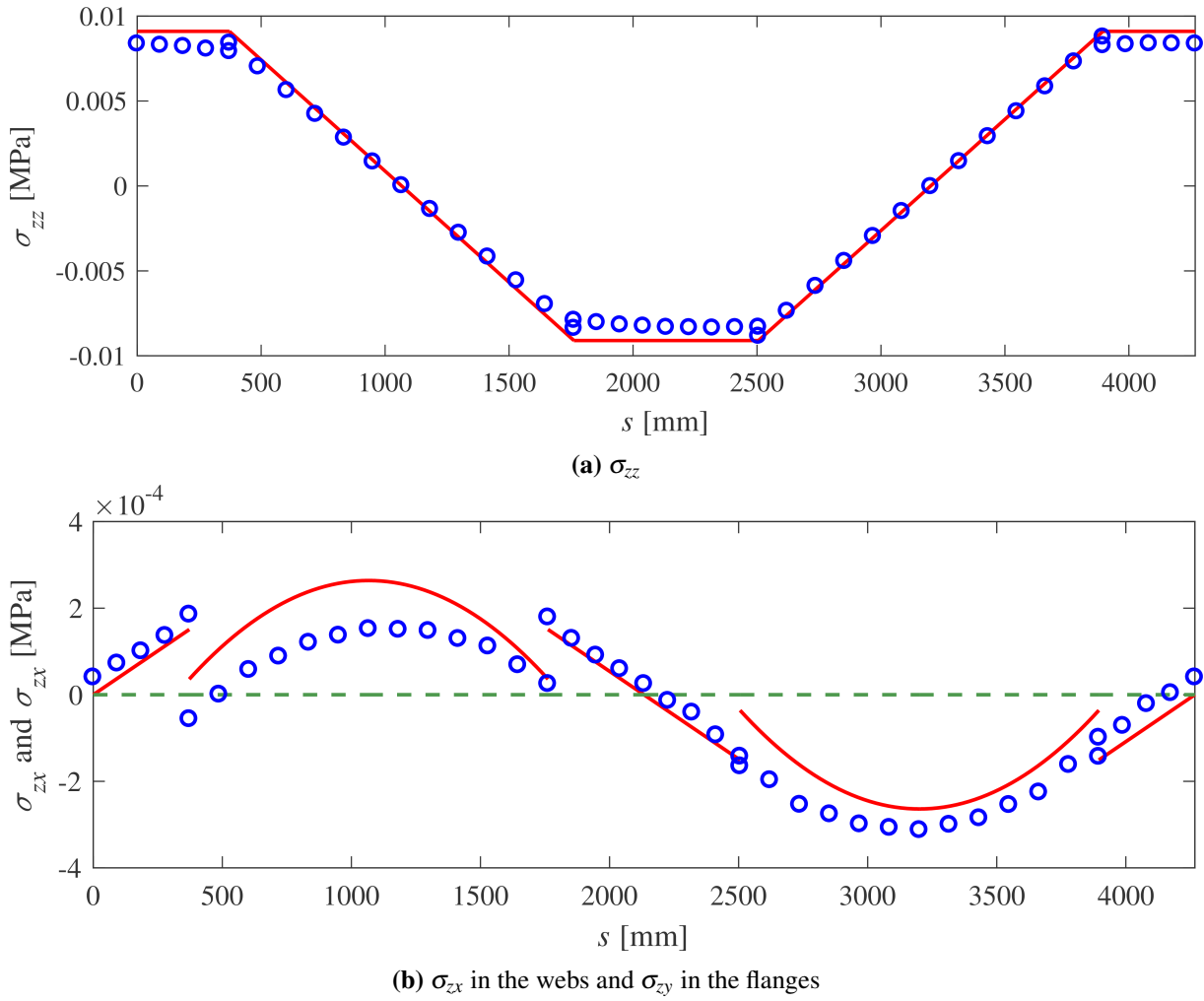


Figure 7.24: stresses in Section 16 for the “bending moment” loading condition: extended shear stress formula (red line); FE analysis (blue dots); Jourawski’s shear stress formula (green dashed line).

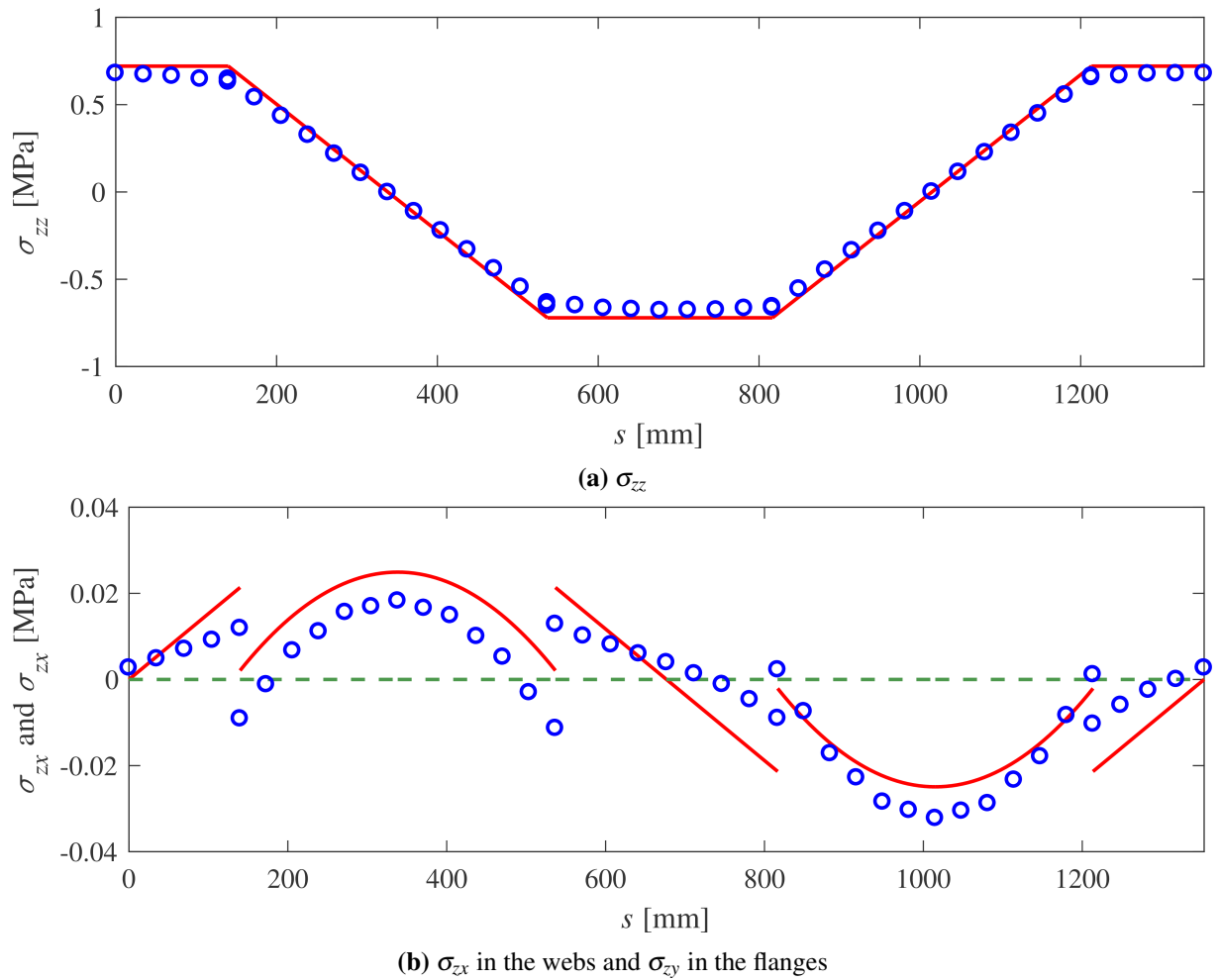


Figure 7.25: stresses in Section 25 for the “bending moment” loading condition: extended shear stress formula (red line); FE analysis (blue dots); Jourawski’s shear stress formula (green dashed line).

somewhat curved. Moreover, and in particular for Section 6, the effective cross section is not symmetric. Many of the differences which appear in the plots can be attributed to these geometric differences.

Nevertheless, we could not identify the real centreline of the beam, and we were forced to refer to cross sections perpendicular to the global z -axis. This is not the optimum for the use of the extended shear stress formula, which should be applied to sections orthogonal to the effective centreline of the beam. This is particularly evident in the “axial force” loading condition. In fact, the shear stresses induced by the axial force are generally very small if compared to those induced by the other internal forces. Being that this is not a straight centreline beam, the eccentricity of the external axial force applied had to be taken into account, but we were not able to quantify the torsional contribution and the shear component of such eccentric axial force. Even if small, these torsional and shear contributions could be present where the cross section is not perpendicular to the direction of the external axial load. This justifies the substantially erroneous prediction of our model in the case of the “axial force” loading condition.

In general, the shear stresses are of an order of magnitude smaller than that of the normal stresses, but are also present when the cross section is loaded by the bending moments and axial forces. Moreover, the contribution of the bending moment and of the axial force affects the stress distribution without changing the overall resultants, but by modifying the shape of the shear stress distributions. In particular, the location where shear stress distributions reach the maximum and the minimum can change, as well as the intensity of such maximum and minimum values.

The comparison between the results of the extended shear stress formula and the classical Jourawski formula proved that the solution for prismatic beams gives unacceptable results in terms of shear stresses for tapered beams. On the other hand, in most cases the extended shear stress formula proves capable of predicting both the trend and the values of the effective shear stresses.

Part IV

Conclusions

Chapter 8

Conclusions and future developments

Summary. In this Chapter the main results achieved during the research activity are recalled and briefly commented. It has been shown that taper affects the distribution of stresses, and in particular the shear stresses. When designing structures with adhesively bonded elements, shear stresses play a primary role: the extended shear stress formula is capable of accurately predicting the distribution of such stresses, unlike the classical prismatic beam theory which may lead to erroneous predictions. Some remarks on aspects in need of further investigation in the future are also listed.

8.1 Conclusions

The aim of the research activity of the present thesis was to verify whether the classical beam theory for prismatic beams is still valid when applied to tapered beams, and to quantify the error committed when this is not possible. We focused on wind turbine blades and their design, which today rely mainly on analysis tool that were developed for prismatic beams.

In the literature, the interest concerning tapered beams is generally focused on specific highly advanced topics (such as the study of buckling, fatigue and damage tolerance, aero-elastic stability, etc.), and the validity of the classical beam theory is often taken for granted. Nevertheless, some authors have emphasised that taper deeply affects the behavior of beams, not only with regard to displacements or stiffness, but also with regard to the distribution of stresses.

Our approach started with a drastic simplification of the initial problem, neglecting some aspects that for the moment were considered of secondary importance, and focusing on the tapered geometry only.

First of all we investigated the planar problem of a cantilever tapered beam, modeled as a truncated wedge. The solution – complete in terms of displacements, strains and stresses – was based on the classical elasticity theory which gave many interesting results. First of all, we had an initial confirmation that the distribution of stresses in tapered structures does not follow the same rules as in prismatic beams.

In particular, shear stresses are not only introduced by shear force, but also by the axial force and the bending moment. The contribution of the shear force is parabolic and is analogous to the one that can be observed in prismatic beams. The axial force induces a linear distribution of shear stresses in the cross section. Lastly, the bending moment (including the bending moment induced by the shear force) produces a parabolic distribution. A completely different distribution of stresses can result from the superposition of those single contributions: in particular, for the interaction between the stresses due to the shear and to the bending, which are both of the same order of magnitude.

Another remarkable result which was possible to deduce from the solution of the truncated wedge is that Navier's equation substantially also applied to tapered beams. The typical linear distribution tends to deviate a little at the top and bottom surfaces only for big taper angles (i.e. greater than 10°).

The solution obtained in terms of the classical elasticity theory, though fundamental, showed little practical applicability due to its complexity. Thus we proposed a different approach, based on equilibrium

considerations which resulted in a corrected version of the well known Jourawski shear stress formula. Such a formula takes into account all the above-mentioned contributions of the internal forces, and has the advantage of both extreme simplicity and generality.

In fact, we used the corrected shear stress formula not only to solve the problem of the truncated wedge, but also to extend the dissertation to three dimensional problems, solving both the conic hollow section beams and the tapered box girder. Finite element analyses proved that for those relatively simple geometries the formula is extremely effective. It has to be said that to date we are aware of very few attempts to extend the study of tapered beams from planar to three dimensional structures.

Now we can confidently state that classical prismatic beam solutions applied to tapered beams could be affected by significant errors. This error is particularly evident with regard to the shear stresses, whose distributions may significantly differ from what is predicted by the classical Jourawski theory. Although this change may have a relatively small impact on the overall stress in the beam in terms of von Mises stresses, the shear stresses introduced by taper could have a significant impact on specific aspects of the design of wind turbine blades. For example, by affecting the many adhesively bonded elements of the cross section.

Being able to predict with less uncertainty the stress state of a bonded joint will inevitably bring to a more wise design, with an optimised use of the quantity of adhesive, and with a potential economical benefit deriving from the reduction of construction materials used. Even a small reduction of adhesive in a specific part of the cross section of a 90m long blade could result in a significant reduction in costs, and such a reduction would be even greater if applied to the entire production in series.

Moreover, a clear and realistic picture of the stresses in the structural elements is mandatory in order to predict fatigue resistance and damage tolerance of the blade: the application of classical prismatic beam solutions could lead to significant errors on the part of designers.

8.2 Future developments

The application to the box girder of the DTU 10MW Reference Wind Turbine highlighted the potentials of the proposed approach, but also its limits.

First of all, the limitation regarding the shape of the cross section must be overcome. In the derivation of the extended shear stress formula, the classical Navier formula was adopted (Equation 5.8), and consequently the reference system taken into account has to be principal of inertia for the cross section. With the adoption of a more general formulation of the Navier equation, cross sections whose principal axes are not aligned with the reference system can be also investigated.

Also, the extended shear stress formula can be used to assess the shear stresses of open thin-walled cross section beams, but in its current formulation it is not applicable to non-symmetric closed thin-walled cross sections. By pending the study on strains and displacements, the derivation of proper compatibility equations could extend the application of the extended shear stress formula to multi-cellular thin-walled beams.

A fundamental development would be the overcoming of the hypothesis of cross sections made up of a homogenous material. As an example, in Figure 8.1, a bi-material cross section is shown: due to the different mechanical properties of materials a and b , the geometrical centre does not coincide with the elastic centre, and Navier's formula must be modified accordingly [Rivello, 1969]. Given adequate hypothesis on the kinematic of the beam and on the distribution of the stresses between layers of different properties, the study of layered and multi-material beams will be feasible by means of a further generalization of Navier's formula to non-homogeneous cross sections.

Modern wind turbine blades are commonly manufactured using fibre-reinforced materials, both in the form of laminate or sandwich (see Section 1.4.2). The introduction of the hypothesis of orthotropic and anisotropic material will allow us to work towards the aim of modelling real composite structures.

As shown in the application to the 10MW DTU Reference Wind Turbine, the results depend on the proper identification of the effective beam centreline, and will be crucial to further test the extended shear stress formula for the complex geometry of the box girder of a blade when an eccentric axial force is

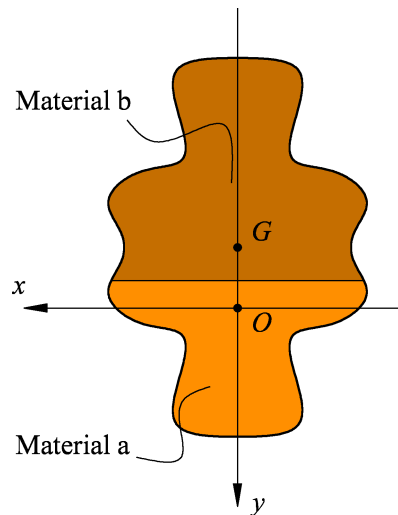


Figure 8.1: an example of bi-material cross section: the geometrical centre of the section, G , do not necessarily coincide with the elastic centre, O .

applied. In particular, it will be interesting to quantify the error committed when the considered cross sections are not orthogonal to the effective centreline of the beam. Taking into account such sections clearly violates the hypothesis of Euler-Bernoulli's beam theory. However, it is common practice for the designers to define the geometry of the blade with respect to a global reference system, so that the cross sections lie on planes parallel to each other and are not necessarily orthogonal to the beam centreline.

As a final step, the development of a proper computational tool which could incorporate the extended shear stress formula – or the updating of the already existing one – will undoubtedly be useful for both the academic and the industrial sectors. This tool should not substitute the 3D finite elements analysis, but should be an extension of a beam model. As discussed in Section 1.5, 1D beam models are widely used in design, because they allow a fast assessment of the displacements of the beam and of the stresses in the cross sections. Unfortunately, the 1D beam models currently in use are based on the hypothesis that the beam is prismatic. The incorporation of the effect of taper in a 1D model could help to avoid potentially faulty results.

Bibliography

- I. H. A. Abbott and A. E. von Doenhoff. *Theory of Wing Sections: including a summary of airfoil data*. Dover Publications, Inc., Mineola, 1959. unabridged republication of the edition published by the McGraw-Hill Book Company, Inc., New York, 1949.
- R. D. Adams and W. C. Wake. Structural adhesive joints in engineering. *Journal of Polymer Science Part C: Polymer Letters*, 23(11), 1984.
- S. S. Antman. *Nonlinear problems of elasticity*. Springer-Verlag, New York, second edition, 2005.
- T. Ashwill and T. Leonard. Developments in blade shape design for a Darrieus Vertical Axis Wind Turbine. *Sandia Report*, 86, 1986.
- E. H. Atkin. Tapered beams: suggested solutions for some typical aircraft cases (Parts I & II). *Aircraft Engineering and Aerospace Technology*, 10(11):347–351, 1938a.
- E. H. Atkin. Tapered beams: suggested solutions for some typical aircraft cases (Part III). *Aircraft Engineering and Aerospace Technology*, 10(12):371–374, 1938b.
- C. Bak, F. Zahle, R. Bitsche, T. Kim, A. Yde, L. C. Henriksen, A. Natarajan, and M. H. Hansen. Description of the DTU 10 MW Reference Wind Turbine. Technical report, DTU Wind Energy, July 2013a. DTU Wind Energy Report-I-0092.
- C. Bak, F. Zahle, R. Bitsche, A. Yde, L. C. Henriksen, and M. H. Hansen. Design and performance of a 10 MW wind turbine. *J. Wind Energy*, July 2013b.
- G. Balduzzi, M. Aminbaghai, E. Sacco, J. Füssl, J. Eberhardsteiner, and F. Auricchio. Non-prismatic beams: A simple and effective Timoshenko-like model. *International Journal of Solids and Structures*, 90:236–250, 2016.
- G. Balduzzi, G. Hochreiner, J. Füssl, and F. Auricchio. Serviceability analysis of non-prismatic timber beams: Derivation and validation of new and effective straightforward formulas. *Open Journal of Civil Engineering*, 7:32–62, 2017a.
- G. Balduzzi, E. Sacco, F. Auricchio, and J. Füssl. Non-prismatic thin-walled beams: critical issues and effective modeling. In *XXIII AIMETA Conference*, Salerno, 2017b.
- G. Balduzzi, M. Amindaghai, F. Auricchio, and J. Füssl. Planar Timoshenko-like model for multilayer non-prismatic beams. *International Journal of Mechanics and Materials in Design*, 14(1):51–70, 2018.
- J. Banerjee and F. Williams. Exact Bernoulli-Euler static stiffness matrix for a range of tapered beams-columns. *International Journal for Numerical Methods in Engineering*, 23:2289–2302, 1985.
- O. A. Bauchau and J. I. Craig. *Structural analysis: with applications to aerospace structures*. Springer, Netherlands, 2009.
- A. Betz. Die windmühlen im lichte neuerer forschung. *Die Naturwissenschaften*, 15(46):905–914, 1927.
- A. Betz. Windmills in the light of modern research. Technical Memorandum, National Advisory Committee for Aeronautics (NACA) [NACA-TM-474], August 1928.
- J. P. Blasques. *Optimal design of laminated composite beams*. PhD thesis, Danish Technical University, August 2011.
- J. P. Blasques, R. Bitsche, B. Lazarov, M. Stolpe, V. Fedorov, and D. Verelst. User manual for BECAS: A cross section analysis tool for anisotropic and inhomogeneous beam sections of arbitrary geometry.

- Technical report, Risø National Laboratory, 2014.
- F. Bleich. *Stahlhochbauten, ihre Theorie, Berechnung und bauliche Gestaltung (1. Band.)*. Springer, 1932.
- B. A. Boley. On the accuracy of the Bernoulli-Euler theory for beams of variable section. *Journal of Applied Mechanics*, 30(3):373–378, 1963.
- O. T. Bruhns. *Advanced mechanics of solids*. Springer-Verlag, Berlin Heidelberg, 2003.
- T. Burton, N. Jenkins, D. Sharpe, and E. Bossanyi. *Wind energy handbook*. John Wiley & Sons Ltd, second edition, 2011.
- S. D. Carothers. Plane strain in a wedge, with applications to masonry dams. *Proceedings of the Royal Society of Edinburgh*, 33:292–306, 1914.
- C. E. S. Cesnik and D. H. Hodges. VABS: A new concept for composite rotor blade cross-sectional modeling. *The Journal of the American Helicopter Society*, 42(1):27–38, 1997.
- F. J. P. Chaves, L. F. M. da Silva, M. S. F. de Moura, D. A. Dillard, and V. H. C. Esteves. Fracture mechanics tests in adhesively bonded joints: A literature review. *The Journal of Adhesion*, 90:955–992, 2014.
- W. L. Cleghorn and B. Tabarrok. Finite element formulation of a tapered Timoshenko beam for free lateral vibration analysis. *Journal of Sound and Vibration*, 152(3):461–470, 1992.
- Commission Européenne. Memo on the renewable energy and climate change package [MEMO/08/33]. Communiqués de presse, January 2008.
- L. F. M. da Silva, P. J. C. das Neves, R. D. Adams, and J. K. Spelt. Analytical models of adhesively bonded joints – Part I: Literature survey. *International Journal of Adhesion & Adhesives*, 29:319–330, 2009.
- Dassault Systèmes. Abaqus, Release 6.13, 2013. Vélizy-Villacoublay Cedex, France.
- DNV-GL-0376. *Rotor blades for wind turbines*. Det Norske Veritas (DNV), Copenhagen, December 2015. [Standard DNV-GL-0376].
- GDWT-2002. *Guidelines for Design of Wind Turbines*. Det Norske Veritas (DNV) and Risø National Laboratory, Copenhagen, second edition, 2002.
- J. D. Downer, K. C. Park, and J. C. Chiou. Dynamics of flexible beams for multibody systems: A computational procedure. *Computer Methods in Applied Mechanics and Engineering*, 96(3):373–408, 1992.
- P. Dumitrache. Shear stresses in beams with variable cross section, subjected to non-uniform bending. *The Annals of “Dunarea De Jos” University of Galati*, Fascicle XIV:39–44, 2012.
- M. Eisenberger and Y. Reich. Static, vibration and stability analysis of non-uniform beams. *Computers & Structures*, 31(4):567–573, 1989.
- S. R. Eugster. *Geometric continuum mechanics and induced beam theories*. Springer International Publishing, 2015.
- B. G. Galerkin. On the problem of stresses in dams and retaining walls with trapezoidal profiles. *Sbornik Leningr. Inst. Inzh. Putei. Soobshch.*, 99:147–170, 1929.
- M. Ghorashi. *Statics and Rotational Dynamics of Composite Beams*. Springer International Publishing, 2016.
- V. Giavotto, M. Borri, P. Mantegazza, G. Ghiringhelli, V. Carmaschi, G. C. Maffioli, and F. Mussi. Anisotropic beam theory and applications. *Computers & Structures*, 16(1-4):403–413, 1983.
- D. M. Gleich. *Stress analysis of structural bonded joints*. PhD thesis, Delft University, 2002.
- M. O. L. Hansen. *Aerodynamics of wind turbines*. Earthscan, second edition, 2008.
- E. Hau. *Wind turbines: fundamentals, technologies, application, economics*. Springer-Verlag, third edition, 2013.
- H. E. Hinnant. Derivation of a tapered p-version beam finite element. National Aeronautics and Space

- Administration, August 1989. [NASA TP-2931].
- J. C. C. Ho. *Modeling spanwise nonuniformity in the cross-sectional analysis of composite beams*. PhD thesis, Georgia Institute of Technology, August 2009.
- D. H. Hodges, A. Rajagopal, J. C. C. Ho, and W. Yu. Stress and strain recovery for the in-plane deformation of an isotropic tapered strip-beam. *J. Mech. Mater. Struct.*, 5(6):963–975, 2010.
- C. Hwu and T. C. T. Ting. Solutions for the anisotropic elastic wedge at critical wedge angles. *Journal of Elasticity*, 24:1–20, 1990.
- D. K. Jadan. Analytical solution of tapered bimodal beams. *Anbar Journal for Engineering Sciences*, pages 79–100, 2012.
- R. M. Jones. *Mechanics Of Composite Materials*. Materials Science and Engineering Series. Taylor & Francis, Inc., Philadelphia, second edition, 1999.
- D. L. Karabalis and D. E. Beskos. Static, dynamic and stability analysis of structures composed of tapered beams. *Computers & Structures*, 16(6):731–748, 1983.
- R. J. Knops and P. Villaggio. Recovery of stresses in a beam from those in a cone. *Journal of Elasticity*, 53:65–75, 1999.
- J. L. Krahula. Shear formula for beams of variable cross section. *AIAA Journal*, 13(10):1390–1391, 1975.
- E. Kreyszig. *Differential geometry*. Dover Publications, Inc., Mineola, 1991. unabridged republication of the edition published by University of Toronto Press, Toronto, 1959.
- A. E. H. Love. *A Treatise on the Mathematical Theory of Elasticity*. Dover Books on Engineering Series. Dover Publications, Inc., New York, fourth edition, 1944. unabridged republication of the fourth edition published by the Cambridge University Press, 1927.
- H. H. Mabie and C. B. Roger. Transverse vibrations of tapered cantilever beams with end loads. *The Journal of the Acoustical Society of America*, 36:463–469, 1964.
- D. J. Malcolm and D. L. Laird. Extraction of equivalent beam properties from blade models. *Wind Energy*, 10:135–157, 2007.
- IEC Online Collections. Online: October 30th, 2017. <https://collections.iec.ch/iec61400>, 2017.
- S. J. Medwadowski. Nonprismatic shear beams. *Journal of Structural Engineering*, 110(5):1067–1082, 1984.
- V. V. Meleshko. Selected topics in the history of the two-dimensional biharmonic problem. *Applied Mechanics Reviews*, 56(1):33–85, 2003.
- J. H. Michell. Elementary distributions of plane stress. *Proceedings London Mathematical Society*, 32(1):35–61, 1900.
- L. M. Milne-Thomson. *Theoretical Aerodynamics*. Dover Publications, Inc., fourth edition, 1973. unabridged republication of the fourth edition published by Macmillan and Company Limited, 1966.
- E. Oñate. *Structural Analysis with the Finite Element Method. Linear Statics. Beams, Plates and Shells*. CIMNE, first edition, 2013.
- A. Paglietti and G. Carta. Remarks on the current theory of shear strength of variable depth beams. *The Open Civil Engineering Journal*, 3:28–33, 2009.
- D. J. Peery. *Aircraft structures*. Dover Publications, Inc., Mineola, 2011. unabridged republication of the edition published by the McGraw-Hill Book Company, Inc., New York, 1950.
- A. Quispitupa, B. Vestergaard, and T. Sieradzan. Certification of wind turbine blades – the DNV procedure. In *European Wind Energy Conference and Exhibition, EWEC 2013*, Vienna, Austria, 2013.
- J. N. Reddy. *Mechanics of Laminated Composite Plates and Shells: Theory and Analysis*. CRC Press, second edition, 2003.
- R. M. Rivello. *Theory and analysis of flight structures*. McGraw-Hill, Inc., 1969.

- F. Romano. Deflections of Timoshenko beam with varying cross-section. *International Journal of Mechanical Sciences*, 38(8–9):1017–1035, 1996.
- H. R. Ronagh, M. A. Bradford, and M. M. Attard. Nonlinear analysis of thin-walled members of variable cross-section. *Computer and Structures*, 77:285–299, 2000.
- E. P. Russo and G. Garic. Shear-stress distribution in symmetrically tapered cantilever beam. *Journal of Structural Engineering*, 118(11):3243–3249, 1992.
- P. J. Schubel and R. J. Crossley. Wind turbine blade design. *Energies*, 5:3425–3449, 2012.
- A. Shooshtari and R. Khajavi. An efficient procedure to find shape functions and stiffness matrices of nonprismatic Euler-Bernoulli and Timoshenko beam elements. *European Journal of Mechanics ASolids*, 29:826–836, 2010.
- B. F. Sørensen, J. W. Holmes, P. Brøndsted, and K. Branner. Blade materials, testing methods and structural design. In W. Tong, editor, *Wind power generation and wind turbine design*, chapter 13, pages 417–465. WIT Press, 2010.
- F. Song, Y. Ni, and Z. Tan. Optimization design, modeling and dynamic analysis for composite wind turbine blade. *Procedia Engineering*, 13:369–375, 2011.
- A. Tena-Culunga. Stiffness formulation for nonprismatic beam elements. *Journal of Structural Engineering*, 122(12):1484–1489, 1996.
- The MathWorks, Inc. Matlab, Release 2016b, 2016. Natick, MA.
- S. P. Timoshenko. *Strength of Materials: Part I – Elementary Theory and Problems*. D Van Nostrand Company, Inc., 1940.
- S. P. Timoshenko. *History of Strength of Materials: With a Brief Account of the History of Theory of Elasticity and Theory of Structures*. Dover Civil and Mechanical Engineering Series. Dover Publications, 1953. unabridged and corrected republication of the edition published by the McGraw-Hill Book Company, Inc., New York, 1953.
- S. P. Timoshenko and J. M. Gere. *Mechanics of Materials*. Van Nostrand Reinhold, New York, 1972.
- S. P. Timoshenko and J. N. Goodier. *Theory of Elasticity*. Engineering Societies Monographs. McGraw–Hill Book Company, Inc., New York, 1951.
- S. P. Timoshenko and D. H. Young. *Theory of structures*. McGraw-Hill, second edition, 1965.
- N. S. Trahair and P. Ansourian. In-plane behaviour of web-tapered beams. *Engineering Structures*, 108: 47–52, 2016.
- I. Troen and E. L. Petersen. *European wind atlas*. Roskilde: Risø National Laboratory, 1989.
- P. Villaggio. Some extensions of Carothers’s paradox in plane elasticity. *Mathematics and Mechanics of Solids*, 3:17–28, 1997.
- V. Z. Vlasov. *Thin-Walled Elastic Beams*. Israel Program for Scientific Translations Ltd., Jerusalem, 1961.
- S. G. Voutsinas. Structural dynamics of wind turbines. In W. Tong, editor, *Wind power generation and wind turbine design*, chapter 4, pages 121–151. WIT Press, 2010.
- L. Vu-Quoc and P. Léger. Efficient evaluation of the flexibility of tapered I-beams accounting for shear deformations. *International Journal for Numerical Methods in Engineering*, 33:553–566, 1992.
- C. H. Wang and L. R. F. Rose. Failure analysis of adhesively bonded joints. In B. L. Karihaloo, Y. W. Mai, M. I. Ripley, and R. O. Ritchie, editors, *Advances in fracture research*, pages 587–594. Pergamon, 1997.
- L. Wang, X. Liu, and A. Kolios. State of the art in the aeroelasticity of wind turbine blades: Aeroelastic modelling. *Re-newable and Sustainable Energy Reviews*, 64:195–210, 2016.
- Wolfram Research, Inc. Mathematica, Version 7.0, 2008. Champaign, IL.
- M. Zhou, J. Zhang, J. Zhong, and Y. Zhao. Shear stress calculation and distribution in variable cross sections of box girders with corrugated steel webs. *Journal of Structural Engineering*, pages 1–10, 2016.

- O. C. Zienkiewicz, R. L. Taylor, and J. Z. Zhu. *The finite element method: its basis & fundamentals*. Elsevier Ltd., seventh edition, 2013.